Coherent terahertz radiation from laser-wakefield-accelerated electron beams

Jeroen van Tilborg

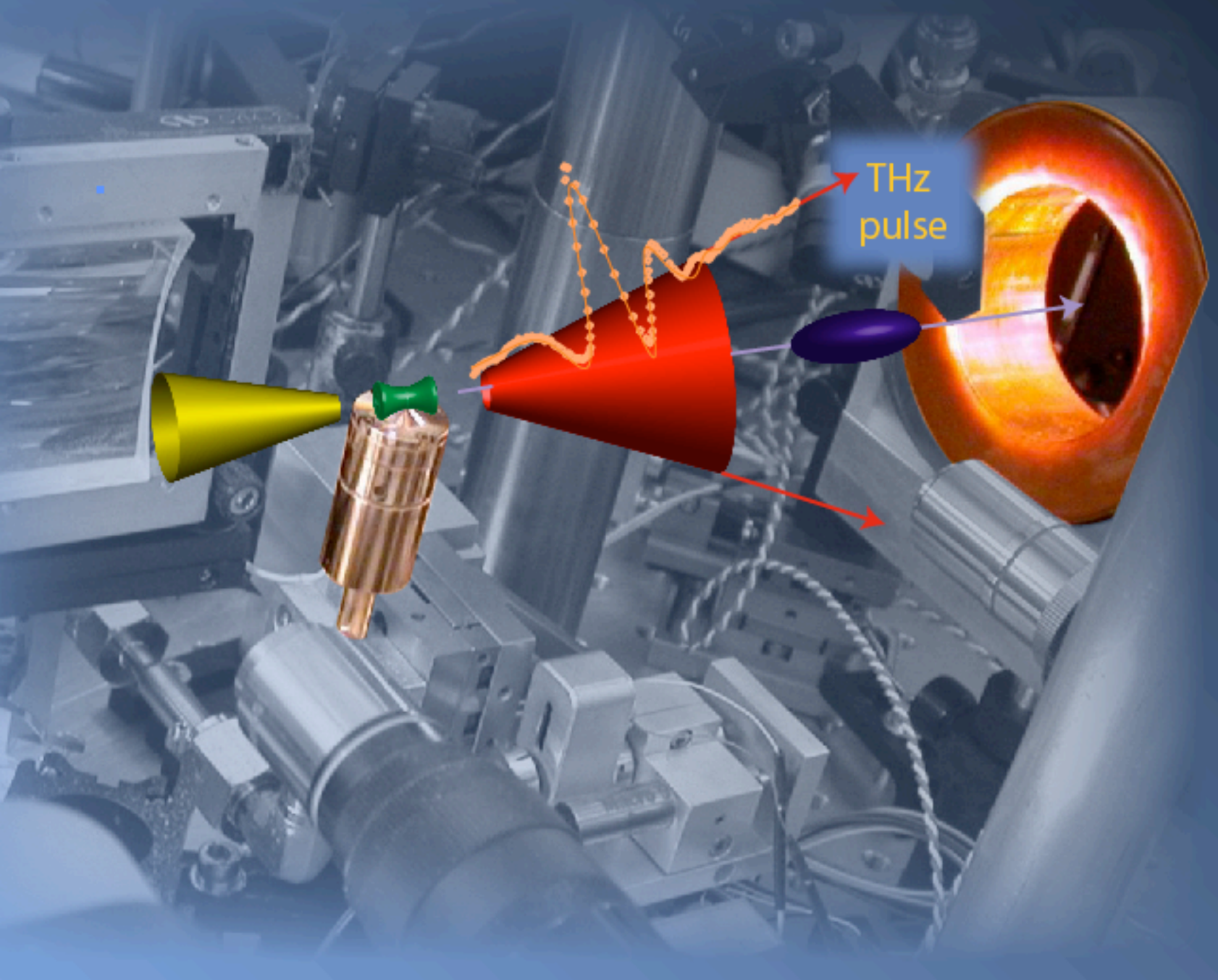

Coherent terahertz radiation from laser-wakefield-accelerated electron beams

PROEFSCHRIFT

ter verkrijging van de graad van doctor
aan de Technische Universiteit Eindhoven,
op gezag van de Rector Magnificus, prof.dr.ir. C.J. van Duijn,
voor een commissie aangewezen door het College voor Promoties
in het openbaar te verdedigen
op dinsdag 4 juli 2006 om 16.00 uur

door

Jeroen van Tilborg

geboren te Eindhoven

Dit proefschrift is goedgekeurd door de promotoren:

prof.dr. M.J. van der Wiel
en
prof.dr.ir. W.P. Leemans

Copromotor:
dr.ir. G.J.H. Brussaard

This research was performed at the Lawrence Berkeley National Laboratory in Berkeley, California.

CIP-DATA LIBRARY TECHNISCHE UNIVERSITEIT EINDHOVEN

Tilborg, Jeroen van

Coherent terahertz radiation from laser-wakefield-accelerated electron beams / by Jeroen van Tilborg. – Eindhoven : Technische Universiteit Eindhoven, 2006. – Proefschrift.
ISBN-10: 90-386-2521-9
ISBN-13: 978-90-386-2521-8
NUR 926
Trefwoorden: deeltjesversnellers / plasmagolven / terahertz-straling / nietlineaire optica
Subject headings: novel accelerators / electron beams / plasma waves /
terahertz radiation / ultrafast science / nonlinear optics

Printed by Printservice Technische Universiteit Eindhoven

Front cover: author's impression of the four components critical to the physics in this thesis, namely the laser (yellow), plasma (green), electrons (blue), and THz emission (red). Back cover: images of the Bay Area, taken by Pierre Michel.

Contents

Chapter 1

General introduction

1.1 Conventional versus plasma-based acceleration

Conventional accelerators (*e.g.* synchrotrons, cyclotrons, and linear accelerators) are widely used for the production of relativistic electron beams. One goal of the accelerator community is to study fundamental particle physics, where properties of sub-atomic particles present themselves for a very short time during high-energy particle collisions. The demands in terms of accelerator performance are aimed at higher and higher particle energies. For example, the International Linear Collider (ILC) is designed to produce electrons (and positrons) with an energy of 1 TeV (one trillion-electron-volt).

Conventional accelerators are based on radio-frequency (RF) electric fields set up in structures such as metallic disks, as depicted in Fig. 1.1(a). One major challenge for the conventional accelerator is its size: in order to produce high-energy electron bunches, long accelerator structures are necessary, as large as several kilometers. For example, to produce a 100 GeV electron bunch, an accelerating structure of $1 - 10$ kilometers long is required. Large structures are inevitable since the maximum sustainable electric field amplitude is limited to 10–100 MV m^{-1}, mainly due to field-induced breakdown of the cavity walls.

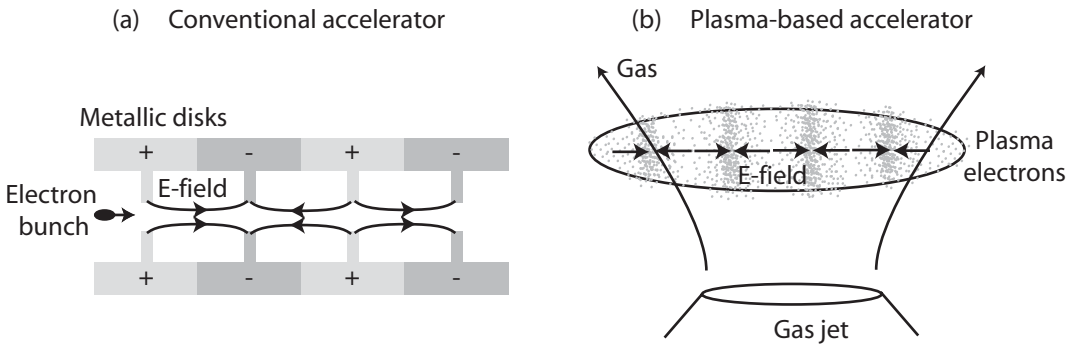

Fig. 1.1. (a) A conventional accelerator, where electric fields are setup in charged metallic structures, and (b) a plasma-based accelerator, where the local surplus and deficit of electrons (over a constant background ion density) yields strong electric fields.

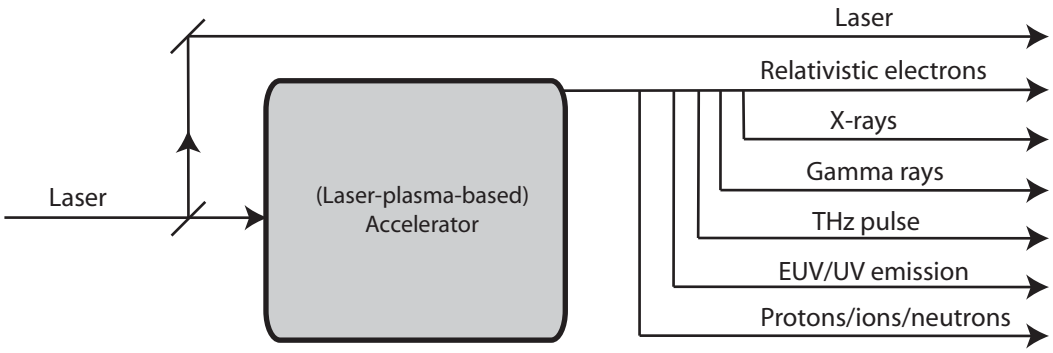

Fig. 1.2. Schematic overview of the possible types of particle and radiation emission that can be produced by relativistic electrons. Note that in the case of the laser-plasma-driven electron accelerator, the electrons and their emissions are intrinsically synchronized with the laser pulse as well, enabling a wide variety of pump-probe experiments.

Electron bunches from conventional accelerators are also used to produce radiation, such as X-rays, gamma rays, (extreme-)ultra-violet photons, and THz pulses, among others, as displayed in Fig. 1.2. Typically, dielectric structures (*e.g.* metallic foils and beam stoppers) or magnetic structures (*e.g.* bend magnets) are inserted in the electron beam path for the production of the radiation. A multi-disciplinary community consisting of scientists in the fields of physics, chemistry, biology, and medicine, use these different types of emission for pump-probe experiments. In a pump-probe experiment, one beam (the pump beam) is used to excite a change in a sample, while a second beam (the probe beam) arrives later in time in order to detect this change. Scanning the temporal delay between the pump and probe beam allows for characterization of the dynamical processes of interest. The time resolution of the pump-probe experiment is limited to the duration of the pump and probe beams, as well as to the stability of the temporal synchronization of the two.

Strong advantages of the conventional accelerator are the high repetition rate (number of bunches per second) that can be achieved, $10 - 1000$ Hz for linear accelerators and $10 - 500$ MHz for storage rings, and the stability in bunch properties such as charge, electron energy and beam pointing. However, the electron bunch duration and temporal synchronization are typically limited to the picosecond time scale, leading to limited time resolution.

The fact that plasmas can sustain much larger electric fields, on the order of $10 - 100$ GV m^{-1}, which is $2 - 3$ orders of magnitude larger than in a conventional accelerator, has inspired researchers to investigate the use of such an accelerator environment as stand-alone accelerator, or as injection stage to conventional accelerators. Furthermore, for laser-plasma-based accelerators, it has been demonstrated [1, 2] that bunches shorter than 50 fs were produced, which were intrinsically synchronized to the laser beam and other types of emission. The simultaneous availability of these beams (see Fig. 1.2) allows for studies of ultra-fast dynamical processes.

In a plasma, it is the local charge imbalance between electrons and ions that yields strong

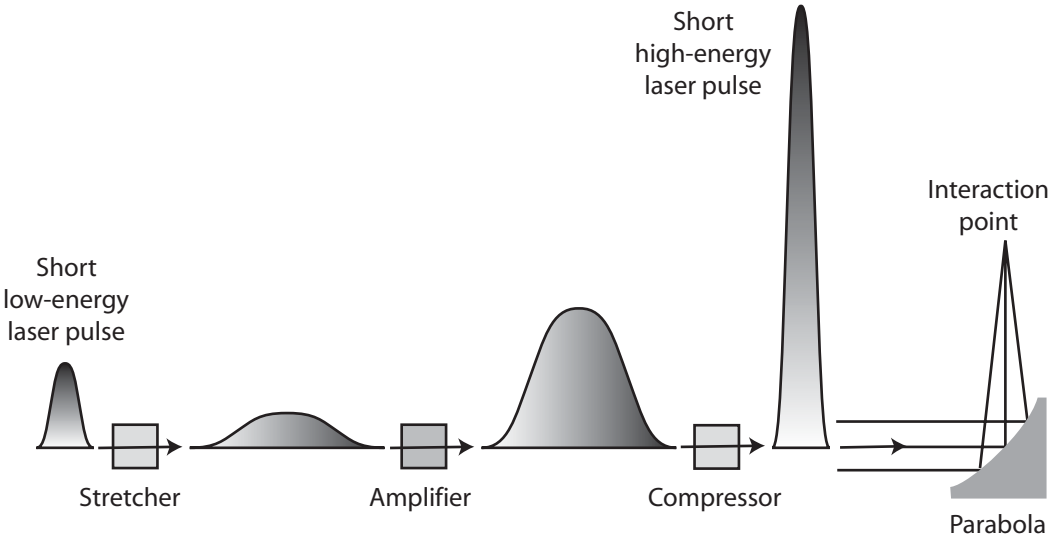

Fig. 1.3. Schematic of a Chirped Pulse Amplification laser system. A short Fourier-limited laser pulse undergoes stretching (without reduction of the bandwidth), amplification, and re-compression. The end result is a short high-energy laser pulse with, when focused by a parabola, an intensity in excess of $10^{18} - 10^{20}\ W\,cm^{-2}$.

fields (Gauss's law), see Fig. 1.1(b). Since the plasma can be confined to a small volume surrounded by vacuum, there are no issues of breakdown of cavity walls. In fact, even if the plasma is destroyed (diffused) after an electron bunch is accelerated, a simple emission of new gas creates a new accelerator structure for the next bunch. The high repetition rates of conventional accelerators can not be matched at present, but the prospect of large accelerating fields is a strong advantage and offers exciting possibilities.

1.2 The laser wakefield accelerator

Various schemes for plasma-based acceleration have been discussed in the literature and demonstrated in the laboratory, with two comprehensive overviews written by Esarey *et al.* [3, 4]. One scheme relies on the interaction of an intense laser beam with a plasma, in which case the accelerator is referred to as the laser wakefield accelerator (LWFA). The LWFA is the type of accelerator discussed in this thesis. This configuration was first proposed by Tajima and Dawson [5]. Through the laser ponderomotive force, the rising edge of the laser pulse envelope pushes away the background plasma electrons. Once the laser pulse is gone, the force resulting from the charge separation initiates a density oscillation. The phase velocity of the electro-static density oscillation is roughly equal to the group velocity of the laser. The charge oscillation is also referred to as the wake or plasma wave. In the most basic scheme, the electron bunch is produced through self-trapping of background plasma electrons in the wake. Since most pump-probe experiments rely on a laser beam (either as pump or probe beam), the availability of a synchronized laser pulse is a strong advantage of the LWFA.

The minimal laser intensity that is needed to drive a suitable plasma wave is on the order of $> 10^{18}$ W cm^{-2} [3]. Up until 1985, the damage threshold for laser amplifying crystals did not allow for production of such intense laser pulses using compact laser systems. The realization of the Chirped Pulse Amplification (CPA) technique, reported in 1985 by Strickland and Mourou [6], led to the production of laser pulses with intensities in excess of $10^{18} - 10^{20}$ W cm^{-2}. The experimental implementation of CPA provided the start for significant experimental progress towards laser-driven plasma-based accelerators.

A typical CPA laser system is depicted in Fig. 1.3. The laser pulse from an oscillator has a relatively large bandwidth (with the various frequency components illustrated by the different grey tones). Since the relative phase of each frequency component is initially zero (the grey tones have a vertical gradient), a short pulse ($\simeq$20–30 fs) is produced, see the left side of Fig. 1.3. The first step towards a high-energy short pulse is the propagation of the laser pulse through a stretcher. The pulse experiences dispersion since some frequencies are delayed with respect to others (the grey tones now have a horizontal gradient), also referred to as "chirp". This results in a longer ($\gtrsim$ 100 ps) low-intensity pulse with conserved bandwidth. The second step is the amplification process, typically in a titanium-sapphire (Ti:Al_2O_3) crystal, where the laser pulse energy can increase to $\gtrsim$ 1 J. The third step is to reverse the dispersion process of step 1 by means of a compressor. The frequencies that were delayed with respect to others now experience a shorter optical path, such that all frequencies are added to reconstruct a short pulse. As a result, a short ($\lesssim$50 fs) high-energy pulse is produced. Focusing optics (final laser spotsize $\simeq 5 - 20$ μm) deliver an intense pulse to an interaction point, with intensities on the order of $10^{18} - 10^{20}$ W cm^{-2}. In generic LWFA experiments, these intense laser pulse are focused onto a plasma from a gas jet or other plasma source, leading to the production of relativistic electron bunches.

1.3 Electron bunch characterization: analysis of THz emission

Over the years, many groups have reported their progress on the LWFA [7–12], with breakthrough results obtained in 2004 [13–15]. In order to understand the physics of LWFAs, to improve their performance, and to demonstrate their applicability, a large variety of diagnostics has been implemented by groups worldwide. Laser properties before and after the plasma interaction have been measured. The plasma density profile, structure of the plasma wake, charge of the electron bunch, energy distribution of the bunch, transverse charge profile, and bunch divergence have been characterized. The community has demonstrated that relativistic bunches, with charge ranging from 10 pC to multi-nC, at energies from several MeV to >500 MeV, and with energy spreads from few-percent to 100%, have been produced under various experimental conditions. Differences in experimental conditions include laser power, laser spot size, plasma density and plasma size.

However, from an experimental point of view, little was known about the temporal bunch profile. Theory predicts [16, 17] bunches with a length of several plasma wavelengths,

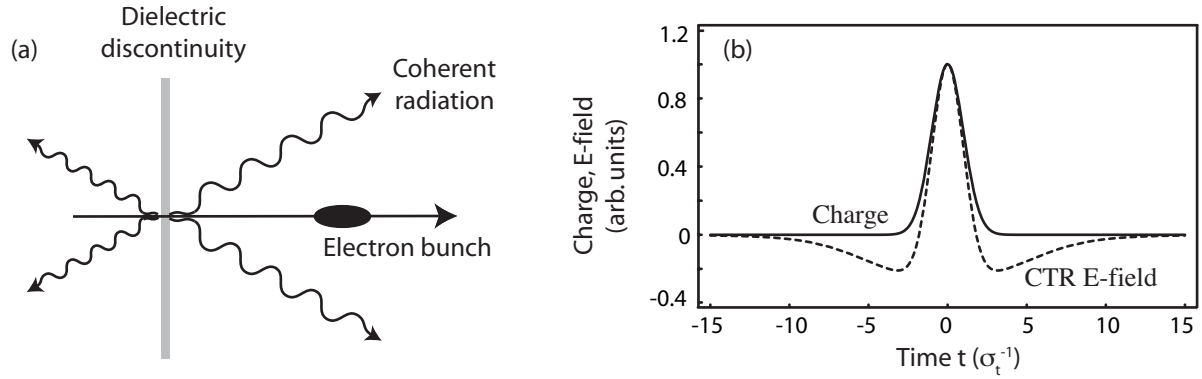

Fig. 1.4. (a) Schematic for the production of coherent transition radiation (CTR) as an electron bunch propagates through a change in dielectric environment (such as the plasma-vacuum interface). (b) Comparison between the temporal charge profile (solid curve) and the electric field profile of the CTR pulse (dashed curve). The horizontal axis (time) is normalized to the (rms) bunch duration σ_t.

typically on the order of 5–30 μm. Direct proof of such short bunch structure is one of the key goals for the laser-plasma community: it demonstrates the production of high-quality bunches as well as the applicability of the LWFA for femtosecond pump-probe applications. This thesis will, for the first time, show [1, 2, 18] that the LWFA-produced bunches are indeed very short [$\leqslant$50 fs (root-mean-square or rms) in length], and that they are intrinsically synchronized to both the laser beam and electron-bunch-produced THz pulse, with a synchronization stability better than 10 fs.

In conventional accelerators, two experimental techniques have recently been used for temporal characterization of electron bunches. One technique relies on the direct measurement of the self-fields of the bunch (Coulomb field). By probing the effect of the bunch self-fields in an electro-optic crystal, the bunch duration can be measured [19–23]. Another technique is based on the emission of coherent radiation by the electron beam [1, 2, 18, 24–33]. The emission is produced when the bunch travels through a magnetic field (emission of coherent synchrotron radiation), or when the bunch travels through a change in dielectric environment. In the latter case, the radiation is referred to as coherent transition radiation (CTR), as conceptually introduced by Ginzburg and Frank in 1946 [34] and treated more extensively by Ter-Mikaelian [35]. The concept of CTR emission is depicted in Fig. 1.4(a). In experiments at conventional accelerators, typically a metallic foil is positioned in the electron bunch path to provide the necessary dielectric discontinuity (dielectric constant changes from $\epsilon = \infty$ to $\epsilon = 1$). To illustrate the close correlation between the temporal bunch profile and the CTR field profile, both profiles are plotted in Fig. 1.4(b). The time axis is normalized to the (rms) bunch duration σ_t. It is due to diffraction effects that negative side-wings are present in the CTR waveform. The CTR field profile in Fig. 1.4(b) was derived from Eq. (3.26), with parameters $\mu = 0.5$ and $u \sin\theta = 0.1$, which will be defined in Sec. 3.4.1.

In the LFWA, it is not necessary to insert a metallic foil in the electron beam path for CTR generation. It was experimentally demonstrated by Leemans *et al.* [29, 31] and van Tilborg *et al.* [1, 2, 18], and theoretically described by Schroeder *et al.* [30] and van Tilborg *et al.* [2, 32], that the plasma-vacuum boundary already acts as the emitting dielectric discontinuity. The dielectric function in a plasma [36] can be approximated by

$$\epsilon(\omega) = 1 - \frac{\omega_p^2}{\omega^2}, \tag{1.1}$$

with ω the angular frequency, $\omega_p = 5.64 \times 10^4 \times \sqrt{n_0\ [\mathrm{cm}^{-3}]}$ the plasma frequency, and n_0 the plasma density in units of $[\mathrm{cm}^{-3}]$. From Eq. (1.1) it can be seen that the plasma-vacuum interface has indeed a strong dielectric discontinuity for frequencies $\omega \lesssim \omega_p$, resulting in LWFA-produced CTR emission.

Because the LWFA-produced electron bunches have a bunch divergence on the order of <50 mrad, a high peak current (> 10 kA), and a finite energy spread ($\gtrsim 1\%$), the electron bunches are subject to ballistic and space-charge-related debunching [37]. The significance of these effects provides a strong motivation for relying on CTR production from the plasma-vacuum boundary rather than from an externally-positioned metallic foil: at the plasma-vacuum boundary, due to partial space-charge shielding in the plasma and the limited propagation distance of the electron bunch towards the boundary ($\lesssim 0.5$ mm), the debunching effects are still negligible. The temporal duration of the bunch is therefore still of femtosecond nature, and the coherent radiation spectrum lies in THz (10^{12} Hz) regime. Henceforth, the LWFA-produced CTR pulse will also be labeled as the "THz pulse".

In addition to the emission of CTR, other mechanisms for THz generation through laser-plasma interactions exist, such as THz radiation from the plasma wave excitation [38, 39], from excitation of Cerenkov wakes in a magnetized plasma [40, 41], and through linear mode conversion [42, 43]. The work in this thesis will show that the intense THz radiation observed from the LWFA is attributed to CTR, and not to the other mechanisms. This conclusion is based on extensive analysis of measured temporal and spectral THz waveforms, THz scaling with charge and polarization, and comparison to theory.

1.4 Applications for intense THz pulses

It was shown in Fig. 1.4(b) that the THz pulse from a compact electron bunch is short (femtosecond scale), has a single-cycle field waveform, and (therefore) has a broad-bandwidth spectrum. For bunches on the order of 50 fs (rms) duration, the spectrum covers the $0 - 10$ THz regime. Further analysis in Sec. 3.5 will show that these THz pulses can contain > 10 μJ of energy, with peak electric fields in excess of 10 MV cm^{-1} at focus.

Intense radiation at THz frequencies is of interest for applications such as medical and biological imaging [44], material characterization [45], semiconductor imaging [46–49], surface chemistry, and high-field condensed matter studies [50]. For THz field amplitudes in

excess of $\simeq 1$ MV cm^{-1}, the THz pulse becomes useful as a pump beam, and not just as a probe beam. For example, Nordstrom *et al.* [47] applied a THz pulse as a pump beam to study the dynamical Franz-Keldysh effect in semiconductors. Since conventional laser-based THz sources (*e.g.* optical rectification or the photoconductive antenna) provide peak THz fields limited to $\lesssim 50$ kV cm^{-1}, the electron-bunch-based THz source might prove useful in future THz-pump experiments. Demonstration of the high-field single-cycle nature of the LWFA-produced THz pulses is therefore relevant for users.

Spatio-temporal coupling of the THz fields at focus will affect the interpretation of the results from THz pump-probe experiments, as well as from experiments on electron bunch characterization. While studies on spatio-temporal coupling have been performed with scanning techniques on conventional low-field laser-based THz sources [51–54], the LWFA-produced high-field THz pulses, which are subject to shot-to-shot fluctuations, require single-shot spatio-temporal measurement techniques. The work described in this thesis will, for the first time, show that spatial, temporal, and spectral characterization techniques (both scanning and single-shot) are experimentally realized, and that LWFA-produced THz pulses are ready to be used in pump-probe experiments.

1.5 About the thesis

The work described in this thesis, both theoretical and experimental, was performed at the LOASIS laser facility, part of the Lawrence Berkeley National Laboratory (LBNL), Berkeley, California. While I was a graduate student in the group of prof.dr. M.J. van der Wiel at the Eindhoven University of Technology, Eindhoven, the Netherlands, I spent the full extent of my Ph.D. at the LOASIS laser facility, under supervision of its group leader prof.dr.ir. W.P. Leemans.

From a theoretical point of view, this thesis will present novel insight on THz emission, such as dependence on electron momentum distribution, plasma-vacuum effects, diffraction effects, temporal field profiles, pulse energy estimates, and spatio-temporal coupling. From an experimental point of view, novel results cover THz characterization with respect to pulse energy, peak electric field, polarization, charge scaling, temporal field profile (scanning and single-shot techniques), coherent spectrum, and 2D imaging. The results demonstrate for the first time the femtosecond LWFA-produced bunch duration, as well as LWFA stability in terms of bunch length and temporal synchronization between the laser, electron bunch, and THz pulse. Also, novel results on single-shot spatio-temporal coupling of the focused broad-bandwidth THz pulses are presented.

Chapter 2 will present an overview of the LWFA, with emphasis on the generation of short electron bunches. The concepts of plasma wave generation, laser self-modulation, self-trapping of electrons, beam loading, and dephasing, will be introduced. The electron bunch production in two different experimental schemes will be presented, namely the unchanneled self-modulated LWFA and the channel-guided LWFA. The first configuration

is applied for the THz experiments described in this thesis, while THz production from the channel-guided LWFA might be advantageous in future experiments.

Chapter 3 will discuss the theoretical framework of CTR (THz radiation). A set of equations derived for CTR from a sharp metal-vacuum boundary will be applied to the LWFA-related plasma-vacuum boundary. Diffraction from the limited-sized transverse boundary and effects related to the electron momentum distribution are included. CTR analysis in both the spectral and temporal domains will be presented. Theoretical estimations on the THz pulse energy and peak electric field are given.

A first set of experimental results will be presented in Chapter 4. These experiments are all based on the measurement of the THz energy with a bolometer (energy detector). Bolometer-based experiments include THz energy scaling with charge and polarization, but also a pump-probe technique (semiconductor switching) that allows for an estimation of the THz pulse duration.

Chapter 5 will present the technique of electro-optic sampling (EOS), applied to the THz pulse. Through this technique the temporal electric field profile (amplitude and phase) and the coherent spectrum (amplitude and phase) are measured. Several experimental approaches have been performed, including a scanning technique and two different single-shot techniques. An extensive theoretical treatment of EOS, including crystal effects, is presented in Appendix C.

While Chapter 5 discusses the temporal and spectral THz characterization, Chapter 6 will focus on 2D THz imaging. An experimental technique based on EOS will be used for single-shot THz spot measurements. Substructure in the spatial THz profile, as well as substructure in the temporal profiles presented in Chapter 5, suggests spatio-temporal coupling. A heuristic 1D-transverse picture of the coupling for a coma-dominated THz pulse will be presented and related to the experimental observations.

The last section, Chapter 7, will present a summary of the work described in this thesis. Ideas on how to further enhance the peak field of the THz pulse will be discussed, including THz production from the channel-guided LWFA.

Chapter 2

Laser wakefield acceleration

Abstract

The concept to use an intense laser pulse to create a plasma wakefield in which electrons can be trapped and accelerated was proposed in 1979 by Tajima and Dawson [5]. Over the last decades, progress has been made both on the theoretical understanding of this laser wakefield accelerator (LWFA), as well as on the experimental realization and characterization. The electron energy gain, energy distribution, and total accelerated charge are a function of an interplay between the accelerator length (plasma length), plasma density, and laser properties. The electron bunch duration is predicted to be on the order of several plasma wavelengths, typically $5 - 30$ μm.

For the unchanneled self-modulated LWFA (SM-LWFA), electron bunches at energies of 0–50 MeV are produced, with typically an exponential energy distribution $g(E) \propto \exp(-E/E_t)$, with $E_t \simeq 4 - 5$ MeV. Each bunch contains over 10^{10} electrons. Typically, the bunch divergence is 25–50 mrad (half-angle). For the channeled LWFA, electron bunches with a few-percent energy spread at energies in excess of 100 MeV are produced. The typical bunch divergence in this geometry is on the order of a few mrad. The experiments on THz radiation, as discussed in this thesis, are performed with the SM-LWFA. THz production from the channeled LWFA will be investigated in future experiments.

2.1 Introduction

It was introduced in Chapter 1 that this thesis focuses on THz pulses (CTR pulses) emitted by short electron bunches produced by the LWFA. The first part of this chapter (Secs. 2.2 and 2.3) will address the theoretical concepts behind the LWFA production of short electron bunches. While Sec. 2.2 focuses on the laser-plasma interaction (plasma waves), Sec. 2.3 addresses the trapping, acceleration, and bunch formation of background electrons.

Sections 2.2 and 2.3 merely serve as a heuristic picture into several important concepts such as plasma waves, laser self-modulation, the separatrix, electron trapping, electron bunch duration, and dephasing. Other effects such as relativistic self-focusing, pulse steepening, pump depletion, 2D wake distortions, beam loading, and plasma temperature effects, are relevant to the LWFA, but are not crucial towards understanding the basic LWFA concepts: they will not be included in this thesis. Two publications by Esarey *et al.* [3, 4] provide a good overview of the full array of effects related to the complex interaction of the laser beam, the plasma, and the electron bunch.

The self-modulated LWFA geometry, defined as the geometry in which the laser pulse length is longer than the plasma wavelength, is the geometry studied in the experiments involving THz radiation described in this thesis. The experimental setup and measured electron bunch characteristics will be discussed in Sec. 2.4.

In order to extend the acceleration length of the LWFA, determined by the range over which the laser pulse is intense enough to generate a plasma wave, a laser guiding structure has been implemented. This geometry is referred to as the channeled LWFA, and an overview to the experimental setup and measured electron bunch characteristics are given in Sec. 2.5. Channel-guided LWFA-produced electrons are expected to deliver high-field THz pulses, and future experiments are aimed at demonstrating this.

The work in this chapter is partly based on the publications

- *Electron-yield enhancement in a laser-wakefield accelerator driven by asymmetric laser pulses*, by W.P. Leemans, P. Catravas, E. Esarey, C.G.R. Geddes, C. Toth, R. Trines, C.B. Schroeder, B.A. Shadwick, J. van Tilborg, and J. Faure, Phys. Rev. Lett. **89**(17), 174802 (2002)

- *Terahertz radiation from laser accelerated electron bunches*, by W.P. Leemans, J. van Tilborg, J. Faure, C.G.R. Geddes, Cs. Tóth, C.B. Schroeder, E. Esarey, G. Fubiani, and G. Dugan, Phys. Plasmas **11**(5), 2899 (2004)

- *High-quality electron beams from a laser wakefield accelerator using plasma-channel guiding*, by C.G.R. Geddes, Cs. Toth, J. van Tilborg, E. Esarey, C.B. Schroeder, D. Bruhwiler, C. Nieter, J. Cary, and W.P. Leemans, Nature **431**(7008), 538 (2004)

2.2 Plasma waves

2.2.1 Wake profiles

Plasmas can sustain electric fields in excess of 100 GV m^{-1} [3]. One way to produce a structure with such strong fields is through the interaction of a short intense laser pulse with the plasma. This concept, which will be described here, was first introduced by Tajima and Dawson [5].

Consider a collection of plasma electrons in the presence of the oscillating laser field: in addition to the quiver motion of the plasma electrons, a net electron drift is initiated if the laser has an intensity gradient (ponderomotive force). Since the ions are much heavier than the electrons, ion motion is ignored. A short laser pulse with a finite transverse width has both a longitudinal and transverse gradient, and therefore a net longitudinal and transverse electron drift is initiated as the laser pulse propagates through the plasma. The net drift results in a charge separation (electrons from ions). After the laser pulse has passed, the restoring force (Gauss's law) initiates a local density oscillation. The periodicity of the (electron) density oscillation is defined as the (angular) plasma frequency $\omega_p = 2\pi c/\lambda_p$. Linear plasma theory [36] relates ω_p to the background plasma electron density n_0 through (cgs units)

$$\omega_p = \sqrt{4\pi e^2 n_0/m_e} \qquad \text{or} \qquad \omega_p\ [\mathrm{s}^{-1}] = 5.64 \times 10^4 \times \sqrt{n_0\ [\mathrm{cm}^{-3}]}, \tag{2.1}$$

with m_e the electron rest mass, and e the unit charge. For example, for a plasma with density $n_0 = 3 \times 10^{19}$, it is found that $\omega_p = 309$ THz, or $t_p = 2\pi/\omega_p = 20$ fs, with t_p the plasma response time.

Since the laser pulse is moving through the plasma at group velocity v_g, it constantly creates new regions of charge imbalance, which will oscillate at ω_p after the laser pulse has passed by. Although the charge oscillation is electro-static, its phase velocity v_p is equal to the group velocity of the laser, or $v_p \simeq v_g$. The charge density oscillation is therefore also referred to as the plasma wave, or the wake.

Instead of expressing the laser fields in terms of $\mathbf{E}$ and $\mathbf{B}$, it is more convenient to introduce the vector potential $\mathbf{A}$, defined as $\mathbf{B} = \nabla \times \mathbf{A}$, and the electro-static potential Φ, defined as $\mathbf{E} = -\nabla\Phi - \partial\mathbf{A}/\partial ct$, with c the speed of light in vacuum. In the Coulomb gauge ($\nabla \cdot \mathbf{A} = 0$), the electro-magnetic fields (laser fields) are described by $\mathbf{A}$, and the electro-static fields (wake) by Φ. It is customary to normalize the potentials by $e/m_e c^2$, yielding the normalized vector potential $\mathbf{a} = e\mathbf{A}/m_e c^2$ and the normalized electro-static potential $\phi = e\Phi/m_e c^2$.

For a given laser pulse shape, the amplitude of the laser vector potential is labeled as the laser strength a_0. Ponderomotive-driven charge separation becomes significant [3] for laser pulses with $a_0 \gtrsim 1$. The laser strength a_0 is related to the laser intensity I to

$$a_0 = 8.6 \times 10^{-10} \times \lambda\ [\mu\mathrm{m}] \times \sqrt{\mathrm{I}\ [\mathrm{W\,cm}^{-2}]}, \tag{2.2}$$

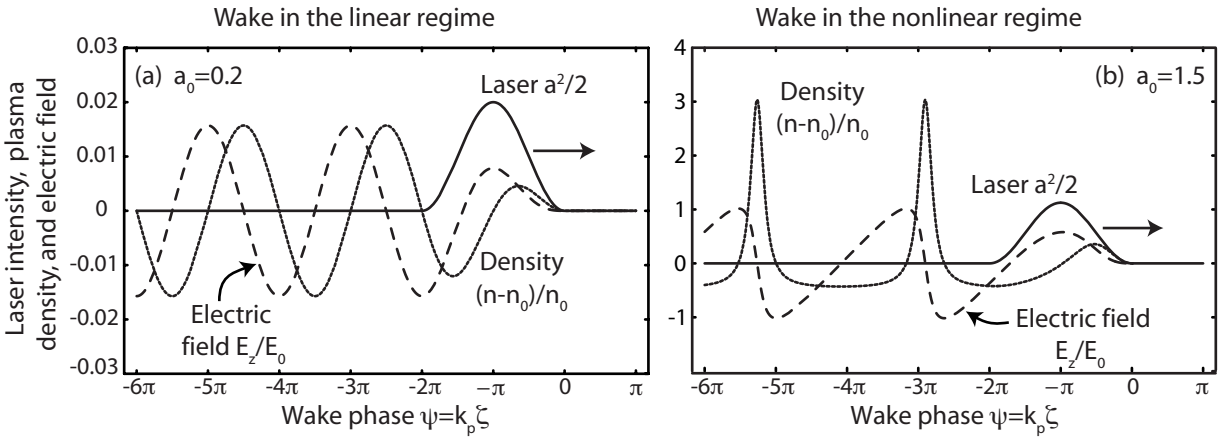

Fig. 2.1. The density profiles $(n-n_0)/n_0$ (dotted curves) and the longitudinal electric field profiles E_z/E_0 (dashed curves) driven by a laser pulse with (a) $a_0 = 0.2$ and (b) $a_0 = 1.5$. The laser pulse is defined as a half-sine with length $L = 2\pi k_p^{-1}$. The horizontal axis represents the wake phase $\psi = k_p\zeta = k_p(z - v_g t)$.

with the wavelength λ in units of [μm], and the intensity I in units of [$\mathrm{W\,cm^{-2}}$]. The intensity is related to the laser power P and spot parameter r_0 through $I = 2P/\pi r_0^2$, with the electric field of the laser E_L decreasing versus radial distance as $E_L \propto \exp(-r^2/r_0^2)$. For example, for a laser pulse with energy of 0.5 J, pulse length of 50 fs [intensity full-width-at-half-maximum (FWHM)], and intensity-FWHM spotsize of 6 μm ($r_0 = 5.1$ μm), one can find that $I = 2.4\times10^{19}$ $\mathrm{W\,cm^{-2}}$ and $a_0 = 3.4$. The relation between the transverse laser field amplitude E_L, the spot parameter r_0, and the pulse power P, is given by

$$E_L\ [\mathrm{TV\,m^{-1}}] = \frac{3.2\mathrm{a_0}}{\lambda\ [\mu\mathrm{m}]} = 3.9\times10^{-5}\sqrt{\frac{\mathrm{P}\ [\mathrm{J\,s^{-1}}]}{\pi(\mathrm{r_0}\ [\mu\mathrm{m}])^2}}, \tag{2.3}$$

with E_L in units of [10^{12} $\mathrm{V\,m^{-1}}$], P in units of [$\mathrm{J\,s^{-1}}$], and r_0 in units of [μm]. For parameters of the previous example, with $\lambda = 0.8$ μm and $a_0 = 3.4$, it can be found that $E_L = 14$ $\mathrm{TV\,m^{-1}}$.

The wake can be expressed in terms of the plasma density n, the longitudinal wake electric field E_z, or the wake potential ϕ. These parameters are related through $\mathbf{E} = -\nabla\Phi$ and Poisson's equation $\nabla\cdot\mathbf{E} = -4\pi e(n - n_0)$. A differential expression for the wake can be derived in the 1D regime (limit of an infinite laser spotsize), resulting in [3]

$$k_p^{-2}\frac{\partial^2\phi(\zeta)}{\partial\zeta^2} = \frac{1+a^2(\zeta)}{2[1+\phi(\zeta)]^2} - \frac{1}{2}, \tag{2.4}$$

where $\zeta = z - v_g t$ represents the coordinate co-propagating with the laser pulse and $k_p = \omega_p/c$. It was assumed for Eq. (2.4) that the laser is non-evolving, and that $\gamma_p \gg 1$, with $\gamma_p = (1-\beta_p)^{-1/2}$ and $\beta_p = v_p/c$.

For a laser pulse with length $L = 2\pi k_p^{-1}$ (half-sine pulse shape), the wake profiles for $a_0 = 0.2$ and $a_0 = 1.5$ are plotted in Fig. 2.1. The horizontal coordinate is expressed in

terms of $\psi = k_p\zeta = k_p(z - v_g t)$, the density profiles are normalized following $(n - n_0)/n_0$, and the field profiles are normalized following E_z/E_0, with E_0 the linear wave-breaking limit defined as (cgs units)

$$E_0 = c\sqrt{4\pi m_e n_0} \qquad \text{or} \qquad E_0\ [\mathrm{V\,cm^{-1}}] = 0.96\sqrt{n_0\ [\mathrm{cm^{-3}}]}. \tag{2.5}$$

Note that the limit E_0 is derived from equations assuming that $a_0 \ll 1$. For laser pulses with $a_0 \gtrsim 1$, the limit needs to be adjusted to a higher a_0-dependent value [3].

In the regime where $a_0 \ll 1$ (linear regime), the wake profiles are of sinusoidal form, as shown in Fig. 2.1(a). In the nonlinear regime ($a_0 \gtrsim 1$), see Fig. 2.1(b), the density profile becomes more spiky and the electric field structure resembles a saw-tooth-like profile with an amplitude that can exceed E_0. Also, the periodicity of the wake structure has increased from $2\pi k_p^{-1}$ to a longer nonlinear wavelength.

For an electron, the wake phase regions where $E_z < 0$ are accelerating in the longitudinal direction. In the radial direction there is also charge separation due to the radial gradient in laser intensity. One can find that there are regions in phase ψ where off-axis electrons will experience a force towards the axis (focusing force), as well as regions where the force is outward (defocusing region). The regions where $\phi > 0$, or $(n - n_0)/n_0 < 0$, are the focusing regions. In the example of Fig. 2.1(a), electrons in the region $-6\pi < \psi < -5\pi$ and $-4\pi < \psi < -3\pi$ are located in the focusing region. In the nonlinear regime, the location of the focusing phase region is more complex since the periodicity of the plasma wave is no longer equal to $2\pi k_p^{-1}$ but has a nonlinear correction term. For the example of $a_0 = 1.5$ in Fig. 2.1(b), the phase region $-5\pi < \psi < -3.2\pi$ is a focusing region.

2.2.2 Laser self-modulation

One can derive from Eq. (2.4) that the maximum amplitude for the wake is realized if the pulse length L matches the plasma wavelength λ_p, or $L \simeq \lambda_p$. The laser-plasma configuration where this condition is met is referred to as the resonant LWFA (or standard LWFA). The minimal laser intensity needed to realize self-injection (to be introduced in Sec. 2.3.2), which is a crucial mechanism towards the electron bunch production, is decreased at higher plasma densities. However, λ_p is also smaller at higher densities and current laser technology does not allow for production of short laser pulses where $L \simeq \lambda_p$, with λ_p on the order of 5–10 μm for densities around 10^{19} cm^{-3}. At first sight, it appears that at lower densities the laser pulse drives a resonant wake without self-injection, while at higher densities the self-injection threshold is reduced, but the wake itself is of smaller amplitude. In reality an instability occurs if $L > \lambda_p$, which does allow for self-injection and bunch production at higher plasma densities. This instability is referred as the self-modulation instability, and the accelerator in the regime $L > \lambda_p$ is referred to as the self-modulated LWFA, or SM-LWFA [3].

The self-modulation instability is a result of the coupling between the laser pulse and the plasma density profile. As the laser pulse propagates through the plasma, the regions

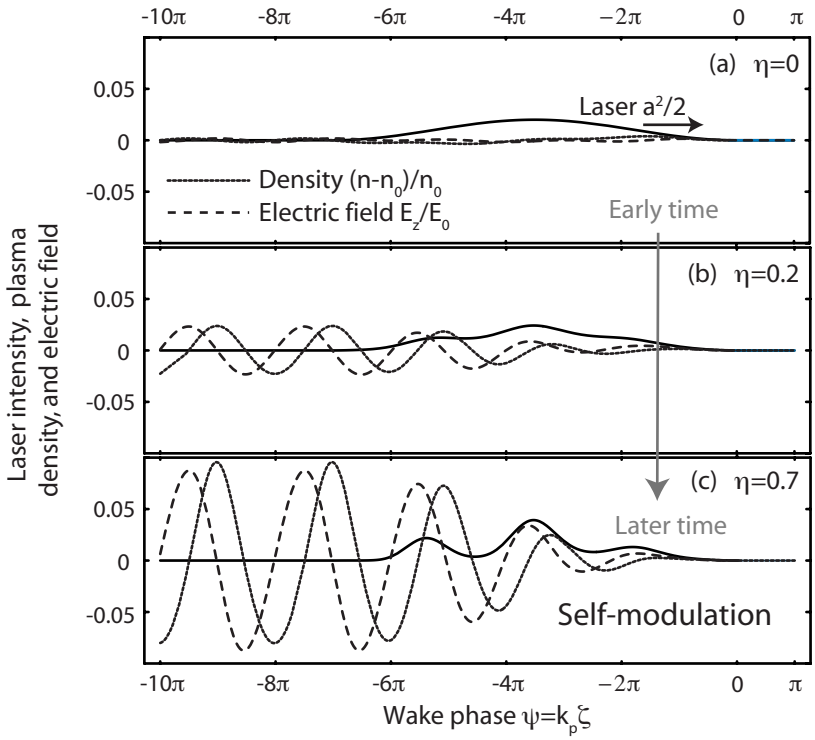

Fig. 2.2. The density profiles $(n - n_0)/n_0$ (dotted curves) and longitudinal electric field profiles E_z/E_0 (dashed curves), driven by a laser pulse with strength $a_0 = 0.2$ and length $L = 7\pi k_p^{-1}$. Plots (a), (b) and (c) are based on a modulated laser profile with modulation strength (a) $\eta = 0$, (b) $\eta = 0.2$, and (c) $\eta = 0.7$.

within the pulse where $n < n_0$ yield a different laser phase velocity than the regions of the pulse where $n > n_0$. As a result, the laser envelope is being modified at periodicity λ_p.

To demonstrate how an initially non-resonant laser pulse can still drive a strong wake, a laser pulse with length $L = 7\pi k_p^{-1}$ is considered (equivalent to length $L^* = 7\pi$ in the ψ frame), such that $L/\lambda_p = 3\frac{1}{2}$. From Eq. (2.4), the density $(n - n_0)/n_0$ and electric field E_z/E_0 profiles are calculated and plotted in Fig. 2.6(a). The laser strength is $a_0 = 0.2$. As predicted, the wake amplitude is very small. Although the self-modulation instability is more complex, a heuristic picture can be obtained by considering a pre-defined λ_p-modulated laser pulse. As an example, the laser envelope $|\sin(\pi\psi/L^*)|$ with $L^* = 7\pi$, which has non-zero values from $\psi = -7\pi$ to $\psi = 0$, is modulated through

$$\sin\left(\frac{\pi\psi}{L^*}\right) \rightarrow \left[1 - \eta\frac{\pi\psi}{L^*}\cos\left(\psi + \frac{L^*}{2}\right)\right]\sin\left(\frac{\pi\psi}{L^*}\right), \tag{2.6}$$

with η a pre-defined strength parameter. Note that Eq. (2.6) is not based on analytic theory, but merely serves as a heuristic picture to illustrate the effect of the self-modulation. Figure 2.6(a) is calculated with $\eta = 0$, Fig. 2.6(b) with $\eta = 0.2$, and Fig. 2.6(b) with $\eta = 0.7$. In each plot the laser envelope profile $a^2/2$ is plotted (solid curve), as well as the density profile $(n - n_0)/n_0$ (dotted curve) and longitudinal electric field profile E_z/E_0 (dashed curve). One can see that at later times, when the modulation has grown, the wakefield

has also increased in amplitude. In a way, instead of one non-resonant laser pulse, the modulation has created several coherent resonant laser pulses. Typically, it takes more than a Rayleigh length z_R of laser propagation for the modulation instability to become effective, with $z_R = \pi r_0^2/\lambda_0$. But if the laser pulse is intense enough over that distance (through relativistic self-focusing for example [3]), a strong wake is realized at densities high enough for self-trapping. Work by Schroeder *et al.* [55] discussed the effects of the laser pulse shape on the growth of the self-modulation, and experimentally the importance of the pulse shape was demonstrated by Leemans *et al.* [12].

2.3 Electron bunch production

2.3.1 The separatrix

In the previous section the concept of the plasma wake has been described, with examples in the linear and nonlinear regime. The next step towards a particle accelerator is to understand how an electron experiences the accelerating and decelerating fields of the wake. Note that the wake is traveling at phase velocity v_p, which can also be expressed as $\beta_p = v_p/c$, $\gamma_p = 1/(1-\beta_p^2)^{1/2}$, or $u_p = \beta_p\gamma_p$. The parameter u is referred to as the normalized electron momentum, since it can also be written as $u = p/m_e c$, with p the electron momentum. It is convenient to express the motion of an electron in the wake in terms of its momentum-phase position, defined as the electron's momentum u and phase ψ at a given time t. If an expression for the wakefield is known, the electron's trajectory in momentum-phase space can be calculated by considering that the total Hamiltonian (electron and wake) is conserved for a specific initial condition (ψ_0 and γ_0). It can be shown [3] that the Hamiltonian H is given by

$$H(\gamma,\psi) = \gamma(1-\beta\beta_p) - \phi(\psi) = H(\gamma_0,\psi_0), \tag{2.7}$$

with ϕ the wakefield. For now, the wakefield expression in Eq. (2.4) will be considered.

Background plasma electrons ahead of the laser pulse and wake are at rest, such that their Hamiltonian is given by $H = 1$. Their trajectories in momentum-phase space are plotted in Fig. 2.3 as the dotted curve. In this plot, the wake was calculated from a half-sine laser pulse with length $L = 2\pi k_p^{-1}$ and strength $a_0 = 0.4$. The plasma density was chosen such that $u_p = 2.8$. Since the frame in Fig. 2.3 is moving at $v_g \simeq v_p$, the background electrons slip back with respect to the wake. These electrons travel to regions of acceleration and deceleration, but the acceleration is not sufficient for the electrons to keep up with the wake.

If an electron already has some initial critical velocity, it can remain trapped in the wake. This critical condition can be found by considering that at the phase ψ_T, which is the phase where the longitudinal electric field is zero (switching from decelerating at $\psi < \psi_T$ to accelerating values at $\psi > \psi_T$), the electron's momentum has to be at least u_p. In the linear regime, see Fig. 2.1(a), one can find that $\psi_T = -2\frac{1}{2}\pi,\ -4\frac{1}{2}\pi,\ -6\frac{1}{2}\pi$, etc,

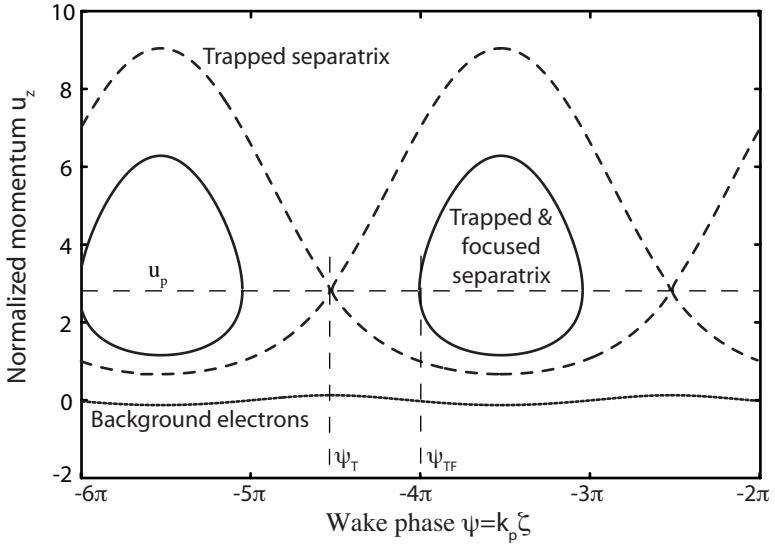

Fig. 2.3. Orbits in momentum-phase space of constant Hamiltonian H. The dotted curve describes the background plasma electrons, where $H = 1$, the dashed curves describe the critical orbits for trapping, where $H = H(\gamma_p, \psi_T)$, and the solid curves describe the critical orbits for electrons that are both trapped and focused [$H = H(\gamma_p, \psi_{TF})$]. The laser pulse strength is $a_0 = 0.4$, with pulse length $L = 2\pi k_p^{-1}$.

while in the nonlinear regime these values have to be corrected for the increase in nonlinear wake wavelength. The critical orbit for trapping, defined as $H = H(\gamma_p, \psi_T)$, is referred to as the trapped separatrix, as shown as the dashed curve in Fig. 2.3.

As discussed at the end of Sec. 2.2.1, there are focusing and defocusing wake regions. For optimal electron bunch quality, it can be preferred that the electrons are trapped in a focusing field region. The critical Hamiltonian for focusing and trapping is defined as $H = H(\gamma_p, \psi_{TF})$. The phase ψ_{TF} is the phase in the accelerating phase region where the focusing force is zero (switching from defocusing at $\psi < \psi_{TF}$ to focusing values at $\psi > \psi_{TF}$). In the linear regime $\psi_{TF} = -2\pi,\ -4\pi,\ -6\pi$, etc. This separatrix is referred to as the trapped-and-focused separatrix, and is plotted as a solid curve in Fig. 2.3.

2.3.2 Electron self-trapping

One way to produce a high-energy electron bunch is to inject a low-energy electron bunch into the accelerating phase of the wake [56, 57]. However, most LWFA-based experiments worldwide do not rely on an external electron bunch. Instead, these experiments rely on the fact that background plasma electrons can be trapped in the plasma wave (self-trapping). Selection of the phase region in which electrons are self-injected is not straightforward. Currently, optical techniques [58, 59] for controlled injection are a hot research topic in the LWFA community and experiments are underway at the LOASIS facility at LBNL [60].

Several mechanisms are relevant to self-trapping of plasma electrons, depending on the experimental conditions. Trapping can be realized by density gradients [61, 62], 2D wake curvature [63], wave-breaking [64–69], or temperature-induced self-injection [67, 69]. In the

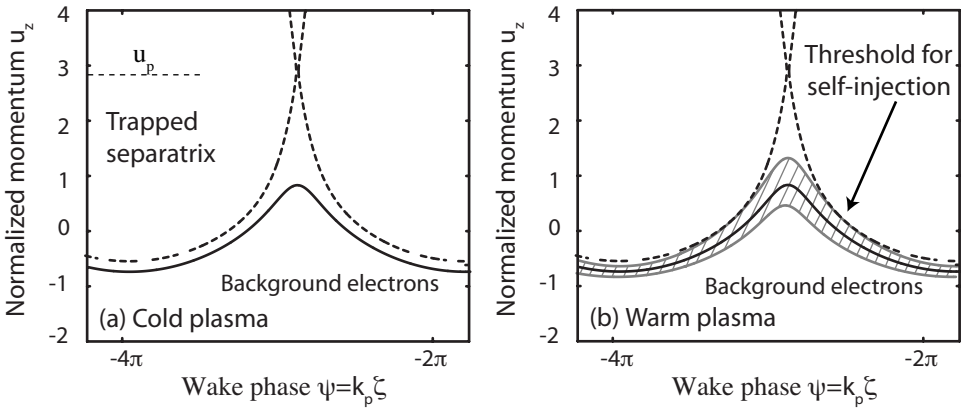

Fig. 2.4. Trapped separatrices (dashed curves) and background electron momentum orbits (solid curves), calculated from a laser pulse with length $L = 2\pi k_p^{-1}$, and strength $a_0 = 1.1$. In contrast to the electrons in a cold plasma, see (a), a fraction of the background electrons in a warm plasma can have enough momentum to be injected in the wake (self-injection). The threshold for self-trapping is indicated in (b). The grey shaded area in (b) depicts the temperature-related spread on the normalized momentum profile.

experiments described in this thesis, trapping due to temperature-induced self-injection is considered the dominant trapping mechanism, and will therefore be presented here.

Figure 2.3 in Sec. 2.3.1 showed the normalized momentum of the background electrons in the wake, calculated for a laser with $a_0 = 0.4$. First, the plasma is assumed to be cold (no energy spread for the background electrons). If one increases the laser pulse strength, the electrons in the wake will gain in momentum amplitude as well. For example, for a laser with $a_0 = 1.1$, the trapped separatrix (dashed curve) and the electron momentum orbits (solid curve) are shown in Fig. 2.4(a). The pulse length was set at $L = 2\pi k_p^{-1}$, and the background density was chosen such that $u_p = 2.8$. At a critical wake strength, the electron momentum becomes so intense that the background electrons enter the trapped separatrix. This phenomenon is referred to as wave-breaking. At the cold wave-breaking threshold, all the background electrons are injected into the wake, leaving no background electrons behind to form the wake. In reality however, injection of electrons into the wake occurs before wave-breaking is reached. The reason for this is related to the finite temperature of the plasma, which will be discussed now.

In a warm plasma, the electron momentum distribution has a certain momentum spread which is related to the inital plasma temperature $T_{e,0}$, typically on the order of ≈ 10 eV. Following the plasma density profile in the wake, the local temperature is further enhanced or reduced following the scaling $T_e \propto T_{e,0}(n/n_0)^2$ [69]. In case of the self-modulated LWFA, the local temperature on the electron momentum distribution is even further enhanced due to the beating of the laser pulse with the backward Raman-scattered light [17]. Even if the wake has not reached wave-breaking yet, a fraction of the background electrons has enough positive momentum to get trapped in the wake. Figure 2.4(b) depicts the same wake as the one of Fig. 2.4(a), but now the background electrons have a finite-width momentum

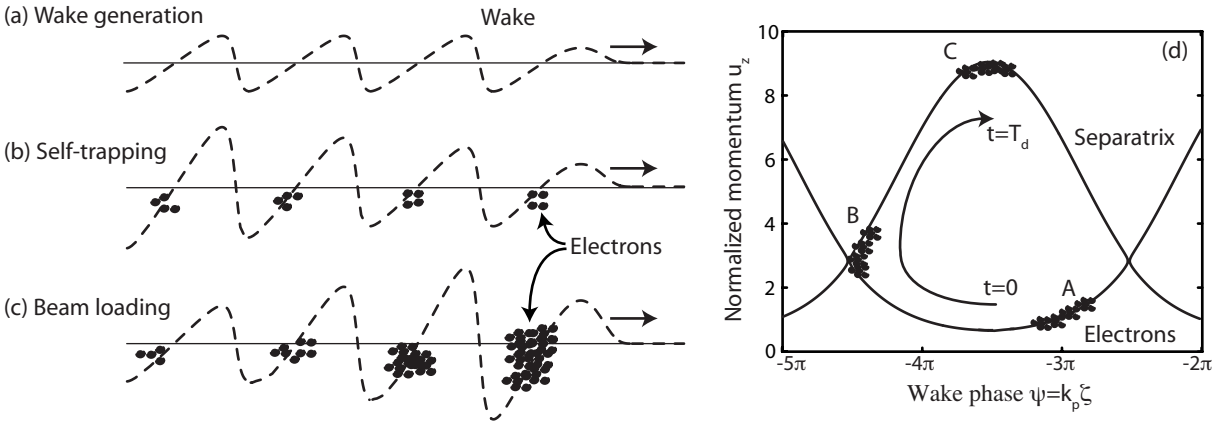

Fig. 2.5. (a)-(c) Dynamics leading to the SM-LWFA production of short electron bunches: (a) the laser pulse has excited a plasma wake, but self-injection has not been reached. (b) At a larger wake strength, trapping is initiated in several phase buckets. (c) Due to beam loading, only the first few buckets will be injected with the majority of the electrons. (d) Diagram of the propagation in momentum-phase space of a trapped electron population: after the electrons are injected (see A), they undergo acceleration (A–C) until the dephasing point (see C) is reached.

spread, see the grey shaded area. One can see that locally, where the upper grey curve for the momentum profile touches the trapped separatrix, self-injection is about to occur. This is referred to as temperature-induced self-injection. In a uniform-amplitude wake, the background electrons get trapped in the first separatrix that overlaps with the momentum profile. However, in the self-modulated LWFA, the wake amplitude has a gradient, see Fig. 2.2, and trapping can occur in several regions in phase space. Note also that at higher plasma densities, the phase velocity of the plasma wave is lower, resulting in a shift downwards of the separatrices in Fig. 2.4. This implies that self-injection can occur at a lower laser intensity.

2.3.3 Production of short electron bunches

The previous section introduced the concept of self-injection. This section will describe how a short bunch is formed as more and more charge is injected into the wake. Each phase region confined by one (nonlinear) plasma period is labeled as a plasma bucket. As more and more charge gets trapped in a series of plasma buckets, the electron bunches in each bucket drive their own wakefield. The bunch-driven wakefield can be included in the calculation for the total wakefield by adding the term $n_b(\zeta)/n_0$ to the right side of Eq. (2.4), with $n_b(\zeta)$ the density profile of the electron bunch.

The bunch-driven wakefields of each collection of trapped electrons will destructively interfere with the laser-driven wakefields, resulting in a reduction of the overall wake strength. This phenomena is referred to as beam loading [70]. While the total (laser- and bunch-driven) wake within the first bucket experiences little reduction in strength, the wake in the second bucket is affected by the bunch-driven wake of the electrons in the first bucket. The total wake in the third bucket is reduced even more in strength, since it is affected by

the bunch-driven wakes of the electrons in the first and second bucket, etc. Consequently, the total wake is only strong enough for sufficient self-injection in the very first few buckets. The schematic in Fig. 2.5(a)-(c) describes the dynamics towards the production of a short electron bunch. In Fig. 2.5(a), the wake strength of the SM-LWFA has not reached the threshold for self-injection yet. At a larger strength parameter, see Fig. 2.5(b), trapping is initiated over many phase buckets. However, due to beam loading, see Fig. 2.5(c), only the first few buckets will be injected with the majority of the electrons. Since the plasma wavelength is typically on the order of $\lambda_p \simeq 5 - 10$ μm, the total bunch duration can be estimated to be $\simeq 5 - 30$ μm. Note that if only a single bucket were to be injected with electrons, μm-size (attosecond) electron bunches could be generated.

The transverse dimension of the electron bunch is predicted to be on the order of the transverse wake dimension, which in turn in roughly equal to the laser spot size ($r_0 \simeq 5 - 10$ μm). More details on the theoretical prediction of the bunch properties can be found in Tzeng *et al.* [16] and Esarey *et al.* [17].

2.3.4 Dephasing

The previous section described how an electron bunch, with a length of a few plasma periods, is trapped in the wake. During the propagation and acceleration of the bunch through the acceleration structure (the wake), the electron bunch parameters such as bunch length, bunch energy, and energy spread, evolve. The following heuristic picture, based on the momentum-phase position in the separatrix, is presented to describe this evolution.

As discussed in Sec. 2.3.3, the self-injected electrons are injected into state A of Fig. 2.5(d). Within a specific bucket, the trapped electrons will initially slip backwards within the wake and experience acceleration (propagation towards state B). Between states B and C, they will propagate faster than the wake, until at state C the electrons enter the decelerating phase region. The time it takes for the particles to move from A to C is referred to as the dephasing time T_d, and its corresponding length the dephasing length $L_d \simeq cT_d$. An analytical approximation for the dephasing length in the 1D regime can be expressed as [3, 4]

$$L_d \simeq \frac{\omega_0^2}{\omega_p^2}\lambda_p \begin{cases} 1 & \text{for} \quad a_0^2 \ll 1 \\ 2a_0^2/\pi & \text{for} \quad a_0^2 \gg 1. \end{cases} \tag{2.8}$$

At a given plasma density, the accelerator performance in terms of maximum acceleration can be optimized by making the plasma length equal to the dephasing length.

Figure 2.5(d) clearly shows that the energy spread of the bunch at state C, where $u_z \simeq 8\frac{1}{2} - 9$, is reduced with respect to state B, where $u_z \simeq 2\frac{1}{2} - 4$. This is a direct result of the rotation in momentum-phase space of the bunch. Also, the bunch in each bucket experiences longitudinal compression or de-compression, depending on the position in momentum-phase space. For example, in states A and C of Fig. 2.5(d), the longitudinal length of the electrons within the bucket is longer than in state B. For a charge profile

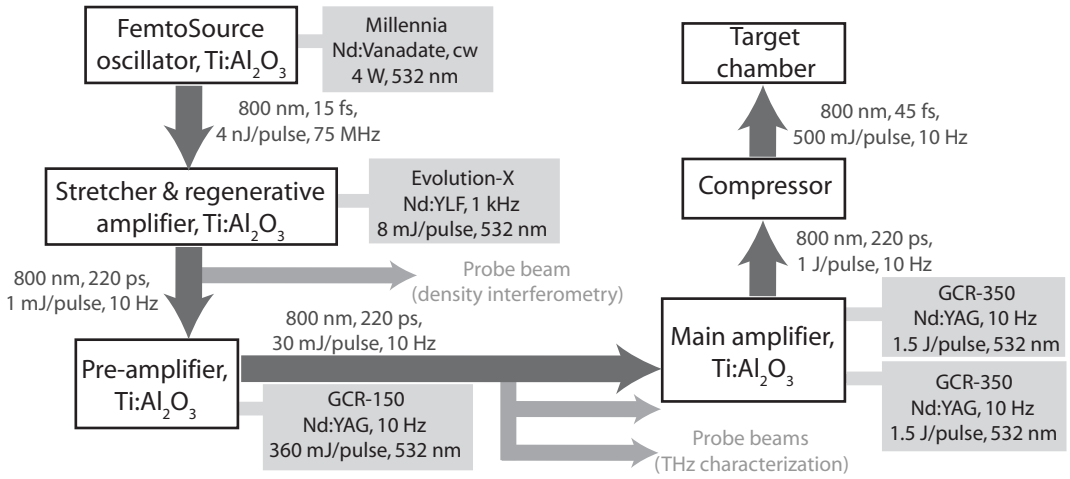

Fig. 2.6. Layout of the 10-TW-class laser system. Laser parameters such as pulse energy, pulse length, and repetition rate, are included. Also indicated is the position in the laser system where several probe pulses are derived from the main beam.

consisting of electrons in several buckets, the total bunch length remains on the order of several plasma periods. If electrons occupy only a single bucket, the bunch length could be shorter than a plasma wavelength.

2.4 Experiment: unchanneled self-modulated LWFA

The experiments on THz pulses described in this thesis are performed with the 10-TW-class system at the LOASIS facility. Although multiple energetic laser pulses can be delivered to the target chamber, the experiments on LWFA-produced THz radiation as presented in this thesis were performed with just one drive laser beam. Some of the details on the laser system have also been discussed by Leemans *et al.* [11, 12, 31], and Tóth *et al.* [71]. A layout of the critical laser components is depicted in Fig. 2.6. The figure lists parameters such as pulse energy, pulse length, repetition rate, and the type of amplification crystal used. The laser system is based on amplification in titanium sapphire ($\mathrm{Ti{:}Al_2O_3}$). The bandwidth of the laser pulse is $\simeq$ 20 nm (intensity FWHM), centered at $\lambda_0 = 800$ nm. Typically the compressor is tuned to produce Fourier-limited laser pulses, although residual chirp can be provided if wanted for pulse shaping. At optimum compression, the pulse length is 50 fs (intensity FWHM), such that $L = 15$ μm. The optical path length from oscillator to target chamber is roughly 90 meters. Beamsplitters are implemented in the system to provide several lower-energy probe beams to the target chamber. Each probe beam is propagated to its own compressor as well as to a controllable temporal delay line (delay with respect to the main laser or electron bunch).

Inside the target chamber, the main laser pulse (driver) was focused by an F/4 90°-off-axis parabola (OAP1, focal distance of 30 cm), see Fig. 2.7. The final spotsize was 6 μm (intensity FWHM), resulting in a peak intensity of 2.4×10^{19} W cm^{-2} or a laser strength

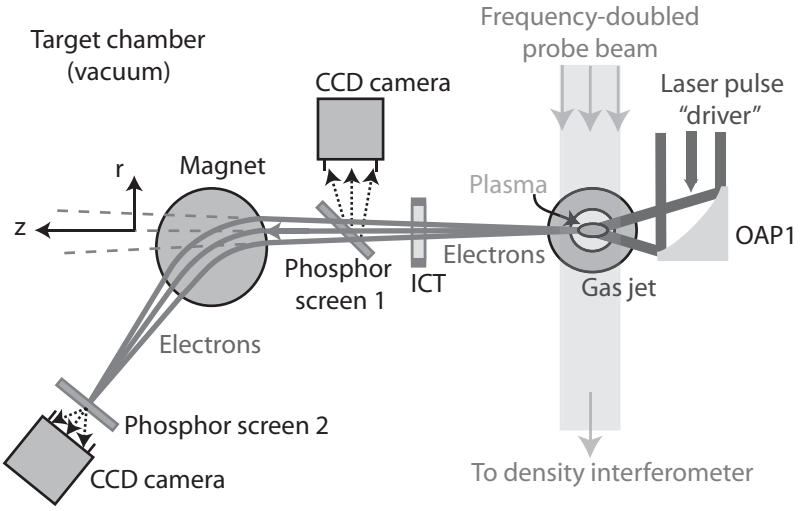

Fig. 2.7. Schematic of several components in the target chamber. The plasma was diagnosed with a frequency-doubled 50-fs-long probe beam. The CCD camera imaging phosphor screen 1 recorded the transverse charge distribution, while the CCD camera imaging phosphor screen 2 was used for electron momentum analysis (in combination with a magnetic spectrometer). The integrated current transformer (ICT) measured the total bunch charge.

of a_0=3.4. The Rayleigh length can be estimated to be $\simeq 150$ μm. Helium gas emanated from a pulsed gas jet with a 2-mm-diameter circular nozzle. The laser-produced plasma had a background density $n_0 = 3 \times 10^{19}$ cm^{-3}, such that the plasma wavelength λ_p=6 μm. Since $L/\lambda_p \simeq 2.5$, the accelerator was operated in the SM-LWFA regime, as discussed in Sec. 2.2.2. The two-dimensional (2D) plasma density distribution (n_0 versus z and r) was characterized by a frequency-doubled (λ_0=400 nm) 50-fs-long probe beam, synchronized to the main driver (see location of pick-off in Fig. 2.6). Through an Abel inversion technique, the density interferogram was converted to an actual 2D density profile. A cylinder-shaped uniform plasma, with length of 2 mm and width of ≈ 200 μm, was found to be a good approximation of the actual density profile. In Sec. 3.6, more details on the density profile will be discussed.

The LWFA-produced electron bunch propagated in the z-direction towards several diagnostics. An integrated current transformer (ICT), see Fig. 2.7 for positioning, measured the time-integrated total charge. The ICT was positioned 50 cm from the gas jet, and had an opening diameter of 10 cm. A typical set of data obtained with the ICT is plotted in Fig. 2.8(a), with 2.5 nC = 1.6×10^{10} electrons. Over a period of 70 minutes, the standard deviation on the total charge was $6-7\%$. The gas flow was turned off for a brief period for background calibration of the ICT signal.

Phosphor screen 1, see Fig. 2.7 for positioning, provided a time-integrated profile of the transverse charge distribution. The screen, positioned 75 cm from the gas jet, can be removed from the beam path. The upstream surface of the phosphor screen was coated with aluminized mylar, such that the remnant laser beam was reflected and only the electron beam interacted with the phosphor. A representative image is shown in Fig. 2.8(b). The

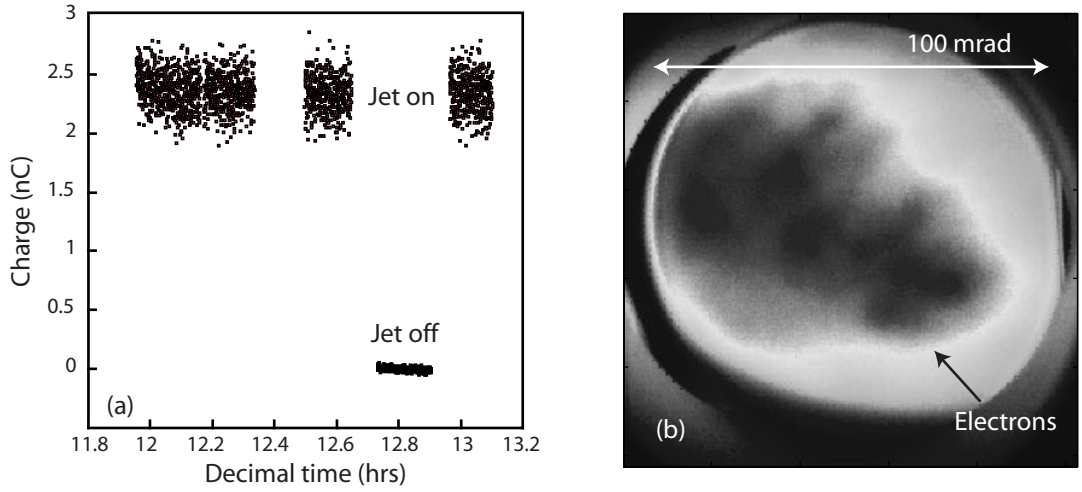

Fig. 2.8. (a) Total charge versus time, measured by the ICT. The standard deviation on the average charge is 6−7%. *Note that* 2.5 *nC corresponds to* 1.5×10^{10} *electrons. (b) A representative image of the transverse charge distribution, measured* 75 *cm from the gas jet. The sharp circular-shaped edge is the edge of the phosphor screen. The bunch divergence was typically on the order of* $25-50$ *mrad (half-angle). (Figure from Ref. [31].)*

bunch divergence was found to be typically on the order of 50–100 mrad (half-angle of 25–50 mrad). The centroid of the bunch was fluctuating over a similar angular range with respect to the z axis ($\simeq$0-25 mrad). The fluctuations appear to be a typical characteristic of the instability-driven SM-LWFA. Although the total charge is fairly constant, fluctuations on the moment of wave-breaking and self-trapping are believed to influence properties such as bunch divergence and bunch pointing. Note that work by Schroeder *et al.* [30] indicates that fluctuations on the bunch divergence and pointing have little or no impact on off-axis THz emission.

In order to obtain an indication for the electron momentum (or energy) distribution, the scanning magnetic spectrometer was used. Phosphor screen 1, see Fig. 2.7, was removed for this measurement. At a given excitation current of the magnet, electrons within a specific momentum range ($\delta p/p_0 \lesssim 2\%$) were imaged onto phosphor screen 2. By scanning the excitation current, the full momentum distribution from 0–100 MeV/c was obtained. A characteristic energy spectrum is shown in Fig. 2.9. Each data point represents the number of electrons dN normalized to the energy acceptance dE at that specific excitation current. The value dN/dE is of arbitrary unit. The inset in Fig. 2.9 shows the same distribution but on a linear scale. The majority of the electrons have energies less than 10 MeV, although the detector sensitivity allows for measurement up to 50 MeV. The spectrum was fitted with a Boltzmann distribution $g(E) \propto \exp(-E/E_t)$, yielding $E_t = 4.2$ MeV. The measured large-energy-spread distribution (100% energy spread) is typical for experiments in the SM-LWFA regime. On a shot-to-shot basis, a quasi-mono-energetic sub-population exists on top of the background Boltzmann distribution. By averaging many shots these features wash away, resulting in an "averaged" Boltzmann curve such as

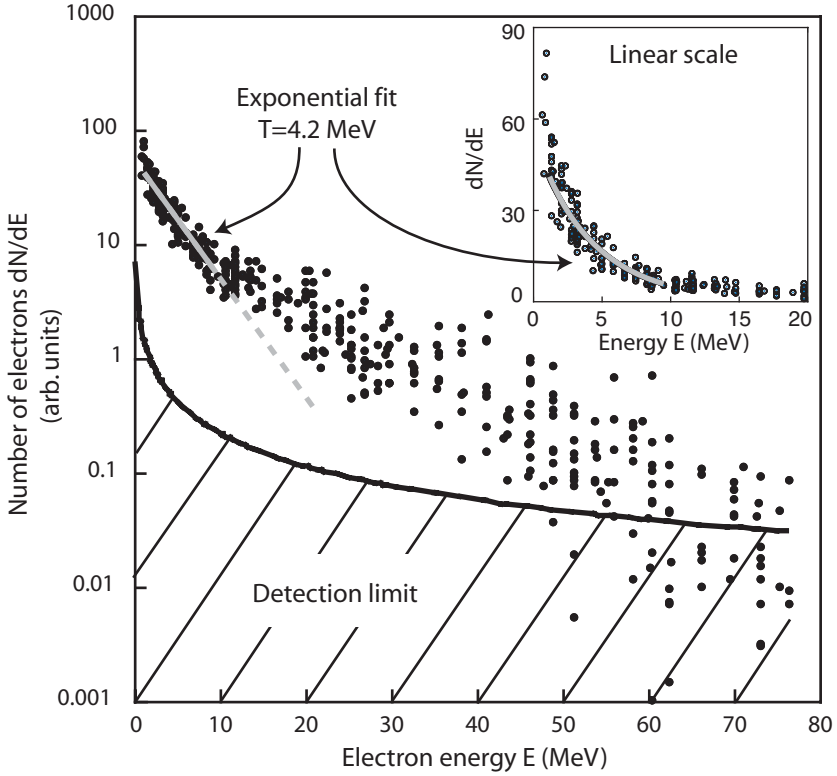

Fig. 2.9. The energy distribution of SM-LWFA-produced electrons, on a logarithmic scale (main plot) and linear scale (inset). The data points at energies $0-10$ *MeV are fitted with a Boltzmann distribution* $g(E) \propto \exp(-E/E_t)$*, indicating a temperature of* $E_t = 4.2$ *MeV. At energies* $\gtrsim 50$ *MeV some of the data points fall within the noise limit (detection limit) of the detector. (Figure from Ref. [31].)*

the one in Fig. 2.9. Section 3.4.4 will demonstrate that fluctuations of the details on the electron energy distribution (over the constant Boltzmann profile) have little or no impact on the THz emission.

2.5 Experiment: channel-guided LWFA

This section will discuss a technique to enhance the acceleration length. The accelerator performance is related to the length over which the laser pulse is intense enough to drive a wake. The effective length of the SM-LWFA, discussed in Sec. 2.4, is limited to one or a few Rayleigh lengths, which is typically $z_R \simeq 100 - 300$ μm. If sufficient laser energy is available, the Rayleigh length can be increased by enlarging the laser spot size. This approach has been demonstrated to yield higher-energy and lower-energy-spread electron bunches [13, 15].

Another approach to a longer effective accelerator length was realized by providing an optical guiding mechanism [72]. This can be done by pre-shaping the density profile such that there is a density minimum on-axis, or $[n(r) - n_0] \propto r^2$ near the axis, with r the radial coordinate. At large r, the density drops to zero. At the LOASIS facility, a guiding

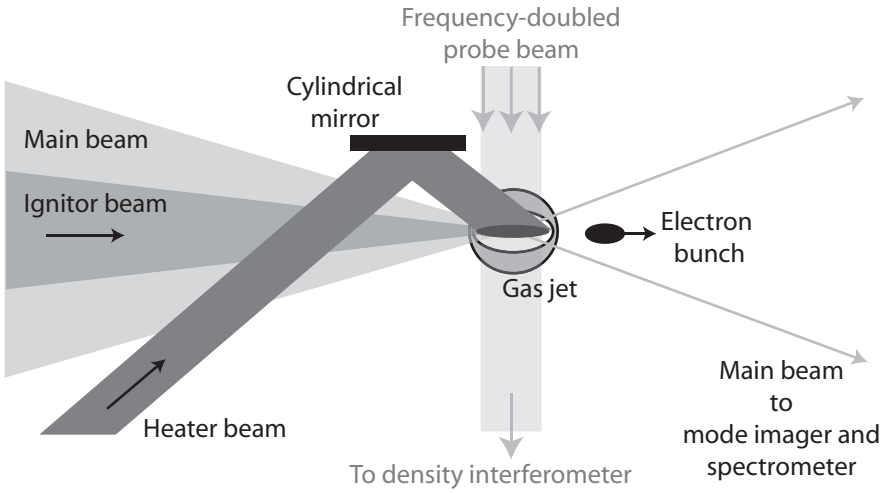

Fig. 2.10. Setup for the optical-guiding scheme referred to as the ignitor-heater approach. The ignitor ionizes the gas, and the heater beam (line focus from the cylindrical mirror) produces a density profile with an on-axis minimum. The main laser pulse (driver) arrives 500 *ps later. Due to the laser-produced density channel, it is able to drive a wake over a distance of* $\simeq 2-2.5$ *mm, resulting in the production of high-quality electron bunches.*

structure in the plasma was produced through an all-optical technique, as described by Volfbeyn *et al.* [73] and Geddes *et al.* [14, 74, 75]. The setup is depicted in Fig. 2.10. Three laser beams were used for the laser-plasma interaction. First, a 60-fs-long (intensity FWHM) ignitor beam, containing $\simeq$15 mJ of energy, was used to ionize Hydrogen gas. The Rayleigh length of the ignitor beam was $\simeq 1$ mm. The gas emerged from a slit-shaped jet, producing a nearly-uniform 2.4-mm long plasma at a density of $n_0 = 3 \times 10^{19}$ cm^{-3}. The 250-ps-long heater beam was focused with a cylindrical mirror (producing a line focus overfilling the plasma) to heat the plasma to tens of eV via inverse Bremsstrahlung, using 50 mJ out of the available 150 mJ. The heating resulted in an on-axis density depletion (as measured 500 ps later) and a quadratic density profile. The final wake-driving laser pulse (main beam, 500 ps after the heater beam) was incident on the guiding plasma structure to produce the electron bunch. The parameters of the main laser beam were discussed in Sec. 2.4.

The details of these experiments were extensively discussed by Geddes *et al.* [14, 74, 75]. The magnetic energy spectrometer, introduced in Sec. 2.4, was used to look at the electron momentum distribution. A typical momentum distribution is shown in Fig. 2.11(a). In a single-shot, the momentum in the energy range 68–92 MeV was recorded, with the vertical axis (undispersed axis) representing the bunch divergence. The profile for dN/dE versus electron energy is shown in Fig. 2.11(b). Charge calibration of the phosphor screen allowed for the estimation that over 2×10^9 electrons had a momentum of 86 ± 1.8 MeV, and within a 3 mrad divergence. Since the accelerator length and the dephasing length were better matched [74], the energy spread of the electron distribution is significantly lower than of the unchanneled SM-LWFA bunches. The production of bunches like the one in Fig. 2.11

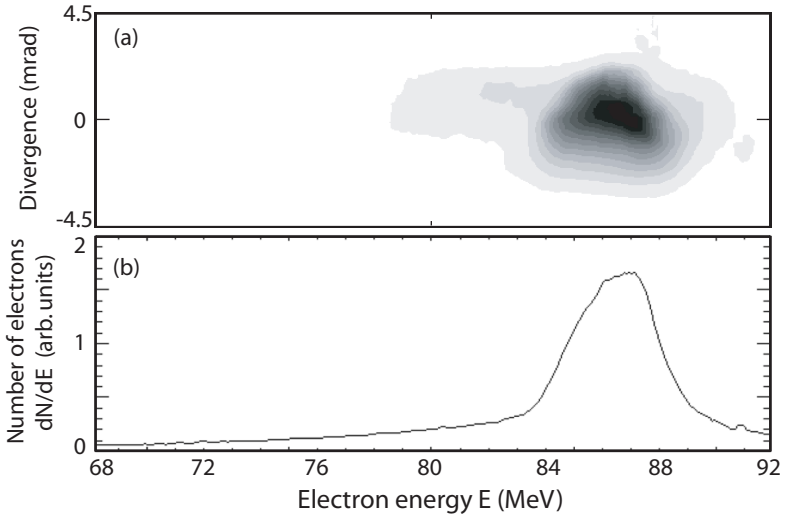

Fig. 2.11. (a) Image taken with the magnetic spectrometer. The charge density versus electron energy and divergence was obtained in a single shot. Based on image (a), the total charge versus electron energy is shown in plot (b). Over 2×10^9 *electrons were measured at a momentum of* 86 ± 1.8 *MeV, and within a* 3 *mrad divergence. (Figure from Ref. [14].)*

signifies progress towards the LWFA production of high-quality electron bunches. It will be discussed in Sec. 3.5.2 that THz radiation from such bunches can potentially exceed peak electric fields of > 1 MV cm^{-1}, which is very interesting for THz applications.

2.6 Summary

The concepts of the LWFA were discussed in this chapter, including plasma waves, the separatrix, wave-breaking (self-trapping), and beam loading. Through the self-modulated instability, the laser pulse shape evolves over time (modulation at λ_p) and the modulated laser pulse is capable of driving strong wakes at non-resonant densities ($L > \lambda_p$). This regime is labeled as the SM-LWFA and experiments on THz radiation as presented in this thesis were based on electron bunches produced in this regime.

In the laboratory, SM-LWFA-produced electron bunches were found to contain $\simeq 1.6 \times 10^{10}$ electrons (2.5 nC), with a bunch divergence on the order of 25–50 mrad (half-angle). The electron energy distribution $g(E)$ can be approximated by an exponential Boltzmann distribution $g(E) \propto \exp(-E/E_t)$, with temperature $E_t \simeq 4.2$ MeV. Theory predicts that the bunches have a length of several plasma wavelengths ($\simeq 5 - 30$ μm), and a bunch size on the order of the laser spot size, typically $5 - 10$ μm. Chapters 3-6 will describe the measurements of the bunch duration, based on THz analysis.

In order to improve the electron bunch quality, an optical-guiding technique was implemented. The technique (ignitor-heater scheme) increased the length over which the laser pulse is intense enough to drive a wake, from several Rayleigh lengths ($\simeq 100 - 300$ μm) to the full plasma length of $\simeq 2.4$ mm. The ignitor and heater laser beams produced a

plasma with an on-axis density minimum, which led to guiding of the main laser pulse. In addition to the increase in electron energy, measured to be 86 MeV, the energy spread was reduced to the few-percent level. Also, the bunch divergence was smaller, on the order of 3 mrad. Future experiments on THz radiation will be focusing on measuring the properties of THz pulses from these channel-guided LWFA-produced bunches.

Chapter 3

Coherent transition radiation

Abstract

Electrons emit transition radiation when they propagate through a boundary between two materials with different dielectric properties. At wavelengths longer than the bunch length, the radiation contributions of the individual electrons interfere constructively (*i.e.* coherence). Analysis of coherent transition radiation (CTR) allows for characterization of the electron bunch profile. In the laser wakefield accelerator (LWFA), electrons propagate through the plasma-vacuum interface, which provides the necessary environment for emission of CTR. A model has been developed to calculate the properties of the LWFA-produced CTR pulse. It is found that the plasma-vacuum interface can be approximated as a sharp metal-vacuum interface. Also, the emission by a bunch with a Boltzmann-like energy distribution (temperature E_t) does not significantly differ from emission by a mono-energetic bunch at that same energy E_t. The temporal radiation waveform can be described as single cycle. The broad-bandwidth spectrum of the radiation, emitted by the femtosecond bunches, lies in the 0–10 THz regime. Diffraction effects, related to the finite boundary size, have been incorporated into the model. Depending on diffraction effects and collection efficiency, the THz pulse (CTR pulse) can contain $0.1 - 10$ μJ of energy, with a peak field of 0.3–3 MV cm^{-1}.

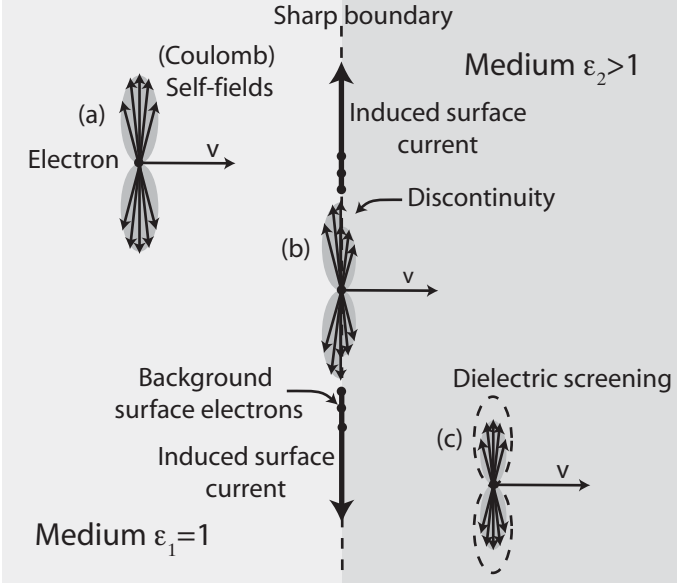

Fig. 3.1. An electron at three different time steps: (a) While propagating in vacuum, where $\epsilon_1 = 1$. (b) At the interface between two media. (c) While propagating in the second medium, where $\epsilon_2 > 1$. The discontinuity of the (Coulomb) self-fields at the sharp boundary leads to the generation of a surface current of background electrons, which in return emits transition radiation.

3.1 Introduction

Section 1.3 motivated the goal for bunch length characterization by means of coherent radiation analysis. The experimental method of choice described in this thesis is analysis of coherent transition radiation (CTR). Transition radiation (TR) is emitted when a charged particle passes through the boundary of two materials with different dielectric properties.

A heuristic picture of the mechanism behind TR is represented by Fig. 3.1. Consider a single electron (a) moving through a medium with dielectric constant $\epsilon_1 = 1$, then (b) passing a sharp boundary, and (c) into a second medium with a different dielectric constant $\epsilon_2 > 1$. With the electrons at relativistic velocities, the (Coulomb) self-fields have a more transverse orientation. As the bunch propagates in the second medium ($\epsilon_2 > 1$), the self-fields of the bunch will experience partial screening by the background electrons. The effectiveness of the screening is proportional to the dielectric constant (complete field cancellation if $\epsilon_2 = \infty$). As the electron passes through the sharp interface, see Fig. 3.1(b), a discontinuity in electric field seems to occur. This would be in violation of Maxwell's equations. In reality, background electrons at the surface are moved transversely in order to cancel this discontinuity. The bunch-driven surface current is the driving force behind the emission of electro-magnetic radiation referred to as transition radiation.

The spectrum $E_{\mathrm{TR}}(\lambda)$ of the emitted TR has a broad bandwidth. Consider now a collection of electrons in a bunch with longitudinal length σ_z. The total electro-magnetic field distribution is calculated by adding the individual contributions of each electron.

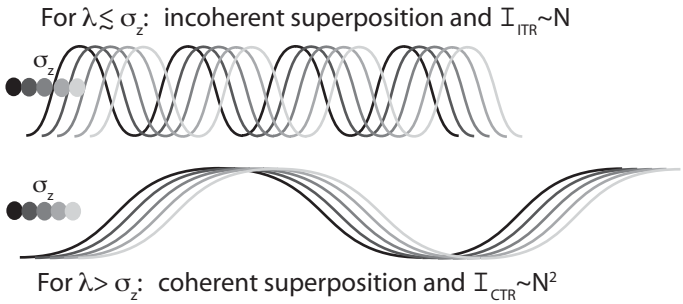

Fig. 3.2. Incoherent (top) and coherent (bottom) superposition of spectral components of TR from a collection of electrons. Radiation at wavelengths λ longer than the bunch length σ_z experiences coherent superposition, leading to scaling $I_{\mathrm{CTR}}(\lambda) \sim |E_{\mathrm{CTR}}(\lambda)|^2 \sim N^2$, with N the number of electrons in the bunch.

As Fig. 3.2 illustrates, radiation at wavelengths $\lambda \lesssim \sigma_z$ will add incoherently [incoherent transition radiation (ITR)], with the total field strength $E_{\mathrm{ITR}}(\lambda)$ scaling with the square-root of the number of electrons, or $E_{\mathrm{ITR}}(\lambda) \sim \sqrt{N}$. Radiation at long wavelengths $\lambda > \sigma_z$ will experience constructive interference (CTR), leading to the scaling $E_{\mathrm{CTR}}(\lambda) \sim N$. Since typical electron bunches have $N \simeq 10^8 - 10^{10}$ electrons, the spectrum at wavelengths $\lambda > \sigma_z$ is very intense. By analyzing the spectral components of the CTR, information on the bunch profile can be obtained.

The CTR (THz) generation discussed in this thesis is based on emission by the LWFA-produced electron bunch as it propagates through the plasma-vacuum boundary, as first experimentally observed by Leemans *et al.* [29]. The general formalism for TR production will be presented in Sec. 3.2. The spectral and angular intensity distribution for CTR will be discussed in Sec. 3.3 and the CTR waveform in the temporal domain in Sec. 3.4. An estimation of the total CTR pulse energy and peak electric field will be provided in Sec. 3.5. Section 3.5.2 describes the expected THz emission parameters from a channel-guided LWFA-produced electron bunch. Note that Secs. 3.2–3.5 are based on a sharp metal-vacuum boundary. Section 3.6 will demonstrate that the plasma-vacuum boundary can indeed be approximated as a sharp metal-vacuum boundary.

The work in this chapter is based on the publications

- *Theory of coherent transition radiation generated at a plasma-vacuum interface*, by C.B. Schroeder, E. Esarey, J. van Tilborg, and W.P. Leemans, Phys. Rev. E **69**(1), 016501 (2004)
- *Pulse shape and spectrum of coherent diffraction-limited transition radiation from electron beams*, by J. van Tilborg, C.B. Schroeder, E. Esarey, and W.P. Leemans, Laser Part. Beams **22**(4), 415 (2004)
- *THz radiation as a bunch diagnostic for laser-wakefield-accelerated electron bunches*, by J. van Tilborg, C.B. Schroeder, C.V. Filip, Cs. Tóth, C.G.R. Geddes, G. Fubiani, E. Esarey, and W.P. Leemans, Phys. Plasmas **13**(5), 056704 (2006)

3.2 General formalism and assumptions

3.2.1 Radiation fields

The theory of transition radiation produced by a single electron was first studied by Ginzburg and Frank [34], and later extensively treated in the monograph by Ter-Mikaelian [35]. Schroeder *et al.* [30] included effects such as diffraction and bunch divergence. Van Tilborg *et al.* [2, 32] extended analysis to the temporal domain, and presented a comparison between the sharp metal-vacuum boundary and the non-sharp plasma-vacuum interface. The underlying theoretical concept of these findings will be discussed here.

Consider an electron bunch with local charge density ρ_b and current density $\mathbf{J}_b$, propagating through a medium. The Maxwell equations can be combined and written as the wave equation [36], or

$$\left(c^2\nabla^2 - \frac{\partial^2}{\partial t^2}\right)\mathbf{E} = 4\pi\frac{\partial}{\partial t}\left(\mathbf{J}_p + \mathbf{J}_b\right) + 4\pi c^2\nabla\left(\rho_p + \rho_b\right), \tag{3.1}$$

with $\mathbf{E}$ the electric field, ρ_p the plasma charge density and $\mathbf{J}_p$ the plasma current. The plasma is assumed to be neutral, with the ions motionless. The ion contribution to the charge density is ρ_0, and the electron contribution is $-\rho_0 + \delta\rho$, with $\delta\rho$ the local density perturbation. For the perturbed plasma, the continuity equation can be written as

$$\frac{\partial}{\partial t}\delta\rho + \nabla\cdot\mathbf{J}_p = 0. \tag{3.2}$$

The linearized fluid momentum equation is given by

$$4\pi\frac{\partial}{\partial t}\mathbf{J}_p = \omega_p^2\mathbf{E}, \tag{3.3}$$

and Poisson's equation reads

$$\nabla\cdot\mathbf{E} = 4\pi(\delta\rho + \rho_b). \tag{3.4}$$

Equation (3.2) can be written as $\partial_t^2\delta\rho + \nabla\cdot\partial_t\mathbf{J}_p = 0$, which, together with Eqs. (3.3) and (3.4) can be expressed as

$$\left(\frac{\partial^2}{\partial t^2} + \omega_p^2\right)4\pi\delta\rho = -\omega_p^2 4\pi\rho_b, \tag{3.5}$$

where it was assumed that the plasma is homogeneous ($\mathbf{E}\cdot\nabla\omega_p^2 = 0$). The continuity equation for the electron bunch can be written as $\partial_t\rho_b + \nabla\cdot\mathbf{J}_b = 0$. In the frequency domain ($\partial_t \rightarrow -\imath\omega$), Eqs. (3.1) and (3.5) can be combined to yield

$$\left(c^2\nabla^2 + \epsilon\omega^2\right)\mathbf{E} = \frac{4\pi}{\imath\omega\epsilon}\left[c^2\nabla\left(\nabla\cdot\mathbf{J}_b\right) + \omega^2\epsilon\mathbf{J}_b\right], \tag{3.6}$$

with $\epsilon = 1 - \omega_p^2/\omega^2$. The complete solution to Eq. (3.6) will yield both the particular solution (particle field $\mathbf{E}_p$) as well as the homogeneous solution (radiation field $\mathbf{E}_h$), or $\mathbf{E} = \mathbf{E}_p + \mathbf{E}_h$.

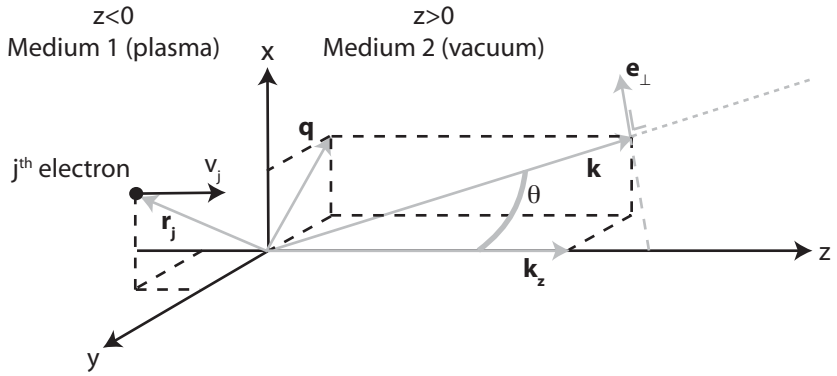

Fig. 3.3. Geometry of calculation: the j^{th} electron, positioned at $\mathbf{r}_j$ at $t = 0$, is propagating at normal incidence to the boundary (located at $z = 0$). The observation angle θ is defined as the angle between the radiation wave vector $\boldsymbol{k}$ and the z axis.

Consider a collection of N electrons incident at the interface between the plasma ($z < 0$, dielectric function ϵ) and vacuum ($z > 0$, dielectric constant $\epsilon = 1$). In the following, an expression for the radiation emitted at a specific observation angle will be derived. The velocity and position of the j^{th} electron at time $t = 0$ are defined as $\mathbf{v}_j$ and $\mathbf{r}_j$, respectively, see Fig. 3.3. The emission angle, or angle of observation, is defined as the angle θ between the wave vector $\mathbf{k}$ and the z axis. For simplicity, the electrons are assumed to move perpendicular to the interface, such that $\mathbf{v}_j = (0, 0, v_j) = c\beta_j \mathbf{e}_z$. Work by Schroeder *et al.* [30] did include non-normal (oblique) velocity vectors, and the effects of bunch divergence were found to be minimal. Section 3.6 will illustrate the main conclusion of this work (see Fig. 3.14).

The beam current can be expressed as $\mathbf{J}_b(\mathbf{x}, t) = -e \sum_{j=1}^{N} c\beta_j \delta(\mathbf{x} - \mathbf{r}_j - \mathbf{v}_j t)$. By Fourier space-decomposing Eq. (3.6), and substituting the Fourier-transformed beam current

$$\mathbf{J}_b(\omega, \mathbf{k}) = -e \sum_{j=1}^{N} c\beta_j 2\pi\delta(\omega - k_z v_j) e^{-\imath \mathbf{k}\cdot\mathbf{r}_j}, \tag{3.7}$$

the particular solution can be found to be

$$\mathbf{E}_p(\omega, \mathbf{k}) = \imath 4\pi e c^2 \sum_{j=1}^{N} \left(\frac{c\mathbf{k}}{\omega\epsilon_1} k_z \beta_j - \frac{\omega\beta_j}{c} \right) \frac{2\pi\delta(\omega - k_z v_j)}{c^2 k^2 - \epsilon\omega^2} e^{-\imath \mathbf{k}\cdot\mathbf{r}_j}. \tag{3.8}$$

It will be assumed that the bunch has an axial-symmetric charge distribution. This implies that the radiation (TR) follows the same symmetry. Both the electron bunch (field $\mathbf{E}_p$) and the radiation field $\mathbf{E}_h$ can be described in terms of a field component perpendicular to the interface E_z and parallel to the interface $E_\perp$ (not to be confused with the vector orientation $\mathbf{e}_\perp$). In the following, the radiation fields will be considered in the far-field only ($kR \gg 1$), with R the distance from the emitting source to the observer. The radiation fields $\mathbf{E}_h$ can be calculated by solving for the wave equation Eq. (3.6) in both media, and applying continuity across the boundary. For the field components perpendicular to the interface, continuity

in electric displacement requires $\epsilon(E_{p,z,1} + E_{h,z,1}) = (E_{p,z,2} + E_{h,z,2})$. Continuity of the field components in the plane of the interface requires $(E_{p,\perp,1} + E_{h,\perp,1}) = (E_{p,\perp,2} + E_{h,\perp,2})$. The four unknowns $E_{h,z,1}$, $E_{h,\perp,1}$, $E_{h,z,2}$, and $E_{h,\perp,2}$, can be calculated by solving the two boundary equations and the two radiation divergence requirements $\nabla \cdot \mathbf{E}_{h,1} = 0$ and $\nabla \cdot \mathbf{E}_{h,2} = 0$. For simplicity, the dielectric constant in the plasma will be approximated to be metal-like, such that $\epsilon \gg 1$. The validity of this assumption with respect to the experimental plasma-vacuum interface will be addressed in Sec. 3.6. The homogeneous solution (radiation field) in the region $z \geq 0$ can be found to be [30]

$$\mathbf{E}_h(\omega, \mathbf{q}, z) = \imath \frac{4\pi e}{\omega} \sum_{j=1}^{N} \frac{\mathcal{E}(\theta, u_j)}{\cos\theta} e^{-\imath\Psi_j} e^{\imath z\sqrt{\omega^2/c^2 - q^2}} \mathbf{e}_\perp, \tag{3.9}$$

with

$$\mathcal{E}(\theta, u) = \frac{u\sqrt{1+u^2}\sin\theta}{1 + u^2\sin^2\theta}, \tag{3.10}$$

$\Psi_j = \mathbf{q} \cdot \mathbf{r}_{\perp,j} + \omega r_{z,j}/v_j$, and $\mathbf{r}_{\perp,j} = r_{x,j}\mathbf{e}_\mathrm{x} + \mathrm{r_{y,j}}\mathbf{e}_\mathrm{y}$. The unit vector $\mathbf{e}_\perp$ lies in the $\mathbf{k}$-$\mathbf{e}_\mathrm{z}$ plane, and is perpendicular to the vector of observation $\mathbf{k}$, see Fig. 3.3. The vector $\mathbf{q}$, see Fig. 3.3, is defined as the projection of $\mathbf{k}$ onto the x-y plane. The ratio $k_z/|\mathbf{k}|$ can be expressed as $\cos\theta$. The normalized electron momentum u_j is related to the electron velocity through $u_j = \gamma_j\beta_j$, with $\gamma_j = 1/\sqrt{1-\beta_j^2} = \sqrt{1+u_j^2}$ and $\beta_j = v_j/c$. Radiation with a polarization vector $\mathbf{e}_\perp$ is referred to as radially polarized radiation. Section 3.5 will discuss the polarization properties in more detail.

3.2.2 Diffraction effects

The above model can be extended to include the effect of a boundary with a finite transverse size [30]. The self-fields of the bunch extend transversely on the order of $\gamma\lambda$. In case of a boundary with transverse size $\rho < \gamma\lambda$, diffraction radiation (DR) is emitted in addition to TR. The effect of the DR on the total radiation field is to reduce its amplitude. Since $\gamma\lambda$ is on the order of 1 mm in the LWFA (based on $\nu = 3$ THz and $\gamma = 10$), and ρ is on the order of 100–200 μm, diffraction effects can not be ignored.

To estimate the effect of diffraction, it is assumed that the beam is propagating through the center of the circular boundary of radius ρ, with $\sigma_r \ll \rho$. Here σ_r is the transverse size of the electron bunch (estimated to be $\simeq 5 - 10$ μm, see Sec. 2.3.3). Babinet's principle [36] expresses the radiation field $\mathbf{E}_\mathrm{DLTR}$ (diffraction-limited transition radiation) from a finite-size boundary as $\mathbf{E}_\mathrm{DLTR} = \mathbf{E}_\mathrm{TR} - \mathbf{E}_\mathrm{DR}$. Here $\mathbf{E}_\mathrm{TR}$ represents the transition radiation from an infinitely-wide boundary and $\mathbf{E}_\mathrm{DR}$ represents the radiated field from an electron bunch passing through an infinitely-wide metallic plane with an aperture of radius ρ. The diffraction radiation $\mathbf{E}_\mathrm{DR}$ in the far-field $R \gg r_\perp \sin\theta$ may be determined by applying Kirchhoff diffraction theory [36] to the incident particle fields of Eq. (3.8). The radiation

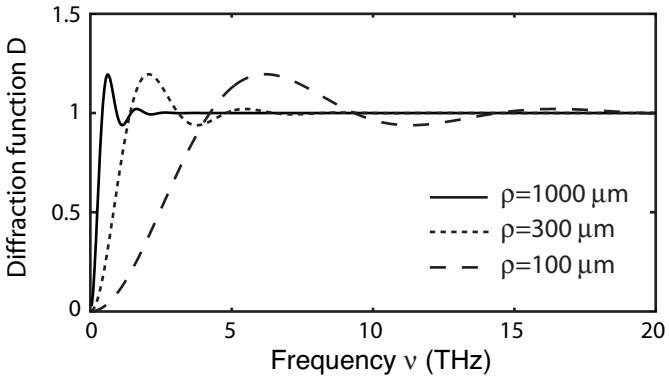

Fig. 3.4. The diffraction function $D(\nu)$ calculated for three different transverse boundary sizes, namely $\rho = 1000$ μm (solid curve), $\rho = 300$ μm (dotted curve), and $\rho = 100$ μm (dashed curve). The parameters u and θ were set to $u = 10$ and $\theta = 0.3$ rad. (Figure from Ref. [30].)

field E_{DLTR} is given by

$$\mathbf{E}_{\mathrm{DLTR}}(\omega, \mathbf{q}, z) = \imath \frac{4\pi e}{\omega} e^{\imath z\sqrt{\omega^2/c^2 - q^2}} \sum_{j=1}^{N} \frac{1}{\cos\theta} \mathcal{E}(\theta, u_j) D(\theta, \omega, u_j, \rho) e^{-\imath\Psi_j} \mathbf{e}_{\perp}, \tag{3.11}$$

where [30]

$$D(\theta, \omega, u, \rho) = 1 - J_0(bu\sin\theta)\left[bK_1(b) + \frac{b^2}{2}K_0(b)\right] - \frac{b^2}{2}K_0(b)J_2(bu\sin\theta). \tag{3.12}$$

Here J_m and K_m are the m^{th} order regular and modified Bessel functions, respectively, and the dimensionless impact parameter b is given by $b = \omega\rho/(cu) = 2\pi\rho/(u\lambda)$. As predicted, the scaling of $u\lambda$ to the boundary size ρ is a crucial parameter for diffraction effects. The second critical parameter is $u\sin\theta$. In the following paragraphs, the subscript DLTR will be replaced by TR, since diffraction effects are intrinsically present (infinite boundaries only exist in theory). Figure 3.4 displays the diffraction function D for three different boundary sizes, namely $\rho = 1000$ μm (solid curve), $\rho = 300$ μm (dotted curve), and $\rho = 100$ μm (dashed curve). For the calculations, $u = 10$ and θ=0.3 rad. One can see that the lower frequencies, where $u\lambda$ is larger, experience suppression due to the diffraction.

3.3 Spectral and angular emission distribution

3.3.1 Theoretical framework

Using the expression for the electric field $\mathbf{E}_{\mathrm{TR}}$ of diffraction-limited transition radiation (previously labeled $\mathbf{E}_{\mathrm{DLTR}}$), see Eq. (3.11), one can derive an expression for the coherent differential energy spectrum. By applying Parseval's theorem one can express the total energy W radiated through the z=z_0 plane in the far-field as

$$\begin{aligned} W &= \frac{c}{4\pi}\int dt \int dxdy\,(\mathbf{E}_{\mathrm{TR}} \times \mathbf{B}_{\mathrm{TR}}) \cdot \mathbf{e}_z \\ &= \frac{c}{2\pi}\int_0^{\infty} \frac{d\omega}{2\pi} \int \frac{d^2\mathbf{q}}{(2\pi)^2} (\mathbf{k}\cdot\mathbf{e}_z)\mathbf{E}^*_{\mathrm{TR}}(\omega, \mathbf{q}, z) \cdot \mathbf{E}_{\mathrm{TR}}(\omega, \mathbf{q}, z). \end{aligned} \tag{3.13}$$

By introducing $dk_x dk_y = 2\pi q dq = k^2 \cos\theta d\Omega$ it can be shown that

$$\begin{aligned}\frac{d^2W}{d\omega d\Omega} &= \frac{\omega^2 \cos^2\theta}{(2\pi)^4 c}\mathbf{E}^*_{\mathrm{TR}}(\omega, q, z)\cdot\mathbf{E}_{\mathrm{TR}}(\omega, q, z) \\ &= \frac{e^2}{\pi^2 c}\sum_{j=1}^{N}\sum_{m=1}^{N}\mathcal{E}_j\mathcal{E}_m D_j D_m e^{\imath(\Psi_m-\Psi_j)},\end{aligned} \tag{3.14}$$

with $d^2W/d\omega d\Omega$ the spectral and angular differential energy distribution. To replace the summation, one can introduce a spatial and momentum distribution function for the electron beam, given by the distribution $f(\mathbf{r}, u)$ with normalization $\int d^3\mathbf{r}duf(\mathbf{r}, u) = 1$. The momentum distribution is defined as $g(u) = \int d^3\mathbf{r} f(\mathbf{r}, u)$. The summations in Eq. (3.14) can be replaced by the ensemble average

$$\begin{aligned}\sum_i\sum_j \mathcal{E}_i D_i \mathcal{E}_j D_j e^{\imath(\Psi_m-\Psi_j)} &= N\int dv g(v)|\mathcal{E}D|^2 \\ &\quad + N(N-1)\left|\int d\mathbf{r}^3 dv f(\mathbf{r}^3, v)\mathcal{E}De^{\imath\Psi}\right|^2,\end{aligned} \tag{3.15}$$

where the first term on the right side of Eq. (3.15) represents the (incoherent) summation contributions where $i = j$. Assuming $N(N-1) \gg N$, this term can be neglected, and Eq. (3.14) can be rewritten as

$$\frac{d^2W_{\mathrm{CTR}}}{d\omega d\Omega} = \frac{e^2}{\pi^2 c}N^2\left|\langle\mathcal{E}DF\rangle\right|^2, \tag{3.16}$$

where the angular brackets indicate an average over momentum distribution $g(u)$. The form factor F is given by

$$F(\omega) = \frac{1}{g(u)}\int d^2\mathbf{r}_\perp\left[e^{-\imath\mathbf{q}\cdot\mathbf{r}_\perp}\int dz e^{-\imath z\omega/v} f(\mathbf{r}, u)\right]. \tag{3.17}$$

Note that F represents the Fourier transform of the charge distribution. For wavelengths much longer than the transverse and longitudinal bunch size it can be found that $F \simeq 1$ (coherence), while $F \to 0$ for small wavelengths. So it is through the form factor that the coherence condition is incorporated in the expression for $d^2W_{\mathrm{CTR}}/d\omega d\Omega$. In the case $D = F = 1$ (full coherence and no diffraction limitation), Eq. (3.16) reduces to the well-known result [34, 35]

$$\frac{d^2W_{\mathrm{CTR}}}{d\omega d\Omega} = N^2\frac{e^2}{\pi^2 c}\frac{u^2(1+u^2)\sin^2\theta}{(1+u^2\sin^2\theta)^2}. \tag{3.18}$$

Although the above analysis is valid for an arbitrary charge distribution $f(\mathbf{r}, u)$, the remainder of this thesis will consider an uncorrelated Gaussian distribution, such that $f(\mathbf{r}, u) = f'_z(r_z)f'_\perp(r_\perp)g(u)$, where $f'_z(r_z)$ and $f'_\perp(r_\perp)$ are the longitudinal and transverse Gaussian distributions (characterized by rms length σ_z and radius σ_r). For the uncorrelated charge distribution, the form factor of Eq. (3.17) reduces to

$$F(\omega) = F_\perp F_z = \exp\left(-\frac{\omega^2\sigma_r^2\sin^2\theta}{2c^2}\right)\exp\left(-\frac{\omega^2\sigma_z^2}{2\beta^2c^2}\right). \tag{3.19}$$

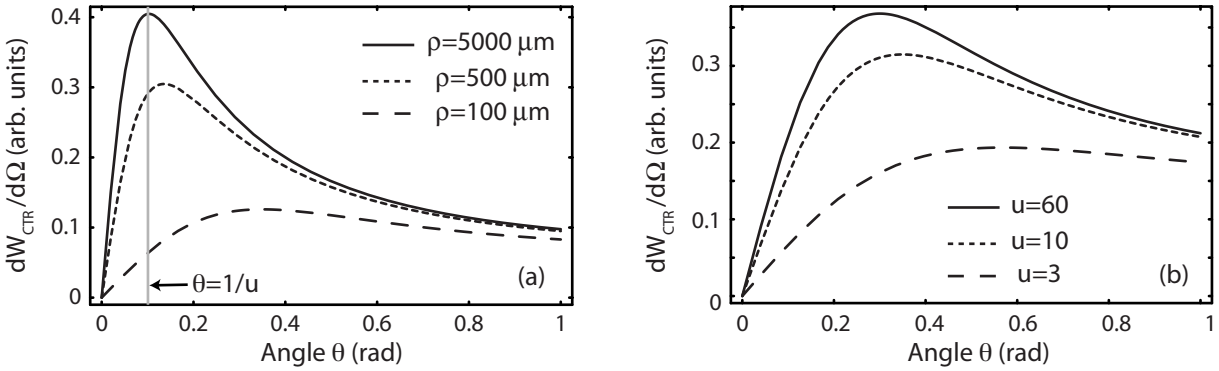

Fig. 3.5. The angular radiation distribution ($dW_{\rm CTR}/d\Omega = \int d\omega d^2W_{\rm CTR}/d\omega d\Omega$) at (a) different boundary sizes ρ and (b) different electron momenta u. Plot (a) was calculated with $u = 10$, $\rho = 5000$ μm (solid curve), $\rho = 500$ μm (dotted curve), and $\rho = 100$ μm (dashed curve). Plot (b) was calculated with $\rho = 100$ μm, $u = 60$ (solid curve), $u = 10$ (dotted curve), and $u = 3$ (dashed curve). For all curves, the bunch length is $\sigma_z = 15$ μm. (Figure from Refs. [2, 30, 32].)

Although the bunch divergence does not affect the calculations for $d^2W_{\rm CTR}/d\omega d\Omega$ directly (the bunch can be approximated as collimated), the bunch divergence does affect the development of the radial charge distribution, which in return affects the coherent spectrum through Eq. (3.19). For example, consider an electron bunch with $\sigma_z = 10$ μm, $\sigma_r = 1$ μm, and a bunch divergence of 100 mrad (half-angle). After propagating a distance of 10 cm, the transverse bunch size is $\sigma_r \simeq 1$ cm. Suppose CTR is emitted as the bunch passes through a dielectric discontinuity (after the propagation of 10 cm). Using Eq. (3.19), it can be seen that the coherence is limited to the < 100 GHz regime (and not the original < 10 THz regime).

For bunches where $\sigma_r \sin\theta \ll \sigma_z$, which is the case for LWFA-produced bunches, Eq. (3.19) can be further reduced to

$$F(\omega) = \exp\left(-\frac{\omega^2\sigma_z^2}{2\beta^2c^2}\right). \tag{3.20}$$

3.3.2 The differential energy distribution

From Eqs. (3.16) and (3.20) the differential angular energy distribution $dW_{\rm CTR}/d\Omega = \int d\omega d^2W_{\rm CTR}/d\omega d\Omega$ can be calculated. Figure 3.5 shows $dW_{\rm CTR}/d\Omega$ at (a) different boundary sizes ρ and (b) different electron momenta u. Figure 3.5(a) was calculated with $\sigma_z = 15$ μm, u=10, ρ=5000 μm (solid curve), ρ=500 μm (dotted curve), and ρ=100 μm (dashed curve). For large ρ (no diffraction limitation), the angular emission is peaked at $\theta = 1/u$, as predicted by Eq. (3.18). However, at smaller ρ, the angle of peak emission is shifted to larger θ. Note also that there is no CTR emission at $\theta = 0$, resulting in a "ring-shaped" angular emission pattern, also discussed in Sec. 3.5.

Figure 3.5(b) was calculated with $\sigma_z = 15$ μm, ρ=100 μm, u=60 (solid curve), u=10 (dotted curve), and u=3 (dashed curve). For larger u, diffraction effects become more dominant, resulting in a peak emission at larger θ [*c.f.* Fig. 3.5(a)]. Figure 3.5(b) also

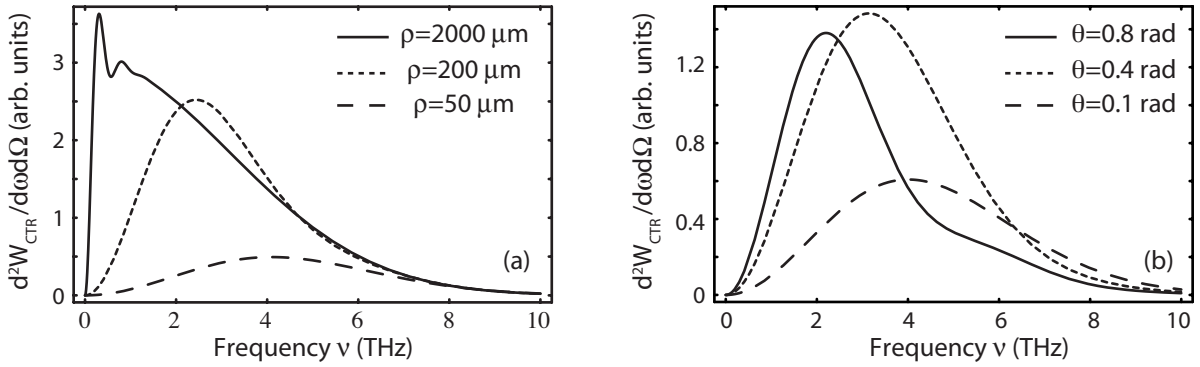

Fig. 3.6. The differential radiation distribution $d^2W_{\mathrm{CTR}}/d\omega d\Omega$ at (a) different boundary sizes ρ and (b) different observation angles θ. Plot (a) was calculated with $\theta = 0.3$ rad, $\rho = 2000$ μm (solid curve), $\rho = 200$ μm (dotted curve), and $\rho = 50$ μm (dashed curve). Plot (b) was calculated with $\rho = 100$ μm, $\theta = 0.8$ rad (solid curve), $\theta = 0.4$ rad (dotted curve), and $\theta = 0.1$ rad (dashed curve). In all curves, the bunch length is $\sigma_z = 15$ μm and the electron momentum is $u = 10$. (Figure from Refs. [2, 30, 32].)

demonstrates that the total emitted energy has a weak dependence on u for relativistic electrons. Although the electron bunch with u=60 has 6 times more momentum than the bunch with u=10, the increase in radiated energy is marginal.

Figure 3.6 shows the differential energy spectrum $d^2W_{\mathrm{CTR}}/d\omega d\Omega$ at (a) different boundary sizes ρ and (b) different observation angles θ. Figure 3.6(a) was calculated with $\sigma_z = 15$ μm, $u = 10$, θ=0.3 rad, ρ=2000 μm (solid curve), ρ=200 μm (dotted curve), and ρ=50 μm (dashed curve). For large ρ (solid curve), the diffraction effects become negligible and the CTR spectrum is almost identical to the Gaussian bunch form factor $F(\omega)$. The effect of the diffraction (smaller ρ) is to reduce the emission amplitude of the lower frequencies. Note that Fig. 3.6(a) indicates that a bunch with $\sigma_z = 15$ μm emits coherently up to $\nu \approx$5 THz, and not up to $1/\sigma_t$ =20 THz as one might intuitively estimate. Since LWFA-produced electrons bunches have typical lengths on the order of $\sigma_z \simeq 5 - 20$ μm, the CTR pulses are also referred to as THz pulses. The temporal field profiles $E_{\mathrm{CTR}}(t)$ corresponding to the curves in Fig. 3.6(a) can be found in Fig. 3.7(a).

Figure 3.6(b) was calculated with $\sigma_z = 15$ μm, $u = 10$, ρ=100 μm, θ=0.8 rad (solid curve), θ=0.4 rad (dotted curve), and θ=0.1 rad (dashed curve). One can observe that the lower frequencies (0–3 THz) are predominantly emitted at larger emission angles. If the observer is positioned at a smaller observation angle, the frequency of maximum radiation shifts to higher frequencies.

3.4 Temporal field profile

3.4.1 Theoretical framework

This section will focus on calculation of the electric field profile of the CTR pulse [32]. The starting point for temporal analysis is Eq. (3.11). By replacing the summation by the

integral over the electron distribution $f(\mathbf{r}, u)$, Eq. (3.11) can be written as

$$\mathbf{E}_{\mathrm{CTR}}(\mathbf{x},\omega) = \frac{\imath 4\pi eN}{(2\pi)^2\omega}\mathbf{e}_\perp \int \frac{dk_x dk_y}{\cos\theta} \left\langle \mathcal{E}(\theta,u) D(\omega,u,\theta,\rho) F(\omega,u,\theta)\right\rangle e^{\imath z\sqrt{k^2-q^2}+\imath \mathbf{x}_\perp\cdot\mathbf{q}}, \quad (3.21)$$

where the subscript DLTR has been replaced by the subscript CTR. The observation location is defined as $\mathbf{x} = \mathbf{x}_\perp + z\mathbf{e}_z = x\mathbf{e}_x + y\mathbf{e}_y + z\mathbf{e}_z$, and $R^2 = x_\perp^2 + z^2$. The integral $\int dk_x dk_y$ can be replaced by $\int q dq d\phi$, with $q = |\mathbf{q}|$ and the orientation of $\mathbf{q}$ depicted in Fig. 3.3. The integration over $\int d\phi$, with $\mathbf{x}_\perp \cdot \mathbf{q} = x_\perp q\cos\phi$, yields

$$\mathbf{E}_{\mathrm{CTR}}(\mathbf{x},\omega) = \imath 2eN\mathbf{e}_\perp \int_0^\infty \frac{dq}{\omega}\tan\theta \left\langle \mathcal{E}DF\right\rangle e^{\imath z\sqrt{k^2-q^2}} J_0(qx_\perp). \quad (3.22)$$

In the far-field, where $\mathbf{x}_\perp \cdot \mathbf{q} \gg 1$, the Bessel function can be approximated using the asymmetric expansion $J_0(qx_\perp) \simeq (2/\pi q x_\perp)^{1/2}\cos(\imath q x_\perp - \imath\pi/4)$, yielding the electric field

$$\mathbf{E}_{\mathrm{CTR}}(\mathbf{x},\omega) = \frac{2eN\imath}{\omega\sqrt{2\pi x_\perp}}\mathbf{e}_\perp \left[e^{\imath\pi/4}\int_{-\infty}^{\infty} dq G(q) e^{\left(\imath\sqrt{k^2-q^2}z + \imath q x_\perp/R\right)} + e^{-\imath\pi/4}\int_{-\infty}^{\infty} dq G(q) e^{\left(\imath\sqrt{k^2-q^2}z - \imath q x_\perp/R\right)}\right], \quad (3.23)$$

with $G(q) = H(q)\sqrt{q}\left\langle \mathcal{E}DF\right\rangle \sec\theta$, where $H(q)$ is the Heaviside function [i.e., $H(x) = 1$ for $x \geq 0$ and zero for $x < 0$].

Since the imaginary part of the exponent in the first integral of Eq. (3.23) has a maximum value at $q^* = kx_\perp/R$, the method of stationary phase [76] can be applied. This method approximates the integral by evaluating the integrand around $q = q^*$ (such that $q^*/k = \sin\theta = x_\perp/R$). Since the imaginary part of the exponent in the second integral of Eq. (3.23) peaks at $q^* = -kx_\perp/R$, the contribution of this integral can be neglected. Applying the method of stationary phase, the integral in Eq. (3.23) can be evaluated in the far-field limit ($kR \gg 1$), and has the solution

$$\mathbf{E}_{\mathrm{CTR}}(\mathbf{x},\omega) = -\frac{2eN}{cR}\left\langle \mathcal{E}(\theta,u) D(\omega,u,\theta,\rho) F(\omega,u,\theta)\right\rangle e^{\imath kR}\mathbf{e}_\perp, \quad (3.24)$$

with $k = \omega/c$. The temporal electric field profile $\mathbf{E}_{\mathrm{CTR}}(\mathbf{x},t)$ in the far-field is given by the inverse Fourier-transform integral

$$\mathbf{E}_{\mathrm{CTR}}(\mathbf{x},t) = -\frac{eN}{\pi R}\mathbf{e}_\perp \int dk \left\langle \mathcal{E}(\theta,u) D(k,u,\theta,\rho) F(k,u,\theta)\right\rangle e^{-\imath k(ct-R)}. \quad (3.25)$$

For a Gaussian form factor $F = F_{\mathrm{G}} = \exp\left[-(\omega\sigma_z/v)^2/2\right]$, see Eq. (3.20), it can be found that

$$\left(\frac{-\sigma_z R}{eN}\right)\mathbf{E}_{\mathrm{CTR}}(\mathbf{x},\tau) = \mathbf{e}_\perp \frac{2}{\pi}\left\langle \beta\mathcal{E}(\theta,u)\int_0^\infty d\eta\cos(\eta\tau) D(\eta\mu, u\sin\theta)\exp\left(-\eta^2/2\right)\right\rangle, \quad (3.26)$$

with the normalizations $\mu = \beta\rho/(u\sigma_z)$, $\tau = \beta(ct-R)/\sigma_z$ and $\eta = k\sigma_z/\beta$. The parameter μ can be interpreted as the ratio of the diffraction-related long-wavelength cut-off ($\sim \beta\rho/u$) to the short wavelength cut-off due to coherence effects ($\sim \sigma_z$). In the original publication by van Tilborg *et al.* [32], the parameter μ was labeled as ν. Since ν already represents the frequency in this thesis, the parameter $\beta\rho/(u\sigma_z)$ will be labeled as μ here.

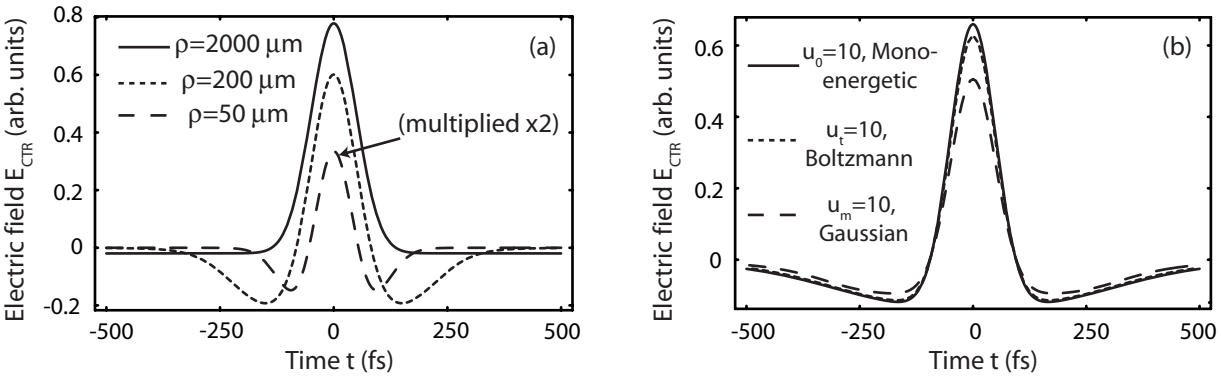

Fig. 3.7. The electric field profile $E_{\mathrm{CTR}}(t)$ at (a) different boundary sizes ρ and (b) different momentum distributions. Plot (a) was calculated with $\sigma_z = 15$ μm, $\theta = 0.3$ rad, $u = 10$, $\rho = 2000$ μm (solid curve, $\mu = 13$), $\rho = 200$ μm (dotted curve, $\mu = 1.3$), and $\rho = 50$ μm (dashed curve, $\mu = 0.33$). The curves in plot (b) were calculated with $\sigma_z = 15$ μm, $\rho = 900$ μm, and $\theta = 0.1$ rad. The solid curve in plot (b) describes $E_{\mathrm{CTR}}(t)$ from a mono-energetic momentum distribution at $u_0 = 10$. The dotted curve is calculated for a Boltzmann distribution with temperature $u_t = 10$, and the dashed curve for a Gaussian distribution with mean $u_m = 10$. (Figure from Refs. [2, 32].)

3.4.2 $E_{\mathrm{CTR}}(t)$ in the ultra-relativistic limit

In the limit $b = k\rho/u \ll 1$ (e.g., an ultra-relativistic electron beam with $u \gg 1$), the diffraction function D [see Eq. (3.12)] can be approximated as $D \simeq (2 + u^2 \sin^2\theta) b^2/4$. In this limit ($b \ll 1$), integrating Eq. (3.26) yields

$$\left(\frac{-\sigma_z R}{eN}\right) \mathbf{E}_{\mathrm{CTR}}(\tau) = \left\langle \frac{\beta}{\sqrt{8\pi}} \left(\frac{u\sqrt{1+u^2}\sin\theta}{1+u^2\sin^2\theta}\right) \left(2+u^2\sin^2\theta\right) \mu^2 (1-\tau^2) \exp\left(-\tau^2/2\right) \right\rangle \mathbf{e}_\perp, \tag{3.27}$$

where a Gaussian charge distribution is assumed, following Eq. (3.20). As can been seen from Eq. (3.27), the length of the waveform (i.e. the rms radiation pulse length) is not a function of ρ or μ in this limit. Equation (3.27), with $\mathbf{E}_{\mathrm{CTR}}(\tau) \propto (1-\tau^2)\exp(-\tau^2/2)\mathbf{e}_\perp$, predicts a single-cycle pulse. The solution also satisfies the Lawson-Woodward-Palmer theorem [77, 78] for electro-magnetic radiation in vacuum, which states that $\int_{-\infty}^{\infty} E(t)dt = 0$.

3.4.3 $E_{\mathrm{CTR}}(t)$ from mono-energetic electron bunches

Figure 3.7(a) displays the solution to Eq. (3.26) for several values of the transverse boundary size ρ, while assuming a mono-energetic momentum distribution $g(u) = \delta(u - u_0)$, with σ_z=15 μm [following Eq. (3.20)], $u_0 = 10$, and θ=0.3 rad. The solid curves displays the solution with ρ=2000 μm (μ=13), the dotted curve with ρ=200 μm (μ=1.3), and the dashed curve ρ=50 μm (μ=0.33). The field profile for ρ=50 μm (dashed curve) is multiplied by 2 for clarity. The parameters of the curves in Fig. 3.7(a) are identical to the ones in Fig. 3.6(a), so that the field profiles in the spectral and temporal domains can be compared directly. All the curves in Fig. 3.7(a) can be described as single-cycle waveforms,

with the field profile approaching a half-cycle profile in the limit $\rho \to \infty$. One can also observe that as ρ decreases i) the amplitude of the field strength is reduced, ii) the negative side-wings in $E_{\mathrm{CTR}}(t)$ become more pronounced, and iii) these side-wings move closer to the center of the pulse.

3.4.4 $E_{\mathrm{CTR}}(t)$ for various electron momentum distributions

It was mentioned in Sec. 3.3.2 that the CTR emission amplitude does not have a strong dependence on momentum u for relativistic electrons. Figure 3.5(b) showed that the emission for $u = 60$ was marginally larger than for $u = 10$. When modeling CTR emission from LWFA-produced bunches, characterized by a large energy spread, the CTR expression can be simplified if the momentum distribution can be approximated by a mono-energetic distribution. For example, a Boltzmann momentum distribution $g(u) \propto \exp(-u/u_t)$ can be approximated (in terms of CTR emission) as $g(u) = \delta(u - u_t)$. To demonstrate that such an approximation is valid, three momentum distributions are considered here. Figure 3.7(b) displays the CTR waveforms for a mono-energetic momentum distribution $g(u) = \delta(u - u_0)$ with $u_0 = 10$ (solid curve), a Boltzmann momentum distribution $g(u) = (1/u_t)\exp(-u/u_t)$ with temperature u_t=10 (dotted curve), and a Gaussian momentum distribution $g(u) = \exp[-(u - u_m)^2/u_{\mathrm{rms}}^2]/(u_{\mathrm{rms}}\sqrt{\pi})$ with mean u_m=10 and spread $u_{\mathrm{rms}} = 3$ (dashed curve). One can see that the pulse shape is fairly insensitive to the type of momentum distribution, with each distribution described by the same value for their characteristic parameter (u_0, u_t, and u_m). Furthermore, the amplitude of the electric field is only weakly influenced by the various momentum distributions.

3.5 Total pulse energy and peak field

3.5.1 THz pulses from the unchanneled SM-LWFA

This section provides an estimation of the total pulse energy and peak electric field of the CTR pulse. Parameters close to the experimental realization of the SM-LWFA are chosen, see Sec. 2.4 for details. For simplicity, the coherent spectrum of the CTR pulse is assumed to be fully coherent from ν=0.3–3 THz (*i.e.* $F = 1$ in this frequency range). The electron bunch is assumed to have a Boltzmann momentum distribution, with temperature u_t=10. The radiation within a cone angle θ (half-angle) will be considered, and the total collected energy W_{CTR} within that cone angle will be normalized to Q^2, with Q the bunch charge. Figure 3.8 shows the collected CTR pulse energy versus the transverse boundary size, within a cone angle of $\theta < 200$ mrad (top curve), $\theta < 100$ mrad (middle curve), and $\theta < 30$ mrad (bottom curve). For example, Fig. 3.8 illustrates that a 1-nC bunch at $\theta < 30$ mrad and $\rho = 100$ μm will emit 1 nJ of radiation, corresponding to the emission of 9 nJ by a 3-nC bunch under the same conditions. Section 4.2.1, which is based on the publication by Leemans *et al.* [29], provides experimental agreement to the model.

As expected, the collection within a larger cone angle leads to an increase of total CTR

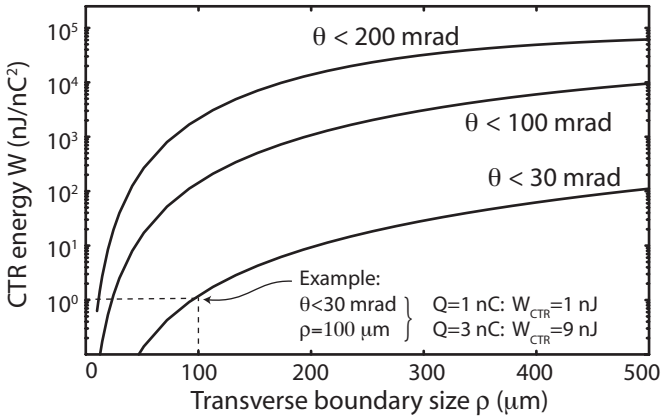

Fig. 3.8. The total CTR pulse energy in units of [nJ nC^{-2}], within a specific angular cone, versus transverse boundary size ρ [29, 30]. The radiated energy in units of [nJ] is normalized to the square of the charge Q^2 (charge in units of [nC]). The radiation is considered to be coherent within the spectral range $\nu = 0.3 - 3$ THz. The bunch has a Boltzmann momentum distribution, with temperature $u_t = 10$. The three curves are calculated based on collection half-angles of $\theta \leq 30$ mrad (bottom curve), $\theta \leq 100$ mrad (middle curve), and $\theta \leq 200$ mrad (top curve). (Figure from Refs. [29, 30].)

pulse energy. Also, the total radiation is larger if the transverse boundary size is increased. As Fig. 3.8 illustrates, by collecting the radiation within a $\theta = 200$ mrad angle, the THz pulse contains over 10 μJ at ρ =200 μm ($Q = 1$ nC). Such a pulse energy is 1–2 orders of magnitude larger than achievable with conventional laser-based sources (*e.g.* optical rectification and the photoconductive antenna). Note that the total electron bunch energy (1 nC at $u = 10$) is on the order of 5 mJ, such that radiative damping effects are not considered dominant.

When considering the peak electric field of a focused THz pulse, it is important to note that the CTR pulse has a radial polarization. Consider a CTR pulse in the far field that is collimated by a lens or a parabola, as sketched on the left side of Fig. 3.9. The field map of the CTR pulse, showing the spatial profile of the field amplitude is plotted in Fig. 3.9(a), based on $u = 10$ and $D = F = 1$. Also indicated are several field vectors, with the vector length representing field strength. In agreement with Eq. (3.18), there is a preferred angle of emission ($\theta \simeq 1/u$ for large boundaries), and there is no emission on axis ($\theta = 0$). If all the rays were collected by a focusing optic, there would be a total field cancelation on axis at focus. Only at off-axis locations is the field cancelation incomplete, and the 2D THz spot profile resembles a ring structure. If the collimated THz pulse is propagated through a polarizer, 50% of the energy is transmitted, with a field map shown in Fig. 3.9(b). The polarizer in this example only transmitted vertical polarized THz fields. If the linearly-polarized THz pulse is now focused, there still is complete field cancelation on axis. The total THz energy is further reduced by 50% if only the upper half of the emission is collected ($y > 0$). In this case, with all field vectors pointing in the same direction, focusing yields a single 2D THz spot (no field cancelation).

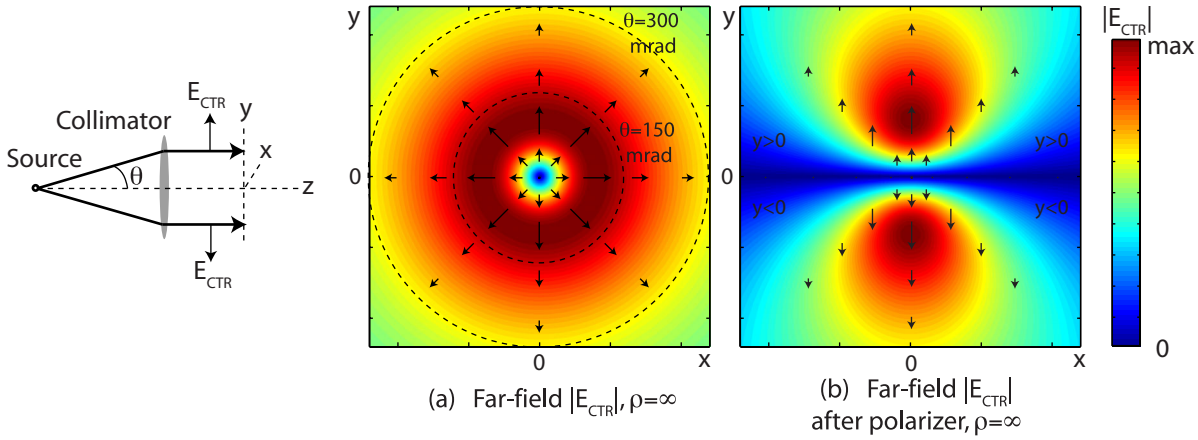

Fig. 3.9. (a) Field map of a radially-polarized THz pulse in the far-field, or $|E_{\mathrm{CTR}}|\mathbf{e}_{\perp}$, after collimation by a lens or parabola. Since the THz emission is collimated, the vector $\mathbf{e}_{\perp}$ lies in the x-y plane, pointing radially outward. There is a preferred angle of emission, while on-axis $E_{\mathrm{CTR}} = 0$. (b) Spatial field map after the CTR pulse is propagated through a polarizer, transmitting only the vertical polarization component. Both field maps were calculated based on $u = 10$, $F = 1$, and $\rho \to \infty$ $(D = 1)$.

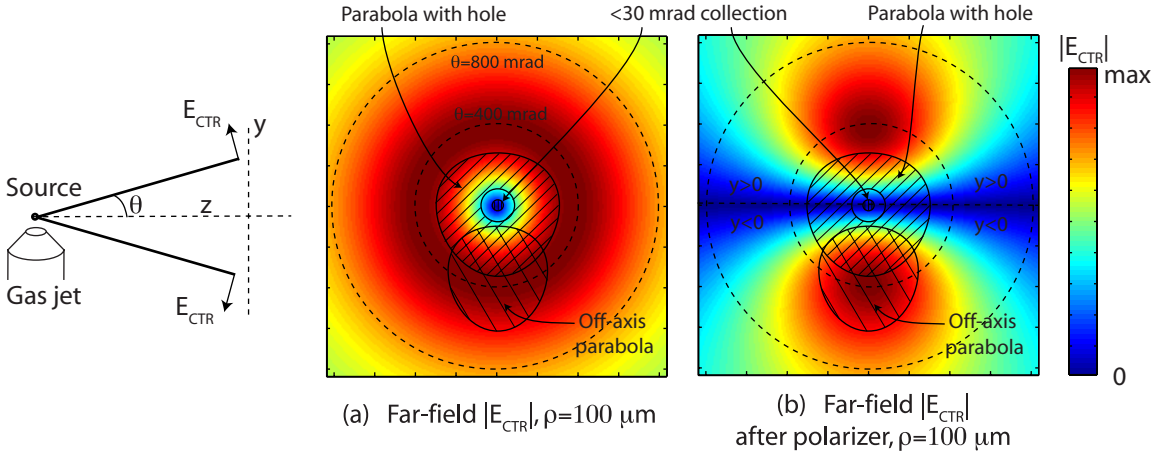

Fig. 3.10. Angular field distribution for $|E_{\mathrm{CTR}}|$ (a) without a polarizer, and (b) with a vertical polarizer. The field pattern is calculated for $u = 10$ and $\rho = 100$ μm. One can see that the emission is peaked at approximately $\theta \simeq 400$ mrad. For three different experimental collection configurations, used in experiments described in Chapters 4, 5, and 6, the angular collection is shown. They include an optic with < 30 mrad collection, a parabola with $\simeq 80 - 300$ mrad collection (parabola with hole), and an off-axis parabola (OAP2) with its center at $\theta = 0.33$ rad.

Note that in the case of incoherent transition radiation (ICT), the collimated ITR profile has no emission on axis ($\theta = 0$), just as in Fig. 3.9(a), but at focus the field cancellations are not complete due to the incoherent nature. Therefore, focusing a radially-polarized ITR pulse does not yield a minimum on axis (instead, the 2D THz spot has a maximum on axis).

In case of a finite boundary size $\rho = 100$ μm, the angular field amplitude distribution

$|E_{\mathrm{CTR}}|$ is shown in Fig. 3.10(a). Figure 3.10(b) depicts the distribution if only the vertical polarization components are considered. Both Figs. 3.10(a) and 3.10(b) also show the angular acceptance of three THz optics, which will be used in experiments described in Chapters 4, 5, and 6. They include an optic with < 30 mrad collection, a parabola with $\simeq 80 - 300$ mrad collection (parabola with hole), and an off-axis parabola with its center at $\theta = 0.33$ rad.

Based on Eq. (2.3), the expression for the THz field amplitude at focus can be expressed as

$$E_{\mathrm{CTR}}\ [\mathrm{kV\,cm^{-1}}] = \frac{390}{\eta}\sqrt{\frac{\mathrm{W_{CTR}\ [J]}}{\pi \times (\mathrm{r_0}\ [\mu\mathrm{m}])^2 \times \sigma_{\mathrm{CTR}}\ [\mathrm{s}]}}, \tag{3.28}$$

with r_0 the spotsize in units of [μm], defined from the electric field profile $E_{\mathrm{CTR}}(r) \propto e^{-r^2/r_0^2}$, σ_{CTR} the CTR pulse duration in units of [s], and W_{CTR} the CTR pulse energy in units of [J]. Note that Eq. (3.28) is derived for narrow-bandwidth pulses, and has to be considered as an approximation to the broad-bandwidth peak CTR field. The factor η in Eq. (3.28) incorporates the collection efficiency and field cancelation at focus. For example, by focusing a CTR pulse as depicted in Fig. 3.9(a), the field cancelation on-axis is complete and $\eta \to \infty$. In another example, consider that only the upper half ($y > 0$) of the fields of Fig. 3.9(b) are collected and focused. At focus, there is no field cancellation, with 25% of the original CTR energy remaining ($\eta = 2$). To continue this example, a previously-presented parameter set is considered, where $\theta < 200$ mrad, $Q = 1$ nC, $\rho = 200$ μm, $\sigma_z \simeq 15$ μm, $u = 10$, and $W_{\mathrm{CTR}} = 10$ μJ. One can estimate that the THz pulse length lies around $\sigma_{\mathrm{CTR}} \simeq 300$ fs, see Fig. 3.7(a), and that the pulse can be focused to a spot with $r_0 \simeq 300$ μm (several wavelengths). With $\eta = 2$, the focused CTR field can be estimated with Eq. (3.28) to be on the order of

$$E_{\mathrm{CTR}} \simeq 2.1\ \mathrm{MV\,cm^{-1}} \quad \text{for} \quad \begin{cases} \sigma_z = 15\ \mu\mathrm{m}, & Q = 1\ \mathrm{nC} \\ \theta < 200\ \mathrm{mrad}, & \rho = 200\ \mu\mathrm{m} \\ \sigma_{\mathrm{CTR}} \simeq 300\ \mathrm{fs}, & r_0 \simeq 300\ \mu\mathrm{m} \\ W_{\mathrm{CTR}} = 10\ \mu\mathrm{J}, & \eta = 2, \end{cases} \tag{3.29}$$

which is well over the $\simeq$1 MV cm^{-1} limit that is useful for future THz applications [47, 49]. Evidently, more charge in the bunch and a larger collection angle will further increase the peak CTR field.

The experiments on THz radiation in this thesis were performed using a plasma of transverse boundary size $\rho \simeq 100$ μm, in which case the total collected energy is reduced by approximately a factor of $\times 10$ (with respect to $\rho = 200$ μm), as shown in Fig. 3.8. Consequently, the peak THz electric field at focus is then also reduced.

3.5.2 THz pulses from the channel-guided LWFA

This section will discuss CTR emission from LWFA-produced bunches propagating through a metallic foil positioned in the bunch path. The advantages of using the foil for THz

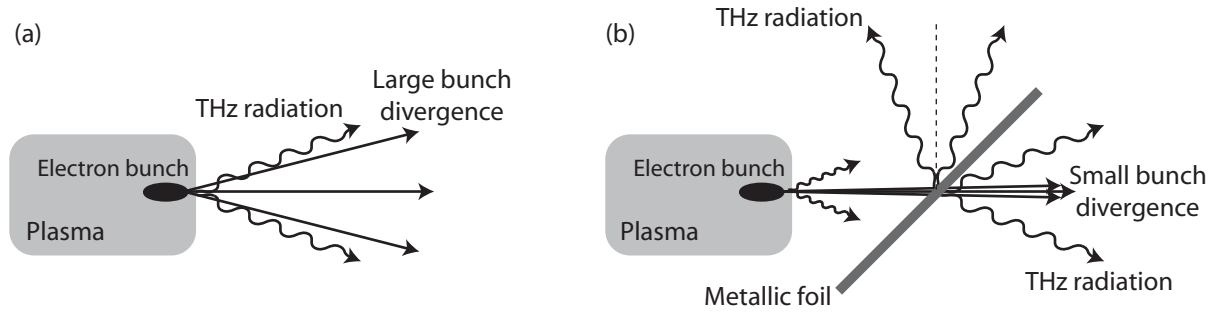

Fig. 3.11. (a) If the LWFA-produced electron bunch has a large energy spread and large bunch divergence, one has to rely on the plasma-vacuum interface for THz emission. (b) However, channel-guided LWFA-produced bunches have a percent-level energy spread, and a divergence of < 3 *mrad. For this reason, the spatial and temporal coherence at the location of a metallic foil is still conserved, and intense THz radiation can be collected.*

emission are the larger transverse transverse size ρ and the enhanced collection efficiency since optics can be placed close to the foil. However, as was discussed at the end of Sec. 3.3.1, the divergence of the electron bunch prevents the emission in the THz regime if the foil is placed too far from the plasma-vacuum boundary. Also, the electron energy spread can lead to significant debunching during propagation towards the foil. For the unchanneled SM-LWFA (see Sec. 2.4 for bunch parameters), foil-based emission in the THz regime is not achievable since the electron energy spread is 100%, the bunch divergence is on the order of 25–50 mrad, and the foil can not be placed close to the plasma due to damage by remnant laser light. Figure 3.11(a) shows that, if the LWFA-produced bunch divergence is too large, one has to rely on THz emission from the plasma-vacuum boundary.

The issues of debunching are of less concern if bunches from the channel-guided LWFA are considered, which were presented in Sec. 2.5. The reduced electron energy spread (few percent) and the small bunch divergence (<3 mrad) conserve the longitudinal and transverse bunch coherence over a longer distance. For example, consider a 1-nC 50-fs-long electron bunch with a 1 mrad bunch divergence. As Fig. 3.11(b) illustrates, the bunch emits a first pulse of radiation as its exits the plasma-vacuum boundary. When the bunch reaches a metallic foil positioned 20 cm from the plasma, its coherence at wavelengths $\lambda > 100$ μm, or $\nu < 3$ THz, is relatively unaffected. A second THz pulse is emitted here. The foil diameter can be on the order of $\rho > 10$ cm, and the collection half-angle on the order of 500 mrad, resulting in the collection of a very intense THz pulse. Although Fig. 3.8 does not show a curve for $\theta < 500$ mrad, a similar calculation of the collected THz pulse energy yields > 200 μJ, which if focused has a peak field in excess of $\gtrsim$10 MV cm^{-1}.

3.6 The metal-vacuum versus plasma-vacuum boundary

In the previous sections, the CTR characteristics were calculated for a sharp metal-vacuum boundary. In the LWFA-based experiments, the bunch propagates through a plasma-

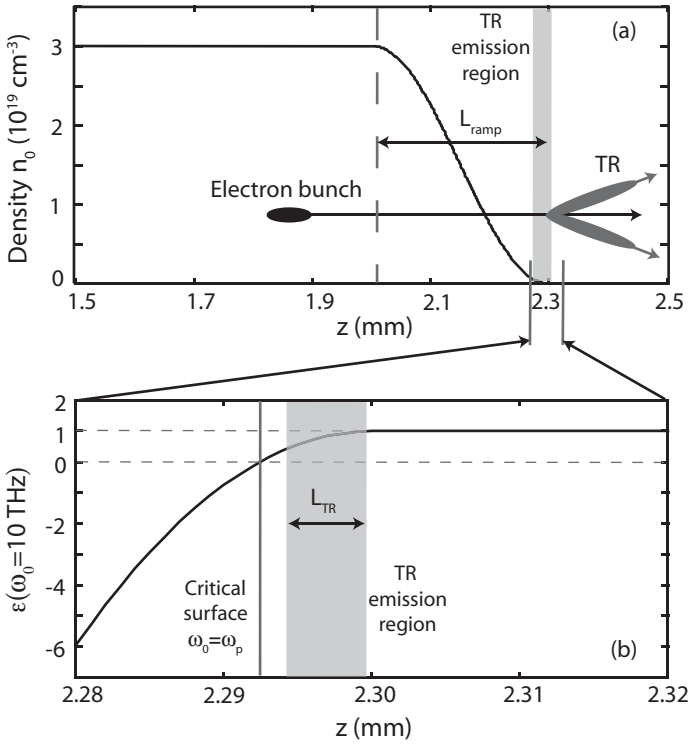

Fig. 3.12. (a) Longitudinal plasma density profile $n_0(z)$. (b) The spatially varying dielectric constant $\epsilon(z, \omega_0)$, for radiation at frequency $\omega_0 = 10$ THz. The electron bunch is propagating from left to right. (Figure from Ref. [2].)

vacuum interface. The dielectric function in a (cold) plasma is given by $\epsilon(\omega) = 1 - \omega_p^2/\omega^2$, with ω_p the plasma (angular) frequency. The longitudinal plasma profile in LWFA experiments is non-uniform, and is determined by the gas emission profile. Since the profile follows the density function $n_0(z)$, with z the propagation direction of the laser, the dielectric function also has a spatial dependence $\epsilon(\omega, z)$. Due to the changing dielectric environment, TR is emitted as the electron bunch propagates through the plasma to vacuum. A heuristic picture is presented here, concerning the location in the plasma where the CTR pulse is emitted, and at what intensity if compared to CTR from a metal-vacuum boundary.

A density profile is plotted in Fig. 3.12(a), which is characteristic for the experiments described in this publication. Density interferometry has confirmed the agreement between modeled and actual density profile. The transverse size of the plasma is on the order of $\rho \simeq 100 - 200$ μm. The density interferometer is less sensitive at low plasma densities $n < 10^{18}$ cm^{-3}, and plasma parameters in this regime are therefore based on estimations. Figure 3.12(a) shows a uniform density profile (up to $z = 2$ mm and starting at $z = 0$ mm), followed by a down ramp with length $L_{\rm ramp}$, which is on the order of $L_{\rm ramp} \simeq 300$ μm. As an example, the analysis will focus on TR with frequency $\omega_0 = 10$ THz, although TR at any arbitrary radiation frequency can be analyzed in a similar manner. For $\omega_0 = 10$ THz, one can derive the spatially varying dielectric constant $\epsilon(z, \omega_0)$, plotted in Fig. 3.12(b).

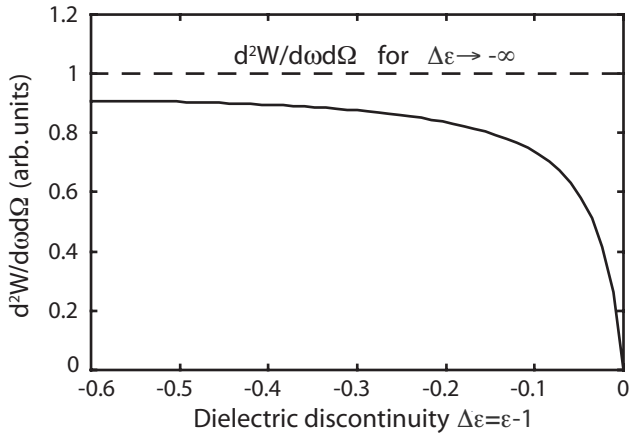

Fig. 3.13. The differential energy distribution $d^2W/d\omega d\Omega$ (solid curve) for an electron passing the dielectric discontinuity of a medium-vacuum interface (from ϵ to $\epsilon = 1$), with $\Delta\epsilon = \epsilon - 1$. The dashed line represents $d^2W/d\omega d\Omega$ in the (metal-vacuum) limit of $\Delta\epsilon \to -\infty$. (Figure from Ref. [2].)

Note that the z-range in Fig. 3.12(b) is only a small fraction of the z-range in Fig. 3.12(a). In the high-density region ($n \approx 10^{17} - 10^{19}$ cm^{-3}), the density is highly overcritical for ω_0 such that $\epsilon(\omega_0) \to -\infty$. Only in the lower-density part of the ramp ($n \lesssim 10^{17}$ cm^{-3}) does the dielectric constant reach positive values, and eventually becomes $\epsilon = 1$ in vacuum.

Before continuing the discussion on the location in the plasma profile where the TR is emitted, a necessary step back is taken by first considering TR from a step-boundary between a medium with dielectric constant ϵ and vacuum ($\epsilon = 1$). In Sec. 3.2.1, the theoretical framework for emission of TR was presented, although the final expressions were derived for the limit $\epsilon \to \infty$. In case of an arbitrary value for ϵ, the expression for the differential energy distribution $d^2W/d\omega d\Omega$ can be found in the literature [35] to be

$$\frac{d^2W}{d\omega d\Omega} = \frac{e^2}{\pi^2 c}\left[\frac{\epsilon - 1}{(1-\beta^2\cos^2\theta)(1-\beta\sqrt{\epsilon - \sin^2\theta})}\right]^2 \times \left[\frac{1-\beta^2-\beta\sqrt{\epsilon-\sin^2\theta}}{\sqrt{\epsilon-\sin^2\theta}+\epsilon\cos\theta}\right]^2 . \tag{3.30}$$

Note that this expression is only valid for a single electron propagating along the z axis at normal incidence to the interface. In Fig. 3.13 one can see (solid curve) the dependency of $d^2W/d\omega d\Omega$ on $\Delta\epsilon = \epsilon - 1$, with values for ϵ in the range of 0.4–1. For this calculation the parameters $\theta = 0.15$ rad and u=10 were used. The dashed line corresponds to the differential energy emitted for the (metal-vacuum) discontinuity where $\epsilon \to -\infty$. One can see that the transition $\Delta\epsilon = -0.2$, or $\epsilon = 0.8$, results in nearly 90% of the radiation emission compared to $\Delta\epsilon = -\infty$. This indicates that TR emission is dominated by the $\epsilon = 0.8$ to $\epsilon = 1$ boundary (the transition $\epsilon = -\infty$ to $\epsilon = 0.8$ will result in emission of only a fraction of the energy of the $\epsilon = 0.8$ to $\epsilon = 1$ interface).

Consider again the emission of TR from the plasma profile in Fig. 3.12(a). When the

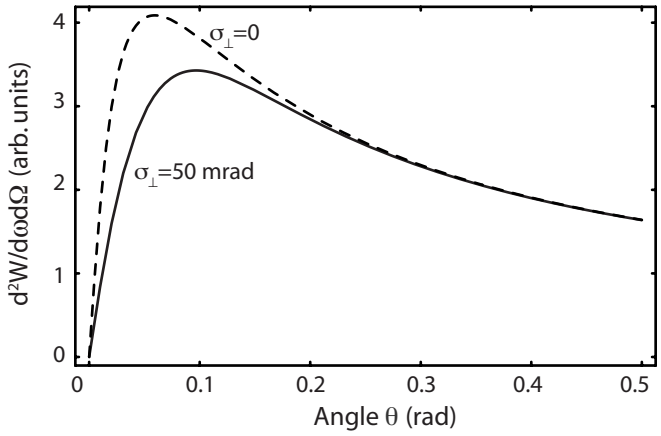

Fig. 3.14. Differential energy distribution $d^2W/d\omega d\Omega$ for a bunch with no divergence (dashed curve) and a bunch with divergence $\sigma_\perp = \langle\psi^2\rangle^{1/2} = 50$ mrad (solid curve). The curves were calculated for a fully coherent diffractionless CTR pulse ($F = D = 1$), and a Boltzmann electron momentum distribution with temperature $u_t = 10$. As can been observed, the effect of the bunch divergence is limited to emission angles $\theta \lesssim 0.1$ rad. (Figure from Ref. [30].)

electron bunch propagates through the density ramp, and passes through a change in dielectric constant from $\epsilon = -\infty$ to $\epsilon = 1$, the TR emission occurs predominantly at the very end of the ramp where $\epsilon \simeq 0.8$. Although the transition $\epsilon \simeq 0.8$ to $\epsilon = 1$ is not a step-boundary, but a region with width $L_{\rm TR}$, it can been shown that the emission region is still well-modeled as a step-boundary [79]. This approximation is valid provided that $L_{\rm TR}$ is smaller than the formation length $L_{\rm form}$, given by

$$L_{\rm form} = \frac{\lambda}{2 - 2\beta\cos\theta}, \tag{3.31}$$

with λ the radiation wavelength and $\beta = v/c$ the normalized velocity of the electron. The formation length is defined as the length it takes for an electron at velocity β to slip back by half a wavelength with respect to radiation of wavelength λ. Although the expression for $L_{\rm form}$ is derived for a vacuum environment, it holds in the underdense region of the plasma. For typical SM-LWFA parameters, the radiation frequencies of interest are in the THz regime, θ is typically on the order of 0–0.3 rad, and the electrons in the bunch contributing to the TR have $\gamma \gtrsim 4$. One can find that for these parameters $L_{\rm form} \gtrsim 1$ mm. Since $L_{\rm TR} \ll 100$ μm, the step boundary approximation is indeed valid. The position of the emission region (approximated as a plane) is drawn in Figs. 3.12(a) and (b).

One final aspect of the SM-LWFA-produced electron bunch that will be discussed in this chapter is the effect of the bunch divergence on the CTR emission. As was measured and discussed in Sec. 2.4, the bunch divergence is on the order of ψ =25–50 mrad (half-angle). The calculations in Sec. 3.2.1 were based on collimated electron bunches normal to the dielectric interface. Work by Schroeder *et al.* [30] included the effect of bunch divergence on the CTR emission. In that publication, a distribution function $g_\perp(\psi)d\psi = (2/\sigma_\perp^2)\exp(-\sin^2\psi/\sigma_\perp^2)\sin\psi\cos\psi d\psi$ was defined, with ψ the angle between the electron

velocity vector and the interface normal, and $\sigma_\perp = \langle\psi^2\rangle^{1/2}$ the rms bunch divergence. The CTR pulse was assumed to be fully coherent and diffractionless ($F = D = 1$). The bunch was defined to have a Boltzmann momentum distribution, with temperature $u_t = 10$. The differential angular and spectral energy distribution $d^2W/d\omega d\Omega$ was calculated for a collimated bunch $\sigma_\perp$=0, see the dashed curve in Fig. 3.14, and for a bunch with divergence $\sigma_\perp = 50$ mrad (solid curve). The effect of the bunch divergence is most dominant for small emission angles $\theta \lesssim 0.1$ rad, although even for these angles the net reduction in radiatied CTR energy is only on the order of $\simeq$20–30% (field amplitude reduction of $\simeq$11–16%). At larger emission angles $\theta > 0.1$, the effect of the bunch divergence is even smaller, and can be neglected. The majority of the THz-related experiments described in this thesis are performed by collecting THz radiation at an observation angle of $0.1 < \theta < 0.4$ rad. For this reason, bunch divergence effects are not considered to be of importance for SM-LWFA-produced THz radiation related to this thesis.

3.7 Summary

A theoretical approach to coherent transition radiation from a metal-vacuum boundary has been developed. The CTR pulses were found to be broad-bandwidth (at THz frequencies) and single-cycle in nature, with a length on the order of the bunch duration. The CTR pulse is radially polarized, which results in partial field cancelation at focus. There are several parameters that affect the spectral, angular, and temporal properties of the CTR pulse. These include the longitudinal and transverse bunch sizes σ_z and σ_r, the electron momentum u, and the transverse boundary size ρ. Due to diffraction effects, the angle of peak emission shifts from $\theta \simeq 1/u$ towards higher values for θ. Also, diffraction suppresses the total emitted energy. Depending on the diffraction effects and the efficiency of radiation collection, a THz pulse energy of 0.1–10 μJ can be collected, corresponding to a peak electric field on the order of 0.3–3 MV cm^{-1}. These estimates demonstrate that LWFA-produced THz radiation is useful for high-field THz applications, which are currently limited to sources with an amplitude that is 1–2 orders of magnitude lower.

The calculated CTR field profiles (temporal and spectral) are relatively insensitive to bunch divergence effects and momentum distribution details. It was shown that a distribution based on a Boltzmann profile (temperature u_t), a mono-energetic profile at $u = u_t$, and a Gaussian profile (at mean u_t), all result in the emission of very similar radiation waveforms. For this reason, the theoretical expressions for CTR emission can be simplified. Also, it was validated that the experimentally-realized plasma-vacuum boundary (with a density gradient length $L_{\text{ramp}} \sim 100$ μm) can be approximated by the sharp metal-vacuum boundary, as long as $L_{\text{ramp}} < L_{\text{form}}$, with L_{form} the radiation formation length ($L_{\text{form}} \gtrsim 1$ mm). The position of the CTR emission plane in the plasma is located at the very end of the plasma, where $\epsilon \simeq 0.8$.

Chapter 4

Bolometric THz characterization

Abstract

A first generation of experiments regarding THz pulse characterization is presented to confirm the emission of THz generation from LWFA-produced electron bunches crossing the plasma-vacuum boundary. The experiments are aimed at the THz scaling with charge, the total THz energy, initial spectral information, and the THz polarization state. A radiation detector (bolometer) is used for these experiments, indicating that indeed coherent radiation in the 0.3–30 THz regime is emitted. Quadratic scaling with charge is observed, with the collected pulse energy in two different geometries 4 nJ and 75 nJ, matching theoretical predictions. An experiment with a polarizer indicates that there is no dominant polarization vector, as predicted for radially-polarized THz pulses. A second set of experiments uses the bolometer for detection of THz pulses, with also a 50-fs-long laser beam present, both incident on a silicon wafer (switch). The ultra-fast dynamic interaction between both pulses and the semiconductor surface electrons allows for temporal THz characterization. This technique (semiconductor switching) is useful to obtain THz-to-laser temporal synchronization, and to get an indication for the THz pulse length. Although the temporal resolution is limited, femtosecond-duration THz pulses have been observed.

4.1 Introduction

Emission of coherent radiation at GHz and THz frequencies can be used to diagnose electron bunches, as discussed in Chapter 3. The multi-nC LWFA-produced electron beam will emit coherent radiation upon exiting the plasma-vacuum boundary. The first generation of experiments on the THz emission is designed to demonstrate the production of THz pulses, and characterize scaling with respect to charge and polarization. A sensitive energy detector (bolometer) is used in the experiments. The results are presented and discussed in Sec. 4.2.

Semiconductor switching (SCS) experiments are presented and discussed in Sec. 4.3. In this experiment, femtosecond THz characterization was performed by involving the bolometer, the THz pulse, a 50-fs-long laser pulse, and a semiconductor (silicon wafer). Scanning the respective delay between both pulses, and measuring the total transmitted THz energy, allowed for the determination of the temporal synchronization between both pulses, and for the estimation of the THz pulse duration.

Note that THz measurements based on a Michelson interferometer will not be discussed in this thesis. Although such a technique is often applied [25, 80] to measure the coherent radiation spectrum (scanning geometry), the spectral and temporal characterization techniques in this thesis will mainly focus on electro-optic methods, which can be applied in a scanning or single-shot geometry.

The work in this chapter is based on the publications

- *Observation of terahertz emission from a laser-plasma accelerated electron bunch crossing a plasma-vacuum boundary*, by W.P. Leemans, C.G.R. Geddes, J. Faure, Cs. Tóth, J. van Tilborg, C.B. Schroeder, E. Esarey, G. Fubiani, D. Auerbach, B. Marcelis, M.A. Carnahan, R.A. Kaindl, J. Byrd, and M.C. Martin, Phys. Rev. Lett. **91**(7), 074802 (2003)

- *Terahertz radiation from laser accelerated electron bunches*, by W.P. Leemans, J. van Tilborg, J. Faure, C.G.R. Geddes, Cs. Tóth, C.B. Schroeder, E. Esarey, G. Fubiani, and G. Dugan, Phys. Plasmas **11**(5), 2899 (2004)

- *THz radiation as a bunch diagnostic for laser-wakefield-accelerated electron bunches*, by J. van Tilborg, C.B. Schroeder, C.V. Filip, Cs. Tóth, C.G.R. Geddes, G. Fubiani, E. Esarey, and W.P. Leemans, Phys. Plasmas **13**(5), 056704 (2006)

4.2 Experiments on THz scaling

A first set of experiments was performed to confirm the emission of THz generation, measure the scaling with charge, obtain initial spectral information, and measure the polarization state [29, 31]. A liquid-helium-cooled bolometer was operated to measure the THz

energy over the range 0.3–30 THz (internal filter 1) or 0.3–3 THz (internal filter 2). Since the bolometer response (see Appendix A) and the material properties (see Appendix B) are known, calibrated energy measurements were possible. The bolometer calibration, see Eq. (A.6), is W_{THz} [nJ] $= (4.0/\chi) \times \Delta$V [V], with ΔV the bolometer signal in units of [V], χ the bolometer gain, and W_{THz} the incident energy of the THz pulse in units of [nJ].

4.2.1 THz energy versus charge

One basic setup to measure the energy of the THz pulse is depicted in Fig. 4.1(a). Details on the laser pulse and electron bunch have been discussed in Sec. 2.4. In the experiment, the laser pulse length was measured to be 50 fs (intensity FWHM), and the laser energy was 0.4 J. A 5-μm-thick metal-coated pellicle was positioned 30 cm from the gas jet in order to reflect the THz radiation out of the target chamber. It is important to note that CTR is emitted at both the plasma-vacuum boundary as well as at the pellicle-vacuum boundary. However, with a LWFA-produced electron bunch divergence of $\simeq 25-50$ mrad (see Sec. 2.4), the electron bunch size at the pellicle is $\simeq 1.5-3$ cm. From Eq. (3.19) one can see that such a large bunch does not radiate coherently in the regime > 0.3 THz (bolometer acceptance). The divergence-induced loss of transverse coherence was also discussed in the last part of Sec. 3.3.1 and in Sec. 3.5.2. In conclusion, only the plasma-vacuum boundary is important as a source of THz radiation.

The window, see Fig. 4.1(a), was made of 1/2-inch-thick Rexolite. An F/30 metal-coated spherical mirror was used to focus the radiation on the bolometer, whose characteristics are discussed in Appendix A. The collection angle from gas jet to spherical mirror was estimated to be 30 mrad (half-angle). The angular collection with respect to the THz angular emission (calculated with $u = 10$ and $\rho = 100$ μm) is depicted in Fig. 3.10. The bolometer was collecting radiation within the 0.3–3 THz regime (filter position 2), and the gain was set at $\chi = 1000$. In front of the bolometer, both a 3/4-inch-thick Teflon block and a 1/2-inch-thick poly-Styrene piece were placed in order to shield the bolometer from remnant laser light.

Figure 4.1(b) shows the measured bolometer signal versus the bunch charge for a series of laser shots (circa 230 shots). The bunch charge was varied by either changing the laser pulse length or by modifying the position of the gas jet with respect to the laser focal volume. In each charge bin (width of $\simeq$40 pC) all measurement points were averaged to yield a data point and corresponding error bar. The large error bars on the signal in Fig. 4.1(b) are believed to be due to pointing fluctuations of the electron beam on the order of $\simeq 0-25$ mrad, which is of comparable magnitude to the 30 mrad collection angle. The solid curve in Fig. 4.1(b) is a quadratic fit to the data. The fit is in good agreement with the theoretical prediction that the energy of coherent radiation scales quadratically with charge.

Individual shots, part of the data of Fig. 4.1(b), showed bolometer signals up to 2 V. In order to estimate the corresponding pulse energy, the material properties have to be

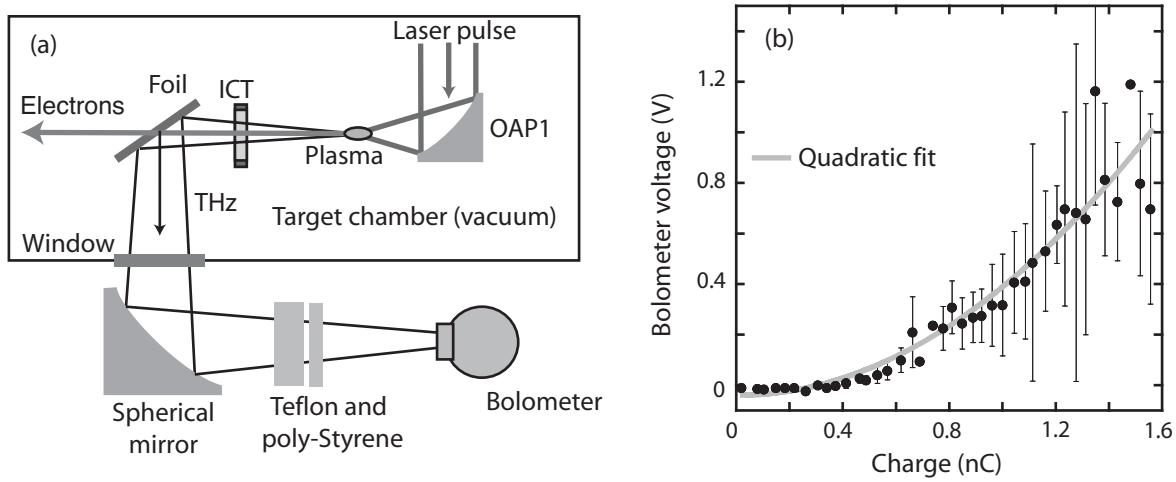

Fig. 4.1. (a) Setup for measurement of the THz pulse energy. The spectral acceptance of the bolometer was $0.3-3$ *THz, at gain* $\chi = 1000$*. A thin foil reflected the THz radiation through the Rexolite window, through pieces of poly-Styrene and Teflon, and onto the bolometer. (b) Measured THz energy (∼bolometer voltage) versus bunch charge. The performance of the accelerator in terms of bunch charge was varied during the data collection. The agreement between the data and a quadratic fit demonstrates the coherent nature of the radiation. (Figure from Ref. [29].)*

considered. The transmission curves for Rexolite and poly-Styrene were measured with an optical rectification and EOS sampling technique. Each transmission curve was approximated as being spectrally flat. The transmission for 1/2-inch-thick Rexolite was found to be ≃0.05, and the transmission for poly-Styrene ≃0.3. Note that these materials have poor transmission at frequencies above 2 THz, and the experiment described in this section is the only experiment in which they were used. The characteristics in the THz domain for several materials are provided in Appendix B. The transmission for 3/4-inch-Teflon in the 0.3–3 THz range can be estimated from Fig. B.1(a) to be $T \simeq (0.7)^6 \simeq 0.12$. From Eq. (A.6) in Appendix A, with $\chi = 1000$, and by considering the overall transmission $T = 0.05 \times 0.3 \times 0.12$ (Rexolite, poly-Styrene, and Teflon, respectively), the pulse energy in the measured angular and spectral domain was found to be $E_{\mathrm{THz}} \simeq 4$ nJ. Note that the measured energy is in quantitative agreement with theory, which was plotted in Fig. 3.8. For a boundary with size ρ=100 μm, and a collection angle of θ <30 mrad, Fig. 3.8 predicts ≈ 1 nJ/nC, or a total pulse energy of ≈ 3 nJ for a 1.6-nC bunch (quantitative agreement).

In order to achieve a larger collection angle, the setup in and outside the target chamber was modified, as depicted in Fig. 4.2. An off-axis parabola (OAP2, collection half-angle of 300 mrad) was used to reflect the THz pulse. The focal distance of the parabola was 5 inch, and a 4/5-inch-diameter hole was drilled in the center in order to prevent damage from remnant laser light. The angular collection with respect to the THz angular emission (calculated with $u = 10$ and $\rho = 100$ μm) is depicted in Fig. 3.10. The THz radiation was focused by a 7-inch-focal-length parabola, through a 1/4-inch-thick low-resistivity (<100 Ohm) silicon window, onto the bolometer. In front of the bolometer, both a silicon wafer and a far-infrared wire-grid polarizer were positioned. The bolometer filtration was set at

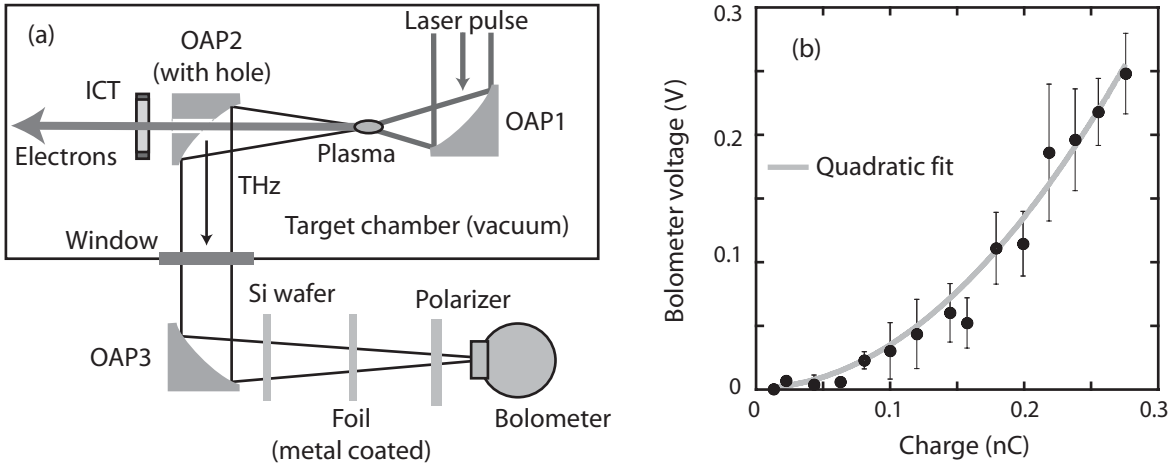

Fig. 4.2. (a) Setup for measurement of the THz pulse energy. The spectral acceptance of the bolometer was $0.3 - 30$ *THz, at gain* $\chi = 1000$*. A 5-inch-focal-length parabola (OAP2, with a 4/5-inch-diameter hole in the center) reflected the THz radiation onto another parabola (OAP3). OAP3 focused the radiation through a silicon window, a silicon wafer, and onto the bolometer. A far-infrared polarizer was positioned in the THz beam path as well. The performance of the accelerator in terms of bunch charge was varied. (b) Measured THz energy (in terms of bolometer voltage) versus bunch charge, including a quadratic fit (solid curve). (Figure from Ref. [31].)*

$0.3 - 30$ THz (filter position 1), and the gain was $\chi = 1000$.

Figure 4.2(b) shows the measured bolometer signal versus the bunch charge for a series of laser shots (circa 210 shots). In this particular measurement, the polarizer was removed from the THz beam path. The bunch charge was varied by either changing the laser pulse length or by modifying the position of the gas jet with respect to the laser focal volume. In each charge bin (width of $\simeq$20 pC) all measurement points were averaged to yield a data point and corresponding error bar. The solid curve in Fig. 4.2(b) is a quadratic fit to the data. Just as for the fit in Fig. 4.1, the fit in Fig. 4.2 is in good agreement with the theoretical prediction that the energy of coherent radiation scales quadratically with charge.

Several laser shots of the measurement plotted in Fig. 4.2(b) produced bolometer signals on the order of 0.5 V. The transmission parameters for the silicon window and silicon wafer were plotted in Fig. B.1(a) of Appendix B, and can be approximated to be $T \simeq 0.28$ (Si window) and $T \simeq 0.5$ (Si wafer). Although the foil used for the data in Fig. 4.2(b) is not the same as the one characterized in Fig. B.2(b), they both are similar in terms of the spectrally-independent transmission profile. The foil used for the data in Fig. 4.2(b) has a (energy) transmission of $T = 1.8 \times 10^{-4}$, as measured by a Michelson interferometer. From Eq. (A.6) with $\chi = 1000$, and by considering the overall transmission $T = 0.28 \times 0.5 \times 1.8 \times 10^{-4}$ (Si window, Si wafer, and metal-coated foil), the measured pulse energy was found to be $W_{\mathrm{THz}} \simeq$75 nJ.

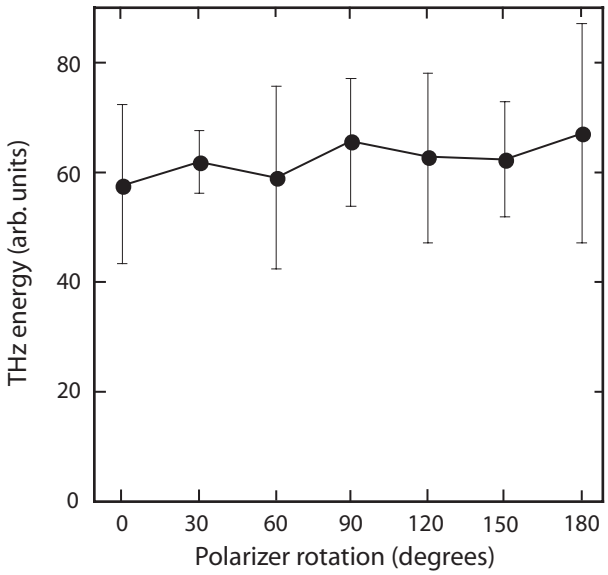

Fig. 4.3. Measured THz energy as a function of rotation of a far-infrared polarizer positioned in front of the bolometer. In agreement with a theoretically predicted radially-polarized CTR pulse, there is no dominant polarization vector in the measured pulse.

4.2.2 Polarization measurement

The same setup as plotted in Fig. 4.2(a) was used to measure the effects of the polarizer rotation on the measured energy. In this experiment the bolometer gain was turned off (χ=1) and the metal-coated foil was removed. The polarizer was a wire-grid far-infrared polarizer consisting of an array of metallic wires (spaced on the order of 50–100 μm). Only radiation with a polarization component parallel to the wires is transmitted. 850 data shots were collected at 7 different polarizer angles. Only data shots with charge within the interval 0.2 ± 0.04 nC were considered. At each polarizer angle, the selected shots were averaged, with the mean and error bar plotted in Fig. 4.3. The measured radiation was found to be have little or no dominant polarization vector. Although this could indicate that the radiation is unpolarized or circularly polarized, it is more likely that, in agreement with theory, the radiation is radially polarized. The theoretical expression for the radiated electric field, see Eq. (3.25), showed that the polarization vector is given by $\mathbf{e}_\perp$, as plotted in Figs. 3.3 and 3.9. Since OAP2 collects all the radiation within a solid angle (angular symmetry), see Fig. 4.2(a), no dominant polarization vector is expected.

4.3 Semiconductor switching

One technique that provides temporal insight into the THz radiation pulse is the technique referred to as semiconductor switching (SCS), or THz switching [81]. The technique has been applied since the 1970s, and was (among others) used for short-pulse production of CO_2 laser pulses [82, 83]. The principle of SCS is that a pump beam excites a dense electron-hole plasma (free carriers) at the surface of a semiconductor. The pump beam

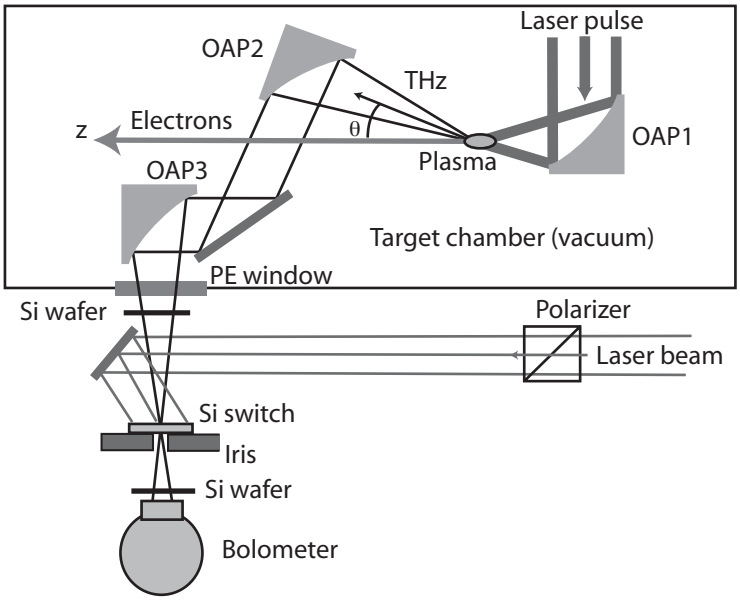

Fig. 4.4. Schematic representation of the setup for semiconductor switching of LWFA-produced THz radiation. The THz pulse is propagated by OAP2 and OAP3 onto a Si wafer. An independent laser beam (pump beam) provides the switching at the Si wafer. The bolometer measures the THz radiation transmitted through the switch. The delay between pump laser beam and THz pulse can be varied with a delay stage.

can be either an electron beam, or (such as in this experiment) a laser beam at an above-semiconductor-bandgap central frequency. The excitation is almost instantaneous (less then a few femtoseconds), although it will remain for many picoseconds. The excitation switches the semiconductor properties from transmissive to reflective regarding THz pulses. The SCS experiment was performed [2] to establish temporal synchronization between the THz pulse and the NIR laser beam (crucial for the EOS experiments described in Chapters 5 and 6), and to provide insight in the envelope profile of the THz pulse. However, this technique is not well-suited for detailed bunch characterization, which instead will be done through the EOS method.

4.3.1 Configuration and model

The setup for SCS is sketched in Fig. 4.4. Details on the laser pulse and electron bunch have been discussed in Sec. 2.4. In the experiment, the laser pulse length was measured to be 50 fs (intensity FWHM), and the laser energy was 0.5 J. The charge of the electron bunch was $\simeq$ 2.4 nC, measured 50 cm from the gas jet. The electron momentum distribution $g(u)$, measured by an imaging magnetic spectrometer and averaged over multiple shots, showed an exponential form $g(u) \propto \exp(-u/u_t)$ with temperature $u_t = 10$.

Part of the THz radiation was collected and collimated by an F/2 90°-off-axis parabola (OAP2, 15 cm focal length), positioned off-axis to avoid damage from the electron or laser beams. THz radiation propagating to the center of OAP2 had an angle of $\theta = 19°$ (0.33 rad) with respect to the z axis. The diameter of OAP2 is 76 mm, corresponding to

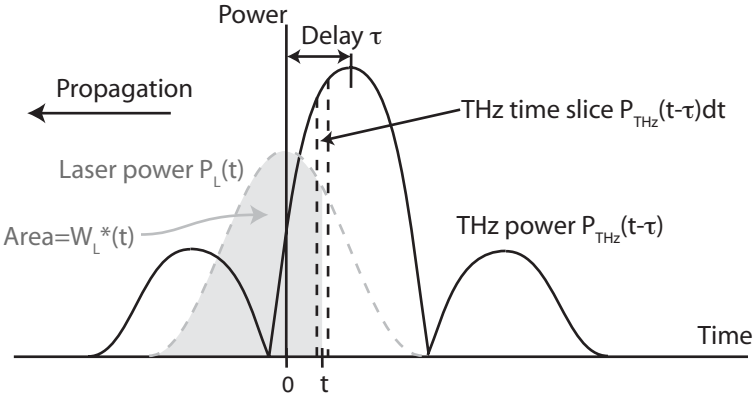

Fig. 4.5. The power profiles of (solid curve) the laser pulse envelope $P_L(t)$ and (dashed curve) THz pulse $P_{\mathrm{THz}}(t-\tau)$. Due to the single-cycle nature of the THz pulse, the power profile P_{THz} consists of three maxima ($P_{\mathrm{THz}} \sim |E_{\mathrm{THz}}|$). In the frame of the laser, the THz pulse is delayed by τ. The transmission of the THz time slice $P_{\mathrm{THz}}(t-\tau)dt$ is a function of the transmission factor T_{scs}, which is determined by the cumulative amount of laser energy $W_L^*(t) = \int_{-\infty}^{t} P_L(t')dt'$ that arrived prior to the THz time slice.

an approximation of the opening half-angle of $\simeq 15°$. The angular collection with respect to the THz angular emission (calculated with $u = 10$ and $\rho = 100$ μm) is depicted in Fig. 3.10. The collimated THz radiation was focused by an F/2.4 90°-off-axis parabola (OAP3, 18 cm focal length) onto a high-resistivity silicon wafer (serving as Si switch), with a thickness of 0.4 mm. A 1/8-inch-thick polyethylene (PE) disk served as vacuum window. An iris was positioned at the THz focal plane just behind the Si switch and had an opening diameter of 1.6 mm. At a distance of 2 cm from the iris, a liquid-helium-cooled bolometer, discussed in Appendix A, measured the incident THz radiation energy. Two internal filters in the bolometer allowed the user to select a 0.3–3 THz or 0.3–30 THz spectral acceptance. The bolometer gain was set at $\chi = 200$. Several other Si wafers were positioned in the THz beam path to block low-intensity remnant laser light. Note that the transmission properties of the silicon wafer (including the switch) and the PE window were measured and plotted in Figs. B.1 and B.2 of Appendix B. It was found that dispersion effects from these materials were negligible. Also incident on the Si switch was a collimated Ti:Al_2O_3 laser beam, used as the pump beam for the excitation of free carriers at the Si surface. The laser spotsize was 3.0 mm (intensity FWHM) and the pulse length was 60 fs (intensity FWHM). The angle of incidence of the pump beam with respect to the normal of the Si surface was 12°. The timing τ between THz pulse and laser beam was varied with a delay stage.

A heuristic model of SCS is presented here. The power profiles for the laser and THz pulse are defined as $P_L(t)$ and $P_{\mathrm{THz}}(t)$, respectively. At a given delay stage position, the THz pulse is delayed with respect to the laser pulse by τ, such that $P_{\mathrm{THz}}(t) \rightarrow P_{\mathrm{THz}}(t-\tau)$, as depicted in Fig. 4.5. The THz transmission T_{scs} through the silicon switch of a specific THz time-slice $P_{\mathrm{THz}}(t-\tau)dt$ depends on the cumulative laser energy $W_L^*(t) = \int_{-\infty}^{t} P_L(t')dt'$

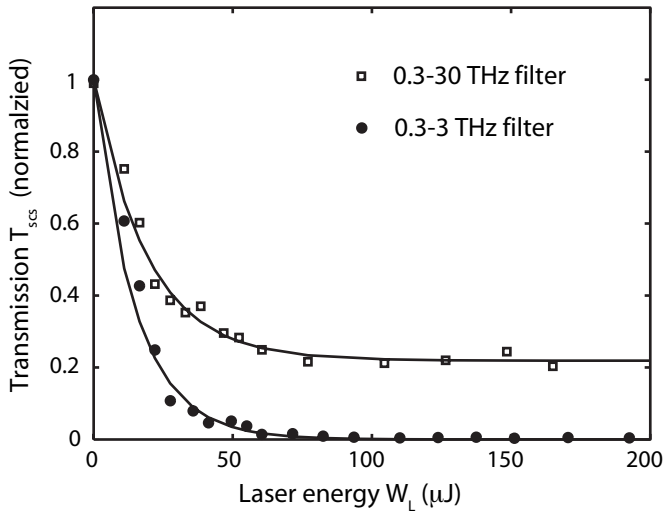

Fig. 4.6. The change in THz transmission $T_{\rm scs}$ (through the silicon switch) as a function of laser pulse energy for $0.3-3$ THz (circles) and $0.3-30$ THz (squares) bolometer filtration. The solid curves are exponential fits $T_{\rm scs} \propto \exp(-\alpha W_L)$, with $\alpha = 0.069$ μJ^{-1} ($0.3-3$ THz filter) and $\alpha = 0.051$ μJ^{-1} ($0.3-30$ THz filter). (Figure from Ref. [2].)

that has arrived prior to this time-slice, or $T_{\rm scs} = T_{\rm scs}(W_L^*)$. For larger W_L^*, the THz transmission approaches $T_{\rm scs} \to 0$. Therefore, the front of the THz pulse (where no laser pulse is present) experiences full transmission $T_{\rm scs} = 1$, while the tail of the THz pulse experience limited transmission, depending on the delay between THz and laser pulse. The bolometer measures the total transmitted THz energy $W^*_{\rm THz}(\tau)$, which can be expressed as

$$W^*_{\rm THz}(\tau) = \int_{-\infty}^{\infty} P_{\rm THz}(t-\tau) T_{\rm scs}\left(W_L^* = \int_{-\infty}^{t} P_L(t')dt'\right) dt. \tag{4.1}$$

In the limit of an intense ultra-short laser beam $P_L(t) \to \delta(t)$, Eq. (4.1) reduces to $W^*_{\rm THz}(\tau) = \int_{-\infty}^{-\tau} P_{\rm THz}(t)dt$, or $P_{\rm THz}(t) \propto \partial W^*_{\rm THz}(t)/\partial t$.

The transmission function $T_{\rm scs}(W_L^*)$ can be experimentally determined by delaying the entire THz pulse (such that the laser beam arrives at the Si first) and recording the transmitted THz energy as a function of laser beam energy. Figure 4.6 displays the measured transmission curve for 0.3–3 THz filtration (bottom curve, circles) and 0.3–30 THz filtration (top curve, squares). Exponential fits to the curves yielded $\alpha = 0.069$ μJ^{-1} ($0.3-3$ THz filter) and $\alpha = 0.051$ μJ^{-1} ($0.3-30$ THz filter), with $T_{\rm scs} \propto \exp(-\alpha W_L)$ and W_L in units of [μJ]. Note that even with no laser pulse present the switch transmission is $\simeq$50%, as measured and plotted in Fig. B.1. The transmission curves in Fig. 4.6 are normalized to the transmission with no laser pulse present. In the case of the 0.3–30 THz spectral acceptance, one can see that the switch is not perfect, since 22% of the normalized THz energy leaks through the switch regardless of pump beam timing and energy. It is likely the laser-induced semiconductor plasma is ineffective in reflecting the radiation with frequencies above its maximum cut-off frequency. This cut-off frequency is a function of the critical density of the semiconductor, and is not further investigated.

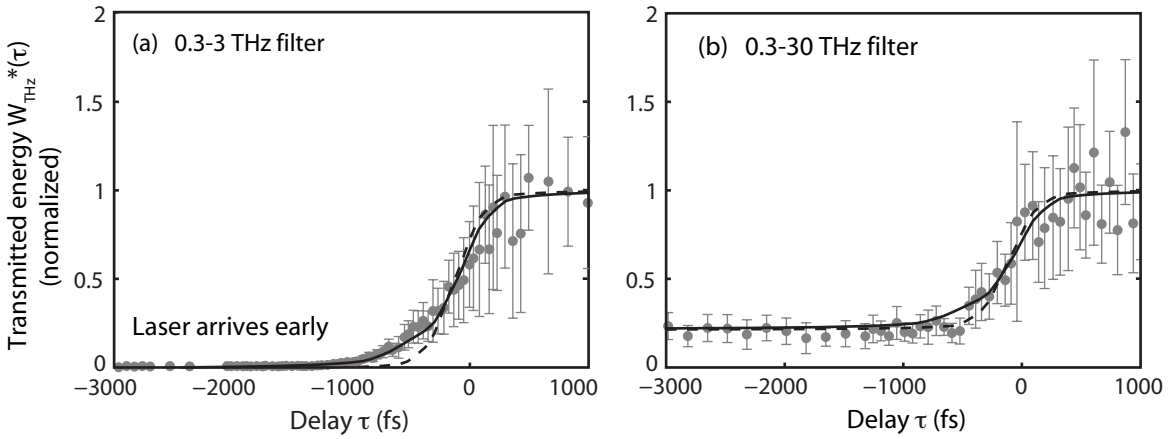

Fig. 4.7. The measured THz energy transmission versus time delay τ: (a) $0.3-3$ THz bolometer filtration and a laser beam energy of 195 μJ. (b) $0.3-30$ THz filtration and a laser energy of 180 μJ. Both (a) and (b) also display modeled transmission curves based on (dashed curve) a single THz pulse and (solid curve) a double-pulse THz profile, with the pulses separated by 300 fs and the leading pulse having a 50% relative field amplitude. Each THz pulse is based on CTR from a bunch with rms length of 50 fs. (Figure from Ref. [2].)

4.3.2 Experimental results

Figure 4.6 indicated that laser energies of > 100 μJ are enough for effective switching. The measured bolometer energy at various values for the pump laser time delay τ is shown for two separate scans in Figs. 4.7(a) and (b). Each data point represents an average of 30 shots (typically at 1 Hz repetition) and the error bars represent the rms spread. Figure 4.7(a) displays a scan taken with the bolometer at 0.3–3 THz filtration, and laser beam energy of 195 μJ (or 3.2×10^{10} Wcm^{-2}). Figure 4.7(b) displays a scan with 0.3–30 THz filtration and 180 μJ of laser energy. As the model from the previous section predicted, the time scale over which the switching occurs is an indication for the THz pulse length. Without going into the details here, the envelope of the measured THz waveform can be estimated to be on the order of $400-700$ fs (intensity FWHM).

Theoretical predicted transmission curves [from Eqs. (3.25) and (4.1)], based on two different THz pulse profiles, were calculated. The non-collinear geometry between THz and laser pulse (see Fig. 4.4) was taken into account by assuming a THz spotsize of 0.5 mm (intensity FWHM). The dashed curves in Figs. 4.7(a) and 4.7(b) represent the modeled transmitted energy profiles for THz emission from a Gaussian electron beam, with a rms length of 50 fs (single-cycle THz pulse).

The solid curves in Figs. 4.7(a) and 4.7(b) represent THz transmission from a double-pulse THz profile, which is defined as the summation of two single-cycle THz waveforms. The two THz pulses are separated by 300 fs, with the leading pulse having a 50% relative field amplitude, and each THz pulse is calculated from a 50 fs (rms) electron bunch. The motivation behind the double-THz-pulse profile will be presented and discussed in Secs. 6.3 and 6.4, where a model indicates that imperfections in the THz optical beam line can lead

to the double-THz-pulse profile. Section 5.3.3 will present detailed single-shot results on temporal THz characterization, confirming the existence of the double-THz-pulse structure, and Sec. 6.2 will show measured 2D THz profiles that strongly indicate imperfections in the THz imaging system. Both solid and dashed modeled curves in Fig. 4.7 reproduce the features of the measurement, with a slight preference for the model based on the double-pulse THz profile. Note that if just one longer single-cycle THz pulse were to be assumed for the model (rms length of $\simeq$400 fs), its modeled transmission curve would also match the data of Figs. 4.7(a) and 4.7(b). However, it would be contradictory to previously obtained energy measurements that clearly indicate that a significant amount of THz energy (more than 70%) is at frequencies above 3 THz [31]. One longer single-cycle pulse would not contain spectral components above 3 THz, indicating that the more complex (double pulse) THz profile was present in the focal volume.

The technique of electro-optic sampling (EOS), which will be introduced in Chapters 5 and 6, is more suitable for characterization of properties such as the coherent spectrum and temporal THz pulse profile. However, if the temporal synchronization between the laser beam and THz beam has not been established, it is very cumbersome to find the temporal overlap between both pulses with EOS. It might literally take thousands of laser shots (several hours) of delay scanning. With the SCS technique, the temporal synchronization can be obtained in a matter of minutes. The reason for this is the following: if the laser pulse arrives 1 ps after the THz pulse there will be no effect for both the EOS and SCS technique. If the laser arrives 1 ps before the THz pulse in the EOS technique, similarly no effect is measured. However, with the SCS technique, the switching is initiated and an effect is measured (namely no THz transmission). With relatively coarse temporal steps, the temporal synchronization can be found.

4.4 Summary

The experiments presented in this chapter were based on THz detection by a bolometer, with its characteristics discussed in Appendix A. The voltage drop measured by the liquid-helium-cooled bolometer is linearly proportional to the incident THz energy if the THz pulse duration is shorter than the τ=0.33 ms bolometer time constant. Since all THz-related experiments in this thesis involve reflective and transmissive THz optics, an overview of several measured material properties in the THz domain was presented in Appendix B. Materials that were found to induce minimal dispersion on the THz pulse are high-resistivity silicon, high- and low-density poly-ethylene, and a thin nitrocellulose foil (pellicle). The poly-ethylene can serve as a vacuum window, and the Si wafer as a blocker of remnant laser light. The metal-coated pellicle is a useful THz attenuator, while the dielectric-coated pellicle can be used a beam combiner for a THz pulse (full transmission) and a laser beam (full reflection).

The THz pulse energy was measured in various experimental configurations. A first

configuration measured the radiation within a small < 30 mrad collection angle (half-angle). The THz energy showed a quadratic dependence on bunch charge, and the peak energy of $\simeq 4$ nJ matched theoretical predictions. A second configuration was based on the collection of THz radiation by a parabola with a hole in the middle, corresponding to a (half-angle) angular collection of $80 < \theta < 300$ mrad. Quadratic scaling to charge was observed, with the peak THz energy on the order of 75 nJ. Rotation of a THz polarizer showed that the total THz energy was not dependent to polarizer rotation, as is predicted for the on-axis collection of radially-polarized CTR pulses. All the above results were presented in Sec. 4.2.

In a third configuration, presented in Sec. 4.3, the THz radiation was collected by a 250 mrad-opening (half-angle) parabola. The parabola was positioned off-axis such that remnant laser light was not incident on the parabola. The collected THz radiation was focused onto a silicon wafer, together with an intense laser pulse. By scanning the delay between both pulses, the total transmitted THz energy was recorded. This measurement technique, referred to as semiconductor switching (SCS), allowed for the realization of femtosecond synchronization between the THz and laser pulse. Synchronization is crucial for the experiments on electro-optic sampling, to be presented in Chapters 5 and 6. The SCS experiments also indicated that THz pulses with a pulse duration in the femtosecond regime were produced by the LWFA. The results did not allow for detailed THz profile reconstruction, which is something that EOS can and will address in the upcoming chapters.

Chapter 5

Electro-optic THz characterization

Abstract

The electric field profile (amplitude and phase) of the THz pulse can be measured through the method of electro-optic sampling (EOS). The technique relies on the interaction of the THz pulse with a laser pulse in an electro-optic (EO) crystal. Through knowledge of the crystal effects, the measured EO signal can be related to the original THz field profile. In one series of experiments, the temporal EO signal is obtained by scanning the delay between the THz and laser pulse. Frequencies up to the 200-μm-thick ZnTe detection limit of 4 THz are observed. A model based on a 50 fs (rms) Gaussian electron bunch indicates agreement with the data.

In another series of experiments, the EO signal (THz waveform) is measured with two single-shot techniques, including use of a 200-μm-thick GaP crystal (detection limit of 8 THz). A spectral-encoding and a cross-correlation technique show that the LWFA-produced CTR spectrum extends to $\simeq 6$ THz, in agreement with a model based on THz from a 50 fs (rms) electron bunch. Peak THz fields on the order of 0.4 MV cm^{-1} are observed. Both the scanning and single-shot EOS results demonstrate LWFA stability in terms of parameters crucial to EOS such as the electron bunch length and the temporal synchronization between THz and laser pulse (jitter is < 10 fs). Observation of temporal substructure in the THz field profile, measured with the cross-correlation technique, provided the motivation for the 2D THz imaging experiments presented in Chapter 6.

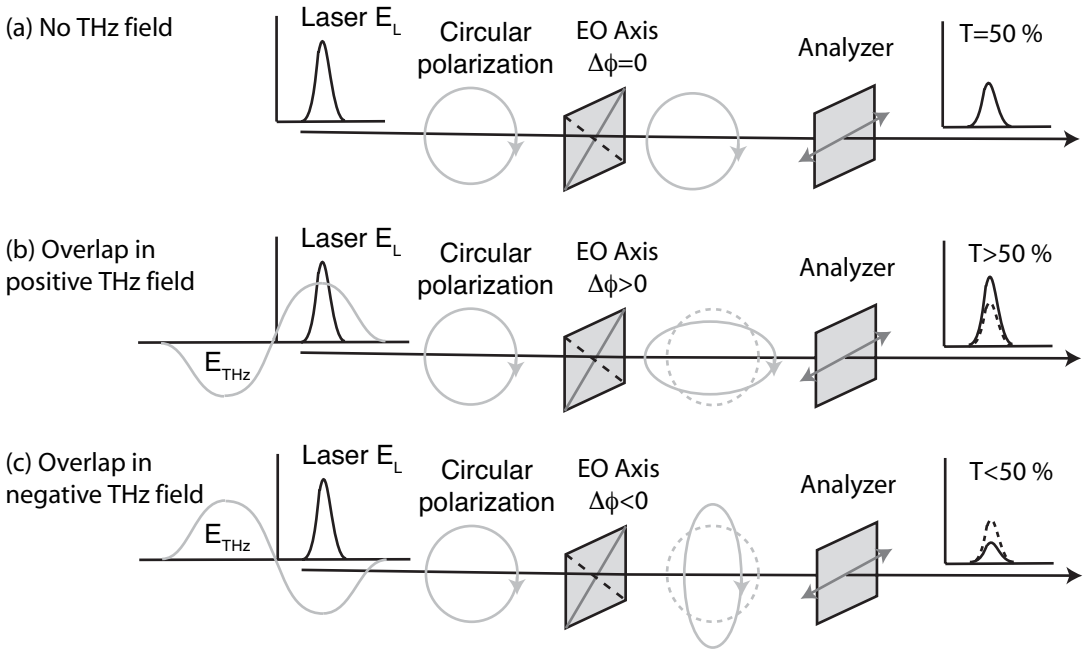

Fig. 5.1. A heuristic picture of electro-optic sampling (EOS): a circularly polarized laser pulse is incident on an electro-optic crystal and an analyzer. The power transmission through the analyzer of the laser beam is 50%*, see (a). However, if the laser pulse is co-propagating with the positive field region of a THz pulse, see (b), a phase difference of the laser field components parallel and orthogonal to the electro-optic axis is induced (THz-induced birefringence). Consequently, the polarization state is modified to elliptical, and the analyzer transmission is* $> 50\%$*. Similarly, the transmission is* $< 50\%$ *if the laser pulse co-propagates with the negative field region of the THz pulse, see (c). Scanning of the delay between the THz and laser pulse allows for measurement of the THz field profile* $E_{\mathrm{THz}}(t)$*.*

5.1 Introduction

The interest in electro-optic sampling (EOS) has risen over the last decades due to the wide-spread realization of table-top laser-based THz sources (*e.g.* optical rectification or the photoconductive antenna). Although these sources have been widely used only since 10–20 years, they are labeled as "conventional" in this thesis, since this thesis describes the more-novel THz production from LWFA-produced electron bunches.

Through EOS, the electric field profile $E_{\mathrm{THz}}(t)$ of a THz pulse can be measured, including phase and amplitude. The electro-optic (EO) effect can be utilized during the interaction in a crystal of a long-wavelength THz field and a short laser beam (probe beam). A heuristic picture of EOS is depicted in Fig. 5.1. In plot (a), a laser pulse (with circular polarization) is incident on an EO crystal and an analyzer. The birefringence of the crystal is a function of an external electric field. With no THz field present, the power transmission through the analyzer is 50%. However, if the laser pulse is co-propagating with a positive field region of the THz pulse [see Fig. 5.1(b)], the phase slippage between the laser field components parallel and perpendicular to the EO axis is $\Delta\phi > 0$. As a result, the polarization state of

the laser will become elliptical, with its major axis in the horizontal plane. The analyzer will now transmit more than >50% of the laser energy. Similarly, if the THz pulse is co-propagating with a negative field region of the THz pulse [see Fig. 5.1(c)], $\Delta\phi < 0$, and the laser transmission is <50%. While scanning the delay between the THz and laser pulse and recording the transmitted laser energy, the temporal field profile of the THz pulse can be reconstructed.

EOS of THz pulses can be achieved with various experimental configurations. For example, the transmitted laser energy can be measured by a single diode, two balanced diodes, or a CCD camera. The probe laser can be short ($\simeq$50 fs) such that the full THz waveform can be reconstructed by scanning the delay between THz and laser pulse. Or, the laser pulse can be chirped (long, *i.e.* > 1 ps) such that single-shot EOS techniques can be applied. This chapter will address several configurations, and discuss the results.

An introduction to EOS is given in Appendix C. The THz-induced change in crystal birefringence will be addressed, including a discussion on the optimal orientation of the THz polarization, laser polarization, and crystal axis. Also, the effect of crystal properties will be introduced. The crystal properties for 200-μm-thick ZnTe and GaP are summarized in Sec. C.5.

A series of experiments based on single-diode and balanced-diode EO detection will be presented in Sec. 5.2. The probe laser pulse is short, and the delay between laser and THz pulse is scanned.

In order to measure the THz waveform in a single-shot manner, a long chirped probe beam is used for EOS. The modulated probe beam is analyzed either with a single-shot spectrometer or a single-shot cross-correlator. These techniques and the results are discussed in Sec. 5.3.

The work in this chapter is based on the publications

- *Temporal characterization of femtosecond laser-plasma-accelerated electron bunches using terahertz radiation*, by J. van Tilborg, C.B. Schroeder, C.V. Filip, Cs. Tóth, C.G.R. Geddes, G. Fubiani, R. Huber, R.A. Kaindl, E. Esarey, and W.P. Leemans, Phys. Rev. Lett. **96**(1), 014801 (2006)

- *THz radiation as a bunch diagnostic for laser-wakefield-accelerated electron bunches*, by J. van Tilborg, C.B. Schroeder, C.V. Filip, Cs. Tóth, C.G.R. Geddes, G. Fubiani, E. Esarey, and W.P. Leemans, Phys. Plasmas **13**(5), 056704 (2006)

- *Single-shot spatio-temporal measurements of high-field terahertz pulses*, by J. van Tilborg, C.B. Schroeder, Cs. Tóth, C.G.R. Geddes, E. Esarey, and W.P. Leemans, Phys. Rev. Lett., submitted (2006)

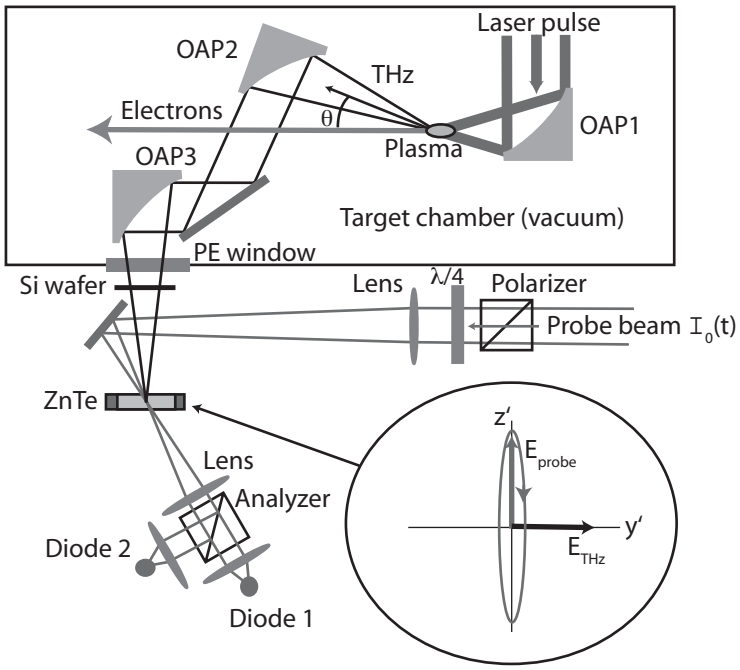

Fig. 5.2. Schematic representation of the setup for electro-optic sampling. If the λ/4 plate transforms the probe beam polarization to circular and both diodes 1 and 2 are in operation, then balanced detection is applied. For linear or elliptical probe polarization, only diode 1 is operated. The inset shows the electric field vectors of the probe and THz pulse in relation to the crystal axis z'.

5.2 Scanning detection

5.2.1 Configuration

In contrast to the SCS experiments of Sec. 4.3, the EOS technique is able to resolve both the phase and amplitude of the THz waveform. The setup for EOS is sketched in Fig. 5.2. The arrangement of THz optics inside the target chamber was identical to the SCS experiments and can be found in Fig. 4.4, with explanatory comments in Sec. 4.3.1. The angular acceptance of OAP2 was depicted in Fig. 3.10. The properties of the LWFA-produced electron bunches were presented and discussed in Sec. 2.4.

As depicted in Fig. 5.2, the THz pulse, coming out of the target chamber, was focused onto a thin electro-optic (EO) crystal. An ultra-short NIR laser beam $I_0(t)$ was used to probe the THz-induced change in crystal birefringence. The probe beam was focused to a spot radius $r_0 \simeq 50 - 100$ μm. By scanning the delay τ between both pulses, a full THz waveform was measured. A polarizer ensured vertical polarization of the probe beam, and a $\lambda/4$ plate was used to modify the probe beam polarization incident on the analyzer. The analyzer was set to transmit the horizontal component to diode 1, and the vertical component to diode 2. The time-integrated energy measured by diode 1 is labeled as $I_{\mathrm{diode}}(\tau)$, and by diode 2 as $I_{\mathrm{diode,2}}(\tau)$. The electric field vectors of the probe

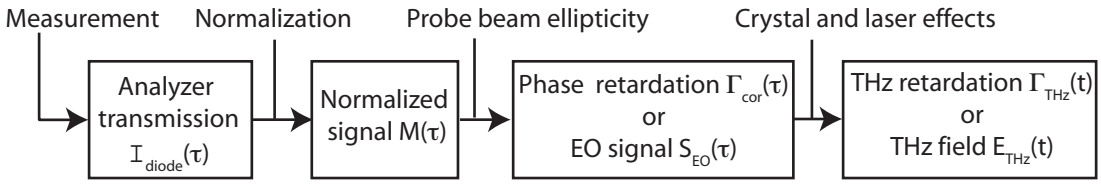

Fig. 5.3. Schematic on how to calculate $E_{\mathrm{THz}}(t)$ from the measured analyzer transmission $I_{\mathrm{diode}}(\tau)$. First the data is normalized to yield $M(\tau)$, after which the measurement is corrected for the influence of the polarization state of the probe laser. This yields the corrected phase retardation $\Gamma_{\mathrm{cor}}(\tau)$ and the EO field signal $S_{\mathrm{EO}}(\tau)$, By taking the crystal and laser effects into account, the original THz field profile $E_{\mathrm{THz}}(t)$ and phase retardation $\Gamma_{\mathrm{THz}}(t)$ can be calculated.

beam and THz pulse are shown in the inset of Fig. 5.2, which is based on the geometry of Fig. C.3(b). Although the emitted THz pulse is radially polarized when coming off the plasma-vacuum interface, OAP2 selects the vertical polarization component which corresponds to horizontal polarization at the crystal surface (see Fig. 3.10). Two types of EO crystals were used in these experiments, namely ZnTe and GaP. Both crystals were 200 μm thick, free-standing, and cut in the $\langle 110 \rangle$ plane. For each crystal, the $\langle 001 \rangle$ axis (or z' axis) was rotated to optimize the signal-to-noise ratio of the EOS measurement.

With single-shot EOS experiments as a motivation, to be presented in Sec. 5.3 and Chapter 6, the single-diode detection (only diode 1 in operation) of the probe beam was applied on a more regular basis than balanced-diode detection [84]. With balanced EOS, both diodes are in operation and the probe beam is circularly polarized. Although the EO effect onto the probe beam is then small (see Figs C.4 and C.5), the balancing allows for strong noise reduction. To resolve the sign of the THz pulse in the single-diode scheme, the $\lambda/4$ plate was rotated to provide elliptical polarization. It has been shown in Fig. C.5 that in the sign-resolving single-diode configuration, the best signal-to-noise is obtained with a small rotation of the $\lambda/4$ plate such that near-zero optical transmission is realized. This conclusion was also reached by Jiang *et al.* [54].

It is shown in Appendix C that the time-integrated laser energy transmission $I_{\mathrm{diode}}(\tau)$, with τ the delay between the THz and laser pulse $I_0(t)$, is given by $I_{\mathrm{diode}}(\tau) = \int G[\Gamma^*(t)] I_0(t-\tau) dt$. Here $\Gamma^*(t)$ represents the EO-induced phase retardation, which is a convolution of the original THz pulse $E_{\mathrm{THz}}(t)$ and crystal effects following Eq. (C.18). The function G depends on the polarization state of the laser ($\lambda/4$ plate rotation δ), and is given by

$$G[\Gamma^*(t)] = \frac{1}{2}\left[1 - \cos\Gamma^*(t)\cos^2 2\delta + \sin\Gamma^*(t)\sin 2\delta\right]. \tag{5.1}$$

A function H_{inv} is defined as the inverse function of H, with $H[\Gamma^*(t)] = G[\Gamma^*(t)] - G[\Gamma^* = 0]$. For linear polarization ($\delta = 0$), Eq. (5.1) reduces to $G[\Gamma^*(t)] = \sin^2[\Gamma^*(t)/2]$. For circular polarization ($\delta = \pi/4$), Eq. (5.1) reads $G[\Gamma^*(t)] = [1 + \sin\Gamma^*(t)]/2$ and $H_{\mathrm{inv}}[\Gamma^*(t)] = \arcsin[2\Gamma^*(t)]$. The transmission measurement $I_{\mathrm{diode}}(\tau)$ can be normalized to $M(\tau)$ follow-

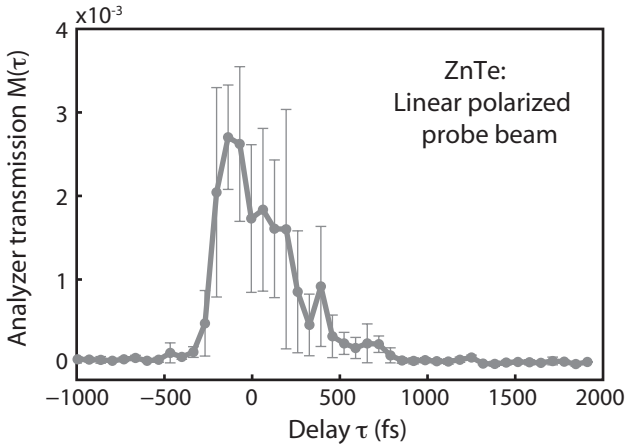

Fig. 5.4. ZnTe-based EOS data taken with a linear polarized probe beam (no sign-resolvement). The normalized transmitted laser energy M is plotted versus delay τ. Due to the linear polarization state of the probe beam, sign-resolved field information is lacking.

ing Eq. (C.21), which can also be expressed as

$$M(\tau) = \frac{I_{\mathrm{diode}}(\tau) - I_{\mathrm{reference}}}{I_{\mathrm{total}}}, \tag{5.2}$$

with $I_{\mathrm{reference}}$ the diode energy in case no THz field is applied and I_{total} the recorded energy in case of no THz field, with the $\lambda/4$ plate removed, and with the analyzer rotated for maximum transmission.

The corrected retardation function $\Gamma_{\mathrm{cor}}(\tau)$ is defined as $\Gamma_{\mathrm{cor}}(\tau) = H_{\mathrm{inv}}[M(\tau)]$, which can be expressed in terms of an electric field profile $S_{\mathrm{EO}}(\tau)$ through Eq. (C.23). The last step towards retrieval of the original THz field $E_{\mathrm{THz}}(t)$ is best understood in the Fourier domain, where

$$S_{\mathrm{EO}}(\omega) \simeq E_{\mathrm{THz}}(\omega) T_{\mathrm{in}}(\omega) T_{\mathrm{crystal}}(\omega) I_{\mathrm{env},0}(\omega), \tag{5.3}$$

with $T_{\mathrm{in}}(\omega)$ and $T_{\mathrm{crystal}}(\omega)$ crystal effects, see Eqs. (C.18) and (C.19), and $I_{\mathrm{env},0}(\omega)$ the Fourier transform of the envelope of $I_0(t)$. To summarize the previous paragraph, a schematic for THz field profile reconstruction is depicted in Fig. 5.3.

5.2.2 Experimental results

In order to observe the largest EO effect, the $\lambda/4$ plate was rotated to $\delta = 0°$ such that linear polarized light is incident on the crystal and analyzer [see Figs C.4(a) and C.5]. For a linear polarized laser beam, such that $G[\Gamma^* = 0] = 0$ and $H[\Gamma^*(t)] = \sin^2[\Gamma^*(t)/2]$, Eq. (C.21) shows that the normalized transmission $M(\tau)$ is related to $|E_{\mathrm{THz}}(t)|^2$, such that sign-resolvement is lacking. The data $I_{\mathrm{diode}}(\tau)$ is normalized to yield $M(\tau)$ following Eq. (5.2). This experiment was performed with the ZnTe crystal such that $T_{\mathrm{crystal}}(\omega) = T_{\mathrm{ZnTe}}(\omega)$, with the latter discussed in Sec. C.5.1. The measured normalized transmission $M(\tau)$ is plotted in Fig. 5.4. Each data point is an average of 8 shots. The measured pulse length of $M(\tau)$ can be found to be 450 fs (FWHM).

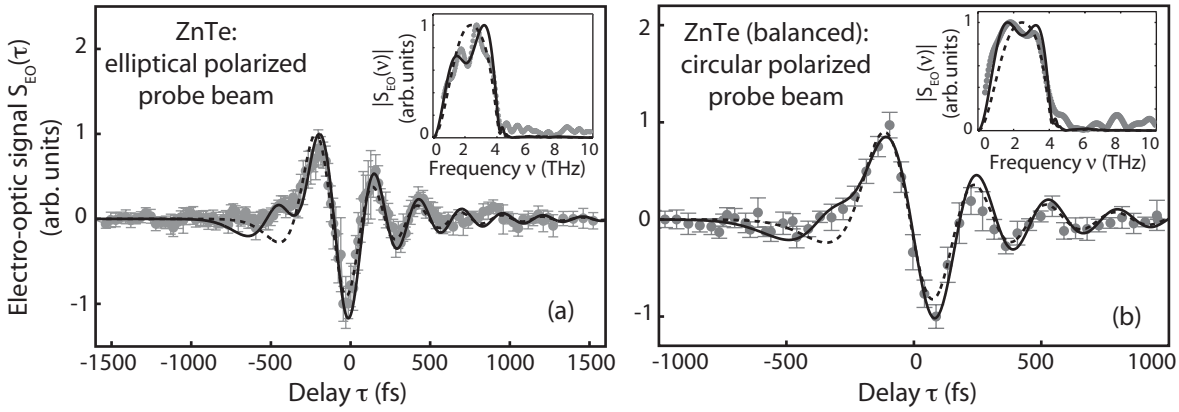

Fig. 5.5. ZnTe-based EOS waveforms $S_{\mathrm{EO}}(\tau)$ (grey circles) measured with (a) an elliptical polarized probe beam and (b) a circular polarized probe beam (balanced detection). The insets show the data in the Fourier domain $|S_{\mathrm{EO}}(\nu)|$. The black curves in all plots represent the modeled EO signal of THz radiation emitted by a 50 fs (rms) electron bunch, either in a single THz pulse (dashed curves) or a double THz pulse (solid curves). For the latter, the two THz pulses are separated by 230 fs. (Figure from Refs. [1, 2].)

The data allows for an estimation of the peak electric field of the THz pulse. Several shots showed a transmission above $M = 5.7 \times 10^{-3}$. The peak phase retardation Γ_{cor}, induced by the THz pulse, is related to the peak transmission M through Eqs. (C.21) and (C.22). In the small-Γ_{THz} limit, and assuming that $I_0(t)$ is much shorter than the THz pulse (which results in a slight underestimation of the peak THz field), Eq. (C.21) reduces to $\Gamma_{\mathrm{cor}} \simeq 2\sqrt{M}$, resulting in $\Gamma_{\mathrm{cor}} \simeq 0.15$ rad. Γ_{cor} can be expressed as an electric field S_{EO} through Eq. (C.23). Using $n = 2.85$ (ZnTe refractive index for λ_0=800 nm), $r_{41} \simeq 4.0 \times 10^{-12}$ m V^{-1}, $L = 200$ μm, it can be found that the peak field $S_{\mathrm{EO}} \simeq 10$ kV cm^{-1}. The crystal effects can be estimated to account for a reduction in amplitude of $\times\frac{1}{4}$: $\times\frac{1}{2}$ for surface losses (T_{in}) and $\times\frac{1}{2}$ for dispersion-induced decrease in peak field (T_{ZnTe}), as presented by Eq. (C.25) and discussed in Sec. C.5.1. The original peak THz field, at the location of the crystal, is then found to be $E_{\mathrm{THz}} \simeq 40$ kV cm^{-1}.

Several EOS scans under different conditions for the laser polarization state were performed. The data (grey circles) in both images (a) and (b) in Fig. 5.5 were taken after rotation of the $\lambda/4$ plate by $\delta = 5°$ (elliptical polarization) and $\delta = 45°$ (circular polarization), respectively. In the latter case, balanced diode detection was applied. Each data point represents an average of 30 shots, taken at 0.5 Hz repetition rate. The signal-to-noise ratios for both plots are of the same order; in the case of balanced detection, the noise could not be further reduced due to accelerator-related electronic background noise on the diodes. For balanced diode detection, M was defined as $M = \frac{1}{2}(I_{\mathrm{diode}} - I_{\mathrm{diode},2})/(I_{\mathrm{diode}} + I_{\mathrm{diode},2})$. In both data sets of Fig. 5.5 the normalized transmission data $M(\tau)$ was corrected with Eq. (C.15) to take the probe beam ellipticity into account, yielding $S_{\mathrm{EO}}(\tau)$, as also discussed in Sec. C.4. Note that the detection of the coherent signals in Fig. 5.5 demonstrates the excellent shot-to-shot stability of bunch parameters that are critical to THz emission

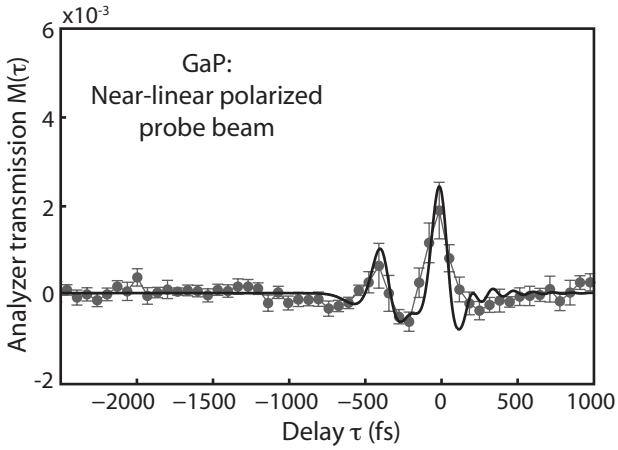

Fig. 5.6. GaP-based EOS-induced analyzer transmission M (grey circles) versus delay τ, taken at near-linear probe beam polarization. A modeled transmission profile based on a double-THz-pulse field profile is displayed as the solid curve. For the model, the pulses were separated by 195 *fs, with the leading pulse having a* 50% *relative field amplitude. Each THz pulse was calculated from a* 50 *fs (rms) bunch. (Figure from Ref. [2].)*

and detection (bunch length and temporal synchronization). The Fourier transforms of the scans are plotted in each inset.

All plots of Fig. 5.5 also contain modeled data based on $S_{\mathrm{EO}}(\tau)$ from THz emission by an electron bunch. Note that plasma density experiments estimated the transverse plasma boundary size at $\rho \simeq 100 - 200$ μm. Although the modeled THz profile does not change significantly over this range, the parameter ρ was varied for each data set for optimum agreement with the model. The dashed curves are based on a single THz pulse from a 50 fs (rms) electron bunch, while the solid curves are based on a double THz pulse profile. Parameters for the double-pulse THz profile in Fig. 5.5(a) are a pulse separation of 230 fs and a relative field amplitude of 43% for the leading pulse, with each pulse based on CTR from a bunch with 50 fs (rms) length. The parameters for the double-pulse THz profile in Fig. 5.5(b) are a 230 fs pulse separation and a relative field amplitude of 28% for the leading pulse, with each pulse based on CTR from a 70 fs (rms) bunch. Although the model based on single-pulse THz radiation provides a good agreement between data and model, the presence of the spectral oscillations (see insets) led to consideration of the double-THz-pulse structure. More EOS data presented in this chapter, combined with 2D THz imaging (data and model) in Chapter 6, supports the presence of the double THz profile. Chapter 6 will provide a detailed discussion on this topic.

Comparing the data of Fig. 5.5 to the models allows for the conclusion that sub-50 fs structure is present in the SM-LWFA-produced electron bunch. The bunch structure could be shorter, but the mismatch-dominated ZnTe would not be able to resolve the higher frequency components (cut-off at 4 THz). However, assuming a longer bunch structure would significantly disagree with the measured spectral intensity in the 3–4 THz range.

Another EOS data-set was taken using the GaP crystal such that $T_{\mathrm{crystal}}(\omega) = T_{\mathrm{GaP}}(\omega)$,

with the latter discussed in Sec. C.5.2. Figure 5.6 displays the measured analyzer transmission $M(\tau)$ (grey circles), without a $\lambda/4$ plate in the probe beam path. Each data point represents an average of 20 shots, taken at 1 Hz repetition rate. Due to residual birefringence in the GaP (equivalent to $\delta \simeq 1.8°$ of $\lambda/4$ plate rotation), the effective probe beam polarization was near-linear (small degree of ellipticity), and sign-resolved information was therefore still available. However, since the polarization state was so close to linear, the data was not corrected to $\Gamma_{\mathrm{cor}}(\tau)$ to take the ellipticity into account. It is for this reason that spectral analysis of the data is omitted. Instead, the modeled THz waveform $\Gamma_{\mathrm{cor}}(t)$ was converted to $M(t)$ for comparison between data and model. The GaP data (with up to 8 THz spectral resolution, and limited dispersion) unambiguously indicates that two THz pulses were produced. The modeled transmission signal (solid curve in Fig. 5.6) is based on a double-pulse THz profile, where the pulses are separated by 195 fs, with a 50% relative field amplitude of the leading pulse. Both THz pulses are calculated from a 50 fs (rms) electron bunch.

5.3 Single-shot detection

The EOS data obtained with the scanning technique proved useful for the determination of the bunch structure. However, the measured curves represent "averaged" waveforms since hundreds of data shot were required for each profile. Also, the THz profiles of the previous section indicated a more-complex field structure, and a double-THz-pulse profile was suggested. This section will introduce three single-shot EOS-based measurement techniques. They allow the user to see the temporal THz profile and obtain a peak field estimation in one shot. Experimental realization of single-shot techniques will be presented and discussed. Future experiments on THz applications can benefit from the availability of these techniques.

5.3.1 Non-collinear technique

The first technique, see Fig. 5.7(a), is referred to as the non-collinear EOS technique [85]. It relies on a collimated THz pulse $E_{\mathrm{THz}}(t)$ and a collimated short laser probe pulse $I_0(t)$ propagating through an EO crystal at non-collinear angles of incidence. Following the geometry of Fig. C.3(a), with the probe beam circularly polarized, the energy recorded by one diode element of the CCD array is presented by Eq. (C.20) as $I_{\mathrm{diode}}(\tau) = \int \frac{1}{2}[1 + \sin\Gamma^*(t)]I_0(t-\tau)dt$. The front of the THz pulse overlaps in a different transverse probe laser region than the tail of the THz pulse. For this reason, the temporal THz properties are transposed to the transverse-spatial laser probe profile through $\tau = \frac{y}{c}\tan(\theta/2)$, with θ the half-angle between both pulses and y the transverse direction, see Fig. 5.7(a). Note that θ is defined within the EO crystal by considering the index of refraction and angle of incidence for both pulses. The time-integrated transverse probe profile $I_{\mathrm{diode}}(y)$ can be recorded by a CCD array or camera, and normalized to $M(y)$ as defined by Eq. (5.2).

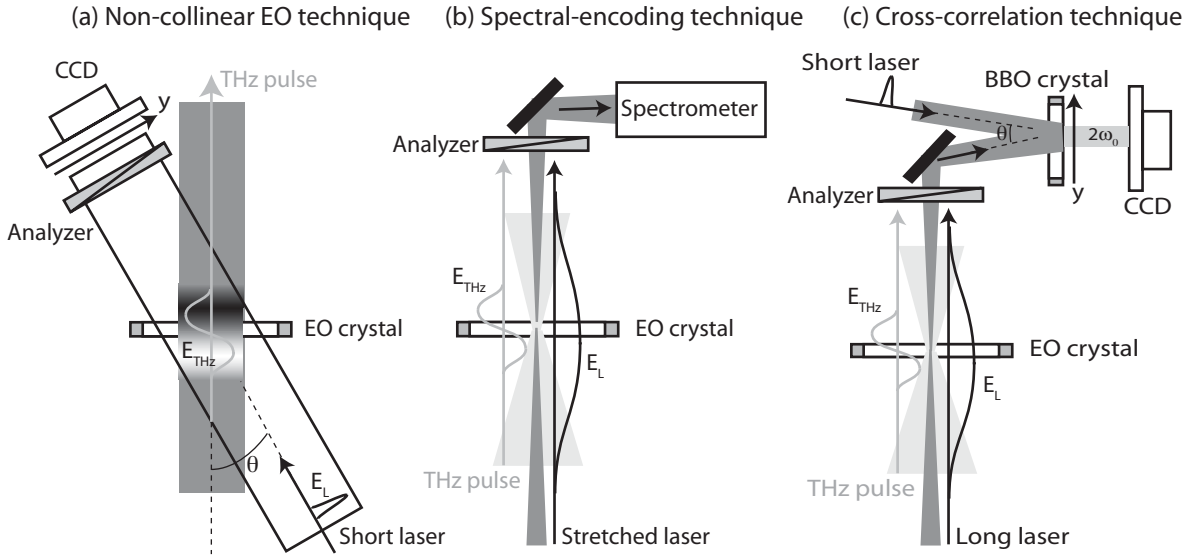

Fig. 5.7. Three techniques for single-shot temporal characterization of THz pulses. (a) In the non-collinear EOS technique, a collimated THz pulse and a collimated short probe beam interact in the EO crystal, at non-collinear angles of incidence. The THz pulse leaves a spatial imprint on the transverse probe field distribution, which is recorded by a CCD camera. (b) Spectral-encoding techqnique: a long probe beam (stretched from a short pulse) is overlapping with the THz waveform in the EO crystal. Both beams are focused. The resulting spectral modulation on the laser is recorded by a spectrometer. (c) Cross-correlation technique: a long probe beam is overlapping with the THz waveform in the EO crystal. Both beams are focused. Due to the EO effect, the envelope of the probe beam is modulated. A second short laser beam is used to measure the modulated envelope in a single-shot manner through non-collinear frequency doubling in a BBO crystal, imaged by a CCD array or camera.

Through the spatial-to-temporal coordinate conversion, and following Eqs. (C.22)-(C.24), $M(y)$ can be rewritten as

$$H_{\mathrm{inv}}[M(y)] \rightarrow H_{\mathrm{inv}}[M(\tau)] \rightarrow \Gamma_{\mathrm{cor}}(\omega) \propto E_{\mathrm{THz}}(\omega). \tag{5.4}$$

In principle, the temporal resolution of this technique is determined by the short probe pulse length, although at larger values for θ additional temporal smearing occurs. Since the THz pulse is not focused, the THz field strength and EO effect are probably weak. This limits the applicability of this technique, which was not implemented experimentally. However, future experiments (see last bullets of Chapter 7) will aim for high peak THz fields ($\gtrsim 1\ \mathrm{MV\,cm^{-1}}$), in which case this lesser-complicated technique can prove useful.

5.3.2 Spectral-encoding technique

A second single-shot EOS technique relies on spectral encoding of the THz waveform onto a stretched laser pulse, referred to as the spectral-encoding technique [21, 86–89], see Fig. 5.7(b).

Theory

For a chirped (stretched) laser pulse, the complex electric field can be defined as

$$E_0(t) = \exp\left[-\frac{(1-\imath\frac{b}{2})t^2}{2\sigma_L^2(1+\frac{b^2}{4})}\right]\exp\left(\imath\omega_0 t\right), \tag{5.5}$$

with b the chirp parameter, σ_L the Fourier-limited pulse length (field rms), and $\sigma_c = \sigma_L\sqrt{1+b^2/4}$ the actual pulse length (field rms). The instantaneous frequency $\omega(t)$ is derived from Eq. (5.5) through $\omega(t) = \partial\phi/\partial t$, with ϕ the phase of $E_0(t)$, leading to

$$\omega(t) = \omega_0 + \chi t, \qquad \text{with} \qquad \chi = \frac{b}{2\sigma_L^2\left(1+b^2/4\right)}. \tag{5.6}$$

While the THz pulse is co-propagating with the chirped probe beam through an EO crystal, the EO effect induces a modulation on the probe beam. Although the EOS imprint of the THz field is more complex, see Eq. (C.16), with the function G defined by Eq. (C.15), a simplified approach will follow here. Following Jiang *et al.* [87] and Yellampalle *et al.* [88], the transmitted modulated probe field will be defined as

$$E_m(t) = E_0(t)\left[1+\beta E_{\mathrm{THz}}(t)\right], \tag{5.7}$$

with β a constant. The spectrum of the modulated probe beam $I_m = |E_m|^2$ can be compared to the original probe spectrum $I_0 = |E_0|^2$. If the THz pulse is shorter than σ_L, then new frequencies are added to the spectrum of I_m. Here however, it is assumed that the THz pulse is longer than σ_L. For the upcoming analysis it is crucial how the temporal features T of the THz radiation, which are on the order of the electron bunch duration ($T \simeq \sigma_z$), compare to the factor $\sqrt{\sigma_L\sigma_c}$. Theory shows [86, 87] that for $T \gtrsim \sqrt{\sigma_L\sigma_c}$, the signal $M(\omega)$, defined in analogy to Eq. (5.2) as $M(\omega) = \Delta I(\omega)/I_0(\omega) = [I_m(\omega) - I_0(\omega)]/I_0(\omega)$, is related to the THz field through

$$M(\omega) = M(\omega_0+\chi t) \propto E_{\mathrm{THz}}(\omega_0+\chi t). \tag{5.8}$$

In other words, the THz field profile can be directly obtained through measurement of the laser spectral modulation $M(\omega)$, using the simple coordinate transformation $\omega \rightarrow \omega_0 + \chi t$.

An example is plotted in Figs. 5.8(a)-(c). A longer THz pulse [see Fig. 5.8(a)], derived from a 400-fs (rms) electron bunch, is co-propagating with a chirped probe beam ($\sigma_L = 42$ fs, $b = 140$, and $\sigma_c = 3000$ fs). For a modulation depth of $\beta = 0.4$, the inset Fig. 5.8(b) shows the spectra $I_0(\lambda)$ (dotted curve) and $I_m(\lambda)$ (solid curve). Figure 5.8(c) shows the normalized signal $M(\lambda)$, indicating the agreement between the single-cycle THz waveform and the single-cycle spectral modulation.

In case of THz-field structure T shorter than $T < \sqrt{\sigma_L\sigma_c}$, the spectral modulation is more complex. Figure 5.8(d) shows the THz waveform from a 50 fs (rms) bunch, resulting in the probe beam spectrum $I_m(\lambda)$ as plotted in Fig. 5.8(e), with $\sigma_L = 42$ fs, $b = 140$, and

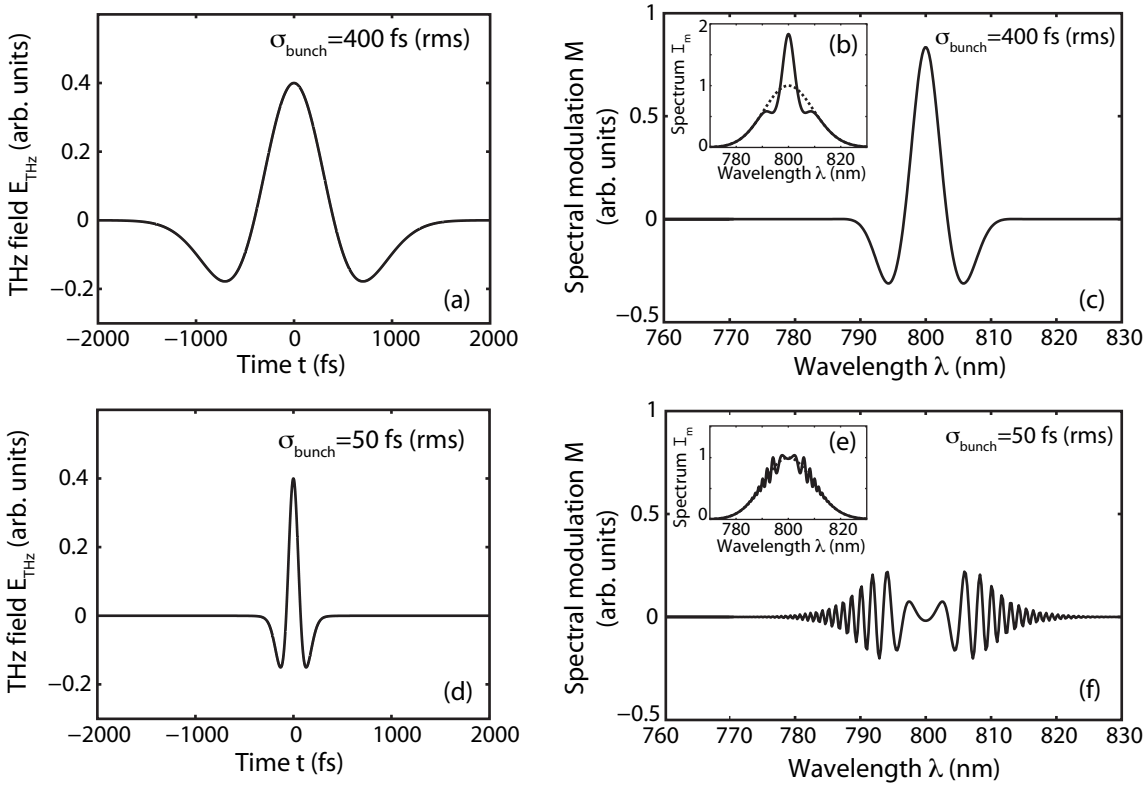

Fig. 5.8. (a) THz field profile, calculated for a 400 fs (rms) electron bunch. (b) Corresponding EOS-induced spectrally-encoded laser spectrum $I_m(\lambda)$ (solid curve), compared to the laser spectrum $I_0(\lambda)$ with no THz field present (dotted curve). (c) The corresponding normalized spectral modulation $M = (I_m - I_0)/I_0$. Plots (d), (e), (f) are identical to (a), (b), and (c), respectively, except that the THz profile is calculated for a 50 fs (rms) electron bunch. In contrast to (b)-(c), the plots (e) and (f) show a spectral modulation that is different from the original THz temporal waveform. The laser chirp parameter was $b = 140$.

$\sigma_c = 3000$ fs. The normalized spectral modulation $M(\lambda)$ is plotted in Fig. 5.8(f). One can see that the spectral modulation has many oscillations, and does not directly resemble the time-domain-based THz waveform. For short THz time structures $T < \sqrt{\sigma_L \sigma_c}$, a simple coordinate transformation $\omega \rightarrow \omega_0 + \chi t$ can not be applied to $M(\lambda)$ to retrieve $E_{\mathrm{THz}}(t)$. However, through an algorithm, the THz profile $E_{\mathrm{THz}}(t)$ can in principle still be reconstructed from $\Delta I(\lambda)$. Theory [88, 89] shows that, in the limit where $\beta E_{\mathrm{THz}} \ll E_0$,

$$\Delta I(\omega) = \beta \mathbf{B}_{\omega,t} E_{\mathrm{THz}}(t), \tag{5.9}$$

with $\mathbf{B}_{\omega,t}$ a two-dimensional matrix whose elements are given by

$$\mathrm{B}_{\omega,t} = E_0^*(\omega) E_0(t) e^{\imath\omega t} + E_0(\omega) E_0^*(t) e^{-\imath\omega t}. \tag{5.10}$$

The THz field $E_{\mathrm{THz}}(t)$ can be derived from the measured $\Delta I(\lambda) = I_m(\lambda) - I_0(\lambda)$ through a matrix inversion. Although the temporal resolution of this technique is only limited to the probe pulse length, the inversion of the complex matrix $\mathbf{B}_{\omega,t}$ is not straightforward. It is

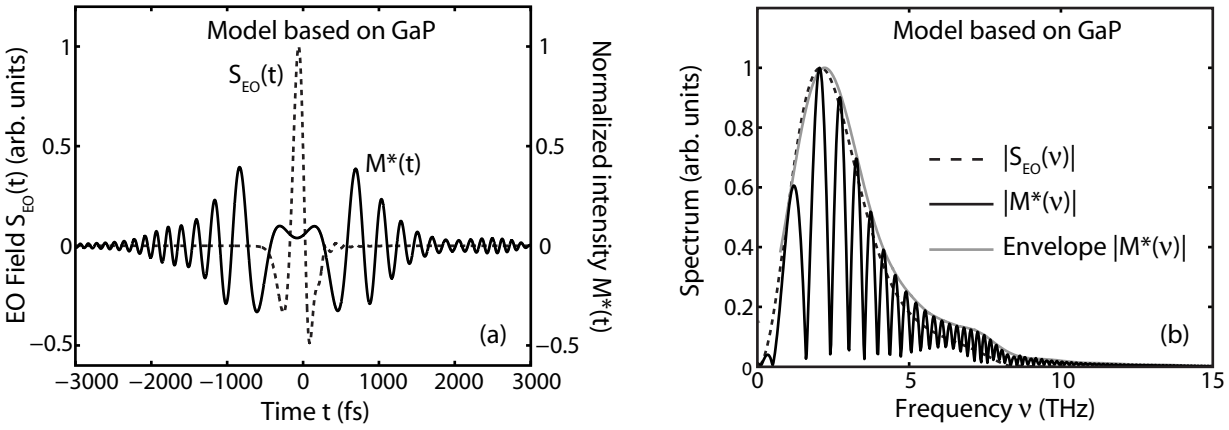

Fig. 5.9. The EO signal $S_{\mathrm{EO}}(t)$ from a 50 fs (rms) electron bunch, modeled with a 200-μm-thick GaP crystal, is plotted as the dashed curves in (a) and (b). The spectrally modulated signal $M(\omega)$ can be converted to the time domain through $\omega = \omega_0 + \chi t$, yielding $M^*(t)$. Figures (a) and (b) show $M^*(t)$ and $|M^*(\nu)|$ as solid curves, with the grey curve in (b) representing the envelope of $|M^*(\nu)|$. Note the strong resemblance between $|S_{\mathrm{EO}}(\nu)|$ and the envelope of $|M^*(\nu)|$.

not clear at this point if the technique is useful for THz retrieval of experimentally-obtained LWFA-produced modulation spectra, which typically include noise contributions.

Even if use of the algorithm [based on the matrix inversion of Eq. (5.9)] does not allow for acceptable retrieval of the THz field $E_{\mathrm{THz}}(t)$, there is another approach to the measured spectral modulation that can be followed. By following this approach, sign-resolved THz field information will not be retrieved, but the coherent spectrum of the THz pulse can be found (even for $T < \sqrt{\sigma_L \sigma_c}$). Instead of approximating the transmitted modulated laser field as $E_m(t) = E_0(t)\,[1 + \beta E_{\mathrm{THz}}(t)]$, the modulated profile is now defined again as $E_m(t) = E_0(t)\left[1 - \imath e^{\imath\Gamma^*(t)}\right]$, which is based on Eq. (C.16), while taking crystal effects into account following Eq. (C.18). For a circular polarized probe beam, and assuming $\Gamma_{\mathrm{THz}} \ll 1$ rad, it can be found that $M(\omega) \propto S_{\mathrm{EO}}(\omega)$, with $M(\omega)$ the previously defined normalized modulation spectrum. The following example demonstrates the idea behind the new approach for retrieval of the THz spectrum.

Consider a THz pulse from a 50 fs (rms) electron bunch, with the EO sampling occurring in a 200-μm-thick GaP crystal. The modeled EO signal S_{EO} is plotted in Figs. 5.9(a) and 5.9(b) as dashed curves in the time and frequency domain. From $S_{\mathrm{EO}}(t)$, the modeled normalized spectrum $M(\omega)$ is obtained. Through Eq. (5.6), the expression $M(\omega)$ can be converted to the time domain, yielding $M^*(t)$. The frequency-to-time-converted profile $M^*(t)$ is plotted in Fig. 5.9(a) as the solid curve, and since the original time structure of the THz pulse was shorter than the resolution limit $T < \sqrt{\sigma_L \sigma_c}$, the multiple oscillations are present. The Fourier-transformation of $M^*(t)$ yields $|M^*(\nu)|$, which is plotted as the black solid curve in Fig. 5.9(b), while the grey solid curve represents its envelope. The similarities between $|M^*(\nu)|$ and $|S_{\mathrm{EO}}(\nu)|$ are very clear: although $|M^*(\nu)|$ contains an interference pattern, the envelope of $|M^*(\nu)|$ strongly resembles $|S_{\mathrm{EO}}(\nu)|$. In other words, by measuring $M(\lambda)$ (which leads to the envelope profile $|M^*(\nu)|$), the envelope of the

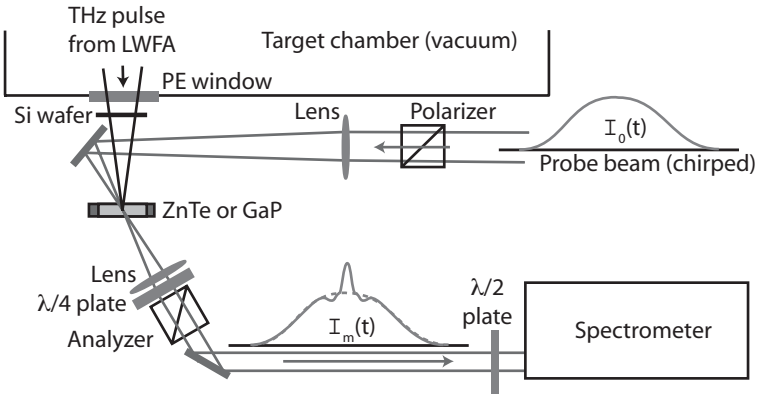

Fig. 5.10. The setup for THz characterization based on the single-shot spectral-encoding technique. The THz pulse and the chirped probe beam (circular polarization) propagate through the EO crystal and analyzer. The analyzer transmission is propagated to an imaging spectrometer. The λ/2 plate was rotated to optimize the grating reflectivity inside the spectrometer.

coherent spectrum of the EO signal (related to the THz pulse) can be retrieved.

Experiments

The experiments on the single-shot spectral-encoding technique are now presented. The setup for the experiments is similar to the setup discussed in Sec. 5.2.1 and Fig. 5.2, with the modifications on the EO part of the setup depicted in Fig. 5.10. Either 200-μm-thick ZnTe or 200-μm-thick GaP was used as EO crystal, and the $\lambda/4$ plate was rotated to $\delta = \pi/4$ such that the polarization state of the laser incident on the analyzer was circular. The probe beam was chirped to a yield Gaussian laser profile with a length of 4.5 ps (intensity FWHM), corresponding to σ_L=25 fs and $b = 150$, as defined in Eq. (5.5). The analyzer transmission was propagated to an imaging optical spectrometer. The imaging spectrometer had a 600-groves-per-mm grating, and the entrance slit had an opening of 100 μm. The spectra were recorded by a 512x512-pixel 16-bit camera, with a resolution of 0.11 nm/pixel. A $\lambda/2$ plate was installed at the entrance to the spectrometer, and was rotated to optimize the internal spectrometer laser transmission.

A first data set was obtained with the ZnTe crystal. The measured normalized spectral modulation $M(\lambda)$ is plotted in Fig. 5.11(b). Through the frequency-to-time conversion $\omega = \omega_0 + \chi t$, see Eq. (5.6), a temporal signal $M^*(t)$ can be derived. The absolute value of its Fourier-transformation $|M^*(\nu)|$ is plotted as the solid curve in Fig. 5.11(a). A modeled ZnTe-based profile $|M^*(\nu)|$ is calculated from a 50 fs (rms) electron bunch, and the modeled envelope of $|M^*(\nu)|$ is plotted in Fig. 5.11(a) as the dotted solid curve. Other parameters for the model were a boundary size $\rho = 200$ μm, an electron bunch momentum $u = 10$, and observation angle θ=0.33 rad. Note that plasma density experiments estimated ρ at $\rho \simeq 100-200$ μm. Although the modeled THz profile does not change significantly over this range, the parameter ρ was varied for each data set for optimum agreement with the model. The data and model show agreement, with the spectral cut-off around 4 THz due to the

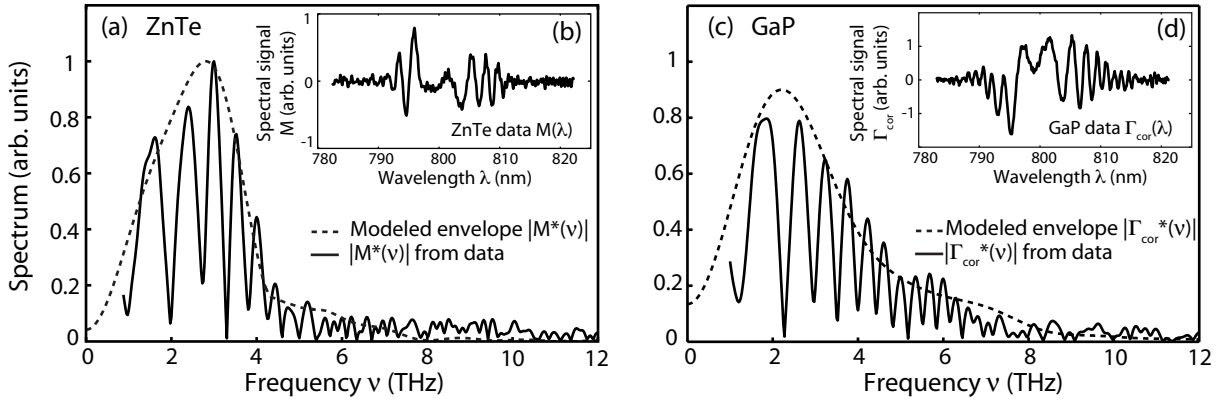

Fig. 5.11. Plot (b) shows the measured modulated laser spectrum $M(\lambda)$, based on a 200-μm-thick ZnTe crystal, which is frequency-to-time transformed to yield $M^*(t)$. The Fourier-transformed $|M^*(\nu)|$ is plotted in (a) as the solid curve, and compared to a modeled envelope based on the THz emission from a 50 fs (rms) electron bunch (dotted curve). Plot (d) shows a measured modulated spectrum $\Gamma_{\rm cor}(\lambda) = H_{\rm inv}[M(\lambda)]$ based on a 200-μm-thick GaP crystal. Its Fourier transformation $|\Gamma^*_{\rm cor}(\nu)|$ (solid curve), and a modeled envelope based on a 50 fs (rms) electron bunch (dotted curve), are shown in plot (c).

velocity mismatch in the ZnTe crystal, as discussed in Sec. C.5 and plotted in Fig. C.7(a). If a longer electron bunch were to be assumed, the modeled envelope of $|M^*(\nu)|$ would not show the sharp spectral fall-off around 4 THz. However, due to the 4 THz crystal response, the envelope of $|M^*(\nu)|$ from a shorter electron bunch would not be different than from the 50 fs (rms) bunch. The measurement demonstrates that the electron bunch has coherent substructure of < 50 fs. It also demonstrates the applicability of the relatively simple (only one probe beam is used) single-shot spectral-encoding technique.

A second data set was obtained with the 200-μm-thick GaP crystal, which has a frequency response up to 8 THz, see Sec. C.5.2. The data [normalized spectral modulation $M(\lambda)$] is plotted in Fig. 5.11(d). For this particluar set of data, the THz-induced EO modulation was lower than during the ZnTe-related scan, which is most likely related to an improper spatial overlap between the focused THz and laser pulse. In order to improve the signal-to-noise ratio, the $\lambda/4$ plate in Fig. 5.10 was rotated to $\delta = 1.5^\circ$ for elliptical (near-linear) polarized laser light. For the model, the new polarization state was taken into account, as discussed in Sec. C.2 of Appendix C: Eq. (C.22) was used to correct $M(\lambda)$ to $\Gamma_{\rm cor}(\lambda)$. The measured normalized spectral modulation $\Gamma_{\rm cor}(\lambda)$ is plotted in Fig. 5.11(d). Through the frequency-to-time conversion, the temporal signal $\Gamma^*_{\rm cor}(t)$ was calculated. The absolute value of the measured Fourier-transformed $|\Gamma^*_{\rm cor}(\nu)|$ is plotted as the solid curve in Fig. 5.11(c). The modeled GaP-based profile $|\Gamma^*_{\rm cor}(\nu)|$ is calculated from a 50 fs (rms) electron bunch, and the modeled envelope of $|\Gamma^*_{\rm cor}(\nu)|$ is plotted in Fig. 5.11(c) as the dotted curve. Other parameters for the model were $\rho = 150$ μm, $u = 10$, and θ=0.33 rad. The data and model indicate agreement, with the measured and modeled spectrum extending to $\simeq 6$ THz. The measurement proves that the electron bunch has coherent substructure of 50 fs. The applicability of the single-shot spectral-encoding technique is demonstrated,

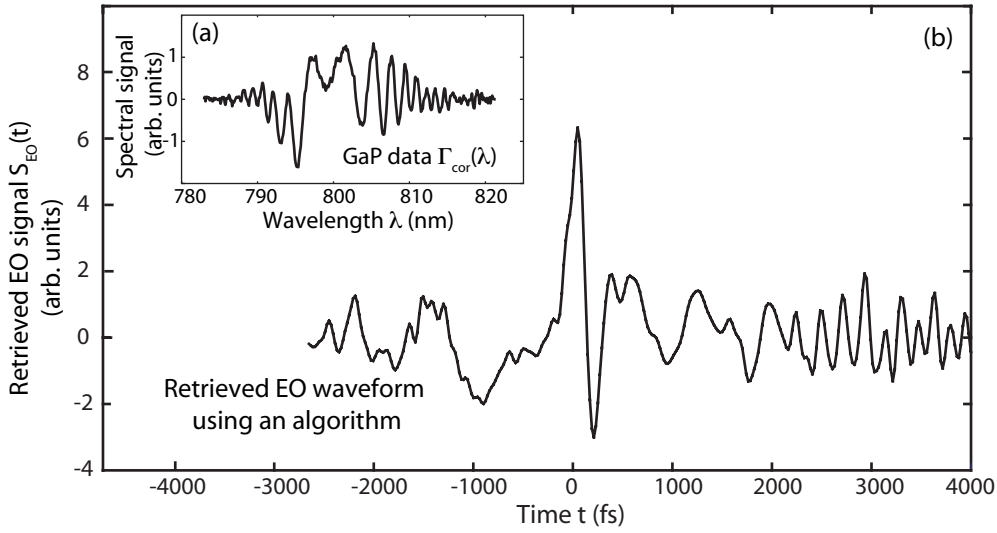

Fig. 5.12. Plot (a) shows the measured modulated laser spectrum $\Gamma_{\mathrm{cor}}(\lambda)$, based on a 200-$\mu$m-thick GaP crystal. Through an algorithm, the temporal field profile for $S_{\mathrm{EO}}(t)$ is retrieved and plotted in (b). However, due to the poor signal-to-noise ratio and the dominant presence of algorithm artifacts such as the fast oscillations, a reliable retrieval has not been achieved. For the moment, the single-shot spectral-encoding technique is only useful for the measurement of the absolute value of the coherent THz spectrum (as demonstrated in Fig. 5.11).

even in a regime where the THz pulse is not very intense (polarization state was changed from circular to near-linear).

The algorithm-based THz retrieval, presented in Eq. (5.9), is at present time limited in its ability to retrieve THz waveforms from the GaP-based data presented in Fig. 5.11(d). The measured spectral modulation $\Gamma_{\mathrm{cor}}(\lambda)$ is shown in Fig. 5.12(a). The mathematical reconstruction of the THz field profile $S_{\mathrm{EO}}(t)$ was performed at the Los Alamos National Laboratory, New Mexico (USA). The group involved there has summarized the algorithm details in publications by Yellampalle *et al.* [88] and Kim *et al.* [89]. The retrieved EO waveform $S_{\mathrm{EO}}(t)$ is shown in Fig. 5.12(b). The oscillations on the left and right side of the main peak around $t = 0$ fs are believed to be artifacts of the retrieval process. The dominant presence of these artifacts (possibly present around $t = 0$ as well) and the low signal-to-noise ratio do not allow for a reliable THz retrieval at present. No conclusions will be derived from the retrieval-based data. Future improvements on the mathematical algorithm will aim at retrieving a more reliable temporal THz field profile.

5.3.3 Cross-correlation technique

The third single-shot EOS technique is referred to as the cross-correlation technique [90], as depicted in Fig. 5.7(c).

Theory

In this single-shot geometry, a long laser probe beam $I_0(t)$ is moving through a $\lambda/4$ plate, an EO crystal, and an analyzer, see Fig. 5.13. Both a Fourier-limited longer laser pulse or

a stretched larger-bandwidth pulse can be used as the long probe beam. Through the EO effect, the THz pulse modulates the envelope of the transmitted laser pulse, resulting in $I_m(t)$, as defined in Eq. (C.26). For a circularly-polarized beam ($\delta = \pi/4$), following the geometry in Fig. C.3(a), the transmitted intensity profile was calculated and expressed by Eq. (C.26) to be $I_m(t) = I_0(t)\frac{1}{2}\left[1 + \sin\Gamma^*(t)\right]$. The envelope-modulated probe pulse $I_m(t)$ is propagated to a frequency-doubling nonlinear crystal (typically BBO). Also incident on the BBO crystal is a short second laser pulse $I_2(t)$, see Fig. 5.13, with a temporal delay τ_2 with respect to $I_m(t)$. Due to the non-collinear geometry, the respective time delay τ_2 between both pulses varies at different transverse locations y. One can find that y is related to τ_2 through $\tau_2 = \frac{y}{c}\tan(\theta/2)$, with θ the half-angle between both pulses within the EO crystal. A 1D or 2D diode array measures the time-integrated frequency-doubled energy profile $I_{2\omega}(y)$. Through the space-to-time coordinate conversion $\tau_2 = \frac{y}{c}\tan(\theta/2)$, the profile $I_{2\omega}(y)$ can be converted to $I_{2\omega}(\tau_2)$, which can be expressed as

$$I_{2\omega}(\tau_2) \propto \int I_0(t)\frac{1}{2}\left[1 + \sin\Gamma^*(t)\right] I_2(t-\tau_2)dt. \tag{5.11}$$

A single-shot measurement of $I_{2\omega}(y)$ and $I_{2\omega}(\tau_2)$ yields the normalized signal $M(\tau_2)$, with $M(\tau_2)$ defined by Eq. (C.28) as

$$M(\tau_2) = \frac{I_{2\omega}(\tau_2) - I_{2\omega,\mathrm{reference}}(\tau_2)}{I_{2\omega,\mathrm{total}}(\tau_2)}, \tag{5.12}$$

with $I_{2\omega,\mathrm{reference}}(\tau_2)$ the measured frequency-doubled profile in case no THz field is applied and $I_{2\omega,\mathrm{total}}(\tau_2)$ the recorded profile in case of no THz field, with the $\lambda/4$ plate removed, and with the analyzer rotated for maximum transmission. Through calculation of the retardation profile $\Gamma_{\mathrm{cor}}(\tau_2) = H_{\mathrm{inv}}[M(\tau_2)] = \arcsin\left[2M(\tau_2)\right]$, it was derived in Appendix C [see Eq. (C.29)] that

$$\Gamma_{\mathrm{cor}}(\omega) \simeq \Gamma_{\mathrm{THz}}(\omega)T_{\mathrm{in}}(\omega)T_{\mathrm{crystal}}(\omega)I_{\mathrm{env},2}(\omega), \tag{5.13}$$

with $I_{\mathrm{env},2}(\omega)$ the Fourier transform of the envelope of laser pulse $I_2(t)$. Note that the profile $\Gamma_{\mathrm{cor}}(\tau_2)$ can be written as an electric field $S_{\mathrm{EO}}(\tau_2)$ through Eq. (C.23).

The benefits of the cross-correlation technique are i) due to THz focusing a strong EO effect is expected, ii) the retrieved probe intensity modulation can be related to $E_{\mathrm{THz}}(t)$ through simple algebra (no matrix inversion), and iii) the time resolution is fast (only limited by the pulse length of probe pulse I_2). Disadvantages include the complexity of the laser system, since a second probe beam is necessary. Also, the energy of both laser pulses has to be sufficiently high to yield the frequency-doubled beam. Since the longer probe beam is also focused onto the EO crystal, damage issues can be a concern.

Experiments

The experiments on the single-shot cross-correlation EOS technique are presented now. The setup for the experiments is similar to the setup discussed in Sec. 5.2.1 and Fig. 5.2,

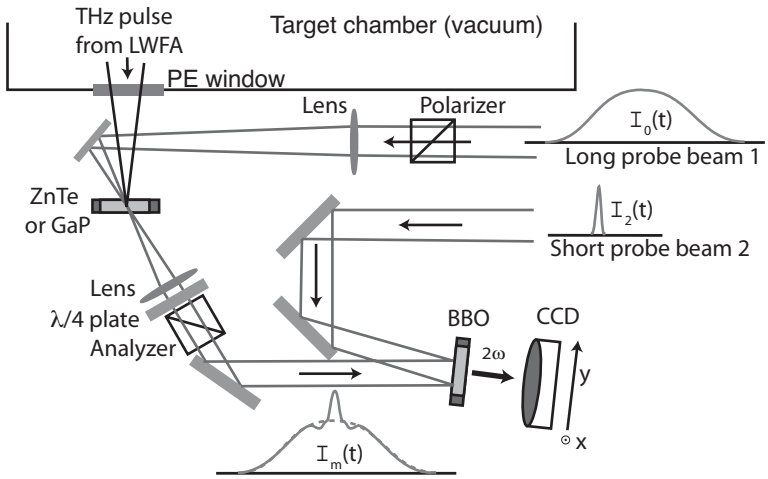

Fig. 5.13. Schematic representation of the setup for single-shot electro-optic sampling with the cross-correlation method. Two laser probe beams are used. Probe beam 1, or $I_0(t)$, which is longer than the THz pulse (2 − 3 ps), propagates through the EO crystal, resulting in a THz-induced laser envelope modulation $I_m(t)$. The λ/4 plate is rotated ($\delta = \pi/4$) such that the polarization state is circular, with 50% analyzer transmission if no THz is present. The second probe beam [probe beam 2 or $I_2(t)$], which has a 50 fs (intensity FWHM) pulse length, is used to obtain a single-shot measurement of $I_m(t)$. This is done through non-collinear frequency doubling in a BBO crystal. The frequency-doubled light is recorded by a CCD camera.

with the modifications on the EO part of the setup depicted in Fig. 5.13. Both laser probe beams 1 and 2 (I_0 and I_2) are intrinsically synchronized to the main laser system. Each probe laser arm has its own compressor, which consists of a single 1500-groves-per-mm grating with a four-folded compressor geometry. The temporal delay between both probe lasers and the THz beam can be modified by a delay stage. A second delay stage was installed to modify the delay of probe beam 2 with respect to probe beam 1. Probe beam 1 was focused through either a 200-μm-thick ZnTe crystal or a 200-μm-thick GaP crystal. A $\lambda/4$ plate was rotated to $\delta = \pi/4$ for circular polarization.

The short probe beam 2 and the modulated probe beam 1 both interact in a 1-mm-thick BBO crystal close to normal incidence, with $\theta = 10°$ between both beams. The beam diameter of each probe beam was $d \simeq 6$ mm (intensity FWHM), resulting in a single-shot temporal window around 1500–2500 fs. The transverse frequency-doubled intensity distribution was measured with a CCD camera, and each image was integrated over x (see Fig. 5.13). The shot-to-shot temporal synchronization between both probe pulses was investigated, and the jitter was found to be less than 8 fs (standard deviation). In order to measure the spatial-to-temporal calibration, two data sets at different delay between the THz and the probe beams were recorded.

For the cross-correlation-based single-shot method, it is assumed that at each shot the reference profile $I_{2\omega,\mathrm{reference}}(\tau_2)$ profile is constant. If the envelope shape for probe laser 1 jitters, it would be impossible to distinguish the THz-induced modulation $[I_{2\omega}(\tau_2) - I_{2\omega,\mathrm{reference}}(\tau_2)]$ from the jitter-induced change in reference $I_{2\omega,\mathrm{reference}}(\tau_2)$. However, the

temporal reproducibility of the envelope of $I_{2\omega,\mathrm{reference}}(\tau_2)$ was investigated, and the envelope jitter was found to be less than 10% (standard deviation). Note that it is less crucial for the laser pulse energy to be constant shot-to-shot. Consider a single-shot profile measurement $I_{2\omega}(\tau_2)$, but with the 2ω-beam only having 80% of the energy of $I_{2\omega,\mathrm{reference}}(\tau_2)$: at the wings, where no THz is present, the normalized signal $M(\tau_2)$ will be $(0.8-1)/2 = -0.1$. Clearly, the THz electric field should be zero at the wings, and $I_{2\omega}(\tau_2)$ can simply be renormalized to $[I_{2\omega}(\tau_2)]/0.8$.

In the experiment, the EO crystal was rotated to yield maximal EO effect. The Silicon wafer next to the PE window, which was present in the scanning measurements (see Fig. 5.2), was removed since remnant laser light did not interfere with the detection of the frequency-doubled radiation. Not indicated in Fig. 5.13 is the fact that both probe beams incident on the BBO crystal each propagated through a $\lambda/2$ plate. The $\lambda/2$ plates were rotated to maximize the frequency-doubling efficiency. Also, the rotation and position of the BBO crystal was optimized for optimum signal.

In order to characterize $I_2(t)$, both probe beams were temporarily compressed. Assuming that both beams are then equally-short ($I_0 = I_2$), the frequency-doubled signal now represents the auto-correlation trace $\int I_2(t)I_2(t-\tau_2)dt$, and the FWHM of the frequency-doubled profile $I_{2\omega}(\tau_2)$ is given by $\sqrt{2}\sigma_2$ for Gaussian beams, with σ_2 the intensity-FWHM of $I_2(t)$. The retrieved profile $I_2(t)$ is plotted in Fig. 5.14(a) as the dashed curve. The intensity-FWHM was found to be 70 fs. Also plotted in Fig. 5.14(a) as empty circles is the cross-correlation signal $I_{2\omega,\mathrm{reference}}(\tau_2)$ (no THz field). The profile $I_{2\omega,\mathrm{reference}}(\tau_2)$ is found to have an intensity-FWHM of 1350 fs. Note that the chirped laser $I_0(t)$ has an estimated intensity-FWHM of $\simeq$4–5 ps, but through transverse-laser-profile effects in the BBO crystal, the measured cross-correlated curve appears as a 1350-fs-long (FWHM) profile. Through the normalization yielding $M(\tau_2)$, these transverse-beam-profile effects are removed from interfering with subsequent analysis.

During one set of experiments, the 200-μm-thick ZnTe crystal was used, see Sec. C.5.1 for details. Although the details of the temporal THz profile can be better investigated with the faster-time-response GaP crystal, the data with the ZnTe crystal allows for determination of the peak electric field. A single-shot frequency-doubled temporal profile $I_{2\omega}(t)$ is plotted as connected solid black circles in Fig. 5.14(a). The data allows for calculation of the normalized intensity modulation $M(t)$. Following Eqs. (C.28) and (C.23), the phase retardation $\Gamma_{\mathrm{cor}}(t)$ and EO field profile $S_{\mathrm{EO}}(t)$ were calculated. Based on $L = 200$ μm, $\lambda_0 = 800$ nm, $r_{41} = 4.0 \times 10^{-12}$ m V^{-1}, and n=2.85, the field profile $S_{\mathrm{EO}}(t)$ can be expressed in units of [kV cm^{-1}], as plotted in Fig. 5.14(b) as connected circles. The crystal surface transmission is $T_{\mathrm{in}} \simeq 0.5$, and the THz dispersion in the ZnTe crystal results in a further amplitude reduction of $\simeq 0.5$, as discussed in Sec. C.5.1. Using these transmission estimates, the original peak THz field (at the position of the crystal) can be estimated to be $E_{\mathrm{THz}} \simeq 0.3$ MV cm^{-1}. Note that the relation between $S_{\mathrm{EO}}(t)$ and $E_{\mathrm{THz}}(t)$ was defined by Eq. (C.30).

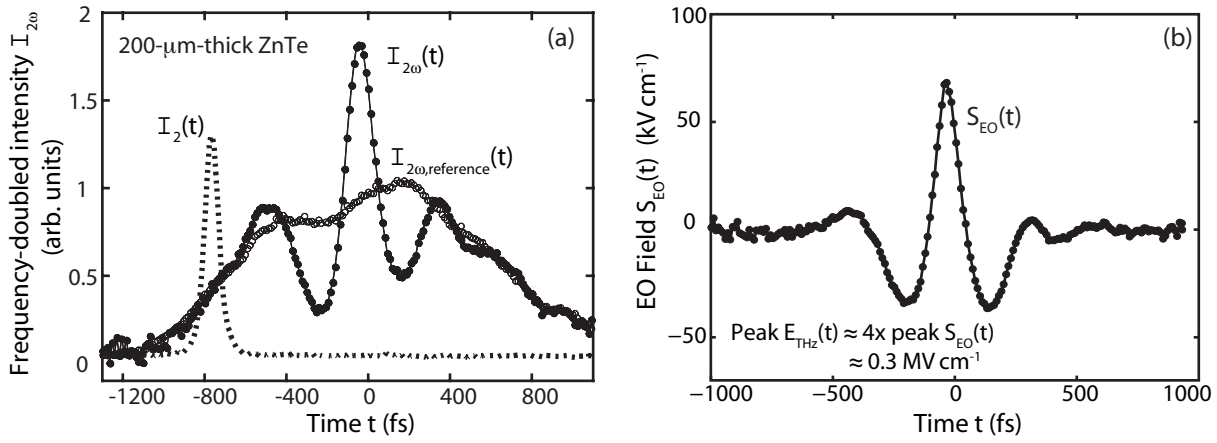

Fig. 5.14. (a) Measured frequency-doubled temporal profile without the THz present [$I_{2\omega,\mathrm{reference}}(t)$, empty circles] and with the THz pulse present [$I_{2\omega}(t)$, solid connected circles]. The temporal profile of the short probe beam $I_2(t)$ is shown as the dashed curve. The EO crystal is 200-μm-thick ZnTe. From the normalized profile $M(t)$, the phase retardation $\Gamma_{\mathrm{cor}}(t)$ and EO signal $S_{\mathrm{EO}}(t)$ were calculated, with the latter plotted in (b). The peak amplitude of the original THz field $E_{\mathrm{THz}}(t)$ can be estimated to be around 0.3 MV cm^{-1}.

The measurement of $S_{\mathrm{EO}}(t)$ as plotted in Fig. 5.14(b) appears to be different than the multi-shot (scanning) waveforms plotted in Figs. 5.5(a) and 5.5(b). The data in Fig. 5.14(b) was taken several months later, and subsequent changes in THz alignment did affect the measured THz profile. Also, the scanning data represented an averaged THz waveform. The shot-to-shot variations on the measured single-shot waveforms will be presented now.

Another set of data was obtained when a 200-μm-thick GaP was used for single-shot THz detection. The properties of GaP were presented in Sec. C.5.2. Just as for the ZnTe-based measurements, the probe beam polarization was circular, and the pulse length was 70 fs (intensity FWHM). The measured fequency-doubled intensity profiles were normalized to yield $M(t)$, from which the phase retardation $\Gamma_{\mathrm{cor}}(t)$ and EO signal $S_{\mathrm{EO}}(t)$ were derived. Several hundreds of single-shot waveforms were obtained, and three curves are presented now as representative for this data set.

The first single-shot measured waveform $\Gamma_{\mathrm{cor}}(t)$ is plotted as empty circles in Fig. 5.15(a), and was labeled as shot #8272. Figure 5.15(b) shows the Fourier-transformed retardation $|\Gamma_{\mathrm{cor}}(\nu)|$. Note that the spectrum of the EO signal falls within the 8-THz GaP spectral response limit. Coherent frequencies up to 6 THz were observed, and the temporal waveform was found to be near-single-cycle. Following Eq. (C.23), the EO field amplitude of $S_{\mathrm{EO}}(t)$ can be calculated. Based on $L = 200$ μm, $\lambda_0 = 800$ nm, $r_{41} \simeq 2 \times 10^{-12}$ m V^{-1} [91], and n=3.19, the field amplitude can be estimated to be $S_{\mathrm{EO}} \simeq 0.1$ MV cm^{-1}. Since surface reflection and dispersion account for a field reduction of $\times 0.25$, as estimated in Sec. C.5.2, the peak THz field at the location of the crystal can be approximated to be $E_{\mathrm{THz}} \simeq 0.4$ MV cm^{-1}. Note that the relation between $S_{\mathrm{EO}}(t)$ and $E_{\mathrm{THz}}(t)$ was defined by Eq. (C.30).

The temporal waveform of Fig. 5.15(a) indicates the presence of a second THz pulse,

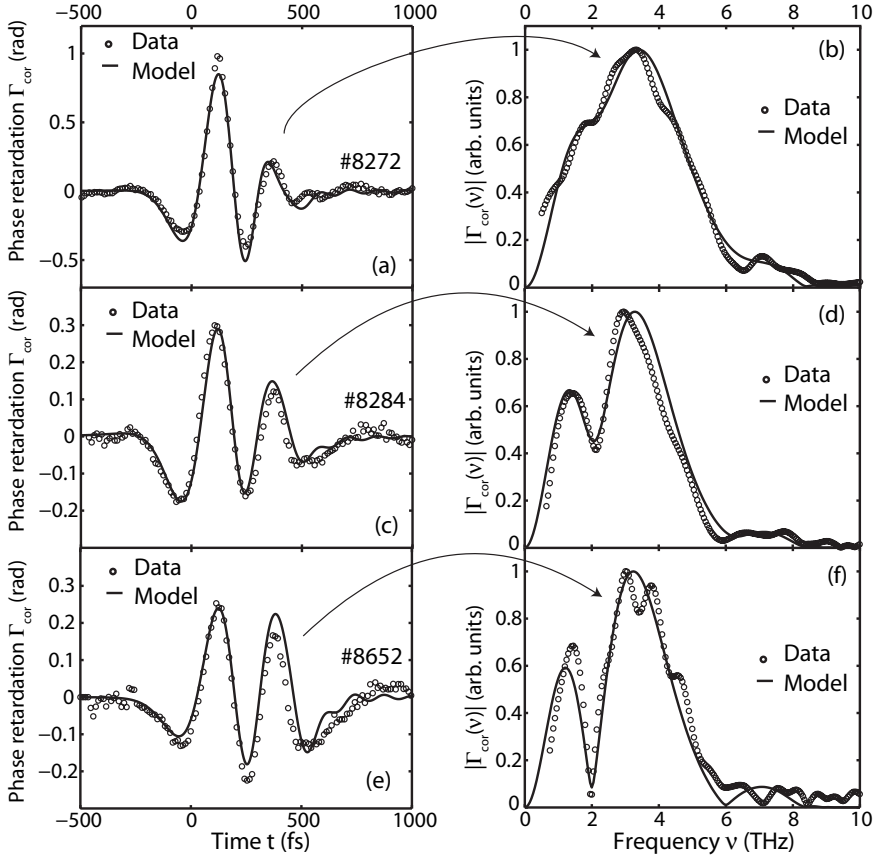

Fig. 5.15. Three measured (open circles) THz-induced retardation profiles $\Gamma_{\mathrm{cor}}(t)$, namely shot #8272 in plot (a), with corresponding Fourier-transformed spectrum $|\Gamma_{\mathrm{cor}}(\nu)|$ (empty circles) in plot (b), shot #8284 in plot (c), with its spectrum in plot (d), and shot #8652 in plot (e), with its spectrum in plot (f). Each set of temporal and spectral curves is also compared to a modeled curve, with the parameters for bunch length and transverse boundary size chosen for best agreement to the data. The THz radiation is modeled from a $40-50$ fs (rms) electron bunch, and a double-THz-pulse profile is assumed (delay of $230-250$ fs between both pulses). The relative field amplitude of the trailing THz pulse is 30% for the model in (a)-(b), 57% for (c)-(d), and 90% for (e)-(f). (Figure from Ref. [18].)

based on the observation of a second cycle around $t = 400$ fs. Note that if only one THz pulse were to be present, and considering the fast temporal response (plotted in Fig. C.8), the EOS waveform would not show a second positive feature. The presence of a double-THz-pulse field structure is more dominant in Fig. 5.15(c) for shot #8284, with the Fourier-transformed data plotted in 5.15(d), and even more strong in 5.15(e) or shot #8652, with the Fourier-transformed data plotted in 5.15(f). A strong spectral oscillation is clearly present in both Figs. 5.15(d) and (f). The fact that the measured temporal waveforms of Figs. 5.15(a), (c), and (e), show two positive peaks, and the fact that the spectra in Figs. 5.15(b), (d), and (f) show spectral interference, demonstrates the presence of two THz pulses. Chapter 6 will discuss the observation and understanding of the double-THz-pulse profile in more detail.

Each set of temporal and spectral waveforms Γ_{cor} was also compared to a modeled EO

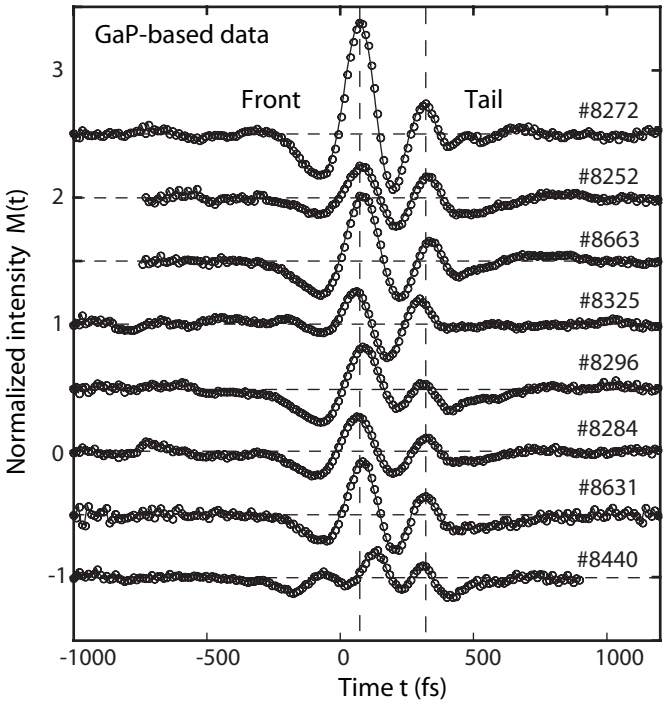

Fig. 5.16. Eight single-shot GaP-based EOS waveforms, represented as the normalized intensity profile $M(t)$, each offset by increments of 0.5 *for clarity. The shot number is listed for each measurement. The presence of the double-THz-profile is almost always present, with a relative stable pulse separation (see dashed vertical lines). The amplitude ratio displays more strong shot-to-shot variation.*

waveform, based on a double-THz-pulse profile. THz radiation from a 45-fs (rms) bunch was assumed. The value for the transverse boundary ρ in the model was also optimized to yield optimum agreement, with each value for ρ within the range $\rho \simeq 100 - 200$ μm, which was estimated based on plasma-density interferometry. For the shots #8272, #8284, and #8652, the parameters used for the model are a temporal separation of 230 fs, 240 fs, and 250 fs, respectively, and a relative field amplitude of the trailing pulse of 30%, 57%, and 90%, respectively.

In order to obtain a better understanding of the shot-to-shot variation (or stability) of the single-shot waveforms, 8 representative waveforms obtained within a 10-minute time period are plotted in Fig. 5.16 as connected circles. The vertical axis represents the normalized fequency-doubled modulated intensity $M(t)$, and each curve is offset by increments of 0.5 for clarity. One can observe from Fig. 5.16 that in seven of the eight curves (all but #8440), the double-THz-profile is present, with a fairly stable pulse separation as indicated by the two vertical dashed lines. For those seven shots, the standard deviation on the location of the leading maximum is found to be 9.7 fs. This demonstrates the excellent stability of the temporal synchronization between the lasers, electron bunch, and THz radiation. However, the amplitude ratio between the leading and trailing pulse varies more strongly, with for shot #8272 the leading pulse very strong, and for shots #8252 and #8325 both pulses more-equally strong. The last shot, shot #8440, indicates three oscillations of the electric

field. Chapter 6 will discuss the observation and understanding of the double-THz-pulse profile in more detail. The occasional appearance of more than two THz pulses (such as shot #8440) will be discussed as well.

5.4 Summary

This chapter, combined with Appendix C, introduced the THz-induced electro-optic modulation of laser pulses in a crystal. Optimum electro-optic sampling (EOS) is realized if the crystal axis z' is perpendicular to the THz field, and if the laser field is either parallel or perpendicular to z'. Crystal effects play an important role in the time resolution of EOS. Two crystal were used in the experiments, namely 200-μm-thick ZnTe and 200-μm-thick GaP, both cut along the $\langle 110 \rangle$ plane. The spectral response of ZnTe is 0–4 THz, resulting in a dispersed EO signal for broad-bandwidth THz pulses. The response of GaP is 0–8 THz, such that the single-cycle nature of an incident THz pulse (based on a 50 fs electron bunch) is conserved.

A scanning technique, where the delay was varied between the THz pulse and a short laser pulse, showed that coherent radiation up the 4-THz detection limit of ZnTe was emitted. Comparison between data and model indicated that bunches of sub-50 fs (rms) duration were emitted by the LWFA. The quality of the data demonstrated the stability of critical parameters for THz production such as bunch length and temporal synchronization between the laser, the electron beam, and the THz pulse.

Two single-shot techniques were demonstrated. With a spectral-encoding technique, the coherent THz spectrum was obtained in a single shot. The data, taken with both the ZnTe and GaP crystal, confirmed the LWFA production of 50 fs (rms) electron bunches. With a cross-correlator technique, the full temporal THz waveform (amplitude and phase) was recorded. Experiments with GaP showed that the coherent spectrum extended to $\simeq 6$ THz, with for some shots a temporal waveform close to a single-cycle shape. Based on experiments with GaP, peak THz fields of $\simeq 0.4$ MV cm^{-1} were demonstrated. The jitter in temporal synchronization between subsequent measured profiles was < 10 fs (standard deviation).

The single-shot experiments unambiguously indicated that a double-THz-pulse structure was incident on the EO crystal. In the time domain a second THz cycle was observed, while in the frequency domain spectral interference was present. The separation between both pulses appeared to be fixed (230–250 fs), although the relative amplitude ratio showed stronger shot-to-shot fluctuation. These findings led to the realization of 2D THz imaging, to be presented in Chapter 6. In the same chapter, a model will be presented, providing an explanation for the double-THz-pulse structure.

Chapter 6

THz imaging and spatio-temporal coupling

Abstract

Motivated by the measured temporal substructure in the THz waveforms, a single-shot 2D THz imaging technique has been developed. The transverse THz profile is found to consist of a dominant main spot and surrounding substructure. The main spot contains 58% of the total THz energy, with an intensity FWHM of 800 μm. The obtained images strongly suggest that diffraction, coma, and other aberrations are present in the THz imaging system. The combination of single-shot temporal and 2D characterization techniques, as demonstrated in this thesis, provides a unique environment to study spatio-temporal coupling of focused single-cycle waveforms.

A model based on ray-optics has calculated the spatio-temporal field evolution of a collection of rays, each defined as a single-cycle waveform with a Gaussian transverse field distribution. If no coma is present, the field profile at focus contains no spatial or temporal substructure. However, in the presence of coma, a double-THz-pulse profile is found, including interference in the spectral domain. The model indicates that an originally-single-cycle waveform appears as a double-pulse profile if diffraction, coma, and other aberrations are present. Since the optical THz path is fixed, the temporal and spatial features of the field profile are also expected to be fixed, just as observed in the single-shot temporal and spatial experiments. However, fluctuations in the THz angular emission distribution can result in relative amplitude fluctuations of the field substructure.

6.1 Introduction

In Sec. 5.3, the single-shot EOS data showed the existence of a double-THz-pulse structure. One possible reason for such a field profile is the LWFA-production of two electron bunches, each emitting a THz pulse. For example, a second phase of charge injection in the wake, at a certain distance behind the laser pulse, can be initiated through 2D transverse wave-breaking [63] or wave-breaking in a non-homogeneous density profile [61, 62]. However, experimental variation of the background plasma density and focal position of the laser pulse with respect to the gas jet, in conjunction with single-shot measurement of the electron energy, had no impact on the double-THz-pulse field structure, which remained unmodified. One would expect the THz pulse separation and field ratios to be strongly correlated to the plasma profile and accelerator performance if these wave-breaking effects were to be present. Since no such correlations were observed, it was concluded that the LWFA-production of two electrons bunches is not a likely scenario.

Another approach that was taken to better understand the temporal structure of the measured THz waveforms of Sec. 5.3 was to measure the transverse 2D THz pulse properties. Through a single-shot 2D EOS technique with femtosecond resolution, this goal has been realized, and the setup and results are discussed in Sec. 6.2. The 2D EOS technique [92] yields knowledge of the THz spot size and spatial structure. Future 2D THz imaging experiments will benefit from the availability of this technique.

The measured 2D THz profiles of Sec. 6.2, in combination with measured temporal THz waveforms from Sec. 5.3, indicate that diffraction, coma, and other aberrations are present in the THz imaging system. Through spatio-temporal coupling, the aberrations affect both the temporal and spatial measurement. In order to support these conclusions, a ray-based model is presented and discussed in Sec. 6.3. The model incorporates a collection of single-cycle rays, reflected by either a perfectly aligned or a coma-dominated off-axis parabola [93]. The conclusions from the model will be compared to the experimental observations.

A publication based on the results in this chapter is in preparation, titled

- *Single-shot spatio-temporal measurements of high-field terahertz pulses*, by J. van Tilborg, C.B. Schroeder, Cs. Tóth, C.G.R. Geddes, E. Esarey, and W.P. Leemans, Phys. Rev. Lett., submitted (2006)

6.2 THz imaging experiments

The setup for 2D characterization of LWFA-produced THz radiation is presented in Fig. 6.1. The arrangement of THz optics inside the target chamber is identical to the SCS experiments and can be found in Fig. 4.4, with explanatory comments in Sec. 4.3.1. The angular acceptance of OAP2 was depicted in Fig. 3.10. The properties of the LWFA-produced electron bunches were presented and discussed in Sec. 2.4.

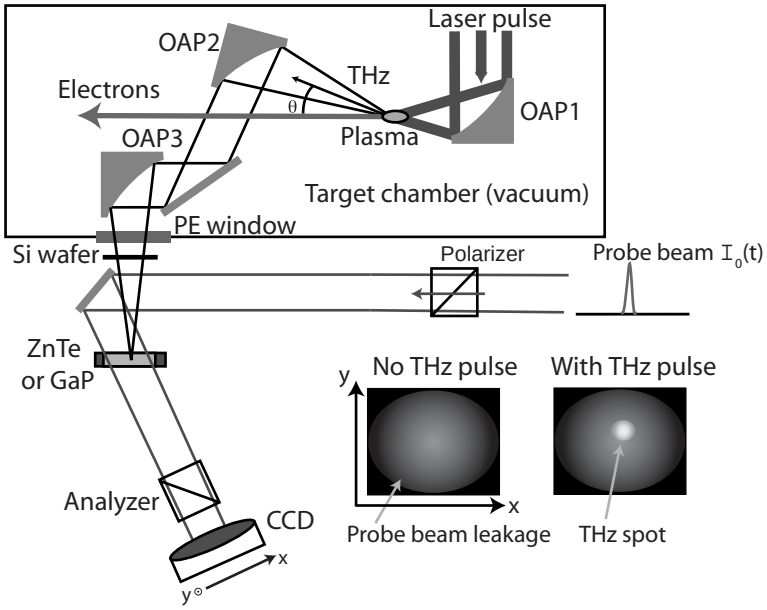

Fig. 6.1. Setup for 2D EO imaging. The probe beam is collimated and overfills the focused THz spot at the crystal plane. The 2D imprint of the THz pulse is recorded by a CCD camera. The cartoon on the bottom right shows the analyzer transmission in absence of a THz pulse (transverse probe beam profile, leaked through the analyzer), and in the presence of a THz pulse.

The setup of the optics outside the target chamber is based on the design for scanning EOS detection (see Fig. 5.2). However, several changes have been implemented, and a schematic of the 2D EOS setup is depicted in Fig. 6.1. The main modification with respect to Fig. 5.2 is that the probe beam $I_0(t)$ is not focused onto the EO crystal, but remains collimated such that it overfills the THz spot at the crystal plane. The probe beam length can be chosen to be longer than the THz pulse, or shorter for optimum temporal resolution. The collimated beam diameter was circa 7 mm (intensity FWHM). The EO crystal (ZnTe or GaP) had a transverse dimension of 10×10 mm. The probe beam was propagated through the analyzer and recorded by a CCD camera. Since both the crystal and transverse probe beam size were roughly equal to the dimension of the CCD array, imaging of the crystal surface was not necessary. Since the polarization state of the laser beam is not pure [see text following Eq. (C.17)], leakage through the analyzer will provide the image background (see left of the two images in the inset of Fig. 6.1). However, with the THz pulse present, a local imprint of the THz pulse on the transverse profile of the probe beam will be recorded (see right of the two images in the inset).

By subtracting the background image from the THz-induced image, a single-shot image $I_{2D}(x, y, \tau)$ is obtained. By assuming that the probe intensity is uniformly distributed over the region where the THz spot is present, it was derived in Sec. C.4 of Appendix C that the profile $I_{2D}(x, y, \tau)$ is related to the original THz field $E_{\mathrm{THz}}(t)$ through

$$I_{2\mathrm{D}}(x, y, \tau) \propto \int \sin^2 [\Gamma^*(x, y, t)/2] I_0(t - \tau) dt, \tag{6.1}$$

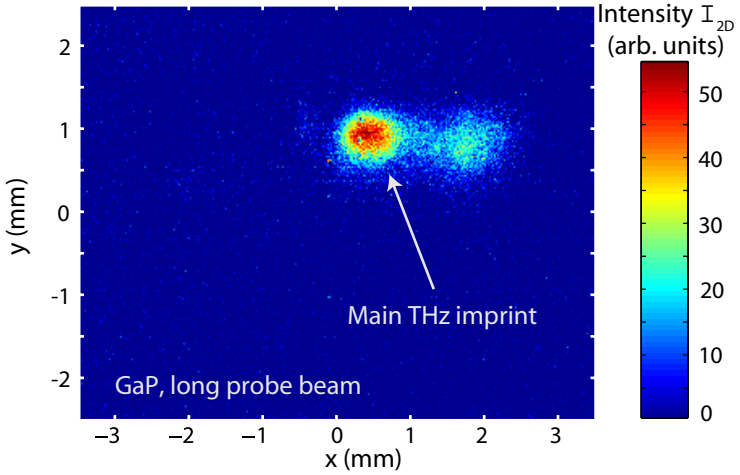

Fig. 6.2. Image $I_{2D}(x, y, \tau)$ obtained with the single-shot 2D EO detection technique, based on GaP. For this measurement, the probe beam was stretched to 1.8 ps (intensity FWHM). The image appears to consist of two spots, with the left one (labeled main spot) the most intense. The main spot, with an intensity FWHM of 800 μm, contains 58% of the total transmitted probe pulse intensity.

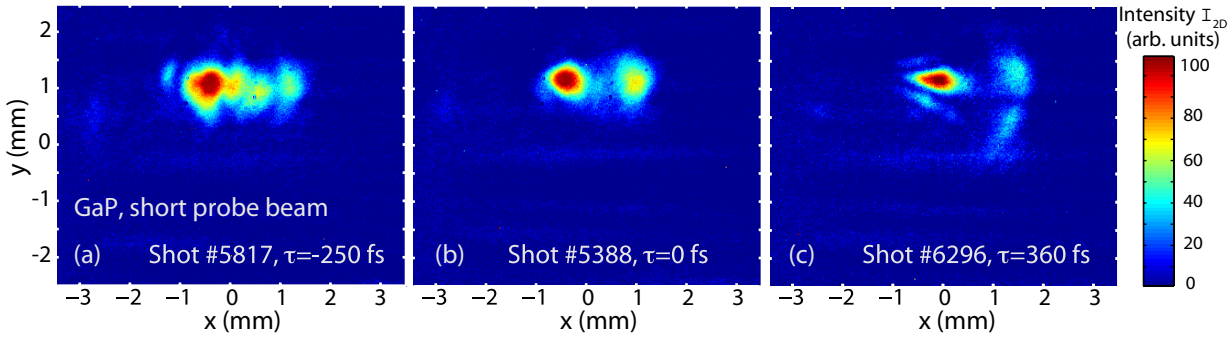

Fig. 6.3. Three characteristic 2D EO images $I_{2D}(x, y, \tau)$, obtained through propagation of a short 60-fs-long (intensity FWHM) probe beam through a GaP crystal. The delay between probe and THz pulse was (a) $\tau = -250$ fs, (b) $\tau = 0$ fs, and (c) $\tau = 360$ fs. The 2D profile of the images varied with respect to delay (spatio-temporal coupling), with effects from aberrations such as diffraction and coma playing a role in the image substructure. (Figure from Ref. [18].)

where $\Gamma^*(t)$ represents the convolution of the THz field $E_{\mathrm{THz}}(t)$ and crystal effects, as presented in Eq. (C.18). The delay τ between the THz pulse and probe beam can be varied with a delay stage.

One has the option of adding a $\lambda/4$ plate in the setup of Fig. 6.1 in order to provide elliptical or circular polarized laser light. Since the $\lambda/4$ plate was not installed in these experiments, sign-resolved information was not present (see discussion in Sec. C.2).

In one set of experiments, based on 200-μm-thick GaP, the probe beam was stretched to 1.8 ps (intensity FWHM) such that the entire THz pulse fell within the laser pulse envelope. A characteristic image [transmitted intensity $I_{2D}(x, y, \tau)$] is shown in Fig. 6.2. One can distinguish two THz spots, with the left one the most intense spot, therefore

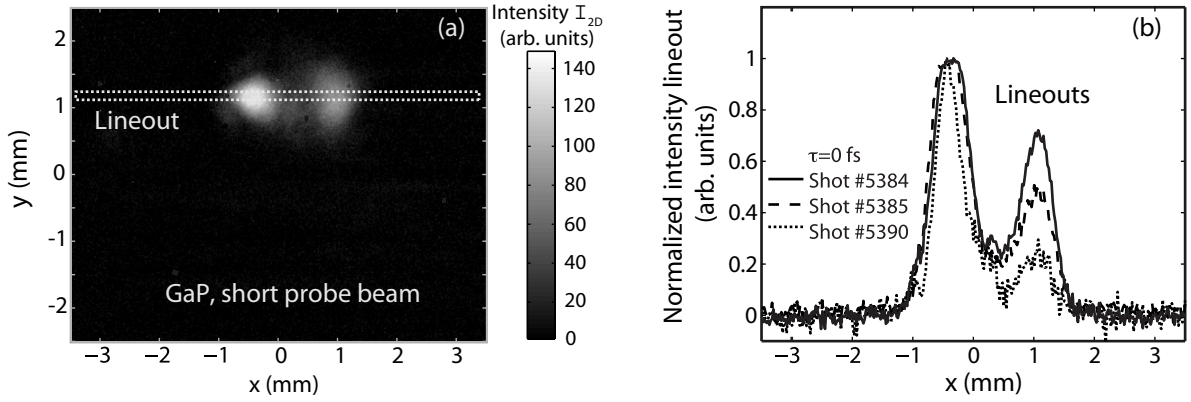

Fig. 6.4. At a fixed delay position $\tau = 0$ fs, lineouts of three single-shot images are compared. The position of the lineout is depicted in (a) as the dashed rectangle. The transverse intensity distribution (along x) for the three different shots is plotted in (b). Each curve is normalized to yield a maximum of 1*. The curves clearly show the presence of a double-spot structure. Although the location of the second spot (right spot) is fixed, its relative amplitude fluctuated. (Figure from Ref. [18].)*

labeled as main spot. The position of the main spot was stable on a shot-to-shot basis, although the position of the second spot (on the right) moved up-down on the order of a spot size. Details on the shot-to-shot stability of the THz profile will be discussed in the next paragraph, where a shorter probe beam is used. From Fig. 6.2 one can calculate that 58% of the total THz energy was concentrated within a circle of radius 475 μm, positioned around the center of the main spot. The intensity FWHM of the main THz imprint is $\simeq 800$ μm.

In order to study the temporal evolution of the structure of the transverse THz profile, such as the double spot in Fig. 6.2, the probe pulse length was compressed to 60 fs (intensity FWHM) in a second set of experiments. The timing between the probe pulse and THz pulse was scanned, yielding a spatio-temporal measurement. Three images are shown in Fig. 6.3, all based on EO imaging with 200-μm-thick GaP. Each image is characteristic for the spatial THz profile at that specific delay position. It was found that, at different delays τ, the 2D image profile changed in identity. In other words, a coupling between space and time is present. While Fig. 6.3(a) shows various concentrations of more-vertical substructure (more likely related to diffraction effects), Fig. 6.3(b) shows only a single secondary THz imprint, and Fig. 6.3(c) contains more characteristic features of the coma aberration [93]. Note that diffraction effects are inevitable since the LWFA-produced THz radiation is overfilling the collection parabola OAP2, see Fig. 6.1. Coma and other aberrations can be present if the THz imaging system is imperfect. Note that the lower-intensity horizontal lines in the images of Figs. 6.3(a)-(c) are not related to the THz field, but are an artifact of local stress-induced crystal birefringence.

At the fixed delay $\tau = 0$ fs between the THz and laser pulse, three characteristic images are compared by taking a horizontal lineout. Each image was obtained with the short probe

beam, and using the 200-μm-thick GaP crystal. The location of the lineout is indicated in Fig. 6.4(a). The dashed rectangle defines an area of 5 pixels (vertical) by 320 pixels (7 mm, horizontal); the lineout is defined as the sum of the 5 different 7-mm-long intensity profiles. Each lineout is normalized to yield a maximum of 1. The three lineouts are plotted in Fig. 6.4(b). The location of the second (right) THz imprint is relatively fixed, with a separation between both pulses around 1.5 mm. However, the relative amplitude of the second spot fluctuates from 30% for shot #5390 to 70% for shot #5390. The possible contributions to the fluctuation in intensity of the THz spatial substructure will be discussed in Sec. 6.4.

The presence of 2D THz substructure, as shown in Figs. 6.3 and 6.4 strongly suggests that aberrations in the THz optical path are present. Signatures of diffraction and coma [93] were observed. It is believed that through spatio-temporal coupling, the temporal profile of the THz pulse is modified as well. The single-shot temporal THz data presented in Sec. 5.3, see for example Fig. 5.15, also indicated substructure. In the latter experiments, the laser pulse was focused to a small spot (radius $r_0 \simeq 50 - 100$ μm), such that only the temporal profile was measured. Both the single-shot temporal and 2D THz observations indicate that the presence of the substructure is fixed in terms of temporal delay and spatial separation: a strong indication that aberrations in a fixed optical path are present.

In order to support the claim that the temporal and 2D waveforms are linked through spatio-temporal coupling, a model is presented here. The model is not implemented to match the EOS results in detail, but rather to demonstrate that alignment imperfections and other aberrations can indeed result in spatio-temporal-coupled field substructure of single-cycle pulses.

6.3 Spatio-temporal coupling: a ray-based model

Although several groups have studied the focusing of broad-bandwidth EM pulses [51–53, 94–98], a more simple ray optics approach is taken here. Note that this approach only yields a heuristic picture into spatio-temporal coupling since effects such as the frequency-dependent Rayleigh range and broad-bandwidth-induced dispersion [52, 94, 95] are not included.

Spatio-temporal coupling of broad-bandwidth pulses was studied for a collection of rays propagating through an optical path in the presence of coma. Coma was induced through misalignment of a parabola. As Fig. 6.5(a) indicates, if the rays are incident on a 90°-off-axis parabola, with the center ray at 45° angle of incidence, all the rays intersect at a specific focal spot. However, if the parabola is tilted by angle κ, the various rays do not intersect at one location anymore. Rather, a more-complex spatial field distribution is expected. The temporal and spatial field profiles in such a coma-dominated focal volume will be presented now.

The EM field in a 2D geometry is defined at a longitudinal coordinate z and a transverse

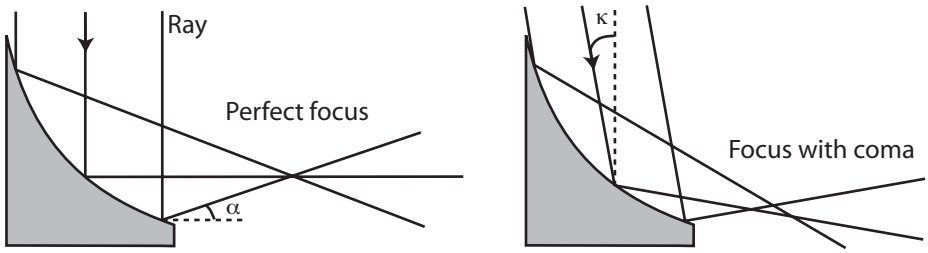

Fig. 6.5. (a) If a collection of rays is incident on a 90°-off-axis parabola, with the center ray at an angle of incidence of 45°, a perfect focus is achieved. However, if the parabola is rotated by angle κ, see (b), the rays do not intersect at the same location anymore [93]. This leads to aberrations in both the temporal and spatial domain.

coordinate r. The temporal field profile $E(r, z, t)$ for each ray is defined as

$$E(r,z,t) = \exp\left[-\frac{r^2}{\sigma_r^2}\right] \times \exp\left[-\frac{(t-\frac{z}{c})^2}{2\sigma_t^2}\right] \times \left[1 - \frac{(t-\frac{z}{c})^2}{\sigma_t^2}\right], \tag{6.2}$$

with σ_r and σ_t the transverse and longitudinal pulse size, respectively. The temporal profile is based on the THz emission profile expressed by Eq. (3.27). Each ray, after being reflected by the parabola, makes a ray-specific angle α with respect to the z axis. The angle α is depicted in Figs. 6.5 and 6.6(a), where the field profile of one ray at a specific time is shown. Figure 6.6(a) indicates both the Gaussian transverse field distribution and the single-cycle temporal (longitudinal) field profile. If the ray propagates at angle α, the transformations $r \rightarrow (r\cos\alpha - z\sin\alpha)$ and $z \rightarrow (z\cos\alpha + r\sin\alpha)$ are applied to Eq. (6.2).

Figure 6.6(b) shows the field profile $E(r, z)$ for a collection of 15 rays at a given time t, using the perfectly aligned parabola. The rays are defined to be collimated when incident on the parabola, see Fig. 6.5. The rays are uniformly distributed over the parabola acceptance, with had a diameter of $10\sigma_r$. The ratio of $\sigma_r/(c\sigma_t)$ was chosen to be 3, and the focal length of the parabola was set at $30c\sigma_t$. The path length for each ray was taken into account in order to calculate the correct cumulative field profile. Since the field profile in Fig. 6.6(b) is plotted at a time where focus has not been reached yet, a curved phase front can be seen.

In order to study the temporal evolution of the EM pulse through focus, the field profile $E(r, z)$ is calculated at various time steps. Figure 6.7(a) shows the field profile in case of a perfectly aligned parabola, at times $t/\sigma_t = -18,\ -9,\ 0,\ 9$, and 18. As one can see, the pulses propagates through focus, with the maximum field strength reached at focus. The single-cycle temporal identity of the rays is conserved.

To mimic the effect of the coma, the parabola is rotated by κ=0.4 rad. If the individual fields of the rays are now added, a series of 5 field profiles $E(r, z)$ at various time steps can be constructed, see Fig. 6.7(a). Note that the profiles in Figs. 6.7(a) and 6.7(b) do not significantly change if more rays were defined. The EM pulse evolution in Fig. 6.7(a) demonstrates the effect of coma. Since the individual rays do not cross at the same location,

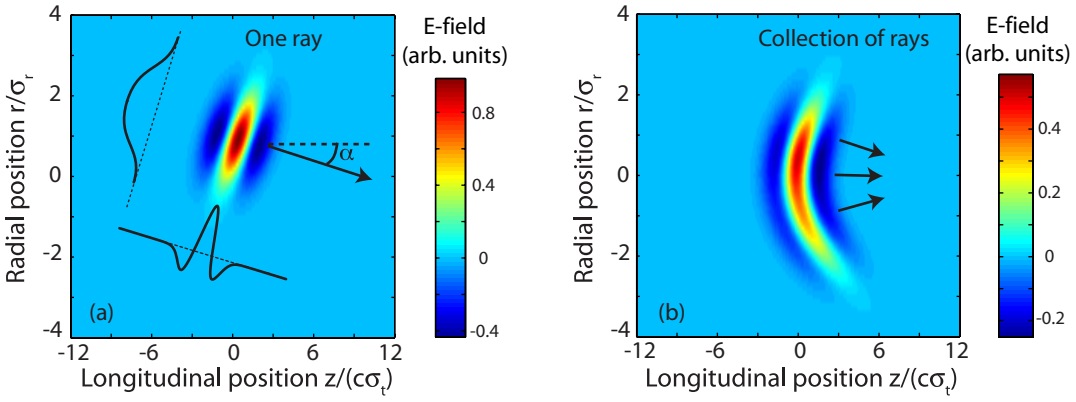

Fig. 6.6. (a) The field profile $E(r, z)$ of a single ray, which is defined to be Gaussian-shaped in the transverse direction. The temporal field dependence is single-cycle. (b) Field profile of a collection of 15 rays reflected from a perfectly aligned 90°-off-axis parabola. Since focus has not been reached yet, the phase front of the field profile is curved.

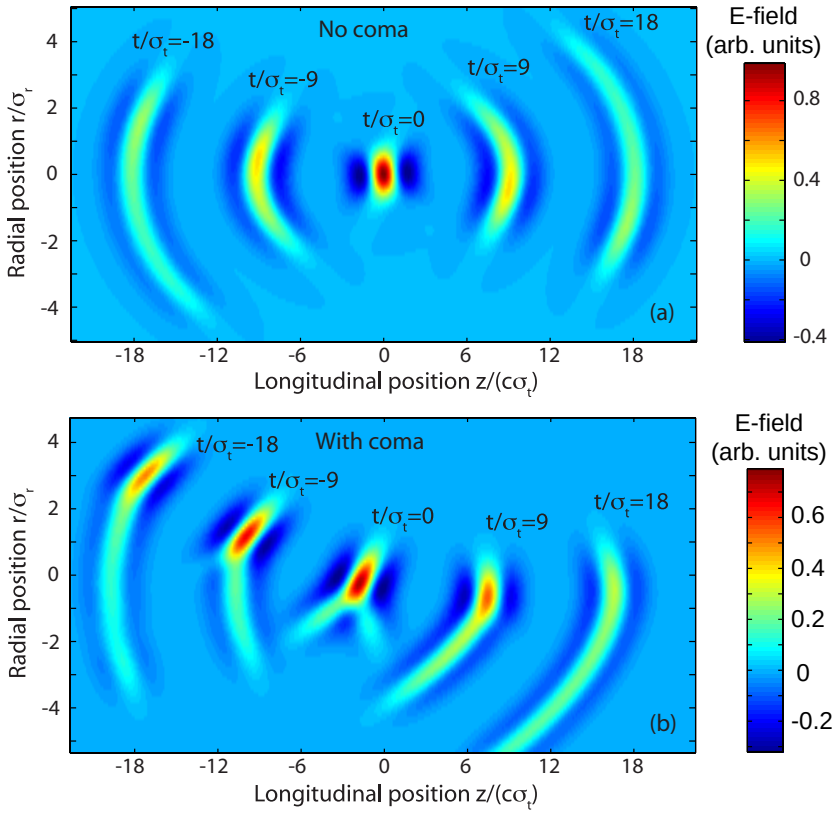

Fig. 6.7. (a) The EM field profile $E(r, z)$ at 5 different time steps, assuming a perfectly aligned parabola. The EM pulse is propagating through focus, and the single-cycle nature of the EM field is conserved. (b) In case of a coma-dominated optical path ($\kappa = 0.4$ rad), the individual rays do not intersect at one fixed location. This results in the appearance of a more-complex transverse and longitudinal (∼temporal) field profile as the EM pulse propagates though the focal volume. The appearance of a double-EM-pulse profile is initiated around $t/\sigma_t = -9$. (Figure from Ref. [18].)

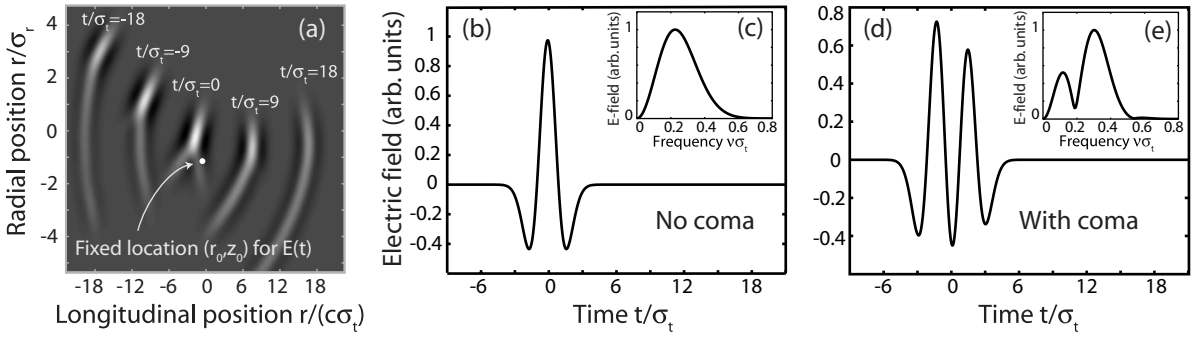

Fig. 6.8. (a) At a fixed location (r_0, z_0) the temporal evolution of the electric field $E(t) = E(r_0, z_0, t)$ is calculated with the ray-based model. Without the presence of coma, the field profiles in the time domain $E(t)$ and frequency domain $|E(\nu)|$ are shown in plots (b) and (c), respectively. The single-cycle nature of the EM pulse is conserved at focus. However, in the presence of coma ($\kappa = 0.4$ rad), the profiles for (d) $E(t)$ and (e) $|E(\nu)|$ are modified. Due to spatio-temporal coupling, a double-EM-field profile is observed, containing spectral interference. The double-pulse separation is a function of the location of (r_0, z_0). (Figure from Ref. [18].)

a more-complex transverse and longitudinal (∼temporal) field profile is found. The EM field profile appears to split up in two profiles as the pulse propagates through focus.

In analogy to a probe beam that is focused in a tiny area within the THz spot, which is the case in the temporal EOS experiments of Chapter 5, the EM field time profile $E(t)$ at a fixed location (r_0, z_0) will be considered now. First $E(t)$ for a perfectly aligned parabola, see Fig. 6.7(a), is considered. At over 100 different time steps, the EM field at $r_0/\sigma_r = -1$ and $z_0 = 0$ is recorded. The temporal profile $E(t)$ is plotted in Fig. 6.8(b), with the Fourier transformation $|E(\nu)|$ in Fig. 6.8(c). Since the parabola was perfectly aligned, the temporal waveform at focus resembled a single-cycle waveform. In the case of the coma-dominated parabola alignment, the field profile $E(t)$ at $r_0/\sigma_r = -1$ and $z_0 = 0$ is shown in Fig. 6.8(d), with the Fourier-transformation in Fig. 6.8(e). The location of $r_0/\sigma_r = -1$ and $z = 0$ is shown in Fig. 6.8(a). As predicted, the effect of the coma is an appearance of a second radiation pulse. The temporal waveform $E(t)$ indicates two peaks, and the spectral field profile $|E(\nu)|$ contains spectral interference. If the position (r_0, z_0) is moved up or down, the respective delay between both pulse will decrease or increase, respectively.

The next section will summarize the experimental results on 2D THz imaging, and provide a discussion on the relationship between the data and the observations from the ray-based model.

6.4 Discussion and conclusions

Knowledge of the temporal and 2D field profiles of THz pulses at focus is crucial if the THz pulses are used for detailed electron bunch analysis or for high-field THz pump-probe studies. Only through complete understanding of the THz imaging can the detailed charge profile (including asymmetries such as skew) be reconstructed.

An experimental setup, based on electro-optic sampling (EOS), was realized in order to obtain single-shot 2D THz field profiles. If the laser pulse is long compared to the THz pulse, the measurement allows for the determination of the THz spot size. It was found that the THz spot consists of a main circular-shaped spot with lower-intensity substructure. Within a circle of radius of 475 μm (overfilling the main spot), circa 58% of the THz energy is concentrated. The intensity FWHM of the main spot was measured to be 800 μm.

Through compression of the probe pulse to 60 fs (intensity FWHM), the temporal evolution of the 2D THz profile was recorded. The substructure on the 2D field profile was found to be a function of temporal location of the probe beam with respect to the THz pulse. At a fixed time slice, the shape of the 2D THz profile (main spot and substructure) was constant, although the relative amplitude fluctuated more strongly. The detailed images indicated that diffraction and aberrations such as coma were present in the THz optical imaging system.

Through a 2D ray model (longitudinal z and transverse r axes), the effect of coma on the spatio-temporal field profile was studied. Each ray was defined as a single-cycle THz waveform, with a finite radial spot size. In case of a perfectly aligned parabola, the field profile of a collection of rays was found to constructively interfere to a nice focal spot. At a fixed location (r_0, z_0), the modeled field profile $E(t)$ remained single cycle. However, in case of a coma-dominated optical alignment, the various rays do not intersect at the same location. The superposition of the fields results in transverse and longitudinal (temporal) substructure. At a fixed location (r_0, z_0) the field profile $E(t)$ showed two pulses, and the spectrum $|E(\nu)|$ indicated spectral interference.

The parameters used for the ray-based model were not chosen to match the experimental parameters of this thesis. However, what the model did show is that coma results in spatio-temporal coupling. In case of broad-bandwidth pulses, such as the THz pulse, the coma affects both the 2D spot profile as well as the temporal profile. This conclusion can be extended to diffraction and other aberrations as well.

It is strongly believed that the artifacts in the THz beam path are responsible for the measured 2D THz profiles of Figs. 6.3 and 6.4. The reproducibility of the substructure profile is in line with the presence of a fixed optical beam path with imperfections. The single-shot temporal measurements of Figs. 5.15 and 5.16 also demonstrated the presence of temporal substructure at a fixed temporal location.

The single-shot temporal and 2D EOS data did indicate that the amplitude of the substructure was more unstable. Although the performance of the LWFA is stable in terms of bunch length and temporal synchronization, as discussed in Sec. 5.2.2, it is believed that fluctuations in the electron bunch momentum distribution and electron bunch pointing are present. These fluctuations do not affect the THz emission in terms of total energy, but they do affect the angular distribution of the radiation. Since the THz collection parabola OAP2 sits at a fixed position, the fluctuations in angular THz distribution can result in a fluctuation in the strength of the aberration. In other words, while the fixed THz beam

line determines the spatial and temporal features of the aberration, the jitter in THz profile incident onto the THz beam line can result in the jitter of the strength of the aberration effects. It is likely that a specific angular emission pattern (in combination with diffraction, coma, and other aberrations) could even lead to triple- or multi-THz-pulse profiles.

Future research will aim at understanding the spatio-temporal coupling in more detail. Through control of the aberrations (*e.g.* motors, stages), in combination with the single-shot temporal and 2D EOS techniques, the focal properties of single-cycle broad-bandwidth THz pulses can be better understood and optimized.

Chapter 7

Discussion and conclusions

This thesis presented both the theoretical and experimental treatment of THz radiation produced by electron bunches from the laser wakefield accelerator (LWFA). The work has been performed at the Lawrence Berkeley National Laboratory in Berkeley, California. A 10 TW laser system (50 fs laser pulse duration) was operated to produce the electron and THz beams.

Originally proposed by Tajima and Dawson [5], the interaction of an intense laser pulse with a plasma results in the generation of plasma density oscillations (plasma waves). Background electrons can get trapped in the wave and accelerated to relativistic energies. As the electron bunches exit the plasma through the plasma-vacuum interface, coherent transition radiation (CTR) at THz frequencies is emitted. The interest for LWFA-produced THz radiation is related to two topics:

- Although electron bunch parameters such as charge, bunch energy, and bunch divergence, have been characterized extensively, little was known about the bunch duration. Direct proof of the femtosecond bunch duration (and femtosecond synchronization to the laser) is a key goal for the LWFA community. It demonstrates the production of high-quality bunches as well as the applicability of the LWFA for femtosecond pump-probe applications. This proof can be delivered through the analysis of LWFA-produced THz radiation (CTR).

- Since the LWFA-produced electron bunch contains over 10^{10} electrons at femtosecond duration, the emitted THz radiation can be 1–2 orders of magnitude more intense than from conventional laser-based THz sources (*e.g.* optical rectification or the photoconductive antenna). LWFA-produced THz pulses with (possible) energies over > 10 μJ and peak fields at several MV cm^{-1} provide a unique source for high-field THz applications.

The focus of this thesis was the characterization of THz radiation emitted by electron bunches produced in the self-modulated LWFA regime (SM-LWFA), where the laser pulse is longer than the plasma period ($L \gtrsim \lambda_p$). Chapter 2 showed that, for the unchanneled

SM-LWFA (no externally-produced laser guiding profile), the energy distribution $g(E)$ of the electron bunch can be described by a Boltzmann distribution $g(E) \propto \exp(-E/E_t)$, with $E_t \simeq 4-5$ MeV. The bunch divergence is typically 25–50 mrad (half-angle), and the bunch contains over 10^{10} electrons. At the plasma-vacuum interface, the transverse electron bunch size is still smaller than the longitudinal bunch size since bunch divergence and space charge effects have not led to bunch blow-up over such a short propagation distance (< 1 mm). In Chapter 3, a model was developed to calculate the THz emission from the LWFA-produced electron bunch as it passes through the plasma-vacuum interface. The model is based on the emission of CTR by electrons propagating through a sharp metal-vacuum boundary. The following conclusions were reached:

- Although the dielectric environment of the non-sharp plasma-vacuum boundary changes from over-critical ($\epsilon < 0$) to $\epsilon = 1$, the effective emission plane is located at the plasma density corresponding to $\epsilon \simeq 0.8$. The plasma-vacuum interface can be approximated as a sharp boundary (step boundary), since the plasma gradient length is smaller than the radiation formation length L_{form}, which is on the order of $\gtrsim 1$ mm. Furthermore, it was validated that the plasma-vacuum boundary can be analytically treated as a metal-vacuum boundary.

- The CTR emission of femtosecond bunches lies in the THz regime, with the spectrum typically at $\nu \simeq$0-10 THz, with $\lambda = c/\nu$. The spectrum is broad bandwidth, and the THz pulses are of single-cycle nature. The THz emission is radially polarized.

- The total emitted THz energy can exceed > 10 μJ, resulting in a peak electric field of > 1 MV cm^{-1} at focus. However, diffraction effects related to the finite transverse boundary size (typically $\rho = 100-200$ μm for the plasma) have to be considered. Also, limited collection capabilities of the setup further reduce the total collected energy.

Experiments involving a bolometer (energy detector) provided a basic insight of the THz characteristics. Several different geometries for the THz collection setup were realized. Chapter 4 discussed the following findings:

- The total measured THz energy scaled quadratically with bunch charge, as predicted for coherent radiation. The rotation of a polarizer in the THz beam path did not affect the measured THz energy, in agreement with the predicted radial polarization state.

- At two different collection geometries, the THz pulse energy was measured to be 4 nJ and 80 nJ, with the first value in agreement with a model (including geometrical and diffraction effects).

- Semiconductor switching was employed, where the THz pulse and a laser pulse were both incident on a semiconductor. The transmitted THz energy was measured while the delay between the laser and THz pulse was scanned. This method allowed for temporal synchronization of both pulses, and demonstrated the femtosecond duration of the THz pulse.

With an electro-optic sampling (EOS) technique, the temporal profile and spectrum of the THz pulse was measured in more detail. For EOS, the change in crystal birefringence, induced by the THz pulse, is probed by a laser pulse. In order to compare the EOS data to a model, crystal effects such as absorption, dispersion, and velocity mismatch were considered. Both a scanning technique, where the delay between the short laser pulse and the THz pulse was scanned, and two single-shot techniques, based on EOS with a chirped laser pulse, were realized. 200-μm-thick ZnTe (response 0–4 THz) and GaP (response 0–8 THz) crystals were used. The results, presented in Chapter 5, led to the following conclusions:

- The EOS data demonstrated the production of femtosecond THz pulses with a coherent spectrum extending to $\simeq$6 THz. Comparison to a model indicated that the electron bunches were of $<$50 fs (rms) duration.

- The scanning data demonstrated the excellent LWFA stability in terms of parameters important to THz emission such as electron bunch length and temporal synchronization.

- A spectral-encoding technique allowed for the single-shot determination of the coherent spectrum with a resolution only limited to the laser pulse length.

- A cross-correlation technique allowed for single-shot temporal THz characterization (amplitude and phase) with fast time resolution ($\sim$ laser pulse length). For several shots, waveforms with near-single-cycle field profiles and peak fields on the order of 0.4 MV cm^{-1} (at the location of the crystal) were observed.

- The single-shot data showed that a double-THz-pulse profile was present. Waveforms consisting of two positive peaks (and spectral interference) led to this conclusion. The temporal separation between both THz pulses was stable at 230–250 fs, although the relative amplitude showed a stronger shot-to-shot fluctuation.

One possible explanation for the double-THz-pulse field profile is the LWFA-production of two electron bunches, each emitting a THz pulse. However, experiments indicated no correlation between the double-THz-pulse characteristics and accelerator parameters such as plasma profile and electron energy (as would be expected for double-electron-bunch-producing mechanisms). It was concluded that the LWFA-production of two electrons

bunches is not a likely scenario. Instead, another approach was taken, in which a single-shot 2D THz imaging technique was developed. The results, presented in Chapter 6, led to a series of conclusions:

- The 2D imprint of the focused THz pulse showed that the main THz spot had a (intensity) FWHM of 800 μm, containing $\simeq$60% of the total THz energy.
- The time-resolved imaging technique revealed spatio-temporal coupling. At a given temporal delay between the THz and laser beam, stable THz substructure was observed, indicating that diffraction, coma, and other aberrations are present in the THz beam path. The relative intensity of the substructure fluctuated shot-to-shot. By scanning the temporal delay, the shape of the substructure evolved.

In order to offer an explanation for the observed double-THz-pulse temporal profile and the spatial substructure, a 1D-transverse ray-optics model was developed (*c.f.* Chapter 6). The model was based on a collection of rays, each consisting of a single-cycle EM field profile with a finite radius. A 90°-off-axis parabola with or without coma was considered. The model led to the following conclusions:

- During the EM pulse propagation through the focal volume, the coma induced spatio-temporal coupling: in addition to spatial substructure also a double-EM-pulse temporal field profile evolved over time. At a fixed location, the modeled temporal field profile showed two EM pulses (including spectral beating).
- Although the model was not designed to match the parameters of the experiments in detail, it did demonstrate the spatio-temporal coupling for single-cycle waveforms when propagating through a focal volume in the presence of aberrations.
- Since the aberrations are related to the fixed optical beam path, the effect in terms of temporal and spatial structure location are expected to be fixed (just as observed in the experiments). However, due to experimental fluctuations in electron bunch energy and pointing, the angular THz emission profile is expected to fluctuate. These fluctuations are suggested to affect the relative intensity of the THz substructure.

Note that electron bunch characterization through analysis of THz emission is one of the key goals (see Sec. 1.3) for THz-related research, as presented in this thesis. In order to obtain detailed information on the temporal electron bunch profile (including asymmetries), it is crucial to understand the spatio-temporal coupling at focus of the THz pulses that are emitted by these bunches. Similarly, the coupling affects results from high-field THz pump-probe studies. Several ideas for future experiments and modeling can be thought of, as listed below:

- Through improved control of the THz beam line, more insight in the spatio-temporal coupling can be obtained. The imperfections in the beam line could be eliminated.

- The production of channel-guided elcetron bunches was already demonstrated by Geddes *et al.* [14]. An all-optical guiding mechanism allowed for production of high-quality electron bunches. Bunches with an energy of $\simeq 86$ MeV, energy spread of a few percent, and bunch divergence of a few mrad, were demonstrated (containing over 2×10^9 electrons). Since the spatial coherence of these low-divergence bunches is conserved over a longer distance, strong THz emission is expected by propagation of these bunches through a metallic foil. In this case, diffraction effects are limited and the angular collection can be improved. Focusing of the THz emission could lead to peak THz fields of > 1 MV cm^{-1}.

- The strong THz fields, currently at $\simeq 0.4$ MV cm^{-1} and possibly higher in the future, can be applied in experiments where the THz pulse serves as a strong pump pulse. THz-induced ionization and carrier dynamics in semi- and superconductors are possible applications.

A final conclusion can be made regarding THz emission from laser-plasma-based sources other than CTR emission. Section 1.3 introduced several alternative emission mechanisms. Through linear-mode conversion [42, 43], THz is emitted at the front vacuum-plasma interface, while resonant wake excitation [38, 39] emits radiation consisting of multiple cycles at the plasma frequency ($\nu_p = c/\lambda_p \simeq 50$ THz for the plasma described in this thesis). Cerenkov radiation is emitted by propagation of an electron bunch through a magnetized plasma [40, 41]. The measured radiation described in this thesis was emitted from the back plasma-vacuum surface, with no external magnetic fields applied. Its scaling with charge and polarization, its broad-bandwidth spectrum in the 0–10 THz domain, its near-single-cycle field profile, and its agreement to a CTR-based model, unambiguously demonstrate that the observed THz radiation was emitted by the LWFA-produced electron bunch propagating through the plasma-vacuum boundary (CTR).

Appendix A

Bolometer basics

A bolometer is a sensitive device that can measure low levels of electro-magnetic radiation ($< 10^{-14}$ J). A good overview of bolometer-based detection has been written by Richards [99]. The response of the bolometer to an ultra-short electro-magnetic signal will be presented here.

Consider a resistor connected to a heat sink at temperature T_s, with constant current I_0 passing through, see Fig. A.1(a). If no radiation is present, and the system is in equilibrium, the temperature of the resistor is T_0, with $T_0 > T_s$. The value for T_0 can be calculated by balancing the power loss to the heat sink $G(T_0 - T_s)$, with G the thermal conductance, to the Ohmic heating in the circuit $I_0^2 R_0$, with R_0 the resistance at temperature T_0. This leads to

$$T_0 = \frac{I_0^2 R_0}{G} + T_s. \tag{A.1}$$

Now consider radiation with a power profile $P(t)$ incident on the resistor, as depicted in Fig. A.1(b). Because of this extra energy flow, the temperature of the resistor will increase. At a given time t the resistor temperature can be defined as $T(t) = T_0 + f(t)$, such that the resistance is given by $R(T_0 + f) \simeq R_0 + \frac{dR}{dT}|_{T=T_0} f$. If $P(t) \neq 0$, the energy loss to the heat sink is less than the energy gained from Ohmic heating and radiation absorption. The net power absorption ΔP results in a temperature increase $f'(t)$ given by $\Delta P = C f'(t)$, with C the heat capacity. Conservation of energy requires that

$$C f'(t) = P(t) + I_0^2 R_0 + I_0^2 \frac{dR}{dT} f(t) - G\left(T_0 + f(t) - T_s\right). \tag{A.2}$$

The homogeneous solution, such that $P(t) = 0$, to Eq. (A.2) is $f(t) \propto \exp\left(-t/\tau\right)$, with response time $\tau = C/(G - I_0^2 \frac{dR}{dT})$.

For simplicity, it is assumed that the incident radiation has the profile $P(t) = P$ for $0 < t < t_L$, and $P(t) = 0$ otherwise, with $t_L \ll \tau$. At time $t < 0$, Eq. (A.2) yields $f(t) = 0$, and at times $t > t_L$ one can find the solution $f(t) = c_0 \exp\left(-t/\tau\right)$, with c_0 a constant. In the time interval $0 < t < t_L$, the solution to Eq. (A.2) is

$$f(t) = \frac{P}{G - I_0^2 \frac{dR}{dT}} \left[1 - \exp\left(-t/\tau\right)\right] = \frac{P\tau}{C} \left[1 - \exp\left(-t/\tau\right)\right], \tag{A.3}$$

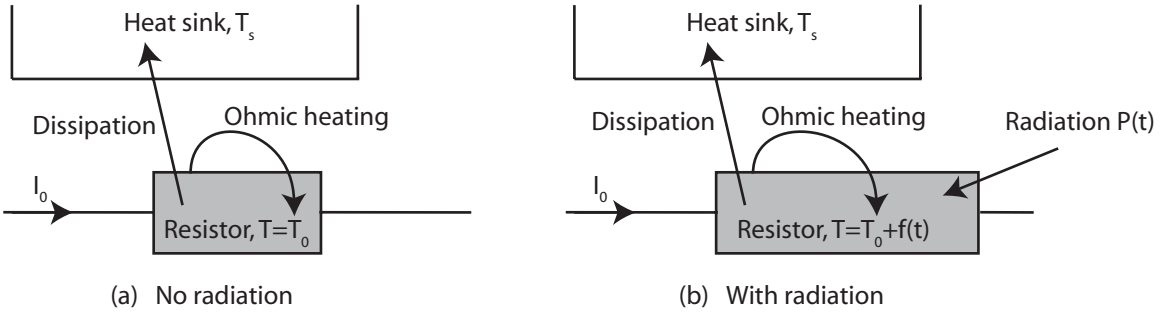

Fig. A.1. Radiation detection principle of a bolometer. (a) With no radiation present, the temperature of a resistor is in thermal equilibrium (T_0) due to the balancing of Ohmic heating ($I_0^2 R$) and energy dissipation $G(T_0 - T_s)$. (b) If radiation is present, a non-zero energy flow exists, leading to a change $f(t)$ in resistor temperature. The change in temperature results in a change in resistance, and an electronic circuit is in place to record the corresponding voltage drop.

such that at $t = t_L$ the constant c_0 can be found. The largest temperature increase is achieved at $t = t_L$, and in the limit $t_L \ll \tau$, the expression for the voltage change $\Delta V = I_0 \frac{dR}{dT} f(t_L)$ is given by

$$\Delta V = P t_L \frac{I_0}{C} \frac{dR}{dT}. \tag{A.4}$$

One can introduce the bolometer voltage responsivity S, given by $S = I_0 \frac{dR}{dT} \tau / C$. Using this expression, Eq. (A.4) can be rewritten as $\Delta V / W_{\mathrm{THz}} = S/\tau$, where $W_{\mathrm{THz}} = P t_L$ is the total radiated energy. If an electronic gain with factor χ is applied, and if only a fraction η of the radiated energy is absorbed by the resistor, a final expression for the induced voltage difference can be written as

$$\Delta V = \chi W_{\mathrm{THz}} \frac{S\eta}{\tau}. \tag{A.5}$$

The bolometer used in the experiments described in this thesis is a liquid-helium-cooled silicon composite bolometer (T_s=4.2 K), manufactured by Infrared Laboratories, Inc. The efficiency of the radiation absorption was estimated by the manufacturer to be $\eta \simeq 0.3$. Other parameters for this bolometer were $S = 2.73 \times 10^5\ \mathrm{V\,W^{-1}}$, $G = 17.0 \times 10^{-6}\ \mathrm{J\,s^{-1}\,K^{-1}}$, and τ=0.33 ms. Using Eq. (A.5) it can be found that

$$W_{\mathrm{THz}}\ [\mathrm{nJ}] = (4.0/\chi) \times \Delta \mathrm{V}\ [\mathrm{V}]. \tag{A.6}$$

The bolometer has the option to set the gain at $\chi = 1$, $\chi = 200$ and χ=1000. Two filters can be inserted in the radiation path towards the resistor. The filter in position 1 has a spectral acceptance of $\simeq$ 0.3–30 THz, and is made of a thin poly-ethylene film with a diamond scatter layer. The filter in position 2 has a spectral acceptance of $\simeq$ 0.3–3.0 THz and is made of crystal quartz with black poly-anti-reflective coating and garnet powder. The input window to the bolometer is made of white poly-ethylene.

Appendix B

THz-domain material characterization

The measurement of THz radiation, either by a bolometer or an electro-optic crystal, typically occurs outside of the target chamber. For this reason, one has to use proper window materials that propagate the THz pulse from the chamber to the outside environment. Also, the detector needs to be shielded from remnant laser light by using a proper beam block (preferably still transmissive for the THz pulse). In addition to material-induced absorption, also dispersion and the fabry-Perot effect (spectral interference) have to be considered. The characterization of several materials will be presented in this section.

To study the absorption characteristic of several materials in the THz regime, a mid- to far-infrared Michelson interferometer was used. In this interferometer, broad-bandwidth light from a Globar or mercury lamp is split up in two paths, and recombined in a bolometer. The path difference can be scanned, and the measured bolometer energy W versus time delay τ can be Fourier transformed to yield the power spectrum $W(\nu)$, with ν the frequency. $W(\nu)$ is related to the radiation electric field $E(\nu)$ through $W(\nu) \sim |E(\nu)|^2$. By inserting a material in front of the lamp one can compare the power spectrum through vacuum $W_{\mathrm{vac}}(\nu)$ to the power spectrum $W_{\mathrm{mat}}(\nu)$ with the material in place. The spectral power transmission can be defined as $T(\nu) = W_{\mathrm{mat}}/W_{\mathrm{vac}}$.

Figure B.1(a) displays the spectral power transmission curves for 1/8-inch-thick Teflon, a 1/8-inch-thick low-resistivity (<100 Ohm) silicon window, and a 400-μm-thick silicon wafer. The Teflon and silicon (Si) window are suitable for use as a vacuum window. However, one can see that applicability of Teflon is limited to < 4 THz frequencies. The silicon wafer, which has a high resistivity ($\simeq 10^5$ Ohm), has a good performance in terms of frequency-independent power transmission. The silicon wafer is reflective for 800 nm laser light, making it an ideal material for THz transmission and laser reflection. Later in this section, THz dispersion in the Si wafer will be discussed.

Figure B.1(b) displays the spectral power transmission curves for 1/8-inch-thick low-density poly-ethylene (LDPE), 1/8-inch-thick high-density poly-ethylene (HDPE), and 100-μm-thick Kapton. All three materials are suitable for use as vacuum windows. Only Kapton is transmissive to 800 nm laser light. The oscillatory pattern in the Kapton mea-

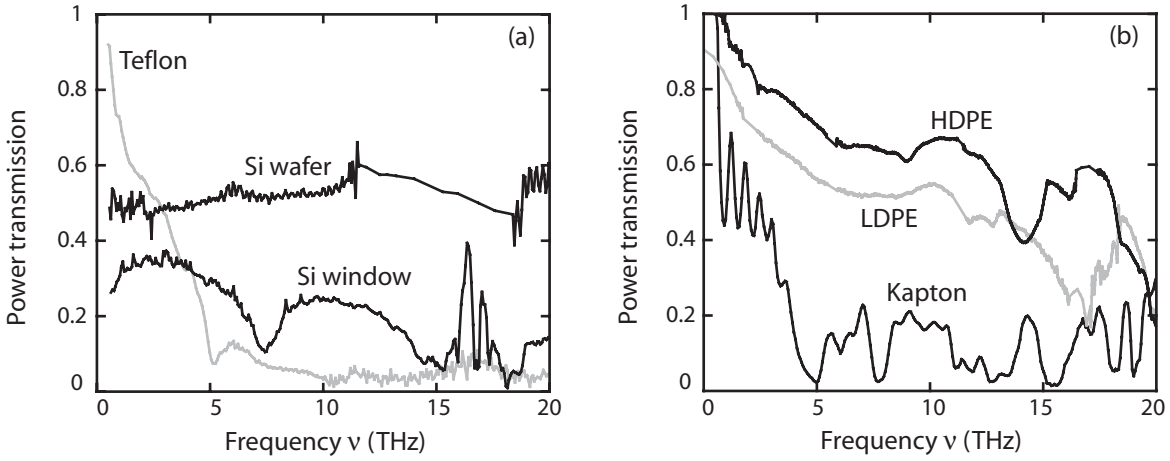

Fig. B.1. (a) Power transmission curves for 1/8*-inch-thick Teflon, a* 1/8*-inch-thick low-resistivity (*$<$ 100 *Ohm) silicon window, and a* 400*-*μ*m-thick high-resistivity (*$\simeq 10^5$ *Ohm) silicon wafer. (b) Power transmission curves for* 1/8*-inch-thick low-density poly-ethylene (LDPE),* 1/8*-inch-thick high-density poly-ethylene (HDPE), and* 100*-*μ*m-thick Kapton.*

surement is a result of the Fabry-Perot effect. It can be seen in Fig. B.1(b) that Kapton is not applicable for transmission of THz sources at frequencies beyond $>$ 4 THz (strong absorption). Both HDPE and LDPE are useful for THz applications, since no major sharp absorption features are found in the 0–15 THz region. For example, in the 0–12 THz regime one can approximate the HDPE power transmission to be $T(\nu) = 0.8 \pm 0.2$. Although HDPE and LDPE are not transmissive to laser light, diffused light through the material can still interfere with detection. Therefore, an additional Si wafer for remnant laser light might still be needed to shield the detector.

The Michelson interferometer technique, presented in the previous paragraphs, does intrinsically not allow for characterization of dispersion and higher-order pulse distortions. These effects can be measured with a system based on optical rectification and electro-optic sampling (EOS). EOS is discussed in great detail in Chapter 5 and Appendix C. Through EOS, the temporal electric field waveform of a short THz pulse can be measured with signal-to-noise ratios in excess of $10^4 - 10^5$. The THz pulses are generated through optical rectification [100], see also Sec. C.5.3, of an ultra-short laser pulse in a ZnTe crystal. Temporal characterization through EOS is realized by propagating the THz pulse and a laser probe beam through a second ZnTe crystal. Figure B.2(a) displays the measured waveforms of a THz pulse propagating through vacuum (reference) and through 1/8-inch-thick HDPE. For comparison, this is the same HDPE as used in the measurements of Fig. B.1(b). The spectral window of this EOS measurement was limited to $\simeq$0-7 THz, mainly due to source characteristics. The two waveforms allow for determination of the real and imaginary part of the index of refraction. The absorption closely matches the results found in Fig. B.1(b), and the real part of the index of refraction is plotted in Fig. B.2(b). In the plots of Figs. B.2(a) and B.2(b) one can see that the pulse distortion is minimal. The real part of the index of refraction n falls within 0.3% of n=1.536, indicating

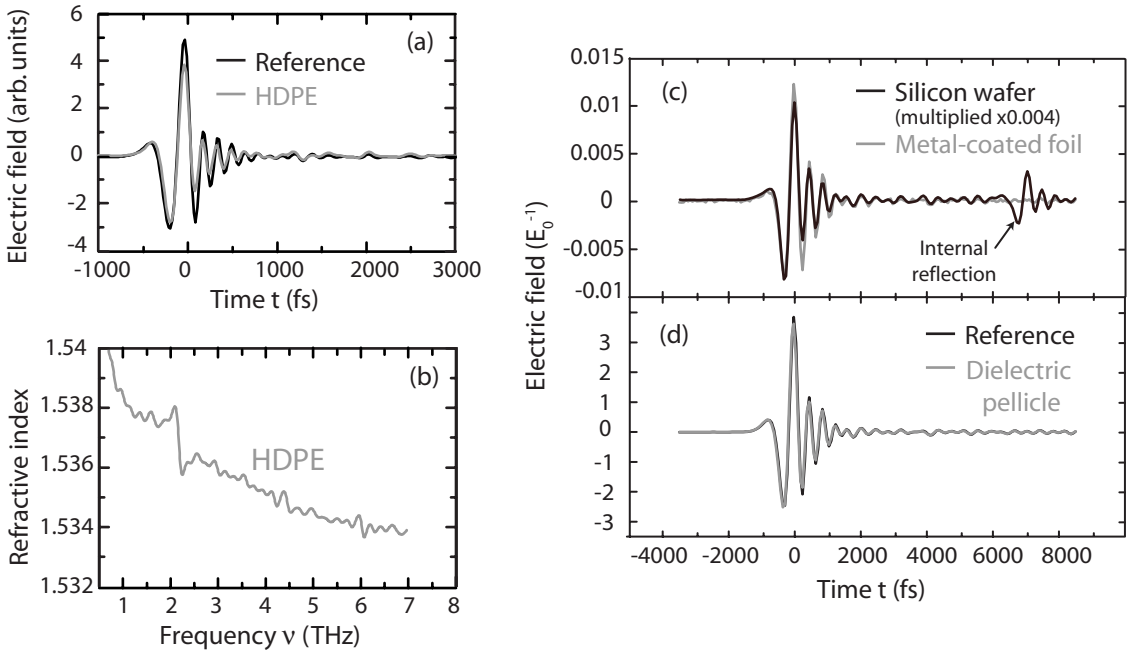

Fig. B.2. (a) Electric field THz waveforms after propagation through vacuum (reference) and through 1/8*-inch-thick HDPE. From the two waveforms, the real and imaginary parts of the index of refraction for HDPE can be found, with the real part plotted in (b). (c)-(d) During another measurement, several THz waveforms were measured after propagation in vacuum (reference), through a dielectric-coated pellicle, through a metal-coated pellicle, and through a high-resistiviy silicon wafer. The fields are normalized to an arbitrary* E_0.

that the effects of dispersion are small. This measurement, although for a limited spectral range, proves the usefulness of HDPE as a suitable THz window material.

During another set of measurements, four EOS waveforms were obtained. The waveforms, see Figs. B.2(c)-(d), were measured after propagation of the THz pulse through vacuum (reference), a dielectric-coated pellicle (nitrocellulose foil), a 400-μm-thick high-resistivity ($\simeq 10^5$ Ohm) silicon wafer, and a 5-μm-thick metal-coated pellicle, respectively. The fields are normalized to an arbitrary E_0. Note that the frequencies of the source were in the 0–7 THz range. The dielectric-coated pellicle shows a near-perfect transmission of the THz pulse (no significant field attenuation or dispersion). It can be used as a beam combiner for a THz pulse and a NIR laser pulse. The waveform through the metal-coated pellicle is also near-identical to the reference waveform (negligible dispersion), although a very strong reduction ($\simeq 300$) in the peak electric field is present (power transmission of $\simeq 1.1 \times 10^{-5}$). The metal-coated pellicle can be useful as a strong THz attenuator. The waveform through the silicon wafer, which is the same as measured in Fig. B.1, is multiplied by $\times 0.004$ for clarity. The actual amplitude of the waveform is $0.01/0.004 = 2.5E_0$, which is $\simeq$70% of the field amplitude of the reference waveform ($\simeq$50% power transmission). Because of the large temporal window of the measurement, the internally-reflected THz pulse was observed as well. Just as for HDPE, the effects of dispersion in the Si wafer are small, emphasizing the usefulness of the Si wafer as a THz transmitter.

Appendix C

Electro-optic sampling

C.1 Index ellipsoid

EOS sampling can be described as the laser probing of a THz-induced change in crystal birefringence. The optical properties of an anisotropic medium are represented by the index ellipsoid. The crystal coordinate system is defined as (x, y, z). The index ellipsoid is expressed as

$$\sum_{ij} \eta_{ij} x_i x_j = 1 \qquad i, j = 1, 2, 3, \tag{C.1}$$

with $(x_1, x_2, x_3) = (x, y, z)$ and $\eta_{ij} = \epsilon_0 \epsilon_{ij}^{-1}$. Equation (C.1) can also be interpreted as

$$\eta_{xx}x^2 + \eta_{xy}xy + \eta_{xz}xz + \eta_{yx}yx + \eta_{yy}y^2 + \eta_{yz}yz + \eta_{zx}zx + \eta_{zy}zy + \eta_{zz}z^2 = 1. \tag{C.2}$$

Equations (C.1) and (C.2) describe a 3D index ellipsoid, characterized by three principle orthogonal axes, each oriented at a specific orientation in the crystal system (x, y, z). The refractive indices along the principle axes of the ellipsoid are defined as n_1, n_2, and n_3. Due to the Pockels effect, also referred to as electro-optic (EO) effect, each element η_{ij} will be a function of the bias (THz) electric field $\mathbf{E} = (E_x, E_y, E_z)$, or

$$\eta_{ij} = \eta_{ij,0} + \sum_k r_{ijk} E_k \qquad i, j, k = 1, 2, 3, \tag{C.3}$$

with r_{ijk} the linear electro-optic (Pockels) coefficient. Note that r_{ijk} has 27 elements. However, since η is symmetric ($\eta_{ij} = \eta_{ji}$), the 9 element combinations (i, j) can be combined to 6, each labeled by a single index I, with $I = 1$ for $(i, j) = (1, 1)$, $I = 2$ for $(i, j) = (2, 2)$, $I = 3$ for $(i, j) = (3, 3)$, $I = 4$ for $(i, j) = (3, 2)$ and $(i, j) = (2, 3)$, $I = 5$ for $(i, j) = (3, 1)$ and $(i, j) = (1, 3)$, and $I = 6$ for $(i, j) = (2, 1)$ and $(i, j) = (1, 2)$. This allows for replacement of η_{ij} by η_I, and r_{ijk} by r_{Ik}, which now has 18 elements.

In crystals with cubic $\overline{4}3m$ crystal configuration, such as zinc telluride (ZnTe) and gallium phosphite (GaP), which is used in the experiments described in this thesis, the number of non-zero elements in r_{Ik} can be further reduced and Eq. (C.3) can be written

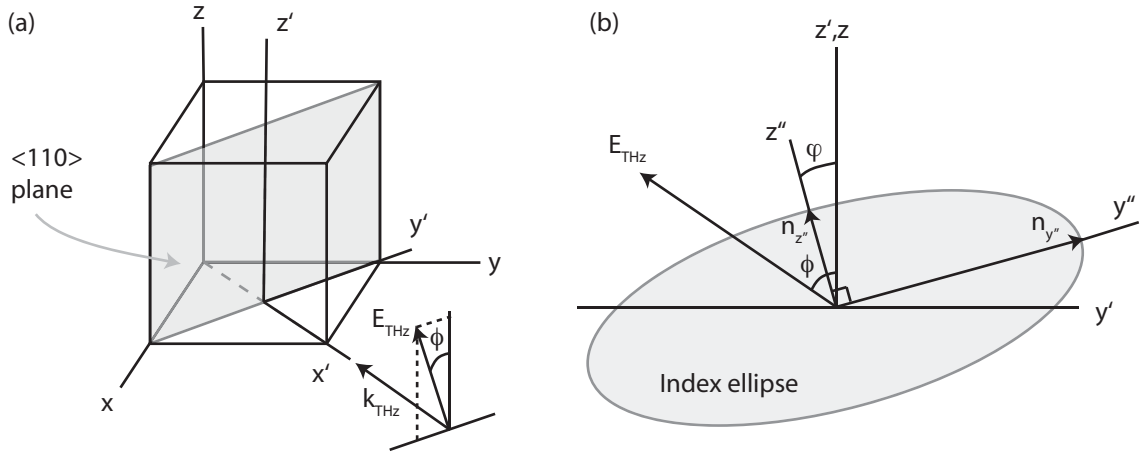

Fig. C.1. (a) Geometry of a ⟨110⟩-cut cubic crystal, depicting the crystal axes (x, y, z), and laboratory axes (x', y', z'). The THz pulse is defined to be normally incident on the ⟨110⟩ plane. The THz electric field $\boldsymbol{E}_{\mathrm{THz}}$ has an angle ϕ to the z' axis. (b) The index ellipse at the $y' - z'$ plane has two principle axes, which define the coordinate system (y'', z''). The axis z'' makes an angle φ with axis z'.

as

$$\begin{bmatrix} \eta_1 \\ \eta_2 \\ \eta_3 \\ \eta_4 \\ \eta_5 \\ \eta_6 \end{bmatrix} = \begin{bmatrix} \eta_{1,0} \\ \eta_{2,0} \\ \eta_{3,0} \\ \eta_{4,0} \\ \eta_{5,0} \\ \eta_{6,0} \end{bmatrix} + \begin{bmatrix} 0 & 0 & 0 \\ 0 & 0 & 0 \\ 0 & 0 & 0 \\ r_{41} & 0 & 0 \\ 0 & r_{41} & 0 \\ 0 & 0 & r_{41} \end{bmatrix} \begin{bmatrix} E_x \\ E_y \\ E_z \end{bmatrix}. \tag{C.4}$$

The cubic $\overline{4}3m$ crystals are isotropic, and with no THz field applied $n_1 = n_2 = n_3 = n$. In this case, $\eta_{1,0} = \eta_{2,0} = \eta_{3,0} = 1/n^2$ and $\eta_{4,0} = \eta_{5,0} = \eta_{6,0} = 0$, such that Eq. (C.2) reads $(x^2 + y^2 + z^2)/n^2 = 1$. The situation changes if a bias electric field is applied. Since the crystals used for the experiments in this thesis were cut along the ⟨110⟩ plane, that same geometry will be considered here. The axes of the ⟨110⟩-cut crystal are labeled (x', y', z'). The two coordinate systems (x, y, z) and (x', y', z') are depicted in Fig. C.1(a). It is assumed that the THz pulse is normally incident on the ⟨110⟩ crystal plane. The electric field $\mathbf{E}_{\mathrm{THz}}$ is linearly polarized, at angle ϕ with respect to the z' axis, as shown in Figs. C.1(a) and C.1(b). The THz electric field vector can be presented in the crystal system (x, y, z) as $\mathbf{E} = \mathbf{E}_{\mathrm{THz}} = E_{\mathrm{THz}}(\sin\phi/\sqrt{2}, -\sin\phi/\sqrt{2}, \cos\phi)$. The index ellipsoid in the (x, y, z) system, defined by Eq. (C.1) with each element given by Eq. (C.4), can then be expressed as

$$\frac{x^2 + y^2 + z^2}{n^2} + \frac{2r_{41}E_{\mathrm{THz}}\sin\phi}{\sqrt{2}}yz - \frac{2r_{41}E_{\mathrm{THz}}\sin\phi}{\sqrt{2}}zx + 2r_{41}E_{\mathrm{THz}}xy\cos\phi = 1. \tag{C.5}$$

In typical EOS experiments, the laser beam used for probing of the index ellipsoid is collinear with the THz pulse. For this reason, the index ellipse at the x'-y' plane needs to

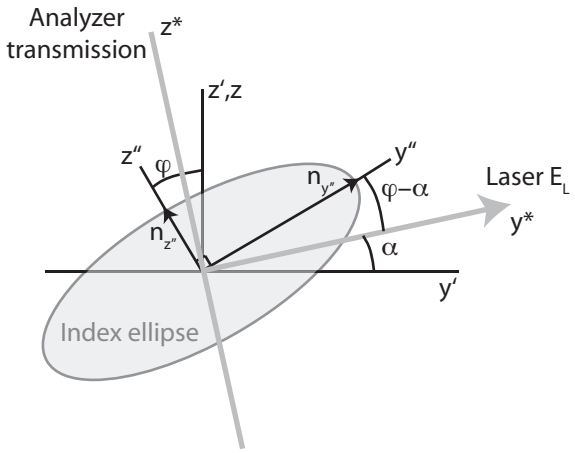

Fig. C.2. Geometry of a probe laser normally incident on the ⟨110⟩ plane ($y'-z'$ plane), with its electric field $\boldsymbol{E}_L$ making an angle α with the y' axis. An analyzer (polarizer) transmits only the field component perpendicular to $\boldsymbol{E}_L$.

be characterized. Equation (C.5) can be rewritten for the (x', y', z') system, and by setting $x' = 0$ the ellipsoid projection on the y'-z' plane is found. The two principle axes of the ellipse set up a third coordinate system (y'', z''), and one can calculate [100] that the angle φ between z'' and z' is given by

$$\tan 2\varphi = -2 \tan \phi. \tag{C.6}$$

The geometry of the system is depicted in Fig. C.1(b), with the index ellipse rotated by φ with respect to the z' axis. The difference in index of refraction between the two principle axes $\Delta n = (n_{z''} - n_{y''})$, see Fig. C.1(b), can be found to be [100]

$$\Delta n = (n_{z''} - n_{y''}) = \frac{n^3 r_{41} E_{\mathrm{THz}} \sqrt{1 + 3\sin^2 \phi}}{2}, \tag{C.7}$$

with n the index of refraction at probe laser wavelength λ_0. As Eq. (C.7) demonstrates, Δn scales linearly with the THz field and is maximum for $\phi = 90°$, in which case $\varphi = \pm 45°$.

C.2 Probing the index ellipse: linear laser polarization

A probe laser beam is used to detect or record the change in index ellipse, from $\Delta n = 0$ with no THz field present to $\Delta n \propto E_{\mathrm{THz}}$ with a THz field present. The polarization of the laser pulse field $\mathbf{E}_L$ is defined to be linear, with $\mathbf{E}_L$ in the (y', z') frame, see Fig. C.2. The angle between $\mathbf{E}_L$ and y' is labeled as α, and a fourth coordinate system (y^*, z^*), based on the laser polarization, is introduced. An analyzer (polarizer) only transmits the laser field vector orthogonal to $\mathbf{E}_L$. The EO-induced phase retardation Γ_{THz} between the projection of $\mathbf{E}_L$ on z'' and its projection on y'' can be found to be

$$\Gamma_{\mathrm{THz}} = \frac{2\pi}{\lambda_0} L \Delta n, \tag{C.8}$$

or, using Eq. (C.7) with $\phi = 90°$,

$$\Gamma_{\mathrm{THz}} = \frac{2\pi}{\lambda_0} L n^3 r_{41} E_{\mathrm{THz}}, \tag{C.9}$$

with L the crystal thickness. A Jones matrix is now constructed to calculate the field vector of the laser pulse $\mathbf{E}_T$ after the analyzer. In the system (y^*, z^*), see Fig. C.2, the laser pulse has a polarization vector $\begin{bmatrix} 1 \\ 0 \end{bmatrix}$, the analyzer matrix is given by $\begin{bmatrix} 0 & 0 \\ 0 & 1 \end{bmatrix}$, and $\begin{bmatrix} \cos\gamma & -\sin\gamma \\ \sin\gamma & \cos\gamma \end{bmatrix}$ represents a coordinate system rotation of γ. The Jones matrix is then

$$\mathbf{E}_T = \begin{bmatrix} 0 & 0 \\ 0 & 1 \end{bmatrix} \begin{bmatrix} \cos\gamma & \sin\gamma \\ -\sin\gamma & \cos\gamma \end{bmatrix} \begin{bmatrix} 1 & 0 \\ 0 & e^{i\Gamma_{\mathrm{THz}}} \end{bmatrix} \begin{bmatrix} \cos\gamma & -\sin\gamma \\ \sin\gamma & \cos\gamma \end{bmatrix} \begin{bmatrix} 1 \\ 0 \end{bmatrix}, \tag{C.10}$$

with $\gamma = \varphi - \alpha$. One can calculate that the transmitted intensity $I_T = |E_T|^2$ is given by

$$I_T = |E_T|^2 = 2(1 - \cos\Gamma_{\mathrm{THz}}) \cos^2(\varphi - \alpha) \sin^2(\varphi - \alpha). \tag{C.11}$$

One can see from Eq. (C.11) that the analyzer transmission is zero if no THz field is present ($\Gamma_{\mathrm{THz}} = 0$). With a THz field present, the maximum transmitted field energy occurs at $\varphi - \alpha = 45°$. In other words, the maximum THz-induced change in laser transmission occurs if the polarization vector of the laser is chosen to be 45° with respect to the principle axes of the index ellipse. In the situation where $\varphi - \alpha = 45°$, Eq. (C.11) reduces to

$$I_T = \sin^2 \frac{\Gamma_{\mathrm{THz}}}{2}. \tag{C.12}$$

For small $\Gamma_{\mathrm{THz}} \ll 1$, this expression further reduces to $I_T \simeq \Gamma_{\mathrm{THz}}^2/4$.

In a typical experimental environment, the THz field vector is fixed, but the crystal axis z' can be rotated more easily. The probe laser transmission I_T is a function of the phase retardation [see Eq. (C.11)], which in return depends on the angle ϕ between $\mathbf{E}_{\mathrm{THz}}$ and z', as expressed by Eq. (C.7). Suppose that at each value for ϕ, the laser polarization is rotated to optimize the analyzer transmission ($\mathbf{E}_L$ at 45° to y''). In this case, I_T versus ϕ is plotted in Fig. C.3(a) as the dashed curve. For the calculation, a fixed THz field amplitude was assumed, with $\Gamma_{\mathrm{THz}} \ll \pi$. The maximum EO effect, see Eq. (C.7), is achieved at point (b) in Fig. C.3(a), where $\phi = 90°$, $\varphi = 45$, and $\mathbf{E}_L$ is polarized along y'. If the crystal is rotated to $\phi = 0°$, see Fig. C.3(c) and point (c) in Fig. C.3(a), then Γ_{THz} is reduced according to Eq. (C.7) to half of its peak value (I_T to a quarter of its peak value).

In the experiments described in Chapters 5 and 6, the probe beam polarization is fixed, with $\mathbf{E}_{\mathrm{THz}}$ and $\mathbf{E}_L$ at 90°. In this fixed geometry, the analyzer transmission versus crystal axis rotation ϕ is shown as the solid curve in Fig. C.3(a). At several values for ϕ, such as point (d), $\mathbf{E}_L$ and y'' are parallel, in which case the laser transmission remains zero. So although a THz-induced birefringence is realized, the laser beam does not probe this birefringence if its polarization vector is not oriented properly.

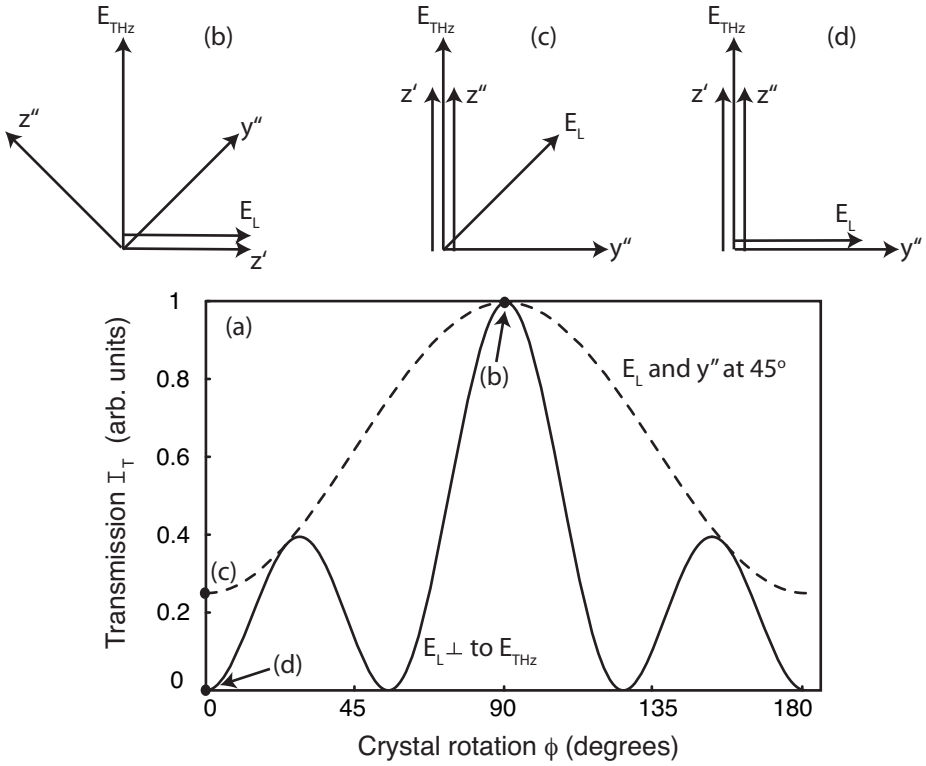

Fig. C.3. The main plot (a) displays the EO transmission as a function of crystal rotation ϕ, defined as the angle between $\boldsymbol{E}_{\mathrm{THz}}$ and z'. The solid curve represents the transmission curve if, at every crystal rotation, an angle of 45° between $\boldsymbol{E}_L$ and y'' is maintained. The dashed curve represents the transmission if $\boldsymbol{E}_L$ is fixed at 90° to $\boldsymbol{E}_{\mathrm{THz}}$. The vector geometries at the points (b)-(d) of the main plot (a) are depicted in the subplots (b), (c), and (d), respectively. Optimum EO transmission is obtained if $\phi = 90°$, such that $\boldsymbol{E}_{\mathrm{THz}}$ is perpendicular to z', and if $\boldsymbol{E}_L$ is either parallel or perpendicular to $\boldsymbol{E}_{\mathrm{THz}}$, such that $\boldsymbol{E}_L$ and y'' are at 45°.

C.3 Probing the index ellipse: elliptical/circular laser polarization

Instead of a linear polarized pulse, treated by the Jones matrices in Eq. (C.10), an elliptical polarized laser pulse will be considered here. The geometry for $\mathbf{E}_{\mathrm{THz}}$ and the crystal axis z' is plotted in Fig. C.3(b). Following Fig. C.3(b), the laser polarization is originally linear, with Jones vector $\begin{bmatrix} 1 \\ 0 \end{bmatrix}$ in the (y^*, z^*) frame. Elliptical polarization is imposed on the laser polarization state by propagation through a quarter-wave plate ($\lambda/4$ plate), with its fast axis (FA) rotated at angle δ with respect to $\mathbf{E}_L$ or y^*. Note that at $\delta = 0°$ and $\delta = 90°$, the polarization state remains linear and parallel to z'. At $\delta = 45°$ the polarization state is circular, and for $0° < \delta < 45°$ and $45° < \delta < 90°$ elliptical. The angle between the FA and the major axis y'' of the index ellipse is $(\pi/4 - \delta)$. The Jones matrix for the electric

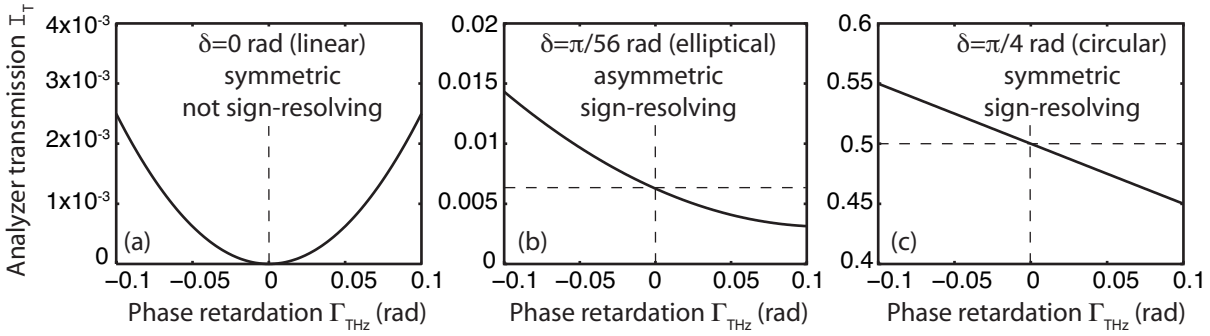

Fig. C.4. Laser energy transmission I_T through the analyzer versus phase retardation Γ_{THz} for three different laser polarization states, namely $\delta = 0$ (linear), $\delta = \pi/56$ (elliptical), and $\delta = \pi/4$ (circular). One can see that sign-resolved transmission measurements are only possible for elliptical and circular polarization states, and only in the latter case is the change in transmission symmetric for equal-but-opposite Γ_{THz}.

field incident on the analyzer [in the (y^*, z^*) frame] is

$$\mathbf{E}_L = \begin{bmatrix} \frac{1}{\sqrt{2}} & \frac{1}{\sqrt{2}} \\ -\frac{1}{\sqrt{2}} & \frac{1}{\sqrt{2}} \end{bmatrix} \begin{bmatrix} 1 & 0 \\ 0 & e^{\imath\Gamma_{\mathrm{THz}}} \end{bmatrix} \begin{bmatrix} \cos\xi & -\sin\xi \\ \sin\xi & \cos\xi \end{bmatrix} \begin{bmatrix} 1 & 0 \\ 0 & e^{\imath\frac{\pi}{2}} \end{bmatrix} \begin{bmatrix} \cos\delta & -\sin\delta \\ \sin\delta & \cos\delta \end{bmatrix} \begin{bmatrix} 1 \\ 0 \end{bmatrix}, \tag{C.13}$$

with $\xi = (\pi/4 - \delta)$. The analyzer transmits only field components orthogonal to y^* (orthogonal to z'), through the matrix $\begin{bmatrix} 0 & 0 \\ 0 & 1 \end{bmatrix}$. The transmitted field in the (y^*, z^*) frame is $\mathbf{E}_T = \begin{bmatrix} 0 \\ E_T \end{bmatrix}$, with

$$E_T = -\frac{1}{\sqrt{2}}\cos\xi\cos\delta + \frac{1}{\sqrt{2}}\sin\xi\sin\delta e^{\imath\frac{\pi}{2}} + \frac{1}{\sqrt{2}}\sin\xi\cos\delta e^{\imath\Gamma_{\mathrm{THz}}} + \frac{1}{\sqrt{2}}\cos\xi\sin\delta e^{\imath(\frac{\pi}{2}+\Gamma_{\mathrm{THz}})}. \tag{C.14}$$

Note that for the construction of the Jones vector $\mathbf{E}_L$ of Eq. (C.13), it does not matter if the $\lambda/4$ plate is placed before or after the EO crystal, as long as it is placed before the analyzer.

From Eq. (C.14) the transmitted energy $I_T = |E_T|^2$ can be calculated, leading to

$$I_T = G(\Gamma_{\mathrm{THz}}) = \frac{1}{2}\left(1 - \cos\Gamma_{\mathrm{THz}}\cos^2 2\delta + \sin\Gamma_{\mathrm{THz}}\sin 2\delta\right). \tag{C.15}$$

Note that for a circular polarized probe beam ($\delta = \pi/4 \rightarrow \xi = 0$), the expression for E_T and I_T can be found to be

$$E_T = -\frac{1}{2} + \frac{1}{2}\imath e^{\imath\Gamma_{\mathrm{THz}}} \qquad \text{and} \qquad I_T = \frac{1}{2}(1 + \sin\Gamma_{\mathrm{THz}}). \tag{C.16}$$

For three different laser polarization states, namely $\delta = 0$ (linear), $\delta = \pi/56$ (elliptical), and $\delta = \pi/4$ (circular), the transmitted energy I_T is plotted versus phase retardation Γ_{THz} in Figs. C.4(a), C.4(b), and C.4(c), respectively. For $\delta = 0$, see Fig. C.4(a), the

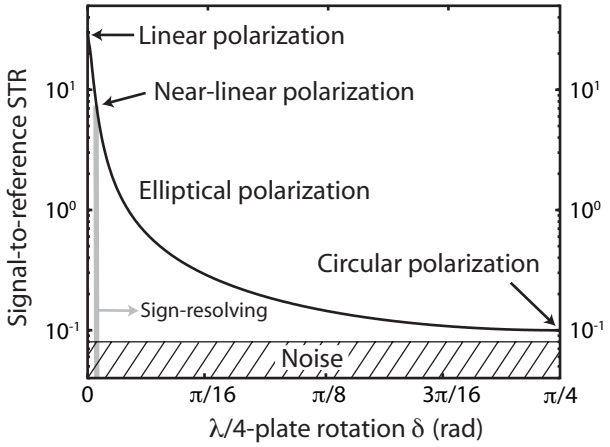

Fig. C.5. Plot of the signal-to-reference parameter (STR) for the parameters $\Gamma_{\mathrm{THz}} = -0.1$ *rad and* $I_{\mathrm{res}} = 10^{-4}$*. The STR, plotted on a logarithmic scale, strongly decreases as the polarization state of the laser is modifed from linear (*$\delta = 0$*) to circular (*$\delta = \pi/4$*). Only for non-zero* δ *is sign-resolved measurement of the phase retardation (and THz field) possible. The noise level in the experimental detection system is estimated to be* 8% *of* $[I_T(\Gamma_{\mathrm{THz}} = 0) + I_{\mathrm{res}}]$.

transmission scales approximately as $I_T \simeq \Gamma^2_{\mathrm{THz}}/4$. Although the EO effect is dramatic (from zero transmission to $\Gamma^2_{\mathrm{THz}}/4$), there is no sign information since equal-but-opposite values for Γ_{THz} result in the same transmission. For non-zero values for δ, the transmission I_T at $\Gamma_{\mathrm{THz}} = 0$ is greater than zero, see Figs. C.4(b) and C.4(c), such that for a non-zero THz field the transmission will be higher or lower than $I_T(\Gamma_{\mathrm{THz}} = 0)$, depending on the sign of Γ_{THz}. However, only in the case of $\delta = \pi/4$ (circular polarization) is the change in transmission symmetric for equal-but-opposite values for Γ_{THz}. Based on knowledge of δ, the expression in Eq. (C.14) has to be used to relate the measured laser transmission to the phase retardation Γ_{THz}.

There is another important consequence of changing the polarization state from linear to circular. A parameter signal-to-reference (STR) is defined to quantify how dramatic the EO effect is by comparing the transmission with and without a THz field present. The STR is defined as

$$\mathrm{STR}(\Gamma_{\mathrm{THz}}) = \frac{\mathrm{I_T}(\Gamma_{\mathrm{THz}}) - \mathrm{I_T}(\Gamma_{\mathrm{THz}} = 0)}{\mathrm{I_T}(\Gamma_{\mathrm{THz}} = 0) + \mathrm{I_{res}}}, \tag{C.17}$$

with I_{res} the scattering contribution to the analyzer transmission. The reason why I_{res} is included is the following: if $\Gamma_{\mathrm{THz}} = 0$ and $\delta = 0$, see Fig. C.4(a), no laser transmission is expected, but due to scattering processes in the crystal and polarizer a residual fraction I_{res} of the laser pulse energy will always be transmitted. Typically, I_{res} is less than 0.01% of the total laser energy.

As Figs. C.4(a)-(c) indicate, the relative change in laser transmission [relative to $I_T(\Gamma_{\mathrm{THz}} = 0)$] decreases as the polarization state is changed from linear to circular. For $\Gamma_{\mathrm{THz}} = -0.1$ rad and $\delta = 0$, the laser transmission changes from zero to $\simeq 2.4 \times 10^{-3}$ (dramatic effect, large STR), while for $\delta = \pi/4$ the transmission only changes from 0.5 to 0.55 (less dramatic, small STR).

The dependence of the STR on the polarization state (rotation δ) is plotted in Fig. C.5, where the STR is analyzed for $\Gamma_{\mathrm{THz}} = -0.1$ rad and $I_{\mathrm{res}} = 10^{-4}$. One can observe that the STR decreases if δ increases. As a typical example, the noise in the detection setup is estimated at 8% of $[I_T(\Gamma_{\mathrm{THz}} = 0) + I_{\mathrm{res}}]$, see Fig. C.5. Contributions to this noise are fluctuations in laser energy and laser pointing. The EO signal strength can be defined as the ratio between STR and the noise level. In the case of $\delta \ll 1$ (linear and near-linear polarization), the ratio of the STR to the noise is much larger than 1 (large signal strength), but at $\delta \to \pi/4$ the parameter STR is of the same order than the noise (small signal strength). To measure the transmission with the largest sign-resolving STR, the polarization state should be chosen to be near-linear, referring to an elliptical polarization state with small $\delta \ll 1$. This conclusion was also reached by Jiang *et al.* [54]. Note that the choice for laser polarization state can change if both the analyzer transmission and reflection are simultaneously recorded. In this balanced-detection scheme, typically based on circular polarized light ($\delta = \pi/4$), the noise contribution can be greatly reduced.

C.4 Electro-optic principles

This section will extend the EO analysis from a static THz field to an evolving THz field profile (THz pulse). As discussed in Sec. C.2, the THz electric field strength E_{THz} can be measured by propagating a laser and THz pulse through an EO crystal and measuring the laser analyzer transmission I_T. By converting the laser transmission to phase retardation Γ_{THz}, the THz field strength E_{THz} was obtained. Although Eq. (C.9) relates Γ_{THz} to E_{THz}, the situation is more complex if a temporal THz field profile $E_{\mathrm{THz}}(t)$ [or a phase retardation profile $\Gamma_{\mathrm{THz}}(t)$] is considered.

In terms of the actual phase retardation $\Gamma^*(t)$ that is induced by the THz field $E_{\mathrm{THz}}(t)$, several effects have to be taken into account, all related to the propagation of the THz and laser pulse in the crystal. These effects include i) THz absorption, ii) THz dispersion, iii) reflective losses at the crystal interface, and iv) mismatch between the laser group velocity and phase velocity of individual THz frequencies. The relation between $\Gamma^*(t)$ and $\Gamma_{\mathrm{THz}}(t)$ can be best understood [101, 102] in the Fourier domain, where it can be shown that

$$\Gamma^*(\omega) = \Gamma_{\mathrm{THz}}(\omega) T_{\mathrm{in}}(\omega) T_{\mathrm{crystal}}(\omega), \tag{C.18}$$

with $T_{\mathrm{in}}(\omega) = 2/(1+n_{\mathrm{THz}})$ the crystal surface transmission. The crystal function $T_{\mathrm{crystal}}(\omega)$ incorporates the THz propagation $\exp[-(\imath\omega z n_{\mathrm{THz}})/c]$ (including absorption and dispersion) with respect to the laser pulse $\exp[(\imath\omega z n_{\mathrm{gr}})/c]$, resulting in

$$\begin{aligned} T_{\mathrm{crystal}}(\omega) &= \int_0^L \exp\left(-\imath\frac{\omega}{c} z n_{\mathrm{THz}}\right) \exp\left(\imath\frac{\omega}{c} z n_{\mathrm{gr}}\right) dz \\ &= \frac{\exp\left[\imath L(n_{\mathrm{gr}} - n_{\mathrm{THz}})\frac{\omega}{c}\right] - 1}{\imath\frac{\omega}{c}(n_{\mathrm{gr}} - n_{\mathrm{THz}})}. \end{aligned} \tag{C.19}$$

Equations (C.9), (C.18), and (C.19), with the crystal and laser parameters known, yield both $E_{\mathrm{THz}}(t)$ and $E_{\mathrm{THz}}(\nu)$. One can see from Eq. (C.19) that the thickness L of the crystal plays an important role. Note that for ultra-short probe pulses ($\sigma_L \lesssim 20$ fs, with σ_L the rms laser pulse length), one can no longer assign one constant group velocity v_{gr} to the laser pulse, but one has to consider a frequency-dependent laser group velocity $v_{\mathrm{gr}}(\lambda)$.

In a typical scanning measurement, such as presented in Sec. 5.2, the delay τ between the THz pulse $E_{\mathrm{THz}}(t)$ and probe laser is varied, while the transmitted laser energy I_{diode} is recorded by an energy detector (diode). In Eq. (C.15) it was defined that $|E_T| = 1$ and $I_T = 1$ for the incoming laser field (before the crystal and analyzer). However, in the experiments, an initial laser intensity profile $I_0(t-\tau)$ is present. In this case the total energy $I_{\mathrm{diode}}(\tau)$ of the transmitted laser light is given by

$$I_{\mathrm{diode}}(\tau) = \int I_T(t) I_0(t-\tau) dt. \tag{C.20}$$

Note that $I_T(t) = G[\Gamma^*(t)]$, with the function $G[\Gamma^*(t)]$ defined in Eq. (C.15): for a linear polarization state, Eq. (C.12) shows that $G[\Gamma^*(t)] = \sin^2[\Gamma^*(t)/2]$, while for a circular polarization state Eq. (C.16) yields $G[\Gamma^*(t)] = [1+\sin\Gamma^*(t)]/2$. A normalization can applied to the measured profile $I_{\mathrm{diode}}(\tau)$, leading to

$$M(\tau) = \frac{I_{\mathrm{diode}}(\tau) - G[\Gamma^*=0]\int I_0(t')dt'}{\int I_0(t')dt'} = \int H[\Gamma^*(t)] \frac{I_0(t-\tau)}{\int I_0(t')dt'} dt, \tag{C.21}$$

with $H[\Gamma^*(t)] = G[\Gamma^*(t)] - G[\Gamma^*=0]$. Note that the factor $G[\Gamma^*=0]\int I_0(t')dt'$ can be considered as the energy measured by the detector in case no THz field is applied. The factor $\int I_0(t')dt'$ can be obtained by recording the detected energy in case of no THz field, with the $\lambda/4$ plate removed, and with the analyzer rotated for maximum transmission. Equation (C.21) shows that the relationship between $\Gamma^*(t)$ and the measured $M(\tau)$ is complex. For this reason, a new function will be derived from the measured $M(\tau)$, namely

$$\Gamma_{\mathrm{cor}}(\tau) = H_{\mathrm{inv}}[M(\tau)], \tag{C.22}$$

with H_{inv} the inverse function of H. For example, for a circular polarized laser beam it can be found that $H[\Gamma^*(t)] = [\sin\Gamma^*(t)]/2$ and $H_{\mathrm{inv}}[\Gamma^*(t)] = \arcsin[2\Gamma^*(t)]$. Just as the THz field $E_{\mathrm{THz}}(t)$ can be expressed as a phase retardation $\Gamma_{\mathrm{THz}}(t)$ following Eq. (C.8), the corrected retardation $\Gamma_{\mathrm{cor}}(\tau)$ can also be linked to an EO field profile $S_{\mathrm{EO}}(\tau)$ according to

$$S_{\mathrm{EO}}(\tau) = \frac{\Gamma_{\mathrm{cor}}(\tau)\lambda_0}{2\pi L n^3 r_{41}}. \tag{C.23}$$

Based on Eqs. (C.21) and (C.22), the following approximation is applied in the Fourier domain:

$$\Gamma_{\mathrm{cor}}(\omega) \simeq \Gamma^*(\omega) I_{\mathrm{env},0}(\omega) = \Gamma_{\mathrm{THz}}(\omega) T_{\mathrm{in}}(\omega) T_{\mathrm{crystal}}(\omega) I_{\mathrm{env},0}(\omega), \tag{C.24}$$

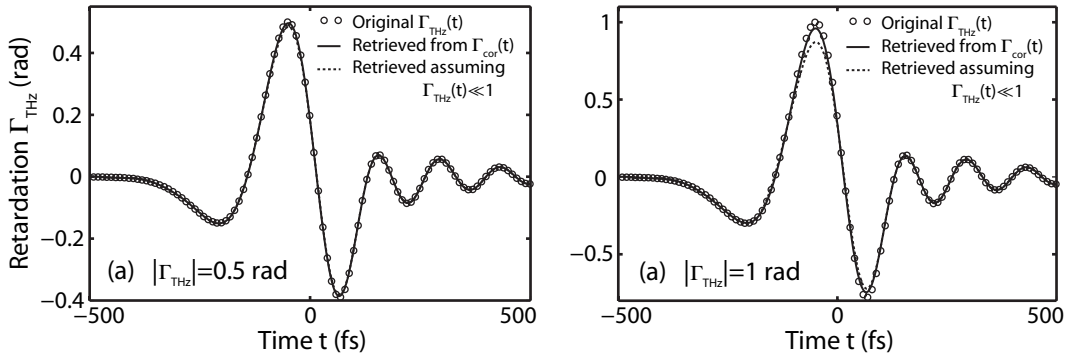

Fig. C.6. Modeled THz retardation profiles $\Gamma_{\mathrm{THz}}(t)$ *(open circles) with (a) a peak amplitude of* $|\Gamma_{\mathrm{THz}}(t)| = 0.5$ *rad and (b)* $|\Gamma_{\mathrm{THz}}(t)| = 1$ *rad. The solid curves are calculated following* $\Gamma_{\mathrm{cor}}(t) = H_{\mathrm{inv}}[M(t)]$ *and the dotted curves are calculated based on the assumption* $\Gamma_{\mathrm{THz}} \ll 1$.

with $I_{\mathrm{env},0}(\omega)$ the Fourier transformation of the envelope of the probe laser $I_0(t)/[\int I_0(t')dt']$. Rewriting Eq. (C.24) as an electric field expression yields

$$S_{\mathrm{EO}}(\omega) \simeq E_{\mathrm{THz}}(\omega) T_{\mathrm{in}}(\omega) T_{\mathrm{crystal}}(\omega) I_{\mathrm{env},0}(\omega), \tag{C.25}$$

which was also derived in Refs. [101, 102]. Note that Eq. (C.24) is exact in either the limit where $\sigma_L \to 0$ (ultra-short laser beam) or if $\Gamma_{\mathrm{THz}} \ll 1$. Only if both $\Gamma_{\mathrm{THz}} \gtrsim 1$ and $\sigma_L > \sigma_{\mathrm{THz}}$, with σ_{THz} the characteristic duration of the THz pulse, is the approximation of Eq. (C.24) no longer valid.

To demonstrate that Eq. (C.24) also holds for the regime that will be discussed in this thesis, the following parameters are considered: a THz retardation profile $\Gamma_{\mathrm{THz}}(t)$ is calculated for a 50 fs (rms) electron bunch, a transverse boundary size of $\rho = 100$ μm, an observation angle of $\theta = 19°$, and a mono-energetic electron distribution at $u = 10$ [derived from Eq. (3.26)]. THz propagation through a 200-μm-thick GaP crystal is considered. Section C.5.2 will discuss the function $T_{\mathrm{crystal}}(\omega) = T_{\mathrm{GaP}}(\omega)$ in more detail, and for now it defined that $T_{\mathrm{in}}(\omega) = 1$. Circular polarization ($\delta = \pi/4$) is considered for the laser beam, which has a length of 50 fs (intensity FWHM). Figure C.6 shows the modeled THz retardation profile $\Gamma_{\mathrm{THz}}(t)$ as open circles, with (a) a peak amplitude of $|\Gamma_{\mathrm{THz}}(t)|$=0.5 rad and (b) $|\Gamma_{\mathrm{THz}}(t)|$=1 rad. From $\Gamma_{\mathrm{THz}}(t)$, a modeled transmission profile $M(\tau)$ is calculated. The solid curves represent the retrieved profiles $\Gamma_{\mathrm{THz}}(t)$ based on the application of $H_{\mathrm{inv}}[M(t)]$ and the approximated expression of Eq. (C.24). The dotted curves represent the retrieved profiles $\Gamma_{\mathrm{THz}}(t)$ based on the assumption that $\Gamma_{\mathrm{THz}} \ll 1$, in which case $\Gamma_{\mathrm{cor}}(t) = M(t)$ and Eq. (C.24) is exact. One can see that in Fig. C.6(a) the dotted and dashed curves overlap with the original THz profile, indicating that both the small-Γ_{THz} approximation as well as the approximation of Eq. (C.24) are valid. However, at larger THz fields, see Fig. C.6(b), the small-Γ_{THz} approximation results in an error on the order of 15%, while the approximation of Eq. (C.24) still only has a maximum deviation less than 4%. Since the EOS experiments presented in this thesis have measured a phase retardation less than

$\Gamma_{\mathrm{THz}} = 1$ rad, the steps leading to Eq. (C.24), summarized by Eqs. (C.22) and (C.23), will be applied to all the measurements.

In the single-shot temporal EOS experiments presented in Sec. 5.3, the geometry is slightly different, although the same expressions as Eqs. (C.24) and (C.25) can be derived. The THz modulation is now induced onto a longer laser pulse $I_0(t)$, yielding the transmitted modulated profile

$$I_m(t) = G[\Gamma^*(t)]I_0(t). \tag{C.26}$$

A second short laser pulse $I_2(t-\tau_2)$, with $\int I_2(t')dt' = 1$, is used to non-collinearly probe the modulation with a spatially-varying delay τ_2. The energy profile $I_{2\omega}(\tau_2)$ of the frequency-doubled light (see Sec. 5.3.3 for explanation), measured by an energy detector (1D or 2D array), is given by

$$I_{2\omega}(\tau_2) = \int G[\Gamma^*(t)]I_0(t)I_2(t-\tau_2)dt. \tag{C.27}$$

Since $I_0(t)$ is much longer than the probe laser $I_2(t)$, the approximation $I_0(t)I_2(t-\tau_2) \simeq I_0(\tau_2)I_2(t-\tau_2)$ is valid. This allows for the construction of the normalized measurement $M(\tau_2)$, given by

$$M(\tau_2) = \frac{I_{2\omega}(\tau_2) - G[\Gamma^* = 0]I_0(\tau_2)}{I_0(\tau_2)} = \int H[\Gamma^*(t)]I_2(t-\tau_2)dt, \tag{C.28}$$

where the factor $G[\Gamma^* = 0]I_0(\tau_2)$ represents the measurement in absence of the THz field and the factor $I_0(\tau_2)$ represents the measurement in absence the THz field, with the $\lambda/4$ plate removed, and with the analyzer rotated for maximum transmission. In analogy to the scanning geometry, a corrected retardation profile $\Gamma_{\mathrm{cor}}(\tau_2)$ is defined as $\Gamma_{\mathrm{cor}}(\tau_2) = H_{\mathrm{inv}}[M(\tau_2)]$, leading to the approximated expressions

$$\Gamma_{\mathrm{cor}}(\omega) \simeq \Gamma^*(\omega)I_{\mathrm{env},2}(\omega) = \Gamma_{\mathrm{THz}}(\omega)T_{\mathrm{in}}(\omega)T_{\mathrm{crystal}}(\omega)I_{\mathrm{env},2}(\omega), \tag{C.29}$$

and

$$S_{\mathrm{EO}}(\omega) \simeq E_{\mathrm{THz}}(\omega)T_{\mathrm{in}}(\omega)T_{\mathrm{crystal}}(\omega)I_{\mathrm{env},2}(\omega), \tag{C.30}$$

with $I_{\mathrm{env},2}(\omega)$ the Fourier transformation of the envelope of the probe laser $I_2(t)$. The validity of Eqs. (C.29) and (C.30) was discussed previously.

C.5 Crystal characterization

In the experiments described in this thesis two different crystals were used, namely 200-μm-thick ZnTe and 200-μm-thick GaP. The properties of each of these crystals, and how they affect the measurements of the THz field, will be discussed here.

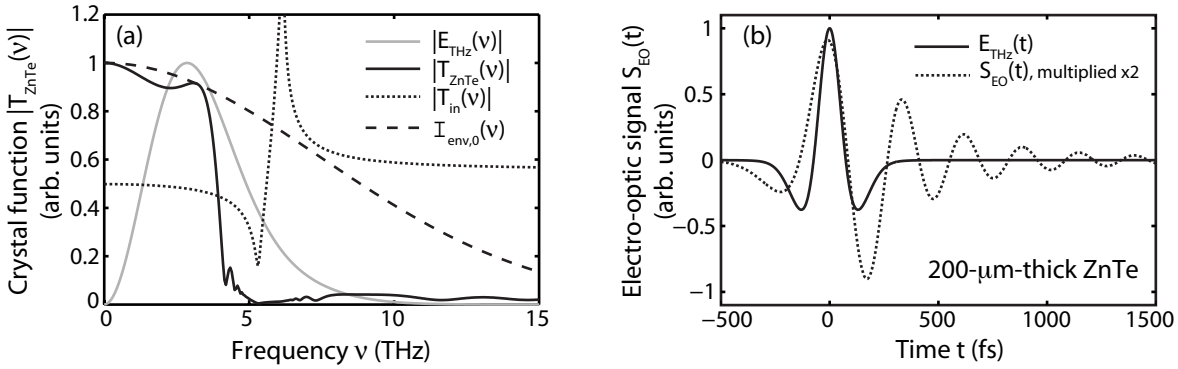

Fig. C.7. (a) Curves for the spectral crystal function $|T_{\mathrm{ZnTe}}(\nu)|$ of 200-μm-thick ZnTe (solid black curve), the laser envelope spectrum $I_{\mathrm{env},0}(\nu)$ (dashed black curve), the surface crystal transmission $|T_{\mathrm{in}}(\nu)|$ (dotted black curve), and THz radiation from a 50 fs (rms) electron bunch $|E_{\mathrm{THz}}(\nu)|$ (grey curve). $|E_{\mathrm{THz}}(\nu)|$ was calculated with electron momentum $u = 10$, observation angle $\theta = 0.3$ rad, and boundary size $\rho = 150$ μm. Note that the crystal response is only effective in the frequency range $0 - 4$ THz. (b) Temporal waveforms for the THz electric field $E_{\mathrm{THz}}(t)$ (solid curve), and the EO signal $S_{\mathrm{EO}}(t)$ (dotted curve). The function $S_{\mathrm{EO}}(t)$ is multiplied by $\times 2$ for clarity. Due to absorption and dispersion, the single-cycle THz waveform appears as a longer multi-cycle EOS waveform. (Figure from Refs. [1, 2].)

C.5.1 ZnTe crystal properties

For ZnTe, the index of refraction can be found in the literature [102–105], and is

$$\begin{aligned} \text{ZnTe}: \qquad n^2_{\mathrm{THz}}(\nu) &= \epsilon_\infty \left(1 + \frac{\nu^2_{LO} - \nu^2_{TO}}{\nu^2_{TO} - \nu^2 - \imath\gamma\nu}\right) \\ n^2_{\mathrm{NIR}}(\lambda) &= 4.27 + \frac{3.01 \times \lambda^2}{\lambda^2 - 0.142}, \end{aligned} \tag{C.31}$$

with n_{NIR} the index of refraction in the near-infrared regime, λ in units of [μm], ν_{TO}=5.31 THz (absorption line), ν_{LO}=6.18 THz, γ=90.3 GHz, $\epsilon_\infty = 6.7$, and $r_{14} = 4.0 \times 10^{-12}$ m V^{-1} [106]. The group velocity of the laser at $\lambda_0 = 0.8$ μm is found to be $v_{\mathrm{gr}} = c/n_{\mathrm{gr}} = c/3.24$.

Figure C.7(a) illustrates, in the frequency domain, the crystal function $|T_{\mathrm{ZnTe}}(\nu)|$ for a 200-μm-thick $\langle 110 \rangle$-cut ZnTe (see black solid curve). Although the main absorption line lies at $\nu = 5.31$ THz, the effective use of the crystal is in the range 0–4 THz, mainly due to the mismatch in velocity between the THz and probe pulse. In the same figure, the dashed black curve indicates the envelope spectrum of the probe beam $I_{\mathrm{env},0}(\nu)$, and the dotted black curve indicates the surface transmission function $|T_{\mathrm{in}}(\nu)|$ for the THz through the front crystal surface. Note that within the effective crystal response 0–4 THz, the surface transmission function can be approximated to be flat. Within the same frequency range, the EO coefficient is also assumed to be frequency independent. The solid grey curve in Fig. C.7(a) illustrates the spectral field profile $|E_{\mathrm{THz}}(\nu)|$ for a THz pulse generated by a 50 fs (rms) electron bunch with momentum $u = 10$, observed at θ =0.3 rad, and at boundary size $\rho = 150$ μm. One can see that the 200-μm-thick ZnTe response is just covering the maximum of the THz field profile around 3 THz.

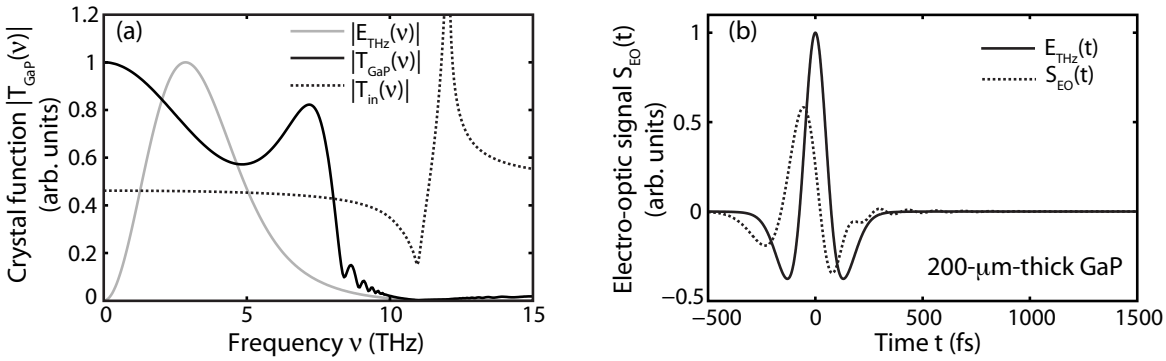

Fig. C.8. a) Curves for the spectral crystal function $|T_{\mathrm{GaP}}(\nu)|$ of 200-μm-thick GaP (solid black curve), the surface crystal transmission $|T_{\mathrm{in}}(\nu)|$ (dotted black curve), and THz radiation from a 50 fs (rms) electron bunch $|E_{\mathrm{THz}}(\nu)|$ with $u = 10$, $\theta = 0.3$ rad, and $\rho = 150$ μm (grey curve). Note that the crystal response is effective for the frequency range 0–8 THz. (b) Temporal waveforms for the THz electric field $E_{\mathrm{THz}}(t)$ (solid curve), and the EO signal $S_{\mathrm{EO}}(t)$ (dotted curve). Due to the absence of strong spectral absorption and dispersion, the single-cycle THz waveform also appears as a single-cycle EOS waveform. (Figure from Ref. [2].)

Figure C.7(b) shows both the original temporal THz profile $E_{\mathrm{THz}}(t)$ (solid curve) as well as the electro-optic signal $S_{\mathrm{EO}}(t)$ (dotted curve) calculated from Eqs. (C.22) and (C.23). For clarity, the function $S_{\mathrm{EO}}(t)$ was multiplied by 2. One can observe from Fig. C.7(b) that the originally-single-cycle THz waveform $E_{\mathrm{THz}}(t)$ is observed electro-optically as a multi-cycle EOS waveform $S_{\mathrm{EO}}(t)$, mainly due to a spectral cut-off around 4 THz and dispersion for the remaining 0–4 THz frequencies. Also, the peak electric field is reduced by a factor of $\simeq 2$.

C.5.2 GaP crystal properties

For GaP, the index of refraction can be found in the literature [102, 104, 107, 108], and is

$$\begin{aligned} \text{GaP}: \qquad & n^2_{\mathrm{THz}}(\nu) = \epsilon_\infty + \frac{S_0\,(1-S_1-S_2)\,\nu_0^2}{\nu_0^2-\nu^2+\imath\nu\gamma_0-\frac{S_1\nu_1^2\nu_0^2}{\nu_1^2-\nu^2+\imath\nu\gamma_1}-\frac{S_2\nu_2^2\nu_0^2}{\nu_2^2-\nu^2+\imath\nu\gamma_2}} \\ & n^2_{\mathrm{NIR}} = 1+\frac{34.9}{13.7-\left(\frac{1.28}{\lambda}\right)^2}+\frac{155}{28.1-\left(\frac{1.28}{\lambda}\right)^2}+\frac{0.00398}{0.00205-\left(\frac{1.28}{\lambda}\right)^2}, \end{aligned} \tag{C.32}$$

with λ in units of [μm], $S_0 = 2.01$, $S_1 = 7.0\times10^{-4}$, $S_2 = 3.5\times10^{-4}$, $\epsilon_\infty = 9.09$, $\nu_0 = 10.9$ THz, $\nu_1 = 10.5$ THz, $\nu_2 = 10.8$ THz, $\gamma_0 = 33.0$ GHz, $\gamma_1 = 630$ GHz, and $\gamma_2 = 378$ GHz. The EO coefficient for GaP is not know but was estimated to be half of equally-thick ZnTe, or $r_{14} \simeq 2\times10^{-12}\,\mathrm{m\,V^{-1}}$. The group velocity of the laser at $\lambda_0 = 0.8$ μm is found to be $v_{\mathrm{gr}} = c/n_{\mathrm{gr}} = c/3.57$.

Figure C.8(a) illustrates, in the frequency domain, the crystal function $|T_{\mathrm{GaP}}(\nu)|$ for 200-μm-thick $\langle110\rangle$-cut GaP (see black solid curve). Although the main absorption lines lie at ν =10.5 THz and ν =10.8 THz, the effective use of the crystal is up to 8 THz, mainly due to the mismatch in velocity between the THz and probe pulse. In Fig. C.8(a), the dashed black curve indicates the envelope spectrum of the probe beam $I_{\mathrm{env},0}(\nu)$, and the

dotted black curve indicates the surface transmission function $|T_{\text{in}}(\nu)|$ for the THz through the front crystal surface. Note that within the effective crystal response 0–8 THz, the surface transmission function can be assumed to be flat. In this same frequency range, the EO coefficient is also assumed to be frequency independent. The solid grey curve in Fig. C.8(a) illustrates the spectral field profile $|E_{\text{THz}}(\nu)|$ for a THz pulse generated by a 50 fs (rms) electron bunch with $u = 10$, θ =0.3 rad, and $\rho = 150$ μm. One can see that the 200-μm-thick GaP response covers almost the entire THz pulse spectrum.

Figure C.8(b) shows both the original temporal THz profile $E_{\text{THz}}(t)$ (solid curve) as well as the electro-optic signal $S_{\text{EO}}(\tau)$ (dotted curve) calculated from Eqs. (C.22) and (C.23). One can observe from Fig. C.8(b) that the originally-single-cycle THz waveform $E_{\text{THz}}(t)$ also appears as a single-cycle EOS waveform $S_{\text{EO}}(t)$, since spectral absorption and dispersion are absent over the 0–8 THz range. The peak electric field is reduced by a factor of $\simeq 1.6$.

C.5.3 Localization of the crystal axis

When using an EO crystal, it might not be clear how the $\langle 001 \rangle$ axis (z or z' axis), see Fig. C.1(a), is oriented. As the solid curve in Fig. C.3(a) illustrates, improper alignment of the crystal axis with respect to the THz and laser fields can lead to zero EO-induced effect on the laser transmission. One can of course simply scan the crystal axis rotation, and optimize the laser transmission. A second technique to find the orientation of the z' axis relies on the use of a laser pulse to generate THz radiation through optical rectification (OR). In case of crystals such as GaP and ZnTe, the total radiated THz energy through OR is a strong function of the orientation of the $\langle 001 \rangle$ crystal axis with respect to the laser polarization. Through the laser-crystal interaction, two frequency components $\omega_0 + \delta\omega_1$ and $\omega_0 + \delta\omega_2$, both within the laser spectrum envelope, can interfere and emit difference frequency radiation at $\delta\omega_1 - \delta\omega_2$. For femtosecond-duration lasers, the spectrum of the radiation lies in the THz regime. This process is referred to as optical rectification [100].

Figure C.9(a) depicts the setup for THz generation through OR. The collimated laser pulse was polarized in the horizontal plane, had a beam diameter of 6 mm (intensity FWHM), and a pulse width of 400 fs (intensity FWHM). The angle of the $\langle 001 \rangle$ axis with respect to the laser polarization is defined as η, which was varied during the experiment. The bolometer, gain of $\chi = 1000$, was operating in the 0.3–30 THz regime. A silicon wafer and a 800-nm-AR-coated nitrocellulose pellicle were positioned in front of the bolometer to reflect remnant laser light. Theory predicts [100] that the emitted THz radiation $|E_{\text{THz}}|^2$, from a $\langle 110 \rangle$-cut ZnTe or GaP crystal, scales with η through

$$|E_{\text{THz}}|^2 \propto r_{14}^2 E_L^4 \left[\sin^2\eta \left(1 + 3\cos^2\eta\right)\right], \tag{C.33}$$

with E_L the laser pulse peak field, and r_{41} the nonlinear coefficient (same as the EO coefficient). As Eq. (C.33) indicates, the THz emission is zero for $\eta = 0°$ and $\eta = 180°$, where the $\langle 001 \rangle$ axis is parallel to the laser polarization.

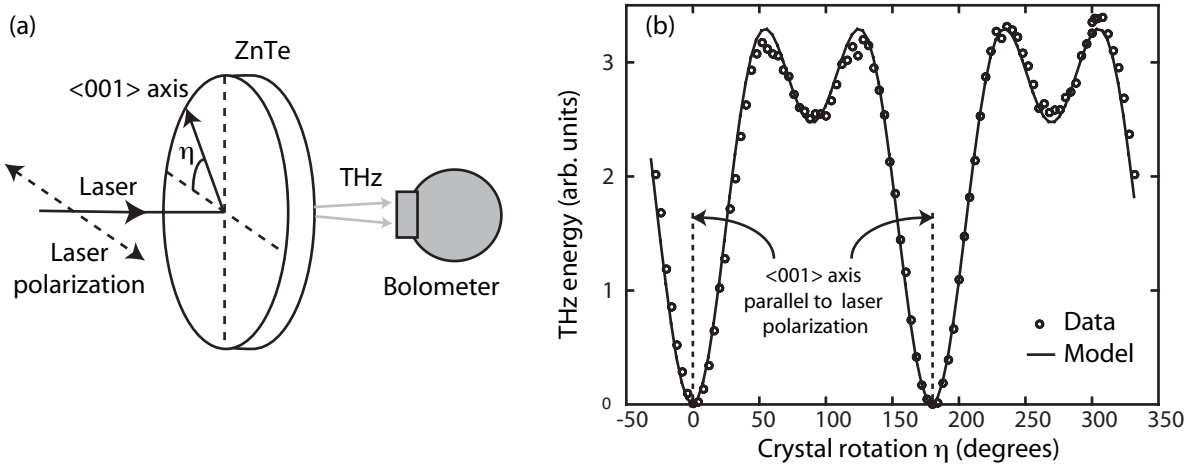

Fig. C.9. (a) Schematic of the setup for THz generation through optical rectification in ZnTe. The collimated laser pulse was polarized in the horizontal plane. The angle η of the $\langle 001 \rangle$ axis (z or z' axis) with respect to the laser polarization was varied during the experiment. A silicon wafer and a 800-nm-AR-coated nitrocellulose pellicle were positioned in front of the bolometer to reflect remnant laser light. (b) THz energy ($\sim$ bolometer voltage) versus crystal axis rotation η. The minima occur at $\eta = 0°$ and $\eta = 180°$, where the $\langle 001 \rangle$ axis is parallel to the laser polarization. The solid curve represents the modeled THz energy, indicating a good agreement between theory and measurement.

Figure C.9(b) shows the measured OR-produced THz energy versus crystal axis rotation η. Each data point represents an average of 15 shots. The error bar is less than 3% of each mean value. A modeled curve, based on Eq. (C.33), is plotted in Fig. C.9(b). Good agreement with data and theory allows for determination of the z' axis, which is the axis parallel to the laser polarization if the crystal is rotated at $\eta = 0°$ or $\eta = 180°$.

Summary

Theoretical and experimental studies are presented of coherent terahertz radiation (THz radiation, wavelength $10 - 1000$ μm), emitted by electron bunches from a laser wakefield accelerator (LWFA). The studies have been performed at the Lawrence Berkeley National Laboratory in Berkeley, California.

Through the nonlinear interaction of an intense laser pulse ($> 10^{19}$ W cm^{-2}) with a helium plasma, longitudinal electric fields ($\approx 10 - 100$ GV m^{-1}), which are roughly 2-3 orders of magnitude stronger than in a conventional accelerator, result in the production of relativistic electron bunches. The femtosecond bunches emit coherent THz radiation as they propagate through the plasma-vacuum boundary (coherent transition radiation).

Characterization of the THz pulse parameters allows for analysis of the electron bunch charge profile. Additionally, since the THz pulse is intense and intrinsically synchronized to the laser pulse and electron bunch, unique possibilities for THz applications exist.

In order to characterize the THz pulse, several measurement techniques have been applied. A THz energy detector shows that the THz energy has a quadratic dependence on electron bunch charge, as is expected for coherent radiation from an electron bunch. The polarization properties of the radiation are also found to agree with theoretical predictions.

Through electro-optic sampling (EOS), the temporal THz field profile is measured with both single- and multi-shot techniques. The data shows that the coherent THz spectrum extends from $0 - 6$ THz, while the temporal profile consists predominantly of a single-cycle field oscillation with a peak field of $\simeq 0.4$ MV cm^{-1}. Through comparison with a model, the electron bunches are found to have a duration of < 50 fs (rms). The temporal jitter in bunch length and synchronization is < 10 fs.

At times, a weaker second field cycle is present in the measured THz profile, and two-dimensional EOS (THz imaging) is implemented to study this double-THz-pulse waveform. The 2D field distribution shows a main THz spot with a diameter of $\simeq 800$ μm, as well as the presence of spatial substructure related to optical aberrations. The measured substructure in both the temporal and 2D experiments indicate spatio-temporal coupling of the THz pulse at focus. A theoretical model, based on the propagation of a single-cycle pulse through an optical system with coma, confirms the coupling. Understanding of the spatio-temporal THz coupling is especially important for THz-based electron bunch analysis.

Samenvatting

Dit proefschrift behandelt een theoretische en experimentele studie naar coherente THz-straling (golflengte $10 - 1000$ μm) afkomstig van elektronenbundels die geproduceerd zijn door de laser-plasmagolf-versneller (LWFA). Het werk is verricht aan het Lawrence Berkeley National Laboratory in Berkeley, Californië.

Tijdens de interactie tussen een krachtige laserpuls ($> 10^{19}$ W cm^{-2}) en een heliumplasma zorgen krachtige longitudinale elektrische velden ($\approx 10 - 100$ GV m^{-1}, $2 - 3$ ordegroottes krachtiger dan in een conventionele deeltjesversneller) voor de productie van relativistische elektronen. De ultrakorte elektronenbundels zenden coherente THz-straling uit als ze de plasma-vacuüm-overgang passeren (coherente transitiestraling).

Enerzijds leidt karakterisatie van de THz-puls tot een tijdsanalyse van de elektronenbundel. Anderzijds biedt de productie van de krachtige THz-puls, intrinsiek gesynchroniseerd met de laserpuls en elektronenbundel, unieke mogelijkheden voor THz-toepassingen.

Om de THz-puls te karakteriseren is een aantal meetmethoden toegepast. Een energiedetector laat zien dat de THz-straling een kwadratische afhankelijkheid van de bundellading vertoont, wat te verwachten valt voor coherente straling van een elektronenbundel. Ook komen de polarisatie-eigenschappen van de THz-puls overeen met de theorie.

Door middel van zowel 'single-shot' als 'multi-shot' elektro-optisch samplen (EOS) is het veldprofiel van de THz-puls gemeten. De data toont aan dat het THz-spectrum frequenties bevat van $0 - 6$ THz, terwijl het veldprofiel in het tijdsdomein uit een enkele oscillatie bestaat met amplitude $\simeq 0{,}4$ MV cm^{-1}. Het vergelijken van de data met een model toont aan dat de tijdsduur van de elektronenbundel kleiner is dan 50 fs (rms). De fluctuatie in de bundellengte en synchronisatie bedraagt minder dan 10 fs.

Soms is een tweede zwakkere THz-puls aanwezig in het gemeten veldprofiel, en tweedimensionaal EOS ('THz imaging') is gebruikt om dit dubbel-THz-profiel te bestuderen. Het 2D-veldprofiel toont een 'hoofd-spot' met een diameter van $\simeq 800$ μm, alsmede de aanwezigheid van een transversale substructuur veroorzaakt door optische aberraties. De substructuur is zowel aanwezig in ruimte als tijd, wat een koppeling tussen beide in het brandpunt suggereert. Een theoretisch model, gebaseerd op de propagatie van een korte puls door een optisch systeem met coma, bevestigt de koppeling. Het is onder andere voor de analyse van de elektronenbundel belangrijk om de koppeling te begrijpen.

List of publications

- *Temporal characterization of femtosecond laser-plasma-accelerated electron bunches using terahertz radiation*, by J. van Tilborg, C.B. Schroeder, C.V. Filip, Cs. Tóth, C.G.R. Geddes, G. Fubiani, R. Huber, R.A. Kaindl, E. Esarey, and W.P. Leemans, Phys. Rev. Lett. **96**(1), 014801 (2006)

- *Single-shot spatio-temporal measurements of high-field terahertz pulses*, by J. van Tilborg, C.B. Schroeder, Cs. Tóth, C.G.R. Geddes, E. Esarey, and W.P. Leemans, Phys. Rev. Lett., submitted (2006)

- *High-quality electron beams from a laser wakefield accelerator using plasma-channel guiding*, by C.G.R. Geddes and Cs. Toth, J. van Tilborg, E. Esarey, C.B. Schroeder, D. Bruhwiler, C. Nieter, J. Cary, and W.P. Leemans, Nature **431**(7008), 538 (2004)

- *Observation of terahertz emission from a laser-plasma accelerated electron bunch crossing a plasma-vacuum boundary*, by W.P. Leemans, C.G.R. Geddes, J. Faure, Cs. Tóth, J. van Tilborg, C.B. Schroeder, E. Esarey, G. Fubiani, D. Auerbach, B. Marcelis, M.A. Carnahan, R.A. Kaindl, J. Byrd, and M.C. Martin, Phys. Rev. Lett. **91**(7), 074802 (2003)

- *Guiding of relativistic laser pulses by preformed plasma channels*, by C.G.R. Geddes, Cs. Tóth, J. van Tilborg, E. Esarey, C.B. Schroeder, J. Cary and W.P. Leemans, Phys. Rev. Lett. **95**(14), 145002 (2005)

- *Electron-yield enhancement in a laser-wakefield accelerator driven by asymmetric laser pulses*, by W.P. Leemans, P. Catravas, E. Esarey, C.G.R. Geddes, C. Toth, R. Trines, C.B. Schroeder, B.A. Shadwick, J. van Tilborg, and J. Faure, Phys. Rev. Lett. **89**(17), 174802 (2002)

- *THz radiation as a bunch diagnostic for laser-wakefield-accelerated electron bunches*, by J. van Tilborg, C.B. Schroeder, C.V. Filip, Cs. Tóth, C.G.R. Geddes, G. Fubiani, E. Esarey, and W.P. Leemans, Phys. Plasmas **13**(5), 056704 (2006)

- *Pulse shape and spectrum of coherent diffraction-limited transition radiation from electron beams*, by J. van Tilborg, C.B. Schroeder, E. Esarey, and W.P. Leemans, Laser Part. Beams **22**(4), 415 (2004)

- *Theory of coherent transition radiation generated at a plasma-vacuum interface*, by C.B. Schroeder, E. Esarey, J. van Tilborg, and W.P. Leemans, Phys. Rev. E **69**(1), 016501 (2004)

- *Terahertz radiation from laser accelerated electron bunches*, by W.P. Leemans, J. van Tilborg, J. Faure, C.G.R. Geddes, Cs. Tóth, C.B. Schroeder, E. Esarey, G. Fubiani, and G. Dugan, Phys. Plasmas **11**(5), 2899 (2004)

- *Modeling laser-based table-top THz sources: Optical Rectification, propagation and electro-optic sampling*, by J. Faure, J. van Tilborg, R.A. Kaindl, and W. P. Leemans, Opt. Quantum Electron. **36**(8), 681 (2004)

- *Radiation from laser accelerated electron bunches: coherent terahertz and femtosecond X-rays*, by W.P. Leemans, E. Esarey, J. van Tilborg, P.A. Michel, C.B. Schroeder, Cs. Tóth, C. G. R. Geddes, and B. A. Shadwick, IEEE Trans. Plasma Sci. **33**, 8 (2005)

- *Production of high-quality electron bunches by dephasing and beam loading in channeled and unchanneled laser plasma accelerators*, by C.G.R. Geddes, Cs. Tóth, J. van Tilborg, E. Esarey, C.B. Schroeder, D. Bruhwiler, C. Nieter, J. Cary, and W.P. Leemans, Phys. Plasmas **12**(5), 056709 (2005)

- *Tuning of laser pulse shapes in grating-based compressors for optimal electron acceleration in plasmas*, by Cs. Tóth, J. Faure, J. van Tilborg, C.G.R. Geddes, C.B. Schroeder, E. Esarey, and W.P. Leemans, Opt. Lett. **28**(19), 1823 (2003)

- *Frequency chirp and pulse shape effects in self-modulated laser wakefield accelerators*, C.B. Schroeder, E. Esarey, C.G.R. Geddes, Cs. Tóth, B.A. Shadwick, J. van Tilborg, J. Faure, and W.P. Leemans, Phys. Plasmas **10**(5), 2039 (2003)

About the author

Jeroen van Tilborg was born in Eindhoven, the Netherlands, on the 14th of January, 1978. He spent his childhood living nearby in Best, and in 1995 he received his "VWO Gymnasium" degree from the Jacob-Roelandslyceum, Boxtel. Starting in 1995, Jeroen studied at the Eindhoven University of Technology, Eindhoven. He obtained his master's degree in Applied Physics in 2001 on the topic "Spin polarization and superconductivity in Andreev point contacts", in the group of prof.dr.ir. W.J.M. de Jonge.

During his undergraduate studies, he participated in a 3-month internship in the group of prof.dr.ir. W.P. Leemans at the Lawrence Berkeley National Laboratory in Berkeley, California. It was through these contacts that Jeroen started his Ph.D. in that same group in the summer of 2001. With prof.dr.ir. W.P. Leemans as the local promotor, prof.dr. M.J. van der Wiel served as the promotor at the Eindhoven University of Technology. After receiving his Ph.D. degree, Jeroen will start a post-doctocal position in August 2006 at the Ultrafast X-ray Science Laboratory at the Lawrence Berkeley National Laboratory.

During his years as a student, Jeroen was active in student organizations and community outreach programs.

Acknowledgements

This Ph.D. has been an incredible experience for me. The opportunity to work in a first-class research laboratory, located within the dynamic social environment of the Bay Area, has made a big impact on my life. At the Lawrence Berkeley National Laboratory (LBNL), Wim Leemans was more than my supervisor: he was my mentor, and I feel lucky that I was exposed to so many of his good qualities. Thanks Wim, for having that infinite amount of energy, great ideas, and confidence in me. You know how to balance your group in terms of work efforts and team spirit, which made it very enjoyable to spend the last few years in Berkeley. I want to thank Marnix van der Wiel (Eindhoven University of Technology) for being my advisor in the Netherlands. Too bad that we did not see each other that often, but your support was indispensable.

At LBNL, the spirit of the experimental team was very motivating. Wim, Csaba, Jérôme, Catalin, Kei, and Cameron, thanks for sharing your experiences with me. We have spent many hours together, and tackled more problems than I can summarize. I want to thank Eric, Brad, and Carl, for their help in my theoretical understanding of the physics behind this thesis. Carl, we have spent a lot of time going through theory, writing papers, and fine-tuning presentations. Your help was always fast, effective, and constructive. Gwenaël, my Ph.D. is, except for the last half year, unambiguously connected to you. Our conversations helped me both in physics as well as in my personal life. I will forgive you for the fact that in your acknowledgements you forgot to thank me for all my free ski lessons. Pierre, Estelle, and Bob, it was very pleasant to be part of the same group. Our lunch breaks and conversations were always of good quality. I also want to thank all the students and post-docs who have spent time side by side with me in the last few years, including Bout, Ned, Guillaume, Luke, Erik R., Benoît, and Vincent. Guillaume, I think it is great that you are continuing our THz efforts.

One critical part of the LOASIS facility is the excellent technical support. Mike, Don, Joe, and Nathan: you are fast, supportive, communicative, and you only deliver the best quality. Thanks for all your help! Olivia and Tom, your administrative support and organization of the social events helped create the pleasant and trouble-free work environment that I enjoyed for all these years. Sorry that I didn't always cook for potluck parties (still practicing).

Many of the ideas and results presented in this thesis have been accomplished through communication and collaboration with experts in various fields. Rupert Huber and Robert Kaindl, thanks for your help regarding electro-optic sampling. Rupert, you made a deep impact towards this understanding. Zhao Hao, Michael Martin, Jason Singley, and John Byrd, your assistance involving THz detection was very useful.

My work in Berkeley did not entirely come at zero cost. I want to thank my family (Henk, Marij, Michiel, and Arlette) for supporting my decision to study abroad. Especially without the guidance of my parents, I would have never achieved this Ph.D. They are the ones who opened my eyes to the world. Luckily, we maintained a close and personal contact over the years.

Christina, you played an important role in my life in the last few years. You know what they say: behind every graduate student stands a strong and supportive girlfriend. Your efforts as a cook, spell checker, shrink, and motivator, were crucial to this thesis. Christina's family has provided me with a home away from home. I want to thank Ali, Winston, Jen, Hugh, and Jenny (+kids), for their welcoming spirit.

Here in the U.S.A., a group of international friends has kept my mind healthy and productive. In addition to some of the people mentioned earlier, I also want to thank Mona, Mathias, Irma, Aarash, Heather, Staffan, Solette, Jim McG., Tony, Clas, Falk, Vanessa, Meg, Ryan, Marilyne, and Igor, for their friendship. Berkeley is a place where people from all over the world come and go, and I hope all of us will stay in touch.

To my friends in the Netherlands I want to say the following: Robbert, Ellen, Martijn, Erik K., Saskia, Erik D., Mechiel, Tatiana, Jim H., and Nicole: thanks for making this long-distance friendship work. We were always motivating and stimulating towards each other during our student years. Eugene, Bas, Jeroen, and Erik M., thanks for being part of my long-term transformation from the Vestdijk to Berkeley.

Ook nog een woordje voor de Klabotsenaren: bedankt voor jullie indirecte bijdrage (al 28 jaar). Yvonne, Cees, Joke, Miriam en Marte: ook jullie bedankt voor jullie steun gedurende mijn Berkeley jaren.

References

[1] J. van Tilborg, C. B. Schroeder, C. V. Filip, Cs. Tóth, C. G. R. Geddes, G. Fubiani, R. Huber, R. A. Kaindl, E. Esarey, and W. P. Leemans, Phys. Rev. Lett. **96**(1), 014801 (2006).

[2] J. van Tilborg, C. B. Schroeder, C. V. Filip, C. Tóth, C. G. R. Geddes, G. Fubiani, E. Esarey, and W. P. Leemans, Phys. Plasmas **13**(5), 056704 (2006).

[3] E. Esarey, P. Sprangle, J. Krall, and A. Ting, IEEE Trans. Plasma Sci. **24**(2), 252 (1996).

[4] E. Esarey, C. B. Schroeder, and W. P. Leemans, Rev. Mod. Phys., in press (2006).

[5] T. Tajima and J. M. Dawson, Phys. Rev. Lett. **43**(4), 267 (1979).

[6] D. Strickland and G. Mourou, Opt. Commun. **56**(3), 219 (1985).

[7] A. Modena, Z. Najmudin, A. E. Dangor, C. E. Clayton, K. A. Marsh, C. Joshi, V. Malka, C. B. Darrow, C. Danson, D. Neely, *et al.*, Nature **377**(6550), 606 (1995).

[8] D. Umstadter, S.-Y. Chen, A. Maksimchuk, G. Mourou, and R. Wagner, Science **273**(5274), 472 (1996).

[9] A. Ting, C. I. Moore, K. Krushelnick, C. Manka, E. Esarey, P. Sprangle, R. Hubbard, H. R. Burris, R. Fischer, and M. Baine, Phys. Plasmas **4**(5), 1889 (1997).

[10] V. Malka, S. Fritzler, E. Lefebvre, M.-M. Aleonard, F. Burgy, J.-P. Chambaret, J.-F. Chemin, K. Krushelnick, G. Malka, S. P. D. Mangles, *et al.*, Science **298**, 1596 (2002).

[11] W. P. Leemans, D. Rodgers, P. E. Catravas, C. G. R. Geddes, G. Fubiani, E. Esarey, B. A. Shadwick, R. Donahue, and A. Smith, Phys. Plasmas **8**(5), 2510 (2001).

[12] W. P. Leemans, P. Catravas, E. Esarey, C. G. R. Geddes, C. Toth, R. Trines, C. B. Schroeder, B. A. Shadwick, J. van Tilborg, and J. Faure, Phys. Rev. Lett. **89**(17), 174802 (2002).

[13] S. P. D. Mangles, C. D. Murphy, Z. Najmudin, A. G. R. Thomas, J. L. Collier, A. E. Dangor, E. J. Divall, P. S. Foster, J. G. Gallacher, C. J. Hooker, *et al.*, Nature **431**(7008), 535 (2004).

[14] C. G. R. Geddes, Cs. Toth, J. van Tilborg, E. Esarey, C. B. Schroeder, D. Bruhwiler, C. Nieter, J. Cary, and W. P. Leemans, Nature **431**(7008), 538 (2004).

[15] J. Faure, Y. Glinec, A. Pukhov, S. Kiselev, S. Gordienko, E. Lefebvre, J.-P. Rousseau, F. Burgy, and V. Malka, Nature **431**(7008), 541 (2004).

[16] K-C. Tzeng, W. B. Mori, and T. Katsouleas, Phys. Rev. Lett. **79**(26), 5258 (1997).

[17] E. Esarey, B. Hafizi, R. Hubbard, and A. Ting, Phys. Rev. Lett. **80**(25), 5552 (1998).

[18] J. van Tilborg, C. B. Schroeder, Cs. Tóth, C. G. R. Geddes, E. Esarey, and W. P. Leemans, Phys. Rev. Lett., submitted (2006).

[19] A. L. Cavalieri, D. M. Fritz, S. H. Lee, P. H. Bucksbaum, D. A. Reis, J. Rudati, D. M. Mills, P. H. Fuoss, G. B. Stephenson, C. C. Kao, *et al.*, Phys. Rev. Lett. **94**(11), 114801 (2005).

[20] X. Yan, A. M. MacLeod, W. A. Gillespie, G. M. H. Knippels, D. Oepts, A. F. G. van der Meer, and W. Seidel, Phys. Rev. Lett. **85**(16), 3404 (2000).

[21] I. Wilke, A. M. MacLeod, W. A. Gillespie, G. Berden, G. M. H. Knippels, and A. F. G. van der Meer, Phys. Rev. Lett. **88**(12), 124801 (2002).

[22] T. Srinivasan-Rao, M. Amin, V. Castillo, D. M. Lazarus, D. Nikas, C. Ozben, Y. K. Semertzidis, A. Stillman, T. Tsang, and L. Kowalski, Phys. Rev. ST Accel. Beams **5**(4), 042801 (2002).

[23] G. Berden, S. P. Jamison, A. M. MacLeod, W. A. Gillespie, B. Redlich, and A. F. G. van der Meer, Phys. Rev. Lett. **93**(11), 114802 (2004).

[24] U. Happek, A. J. Sievers, and E. B. Blum, Phys. Rev. Lett. **67**(21), 2962 (1991).

[25] P. Kung, H.-C. Lihn, H. Wiedemann, and D. Bocek, Phys. Rev. Lett. **73**(7), 967 (1994).

[26] Y. Shibata, T. Takahashi, T. Kanai, K. Ishi, M. Ikezawa, J. Ohkuma, S. Okuda, and T. Okada, Phys. Rev. E **50**(2), 1479 (1994).

[27] A. H. Lumpkin, R. Dejus, W. J. Berg, M. Borland, Y. C. Chae, E. Moog, N. S. Sereno, and B. X. Yang, Phys. Rev. Lett. **86**(1), 79 (2001).

[28] G. L. Carr, M. C. Martin, W. R. McKinney, K. Jordan, G. R. Neil, and G. P. Williams, Nature **420**(14), 153 (2002).

[29] W. P. Leemans, C. G. R. Geddes, J. Faure, Cs. Tóth, J. van Tilborg, C. B. Schroeder, E. Esarey, G. Fubiani, D. Auerbach, B. Marcelis, *et al.*, Phys. Rev. Lett. **91**(7), 074802 (2003).

[30] C. B. Schroeder, E. Esarey, J. van Tilborg, and W. P. Leemans, Phys. Rev. E **69**(1), 016501 (2004).

[31] W. P. Leemans, J. van Tilborg, J. Faure, C. G. R. Geddes, Cs. Tóth, C. B. Schroeder, E. Esarey, G. Fubiani, and G. Dugan, Phys. Plasmas **11**(5), 2899 (2004).

[32] J. van Tilborg, C. B. Schroeder, E. Esarey, and W. P. Leemans, Laser Part. Beams **22**(4), 415 (2004).

[33] J. M. Byrd, Z. Hao, M. C. Martin, D. S. Robin, F. Sannibale, R. W. Schoenlein, A. A. Zholents, and M. S. Zolotorev, Phys. Rev. Lett. **96**(16), 164801 (2006).

[34] V. L. Ginzburg and I. M. Frank, Zh. Eksp. Teor. Fiz. **16**, 15 (1946).

[35] M. L. Ter-Mikaelian, *High-energy electromagnetic processes in condensed media* (Wiley, New York, 1972).

[36] J. D. Jackson, *Classical Electrodynamics* (Wiley, New York, 1975).

[37] G. Fubiani, G. Dugan, W. Leemans, E. Esarey, and J. L. Bobin, in *Proceedings of the 2002 Advanced Accelerator Concepts Workshop*, edited by C. E. Clayton and P. Muggli (Amer. Inst. Phys., New York, 2002), vol. 647, pp. 203–212.

[38] H. Hamster, A. Sullivan, S. Gordon, W. White, and R. W. Falcone, Phys. Rev. Lett. **71**(17), 2725 (1993).

[39] H. Hamster, A. Sullivan, S. Gordon, and R. W. Falcone, Phys. Rev. E **49**(1), 671 (1994).

[40] J. Yoshii, C. H. Lai, T. Katsouleas, C. Joshi, and W. B. Mori, Phys. Rev. Lett. **79**(21), 4194 (1997).

[41] N. Yugami, T. Higashiguchi, H. Gao, S. Sakai, K. Takahashi, H. Ito, Y. Nishida, and T. Katsouleas, Phys. Rev. Lett. **89**(6), 065003 (2002).

[42] Z.-M. Sheng, K. Mima, J. Zhang, and H. Sanuki, Phys. Rev. Lett. **94**(9), 095003 (2005).

[43] Z.-M. Sheng, K. Mima, and J. Zhang, Phys. Plasmas **12**(12), 123103 (2005).

[44] B. Ferguson, S. Wang, D. Gray, D. Abbot, and X.-C. Zhang, Opt. Lett. **27**(15), 1312 (2002).

[45] C. Li, K. Lu, Y. Wang, K. Tamura, S. Hosokawa, and M. Inui, Phys. Rev. B **59**(3), 1571 (1999).

[46] T.-I. Jeon and D. Grischkowsky, Phys. Rev. Let. **78**(6), 1106 (1997).

[47] K. B. Nordstrom, K. Johnsen, S. J. Allen, A.-P. Jauho, B. Birnir, J. Kono, T. Noda, H. Akiyama, and H. Sakaki, Phys. Rev. Lett. **81**(2), 457 (1998).

[48] R. A. Kaindl, M. A. Carnahan, D. Hägele, R. Lövenich, and D. S. Chemla, Nature **423**(6941), 734 (2003).

[49] R. Huber, B. A. Schmid, Y. R. Shen, D. S. Chemla, and R. A. Kaindl, Phys. Rev. Lett. **96**(1), 017402 (2006).

[50] J. Orenstein and A. J. Millis, Science **288**(5465), 468 (2000).

[51] M. Kempe and W. Rudolph, Phys. Rev. A **48**(6), 4721 (1993).

[52] M. A. Porras, Phys. Rev. E **65**(2), 026606 (2002).

[53] S. Hunsche, S. Feng, H. G. Winful, A. Leitenstorfer, M. C. Nuss, and E. P. Ippen, J. Opt. Soc. Am. A **16**(8), 2025 (1999).

[54] Zhiping Jiang, F. G. Sun, Q. Chen, and X.-C. Zhang, Appl. Phys. Lett. **74**(9), 1191 (1999).

[55] C. B. Schroeder, E. Esarey, B. A. Shadwick, and W. P. Leemans, Phys. Plasmas **10**(1), 285 (2003).

[56] C. E. Clayton, K. A. Marsh, A. Dyson, M. Everett, A. Lal, W. P. Leemans, R. Williams, and C. Joshi, Phys. Rev. Lett. **70**(1), 37 (1993).

[57] F. Amiranoff, D. Bernard, B. Cros, F. Jacquet, G. Matthieussent, P. Miné, P. Mora, J. Morillo, F. Moulin, A. E. Specka, *et al.*, Phys. Rev. Lett. **74**(26), 5220 (1995).

[58] D. Umstadter, J. K. Kim, and E. Dodd, Phys. Rev. Lett. **76**(12), 2073 (1996).

[59] E. Esarey, R. F. Hubbard, W. P. Leemans, A. Ting, and P. Sprangle, Phys. Rev. Lett. **79**(14), 2682 (1997).

[60] K. Nakamura, G. Fubiani, C. Geddes, P. Michel, J. van Tilborg, C. Tóth, E. Esarey, C. B. Schroeder, and W. P. Leemans, in *Proceedings of the 2004 Advanced Accelerator Concepts Workshop*, edited by V. Yakimenko (2004), vol. 737, pp. 901–906.

[61] S. Bulanov, N. Naumova, F. Pegoraro, and J. Sakai, Phys. Rev. E **58**(5), R5257 (1998).

[62] P. Tomassini, M. Galimberti, A. Giulietti, D. Giulietti, L. A. Gizzi, L. Labate, and F. Pegoraro, Phys. Rev. ST Accel. Beams **6**(12), 121301 (2003).

[63] S. V. Bulanov, F. Pegoraro, A. M. Pukhov, and A. S. Sakharov, Phys. Rev. Lett. **78**(22), 4205 (1997).

[64] J. M. Dawson, Phys. Rev. **113**(2), 383 (1959).

[65] T. P. Coffey, Phys. Fluids **14**(7), 1402 (1971).

[66] T. Katsouleas and W. B. Mori, Phys. Rev. Lett. **61**(1), 90 (1988).

[67] J. B. Rosenzweig, Phys. Rev. A **38**(7), 3634 (1988).

[68] C. B. Schroeder, E. Esarey, and B. A. Shadwick, Phys. Rev. E **72**(05), 055401 (2005).

[69] C. B. Schroeder, E. Esarey, B. A. Shadwick, and W. P. Leemans, Phys. Plasmas **13**(3), 033103 (2006).

[70] T. Katsouleas, S. Wilks, P. Chen, J. M. Dawson, and J. J. Su, Part. Accel. **22**(1), 81 (1987).

[71] Cs. Tóth, J. Faure, J. van Tilborg, C. G. R. Geddes, C. B. Schroeder, E. Esarey, and W. P. Leemans, Opt. Lett. **28**(19), 1823 (2003).

[72] W. P. Leemans, C. W. Siders, E. Esarey, N. E. Andreev, G. Shvets, and W. B. Mori, IEEE Trans. Plasma Sci. **24**(2), 331 (1996).

[73] P. Volfbeyn, E. Esarey, and W. P. Leemans, Phys. Plasmas **6**(5), 2269 (1999).

[74] C. G. R. Geddes, Cs. Tóth, J. van Tilborg, E. Esarey, C. B. Schroeder, D. Bruhwiler, C. Nieter, J. Cary, and W. P. Leemans, Phys. Plasmas **12**(5), 056709 (2005).

[75] C. G. R. Geddes, Cs. Tóth, J. van Tilborg, E. Esarey, C. B. Schroeder, J. Cary, and W. P. Leemans, Phys. Rev. Lett. **95**(14), 145002 (2005).

[76] L. Mandel and E. Wolf, *Optical coherence and quantum optics* (Cambridge university press, New York, 1995).

[77] J. D. Lawson, IEEE Trans. Nucl. Sci. **NS-26**(3), 4217 (1979).

[78] R. B. Palmer, Part. Accel. **11**(2), 81 (1980).

[79] J. V. Lepore and R. J. Riddell, Jr., Phys. Rev. D **13**(8), 2300 (1976).

[80] T. Watanabe, J. Sugahara, T. Yoshimatsu, S. Sasaki, Y. Sugiyama, K. Ishi, Y. Shibata, Y. Kondo, K. Yoshii, T. Ueda, *et al.*, Nucl. Instrum. Methods Phys. Res. A **480**, 315 (2002).

[81] A. J. Alcock and P. B. Corkum, Can. J. Phys. **57**, 1280 (1979).

[82] P. B. Corkum, IEEE J. Quantum Electron. **21**(3), 216 (1985).

[83] C. Rolland and P. B. Corkum, J. Opt. Soc. Am. B **3**(12), 1625 (1986).

[84] J. A. Valdmanis, G. Mourou, and C. W. Gabel, Appl. Phys. Lett. **41**(3), 211 (1982).

[85] J. Shan, A. S. Weling, E. Knoesel, L. Bartels, M. Bonn, A. Nahata, G. A. Reider, and T. F. Heinz, Opt. Lett. **25**(6), 426 (2000).

[86] F. G. Sun, Zhiping Jiang, and X.-C. Zhang, Appl. Phys. Lett. **73**(16), 2233 (1998).

[87] Zhiping Jiang and X.-C. Zhang, Appl. Phys. Lett. **72**(16), 1945 (1998).

[88] B. Yellampalle, K. Y. Kim, G. Rodriguez, J. H. Glownia, and A. J. Taylor, Appl. Phys. Lett. **87**(21), 211109 (2005).

[89] K. Y. Kim, B. Yellampalle, G. Rodriguez, R. D. Averitt, A. J. Taylor, and J. H. Glownia, Appl. Phys. Lett. **88**(4), 041123 (2006).

[90] S. P. Jamison, Jingling Shen, A. M. MacLeod, W. A. Gillespie, and D. A. Jaroszynski, Opt. Lett. **28**(18), 1710 (2003).

[91] Q. Wu and X.-C. Zhang, Appl. Phys. Lett. **70**(14), 1784 (1997).

[92] Q. Wu, T. D. Hewitt, and X.-C. Zhang, Appl. Phys. Lett. **69**(8), 1026 (1996).

[93] M. Born and E. Wolf, *Principles of Optics* (Pergamom Press, Oxford, 1980).

[94] S. Feng, H. G. Winful, and R. W. Hellwarth, Opt. Lett. **23**(5), 385 (1998).

[95] D. You and P. H. Bucksbaum, J. Opt. Soc. Am. B **14**(7), 1651 (1997).

[96] Zhiping Jiang and X.-C. Zhang, Opt. Express **5**(11), 243 (1999).

[97] Z. L. Horváth and Zs. Bor, Phys. Rev. E **63**(2), 026601 (2001).

[98] U. Fuchs, U. Zeitner, and A. Tünnermann, Opt. Express **13**(10), 3852 (2005).

[99] P. L. Richards, J. Appl. Phys. **76**(1), 1 (1994).

[100] Q. Chen, M. Tani, Zhiping Jiang, and X.-C. Zhang, J. Opt. Soc. Am. B **18**(6), 823 (2001).

[101] G. Gallot and D. Grischkowsky, J. Opt. Soc. Am. B **16**(8), 1204 (1999).

[102] J. Faure, J. van Tilborg, R. A. Kaindl, and W. P. Leemans, Opt. Quantum Electron. **36**(8), 681 (2004).

[103] A. Manabe, A. Mitsuishi, and H. Yoshinaga, Jap. J. Appl. Phys. **6**(5), 593 (1967).

[104] G. Gallot, Jiangquan Zhang, R. W. McGowan, T.-I. Jeon, and D. Grischkowsky, Appl. Phys. Lett. **74**(23), 3450 (1999).

[105] D. T. F. Marple, J. Appl. Phys. **35**(3), 539 (1964).

[106] Q. Wu and X.-C. Zhang, Appl. Phys. Lett. **68**(12), 1604 (1996).

[107] A. N. Pikhtin, V. T. Prokopenko, and A. D. Yas'kov, Sov. Phys. Semicond. **10**(11), 1224 (1976).

[108] A. S. Barker, Jr., Phys. Rev. **165**(3), 917 (1968).